Drivers of Solar Coronal Dynamics

Deborah Baker

Mullard Space Science Laboratory
Department of Space and Climate Physics
University College London

A thesis submitted to University College London
for the degree of Doctor of Philosophy

October 2010

I, Deborah Baker, confirm that the work presented in this thesis is my own. Where information has been derived from other sources, I confirm that this has been indicated in the thesis.

List of Publications:

1. Murray, M., **Baker, D.**, van Driel-Gesztelyi, L.: Outflows at the Edges of an Active Region in a Coronal Hole: A Signature of Active Region Expansion?, *Sol. Phys.*, **261**, 253, 2010.

2. **Baker, D.**, *et al.*: Identifying the Main Driver of Active Region Outflows, *ASPC*, submitted, 2010.

3. **Baker, D.**, *et al.*: Magnetic Reconnection along Quasi-Separatrix Layers as a Driver of Ubiquitous Active Region Outflows, *ApJ*, **705**, 926B, 2009.

4. **Baker, D.**, *et al.*: Signatures of Interchange Reconnection: STEREO, ACE and Hinode Observations Combined, *Ann.Geophys.*, **27**, 3883B, 2009.

5. **Baker, D.**, *et al.*: Intensification of Plasma Upflows in an Active Region-Coronal Hole Complex: A CME Precursor, *ASPC*, **415**, 75B, 2009.

6. Murray, M., van Driel-Gesztelyi, L., **Baker, D.**: Simulations of emerging flux in a coronal hole: oscillatory reconnection, *A&A*, **494**, 329M, 2009.

7. Harra, L.K., Sakao, T., Mandrini, C.H., Hara, H., Imada, S., Young, P. R., vanDriel-Gesztelyi, L., **Baker, D.**: Outflows at the Edges of Active Regions: Contribution to Solar Wind Formation?, *ApJ*, **676L**, 159H, 2008.

8. **Baker, D.**, *et al.*: Hinode EIS and XRT Observations of Hot Jets in Coronal Holes - Does the Plasma Escape?, *ASPC*, **397**, 23B, 2008.

9. **Baker, D.**, van Driel-Gesztelyi, L., Attrill, G. D. R., *AN*, **328**, 773B, 2007.

10. Culhane, L., Harra, L. K., **Baker, D.**, van Driel-Gesztelyi, L., Sun, J., Doschek, G. A., Brooks, D. H., Lundquist, L. L., Kamio, S., Young, P. R., and Hansteen, V. H.: Hinode EUV Study of Jets in the Suns South Polar Corona, *PASJ*, **59**, 751, 2007.

Abstract

Multi-wavelength observations from various solar missions have revealed the dynamic nature of the solar corona. The work presented in this thesis represents a contribution towards understanding some of the physical mechanisms that drive the activity observed in the corona and out into the heliosphere. In particular, the role of reconnection in active region (AR) outflows and AR-coronal hole (CH) interactions using observations of the associated plasma flow signatures and their relationship to the underlying magnetic field topology is examined.

Persistent outflows discovered by *Hinode* EUV Imaging Spectrometer (EIS) occur at the boundary of all ARs over monopolar magnetic regions. It is demonstrated that the outflows originate from specific locations of the magnetic topology where field lines display strong gradients of magnetic connectivity, namely quasi-separatrix layers (QSLs). Magnetic reconnection at QSLs is shown to be a viable mechanism for driving AR outflows which are likely sources of the slow solar wind.

Observational signatures and consequences of interchange reconnection (IR) are identified and analyzed in a number of solar configurations. Jet light curves of several emission lines show a post-jet enhancement in cooler coronal lines which has not been previously observed. In the case of emerging flux near a CH, it is shown that closed loops forming between the AR and CH leads to the retreat of the CH and a dimming of the corona in the vicinity of the like-polarity region. A filament eruption and coronal mass ejection (CME) from an AR inside a CH are observed from the solar disk into the heliosphere. An anemone structure of the erupting AR and the passage in-situ of an interplanetary CME (ICME) with open magnetic topology are interpreted to be a direct result of IR.

Plasma flows resulting from the interaction between an AR embedded in a CH observed by *Hinode* EIS are investigated. Velocity profiles of hotter coronal lines reveal intensification in outflow velocities prior to a CME. The AR's plasma flows are compared with 3D magnetohydrodynamic (MHD) numerical simulations which show that expansion of AR loops drives outflows along the neighboring CH field. The intensification of outflows observed prior to the CME is likely to result from the expansion of a flux rope containing a filament further compressing the neighboring CH field.

Acknowledgements

It is impossible to express my gratitude to my academic supervisor, Dr. Lidia van Driel-Gesztelyi. Lidia is not only a world class scientist but one of the most decent and generous people I have had the honor to know in all of my years. Her support, encouragement, patience, curiosity, and inspiration have been constant throughout my time at MSSL. You turned a bond trader into a scientist.

Far too many people to mention individually have assisted in so many ways during my PhD at MSSL. I am indebted to all of you. In particular, I would like to thank Prof. Louise Harra who has provided so many opportunities to be involved with the 'cool stuff' like EIS and has made it possible to remain at MSSL in solar physics. Dr. Sarah Matthews, Prof. Len Culhane, and Dr. Lucie Green have never hesitated in sharing their knowledge and kindness. The G01 crew kept me sane, especially Dr. Gemma Attrill. Many thanks to all of my co-authors, especially Dr. Alexis Rouillard.

I have the greatest respect and fondness for the QSL gang of Prof. Cristina Mandrini, Dr. Pascal Démoulin, and of course Lidia. You taught me the power of collaborative science. I hope this is just the beginning.

Prof. Saku Tsuneta is a titan of solar physics who always made time for this PhD student. I am grateful for his support, wisdom, and straight forward approach.

A penultimate thank you goes to my parents, Mary Jane and Bob McNally. They deserve far more credit than I can ever give them.

My final, and most heartfelt, acknowledgment must go to my husband, Mike. Mike has been my safety net for this high-wire journey. I could not have done it without him and for this and everything else, he has my everlasting love.

Contents

List of Figures

List of Tables

Chapter 1

Introduction

1.1 Solar Basics

The Sun is a main sequence star of spectral class G2V. Stars in this spectral class have as their energy source nuclear fusion of hydrogen into helium in their cores. Energy generated in the core is transported to the surfaces by convection. It is the coupling of convective motions with differential rotation that is ultimately responsible for stellar dynamos, magnetic fields, and stellar activity. Table 1.1 lists the vital statistics of the Sun (photospheric composition from `http://imagine.gsfc.nasa.gov/docs/ask_astro/answers/961112a.html`).

1.2 Inside the Sun

The interior structure of the Sun is thought to consist of an energy source at its core from 0 to 0.25 R_{sun}, a radiative zone from 0.25 to 0.71 R_{sun} where the energy generated in the core is transported by radiation, and a convective zone from 0.71 R_{sun} to the surface where convection is the main energy transport mechanism. Figure 1.1 shows how temperature, density, and composition change as a function of radius within the interior (Bahcall and Ulrich, 1988). Broadly, density and temperature fall off rapidly within the core whereas the hydrogen fraction and luminosity increase within the core and level off in the outer two-thirds of the Sun.

Table 1.1: Solar statistics.

Mass (M_{sun})	1.989×10^{30} kg
Radius (R_{sun})	696,000 km
Mean Density	1.410 kg m^{-3}
Irradiance (at 1 AU)	1.368 kW m^{-2}
Luminosity	3.85×10^{23} kW
Effective Temperature	5,778 K
Age	4.6×10^{9} years
Rotational Period	
at Equator	25 days
at Poles	35 days
Rotational speed (at the photosphere)	2 km s^{-1}
Magnetic Field Strength (typical values)	
General Solar Field (at the photosphere)	10^{-4} T
Large Sunspot	0.4 T
Small Sunspots or Pores	0.2 T
Plage	0.02 T
Active Region Loops in the Corona	0.01 T
Chromospheric Network Boundaries	0.003 T
Prominence	0.001 - 0.01 T
Photospheric Composition	% by number / % by mass
Hydrogen	91.2 / 71.0
Helium	8.7 / 27.1
Oxygen	0.078 / 0.97
Carbon	0.043 / 0.40
Nitrogen	0.0088 / 0.096
Silicon	0.0045 / 0.099
Magnesium	0.0038 / 0.076
Neon	0.0035 / 0.058
Iron	0.0030 / 0.14
Sulfur	0.0015 / 0.040

1.2.1 Core

The energy source of the Sun is in its core where the temperature is 15×10^6 K and the density is 1.48×10^5 kg m^{-3}. The proton-proton chain is the dominant energy generation process that converts hydrogen into helium by fusing together four protons. In order for fusion to take place, the kinetic energy of the protons must be greater than the electrostatic force of like charges. The 3-stage process begins with the fusion of two protons and the release of a positron and neutrino:

$$p + p \rightarrow {}^{2}\mathrm{D} + \mathrm{e}^{+} + \nu_{\mathrm{e}}, \tag{1.1}$$

where p is a proton, ^2D is a deuteron, e^+ is a positron, and ν_e is a neutrino. The next reaction is the fusion of a third proton with the deuteron to produce a helium isotope and a gamma ray:

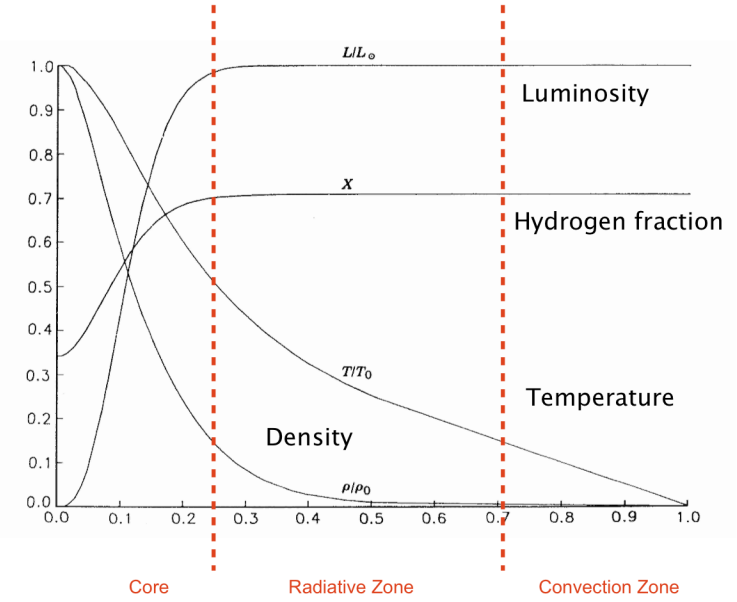

Figure 1.1: Temperature, density, luminosity, and composition models in the solar interior. Adapted from Bahcall and Ulrich (1988).

$$^2\mathrm{D} + \mathrm{p} \rightarrow \ ^3\mathrm{He} + \gamma, \tag{1.2}$$

where He is helium and γ is a gamma ray. Finally, an alpha particle is created by the fusion of two helium nuclei:

$$^3\mathrm{He} + ^3\mathrm{He} \rightarrow \ ^4\mathrm{He} + \mathrm{p} + \mathrm{p}. \tag{1.3}$$

Throughout the fusion process, energy is released through Einstein's equivalence of mass and energy (Harra and Mason, 2004). Total energy released is 4.3×10^{-12} J with neutrinos removing a small portion in the process (Harra and Mason, 2004).

1.2.2 Radiative Zone

In the radiative zone, energy diffuses outward from the core. Heat is transferred by ions emitting photons which travel a short distance before being reabsorbed by other ions. Photons move very slowly from the core to the solar surface as they are Thomson scattered by free electrons. The random walk travel time for a photon to reach the surface is approximately 3000 years.

Occasionally, a proton or atomic nucleus will capture one or more electrons, however, at the bottom of the radiative zone close to the core, the temperature is greater than 7 MK, and the electrons are readily stripped away. The gas is

fully ionized. Further from the core towards the top of the radiative zone, the temperature is low enough (1 - 2 MK) for atoms, especially heavier elements such as iron, oxygen, carbon, and nitrogen, to keep their orbiting electrons. This results in increasing absorption of radiation and increasing opacity of the gas.

1.2.3 Convection Zone

As the temperature cools with increasing R_{sun}, opacity increases so that it is more difficult for radiation to escape. Heat becomes trapped and the gas becomes unstable. This instability is the driving force of convection. Convection occurs at approximately 1 MK where the temperature gradient becomes greater than the adiabatic gradient which is the rate at which the temperature would fall if a 'parcel' of gas has risen without exchanging heat with the surrounding medium. If a 'parcel' of gas is less dense than its surroundings, it rises. Whether this happens depends on the rate at which the 'parcel' expands due to decreasing pressure and/or the rate at which the surrounding density decreases with height. Once convection begins, hot gas is carried from the base of the convection zone, where the temperature is 1 - 2 MK, to the solar surface surface where the temperature is 6,000 K. The gas then cools and falls back to the base of the convection zone to repeat the process. These convective cells continually transfer gas and magnetic field from the bottom of the convective zone to the surface and back.

1.2.4 Helioseismology

The solar interior is mainly observed indirectly, therefore, subsurface structures and processes must be inferred from measurements made at the solar surface (or photosphere - see §1.3.1). Small amplitude (0.1 km s^{-1} - 0.5 km s^{-1}) and low frequency oscillations (2.5 - 4.5 mHz or approximately 5 min) were first detected at the solar surface in 1960. Over the years, detailed study of the oscillations has provided information about the Sun's interior. By measuring travel times and resonant frequencies of solar oscillations, internal properties such as the sound speed, density stratification, differential rotation, mass flows, and temperature are inferred and used to constrain solar interior models.

The source of the solar oscillations, or waves, is believed to be the turbulent processes (e.g. fluctuating Reynolds stresses and gas pressure) of the convective region in the subphotospheric layers of the Sun. Ulrich (1970) and Leibacher and Stein (1971) proposed that the oscillations are due to standing acoustic waves trapped in

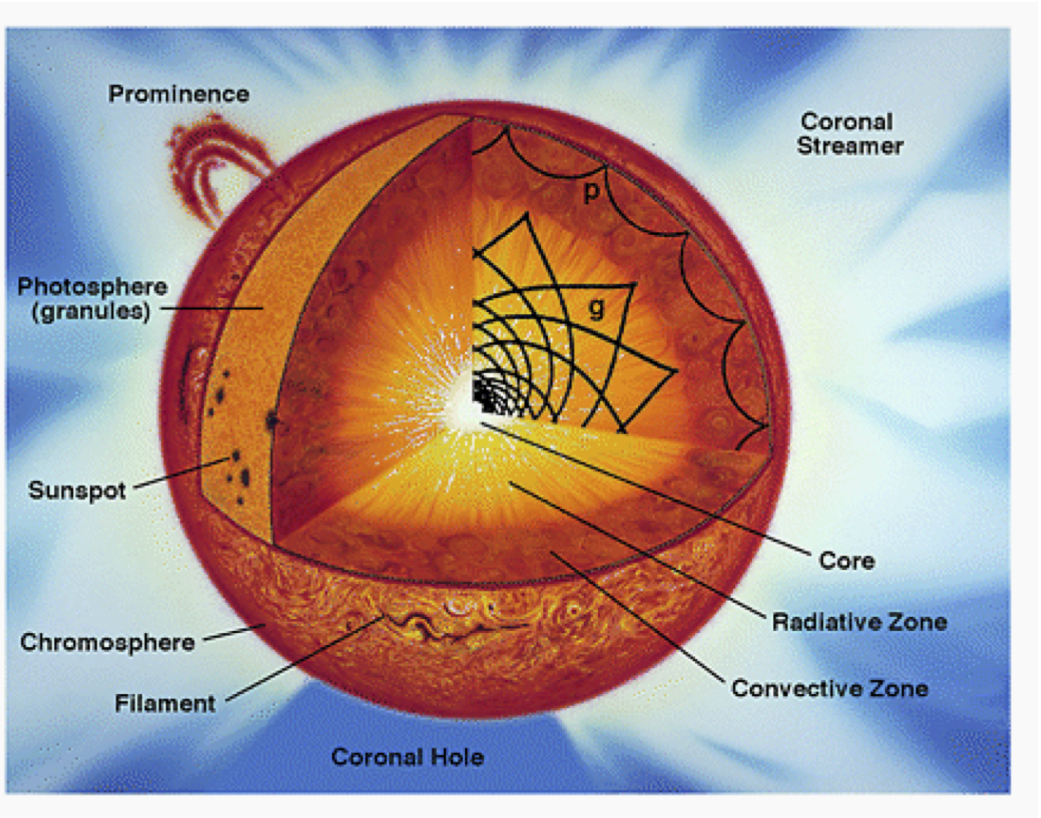

Figure 1.2: Solar interior from SOHO.

cavities inside the Sun. A cavity is bounded at the top by the steep density gradient near the solar surface and at the bottom by refraction. As an acoustic wave propagates from the solar surface to the interior at an angle, the upper edge of its wavefront travels faster than its lower edge due to the fact that the sound speed, which is proportional to temperature $T^{1/2}$, increases towards the center. This leads to the arc-shaped travel paths shown in Figure 1.2 and total internal refraction. There are three types of wave modes in the Sun:

- high-amplitude, high frequency acoustic p-modes (restoring force is pressure),
- low-frequency gravity g-modes (restoring force is buoyancy), and
- fundamental f-modes (or surface gravity modes).

P-mode waves provide the means by which the outer regions of the Sun can be probed whereas unobserved g-mode waves have very weak photospheric signatures. G-mode waves reach their highest amplification in the solar core.

There are a number of significant results from the study of solar seismic waves, two of which are briefly discussed here. First, the angular velocity as a function of latitude and depth for most of the solar interior has been inferred. Angular velocity

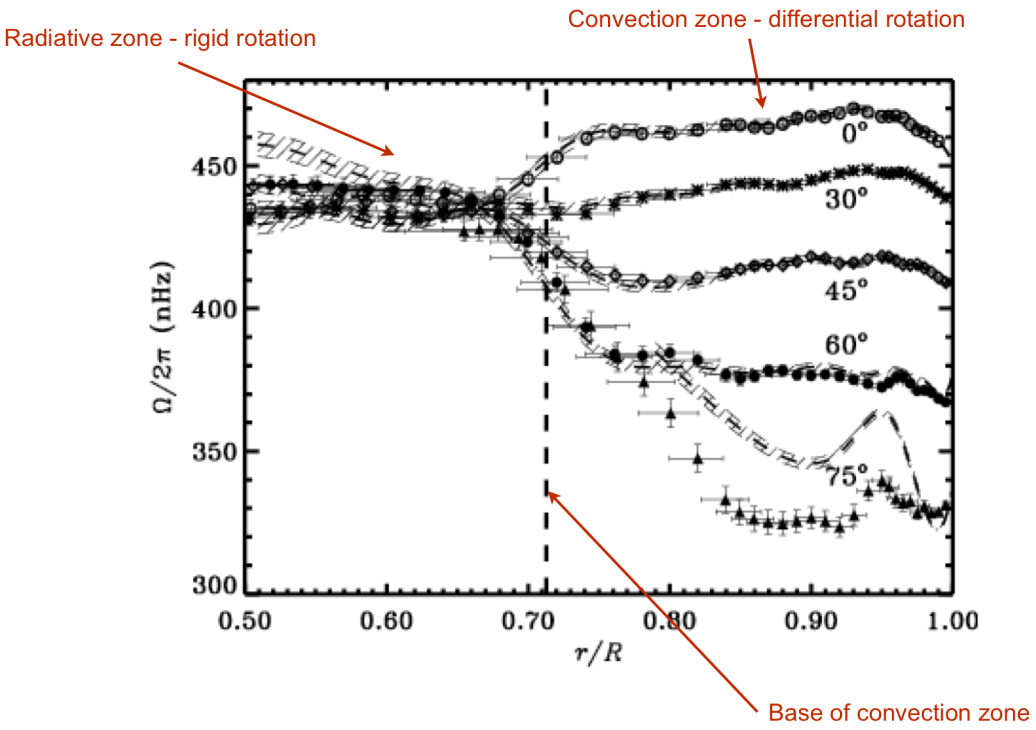

Figure 1.3: Rotation rate as a function of depth and latitude inside the Sun. Adapted from Thompson *et al.* (2003).

profiles are shown in Figure 1.3 (Thompson *et al.*, 2003). Within the convection zone, the rotation rate decreases towards the poles by approximately one third. In the activity belt at approximately 30°, the differential rotation rate in the convection zone is almost the same as that on the surface. In addition, a thin layer of relatively large radial shear is found at 0.95 R_{sun} for low to mid-latitudes where the rotation rate increases with depth. This is evident in the angular velocity profiles for 0°, 30°, and 45° latitudes in Figure 1.3. The rotation rate in the radiative zone (< 0.71 R_{sun}) is nearly uniform, roughly similar to the rates at mid-latitudes.

Another major success of helioseismology is the identification of a thin transition layer, the tachocline, between the differentially rotating convection zone and rigid rotation of the radiative zone (Charbonneau *et al.*, 1999). The transition occurs just at or below the base of the convection zone at approximately 0.69 R_{sun}. The tachocline has a strong radial rotational shear and is generally believed to play an important role in the generation of large scale magnetic fields in the solar dynamo (see §1.4.1).

Table 1.2: Solar atmosphere parameters. From Schrijver and Siscoe (2009).

Region	n (m^{-3})	n_e/n_H	T (K)	B (gauss)	β
Photosphere	10^{23}	10^{-4}	6×10^3	1 - 1500	> 10
Chromosphere	10^{19}	10^{-3}	1 - 2×10^4	10 - 100	10 - 0.1
Transition Region	10^{15}	1	10^4 - 10^6	1 - 10	10^{-2}
Corona	10^{14}	1	10^6	1 - 10	10^{-2} - 1

1.3 Solar Atmosphere

The solar atmosphere is comprised of the photosphere, chromosphere, transition region (TR) and corona. Table 1.2 summarizes the key physical parameters of the four layers. In general, the photospheric thermal pressure (10^4 Pa) is much greater than the magnetic pressure (< 1 Pa). This is very different to the chromosphere where the thermal pressure falls off exponentially and the magnetic pressure falls off much less rapidly. Approaching the top of the chromosphere where plasma β is greater than unity, the plasma's ability to radiate diminishes while the magnetic field becomes more dominant (see §1.7.4). Any heat input from below would then raise the plasma temperature to more than 1 MK as is observed in the corona. The corona is entirely dominated by the evolution of the magnetic field which in turn is driven by motions in the photosphere. A brief account of the photosphere, chromosphere, and TR is provided below. The solar corona is treated more extensively in §1.7.

1.3.1 Photosphere

The lower boundary of the solar atmosphere is the visible surface of the Sun or photosphere ($= 1$ R_{sun}). It is a thin layer of tens - hundreds of kilometers. Sunspots are the most prominent feature on the visible surface. They appear as dark regions of lower temperature, approximately 4,000 - 6,000 K, where strong magnetic field dominates the convective motions. Typical field strength can exceed a few kilogauss (or tenths of a tesla). The sunspots are roughly circular and range in size from a few megameters to tens of megameters in diameter. Two sunspots of opposite polarity form a bipolar region or active region (AR). The solar magnetic cycle determines the surface distribution of the sunspots which varies over approximately 11 years (see §1.4.2).

Sunspots cover a small area of the visible Sun ($< 1\%$). The rest of the surface is formed of granules that have dimensions of order 1 Mm though smaller granules exist. Their lifetimes are between 10 and 20 minutes. Granules are separated by dark, cooler intergranular lanes. The granulation is caused by convection currents of

plasma within the convective zone just below the photosphere and thus, it is a surface signature of the convective motions. Doppler measurements of the solar surface show that granules have a typical upward velocity of 2 km s^{-1} and intergranular lanes are associated with downward motions. Larger-scale convection patterns are outlined by the quiet-Sun network (also known as the chromospheric network) made of supergranules of roughly 20 - 30 Mm. They have a lifetime of approximately 1 - 2 days and typical velocities in the range of 0.3 - 0.5 km s^{-1}. Fluid motions within supergranules concentrate bundles of magnetic field lines in the network i.e. along the supergranular boundaries. Supergranules are suggestive of larger convection cells extending deeper into the solar interior (Schrijver and Siscoe, 2009). See Figure 1.4 for a cartoon depicting among other things, the relationship between granules, intergranular lanes, the network, and supergranulation.

The photosphere is characterized by high opacity. Continuous absorption in the ultraviolet (UV) and infrared wavelength ranges is the dominant source of the opacity. In the photosphere, there are neutral atoms of mainly hydrogen, some ions, and free electrons. The free electrons attach themselves to neutral hydrogen atoms to form the negative hydrogen ion, H^-. H^- ions absorb photons with wavelengths from the visible to the infrared. Though the process of electron capture is rare, the abundance of H^- ions is sufficient to be the main source of the photosphere's high opacity.

The predominant wavelength range of the photosphere is in the visible section of the solar spectrum. The strongest lines include the Fraunhofer absorption lines, especially the Balmer series (n = 2), and resonance lines Na I D and Ca II H and K.

1.3.2 Chromosphere

The temperature of the solar atmosphere begins to rise with height from the temperature minimum of approximately 4,000 K at the top of the photosphere. Across roughly 2,500 km in height, the chromospheric temperature increases to 20,000 K. Characteristic features of this narrow layer are observed in the optically thick Hα line, which is photoelectrically controlled, and the collisionally controlled Ca II H and K lines (Harra and Mason, 2004). The chromospheric network is visible in the Hα and Ca II K lines as are sunspots. Sunspots are surrounded by patches of bright emission, or plage regions, associated with concentrations of magnetic fields. Dark filaments consisting of dense, cool plasma suspended above the solar surface by magnetic field are viewed in absorption on the solar disk but are observed in emission at the solar limb and are referred to as prominences (see §1.7.9).

A common and dynamic chromospheric feature are spicules. These are thin, elongated, jet-like structures that delineate the network and are also known as mottles and fibrils. De Pontieu *et al.* (2007) classified spicules into two categories based on *Hinode* Solar Optical Telescope (SOT) Ca II observations. Type I spicules (fibrils) have lifetimes of 3 - 10 min and propel cool matter to coronal heights with velocities of 20 - 30 km s^{-1}. Type II spicules (known as chromospheric jets) are highly dynamic in that they form in approximately 10 s, have lifetimes of 10 - 100 s and are more violent with velocities of order 50 - 150 km s^{-1}. De Pontieu *et al.* (2009) suggest that chromospheric jets play a significant role in the heating of the corona (§1.7.1.2). See Figure 1.4 for Type I spicules shown as fibrils and Type II spicules.

1.3.3 Transition Region

The TR is the interface between chromosphere and the corona. It is the least understood region of the solar atmosphere as it represents a boundary that demarcates a temperature jump from 20,000 K to 2 MK, a density jump of two orders of magnitude, a drastic change in plasma β environment (see §1.49), and a transition from non-force-free to force-free magnetic field (Aschwanden, 2005)). (See §1.32 for a discussion of magnetic topologies). The thickness of the TR varies across the solar atmosphere and may be vertical in some places where hot coronal structures penetrate downward (Golub and Pasachoff, 1997).

Simultaneous observations of spectral lines that originate in the chromosphere, TR, and corona reveal the chromospheric network is clear through the TR but becomes diffuse in the corona. This is suggestive of a canopy structure. Horizontal flows within the supergranular cells organize the chromospheric network by transporting and concentrating magnetic field lines along the network in the lower atmosphere. The bundles of magnetic field lines then spread out in the upper atmosphere as the magnetic field expands in the lower plasma β in the TR and corona. See Figure 1.4 for a cartoon representation of what Gabriel (1976) called the magnetic canopy.

The TR is observed primarily in the UV wavelength range. Two optically thick Fraunhofer lines are found in this range - Mg II H, K and Lyman α (n = 2 to n = 1 transition) lines. Since hydrogen is ionized at TR temperatures, emission is dominated by such ions as Mg II, C IV, O IV and V, and Si IV. These are optically thin spectral lines formed at higher temperatures.

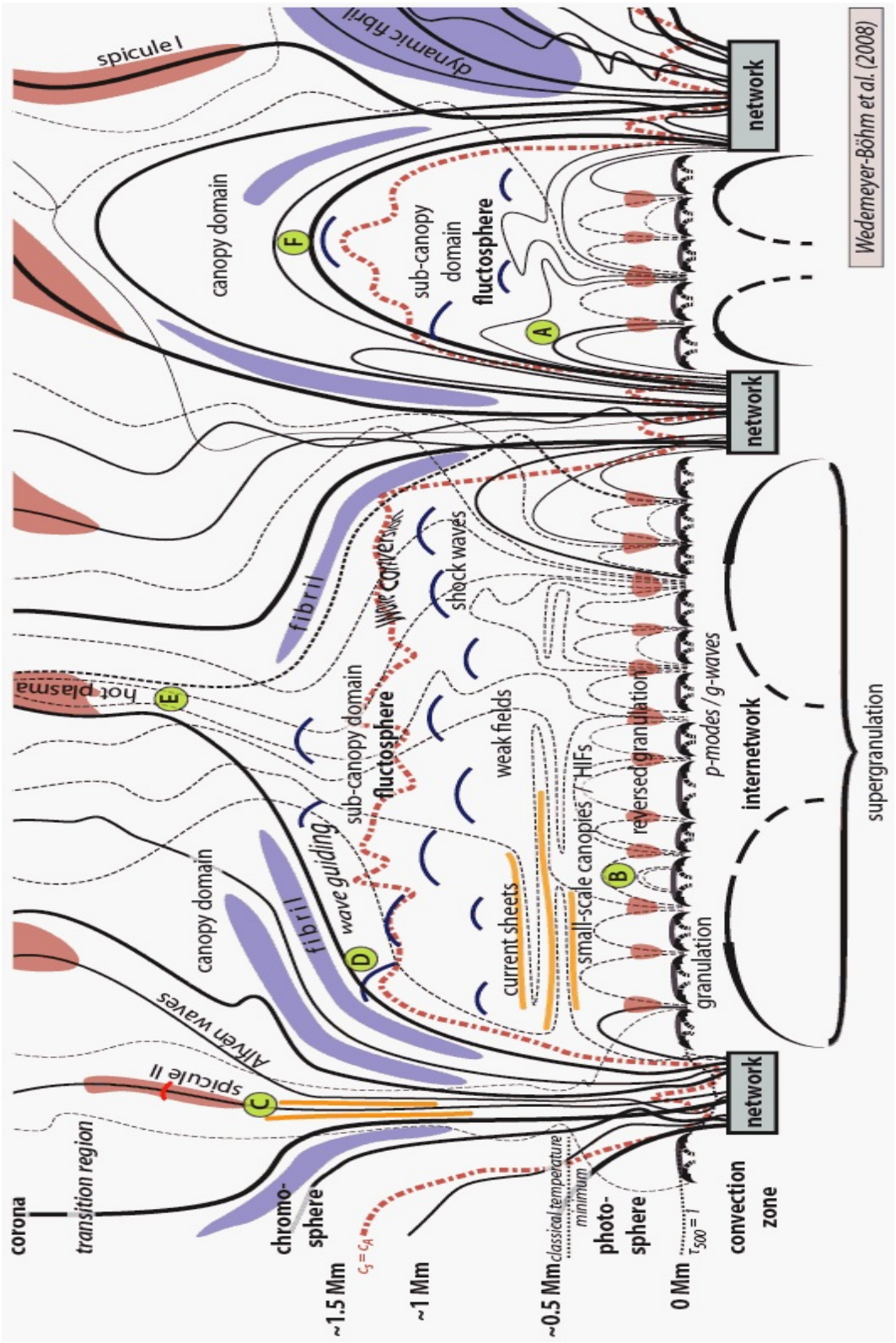

Figure 1.4: Schematic view of the domains in the solar atmosphere that summarizes most of the structures and processes described in sections 1.2.3 - 1.3.3. From Wedemeyer-Böhm and Wöger (2008).

1.3.4 Corona

The solar corona, which is the focus of this thesis, is described in detail in §1.7.

1.4 The Magnetic Sun

1.4.1 Solar Dynamo

A conductor contains a large number of free electrons. When it is forced to move through a magnetic field, the electrons experience a force and an electric current is generated. In turn, the current flows through the conductor and generates an additional magnetic field. This process describes a simple dynamo. The likely location of the highly complex solar dynamo is the tachocline where plasma motions generate electric currents which leads to an amplification of the original magnetic field to a field strength of the order of 10 T. Essentially, kinetic energy is converted into magnetic energy. Basic processes in the creation of the solar magnetic field in the dynamo can be summarized by considering the mean-field dynamo theory which suggests that the evolution of the mean magnetic field is a function of the following (Miesch, 2005):

- conversion of poloidal to toroidal field by differential rotation,
- amplification of magnetic fields by fluctuating motions of the rotational shear and stretching,
- generation of electromotive forces by turbulent convection and other processes such as shear instabilities, and
- destruction of magnetic field by turbulent diffusion.

1.4.2 Solar Magnetic Cycle

The solar dynamo is far more complex than what is described by the mean-field dynamo theory. Any dynamo theory or model of the generation of the solar magnetic field must account for the Sun's magnetic cycle and solar activity.

There are three main components to the solar magnetic cycle - the generation of strong, large-scale magnetic fields that reverse polarity every 11 years; the rise

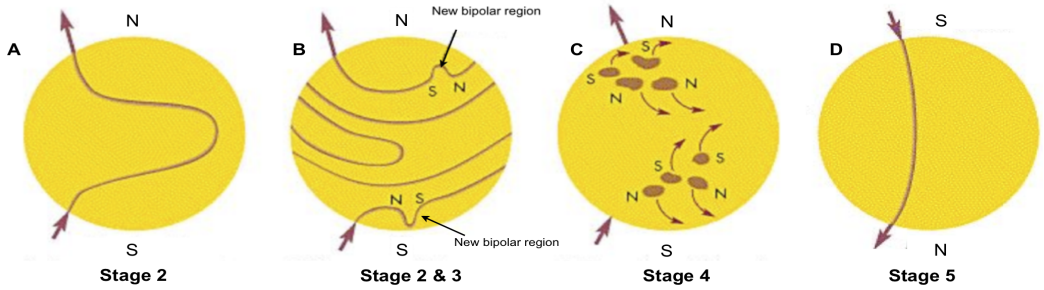

Figure 1.5: Stages 2 - 5 of the Babcock Model. A: Stage 2 - Differential rotation begins to change the magnetic field from poloidal to toroidal configuration. B: Stages 2 and 3 - More rotation leads to twisting and stretching of magnetic field. When the field is sufficiently amplified, magnetic buoyancy leads to the emergence of new Ω-shaped magnetic loops through the solar surface within $\phi \pm 30°$ activity latitudes (Spörer's law). N leading polarity is the same as the polarity of the northern hemisphere and visa versa (Hale's law). C: Stage 4 - Bipolar regions have tilts (Joy's law) so that the following polarities are closer to the poles. As the field disperses, following polarities migrate towards the poles and neutralize the field until polarity reversal occurs. Leading polarities migrate with higher probablitiy towards the equator where they cancel with opposite leading polarity flux from the other hemisphere. D: Stage 5 - The new cycle begins with a poloidal field of reversed polarity from that of the previous cycle. (Figure has been adapted from original - Copyright ©1998 The McGraw-Hill Companies).

of the magnetic field from the interior and its emergence at the photosphere; and, the processing, dispersal, and removal of the magnetic field from the photosphere. Within these main stages of the cycle, there are several observations which produce significant complications for dynamo models including the periodicity of the cycle, the drift towards the solar equator of activity latitude, the systematic behavior of bipolar regions, and the reversal of polar magnetic fields. Babcock (1961) proposed a qualitative model which describes the 22-year cycle in five stages (see Figure 1.5).

1. Stage 1 - The magnetic field of a new cycle is approximated by a dipole field aligned along the solar rotation axis. This is a poloidal field configuration. (Year 1 of new cycle at solar minimum).

2. Stage 2 - Differential solar surface rotation results in the twisting, stretching, and bundling of the magnetic field into a toroidal configuration (Figure 1.5A). In the process, the field is amplified.

3. Stage 3 - Ω-shaped loops emerge through the photosphere to form a bipolar AR, or a pair of sunspots, with leading and following polarities. According to Hale's polarity law (Hale and Nicholson, 1925), the leading polarity of the AR in one hemisphere is opposite to that of the leading polarity in the other hemisphere and the polarities reverse in a new cycle. Leading polarities also have the same polarity as the pole of the solar hemisphere into which they have emerged. Figure 1.6 shows Hale's law for the period 1975 to 2010.

   As stated by Spörer's law, new bipolar regions tend to appear between 30° to

45° latitude (ϕ) at the beginning of a new cycle (Figure 1.5B). Intensification occurs most rapidly at $\phi \pm 30°$ because of the $\sin^2\phi$ term in the equation for solar differential rotation for magnetic features which is:

$$\Omega(\phi) = 14.38 - 1.95 \sin^2 \phi - 2.17 \sin^4 \phi. \quad (1.4)$$

Activity shifts towards lower latitudes as the cycle progresses to form the famous butterfly pattern. Figure 1.7 contains the daily sunspot area for solar cycles dating back to the late 1800s. (Years 3^+ of new cycle including solar maximum period at approximately halfway through the 11 year period).

4. Stage 4 - The magnetic field in each hemisphere is neutralized and subsequently reversed as a result of the systematic tilt of bipolar field (Joy's Law). Howard (1991) deduced from Mount Wilson data that the average tilt angle of all sunspot groups during the period 1917 to 1985 was 4.2° ± 0.18°. In general, magnetic flux of bipolar regions cancels with the remnant flux in the surrounding areas in each hemisphere, however, <1% of following polarities succeeds to reach the nearest pole. At first, the existing polar field is neutralized but, eventually the polarity is reversed. Leading polarity remnant flux migrates towards the solar equator and cancels with the opposite polarity flux of the other hemisphere (Figure 1.5C). Due to the tilt, there is a higher probability for the following polarity to reach the pole and the leading polarity to cancel across the equator. Polar reversal is evident in Figure 1.6 as the (blue) negative polarity of the northern polar region of the current cycle followed the (yellow) positive polarity of the previous cycle. (Just after solar maximum period of new cycle).

5. Stage 5 - The process starts again after approximately 11 years with a poloidal field configuration opposite to that of the previous cycle (Figure 1.5D).

Babcock's qualitative model has obvious short comings, as do the various dynamo models, however the main features of the solar cycle are addressed to varying degrees. The challenge is for all of the solar cycle features to be incorporated into theoretical and numerical models of the solar interior.

1.4.3 Large Scale Flux Emergence and Active Region Evolution

The solar flux budget is dominated by small-scale flux with a very short overturn time, however, large-scale flux determines the magnetic properties of the Sun (van

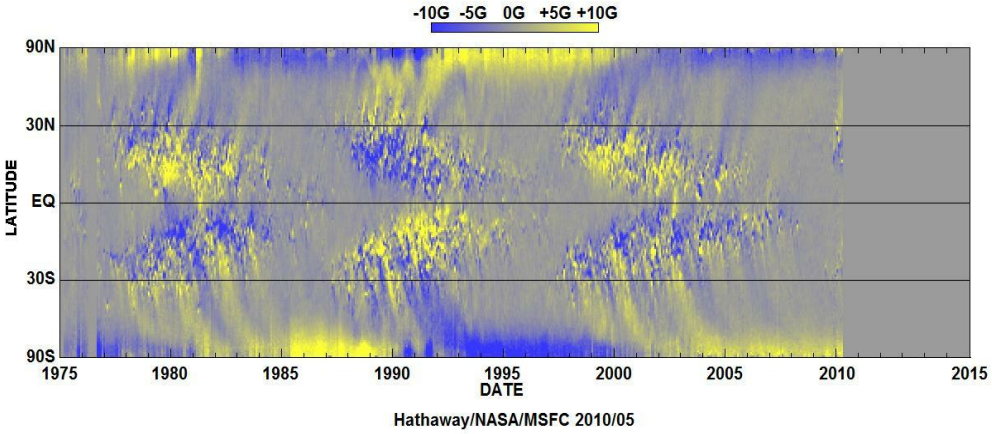

Figure 1.6: Plot of global solar magnetic field evolution during three solar cycles (1975 to 2010) illustrating the evolution of latitudinal patterns: the gradual shift in AR emergence sites, polar field reversal, and Hale's polarity law. Credit: Hathaway/NASA/MSFC 2010/05.

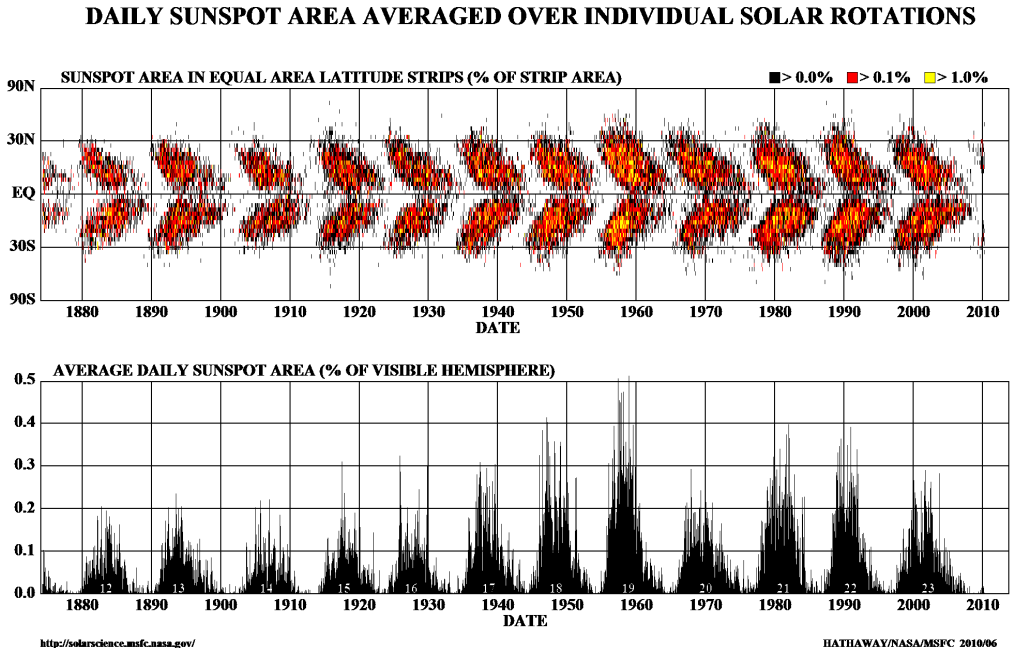

Figure 1.7: Cyclic solar activity since the late 1800s. Top panel - Classic butterfly diagram showing activity latitudes over time. Bottom panel - Daily sunspot area as a percentage of the visible hemisphere averaged over solar rotations provides a sense of solar cycle minimums and maximums for the same period. Hathaway/NASA/MSFC 2010/05.

Driel-Gesztelyi and Culhane, 2009). Large-scale flux is responsible for most of the solar activity such as solar flares and coronal mass ejections (CME). Here the focus will be on large-scale flux emergence forming ARs.

The life cycle of an AR begins with emergence of a buoyant magnetic flux tube that originates at the bottom of the convection zone. Flux tubes rise as a result of the magnetic buoyancy force. Consider a flux tube in local hydrostatic equilibrium with the surrounding plasma so that total external pressure is in balance with the internal pressure. Plasma β (§1.7.4) within the solar interior $\gg 1$ and the plasma surrounding the flux tube is considered free of magnetic field. For a depth h:

$$p_i(h) + \frac{B_i^2(h)}{2\mu_0} = p_e(h), \tag{1.5}$$

where p_i and p_e are the thermal internal and external pressures, B_i is internal magnetic field strength, and μ_0 is magnetic permeability. Assume for a given height the external and internal temperatures are equal, then the ideal gas law provides:

$$\frac{\rho_i(h)}{p_i(h)} = \frac{\rho_e(h)}{p_e(h)}, \tag{1.6}$$

where ρ_i and ρ_e are internal and external densities, therefore,

$$\rho_e(h) - \rho_i(h) = \rho_e(h)\frac{B_i^2(h)}{2\mu_0 p_e(h)}. \tag{1.7}$$

As the internal plasma density is lower than the external density, the flux tube becomes buoyant when ρ_e - $\rho_i > 0$. This occurs when the magnetic field is amplified to a field strength of approximately 10 T.

Flux emergence is far from a random process. There are three observationally established rules related to the organization of bipoles - the laws of Hale, Spörer, and Joy, all of which are briefly described in §1.4.2. Further, there is a tendency for ARs to form 'activity nests' where there is a higher emergence rate within and a likelihood to emerge in the vicinity of existing ARs (van Driel-Gesztelyi and Culhane (2009) and references therein).

ARs are fully developed within 3 - 5 days of emergence, however, they spend from many weeks to months decaying. Specifically, they spend 70 - 90% of their lifetimes in the decay phase (Harvey and Zwaan, 1993; van Driel-Gesztelyi and Culhane, 2009). Following polarities begin to deteriorate before the leading polarities. Magnetic complexity diminishes and the field spreads over an increasing area as it is dispersed by persistent large-scale flows in the photosphere and more rapidly evolving supergranular and granular convective flows (van Driel-Gesztelyi, 2002). Ohmic

diffusion and small-scale magnetic cancellation involving flux subtraction are the main methods by which flux is removed from the photosphere.

1.4.4 The Eruptive Sun

Distinguishing magnetic characteristics of ARs in which solar eruptive activity occurs include: flux emergence, high magnetic flux, complex magnetic topology, high magnetic shear, strong field gradients, high helicity, and high free energy content (van Driel-Gesztelyi and Culhane (2009) and references therein). It is beyond the scope of this thesis to expand on these topics, however, it is very clear that violent eruptive activity is associated with the solar magnetic field and free energy stored within it. A brief discussion of the standard flare and CME models follows, though the delineation between flare models and CME models is not clear. Many texts refer to a standard flare/CME model. Over the last few years, the so-called standard model has been increasingly put to the test by a powerful combination of new observations, numerical simulations, and 3D magnetic modeling.

1.4.5 Flares

A solar flare is an explosive event, releasing energy up to 10^{25} J . During the process, free magnetic energy is converted to kinetic energy of fast particles, mass motions, and radiation in all wavelengths across the electromagnetic spectrum affecting all layers of the solar atmosphere. Flare emission is caused by hot plasma emitting in radio, visible, UV, and soft X-ray wavelengths and non-thermal energetic particles emitting in radio, hard X-ray and γ-ray wavelengths. Flares are categorized by their total soft X-ray emission in the 1 - 8 Å passband defined on a logarithmic scale from small A1 flares at 10^{-8} W m^{-2} to large X1 flares at 10^{-4} W m^{-2}. Large-scale flares are often associated with effects on the space environment at 1 astronomical unit (AU) and beyond.

Figure 1.8 shows typical soft X-ray, hard X-ray, and γ-ray light curves for a flare on 1989 March 6. The flare presents different appearances in terms of intensity vs. time at these wavelengths (and others not shown), thereby suggesting that flares have different phases. Essentially, there are three main phases of flare evolution:

1. pre-flare - a small amount of stored magnetic energy is released by some trigger mechanism and the soft X-ray flux rises slowly;

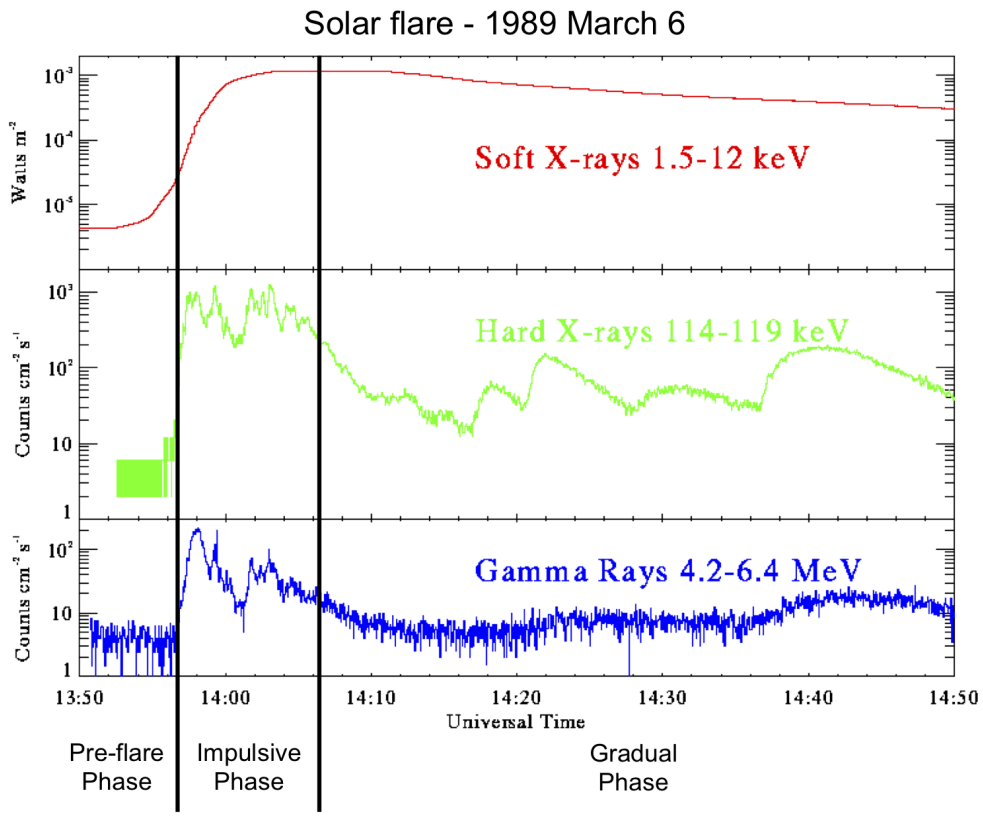

Figure 1.8: Soft X-ray, hard X-ray, and γ-ray light curves for a flare on 1989 March 6. The three main phases of flare evolution are indicated. Courtesy of K. Phillips.

2. impulsive - a sudden rapid release of energy accelerates particles to energies exceeding 1 MeV accompanied by radio, hard X-ray, and γ-ray emission; and,

3. gradual or main - energy is released more gradually and soft X-ray flux begins to decay.

One of the many flare models, the so-called CSHKP standard flare model (Carmichael, 1964; Sturrock, 1966; Hirayama, 1974; Kopp and Pneuman, 1976), has evolved over several decades and it applies to the classic two-ribbon flares. Figure 1.9 shows a schematic 2D view of the standard flare model from Lin and Forbes (2000). The illustration incorporates most of the physical processes that occur during flares and the observational consequences of the processes.

The basic scenario involves the build up of stored magnetic energy in the corona. A filament comprised of cool, dense plasma forms and is suspended in the magnetic field along the magnetic inversion line. As the magnetic field expands as its non-potentiality increases, the filament rises and a current sheet above the neutral line forms and gets stretched (see bottom panel of Figure 1.9). When the current sheet becomes thin enough, reconnection takes place and the filament and/or coronal mass

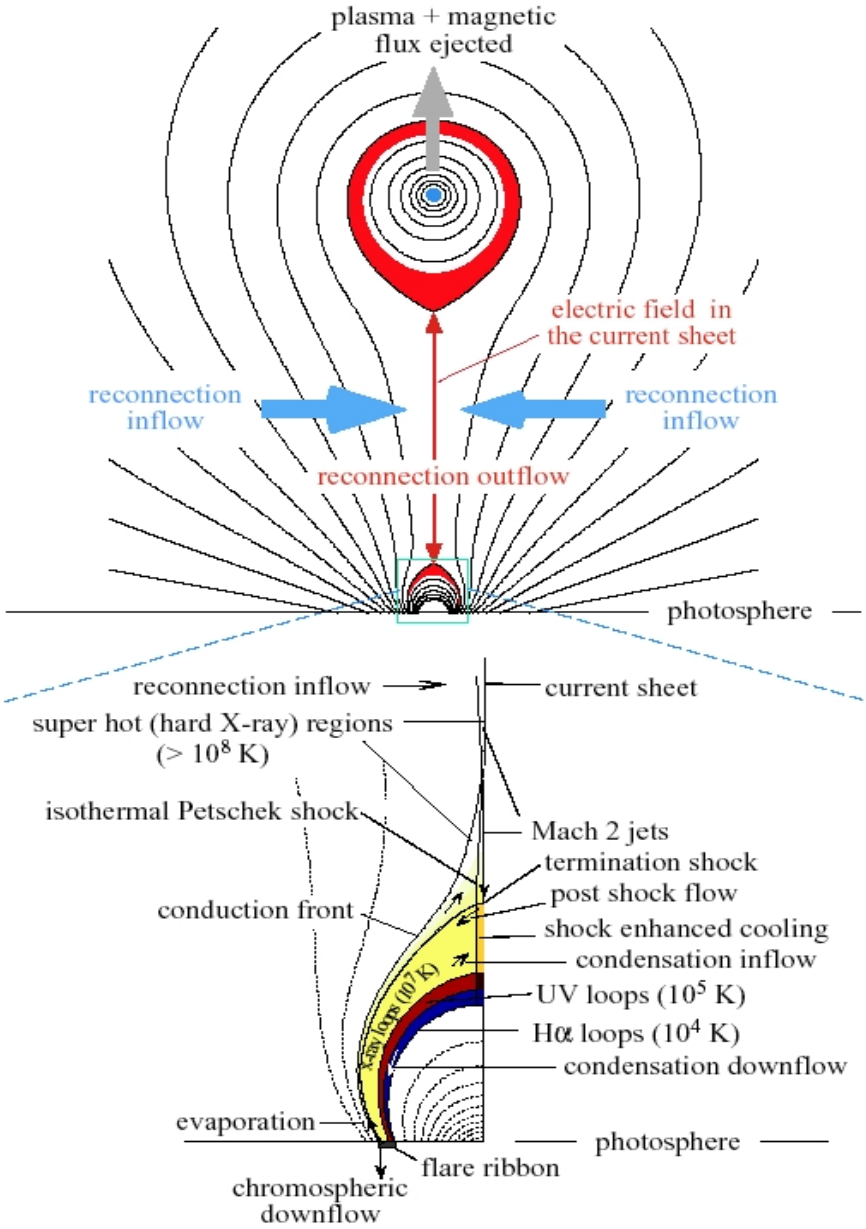

Figure 1.9: 2D schematic view of the standard flare model. From Lin and Forbes (2000).

is ejected. Not all flares involve filaments, however. In the case where a filament is present, the driver of the flare process is the rising filament and the location of the driver is above the flare site. In the absence of a filament, then the driver, located below the flaring site, is photospheric motions such as shearing along the neutral line or flux emergence (Aschwanden, 2005).

Magnetic reconnection of anti-parallel field heats the plasma to temperatures exceeding 10 - 20 MK and accelerates particles. Energetic electrons accelerated in the reconnection process are moving down the loop legs, decelerating as they hit denser plasma layers, emitting hard X-rays in the process and forming hard X-ray sources at the loop's footpoints. As a consequence, kinetic energy is transferred and the high-energy electrons heat the dense chromosphere and hot, dense plasma is evaporated into the loops. Chromospheric evaporation fills coronal loops and is observed as blue-shifted plasma emission at the external edges of flare ribbons (Czaykowska *et al.* (1999) and Harra *et al.* (2005)). The loops are observed as thermal emission in soft X-rays and become visible in extreme ultraviolet (EUV) after they have cooled by thermal conduction and radiative loss.

The standard model involving a rising filament predicts a rising reconnection point (X-type 2D reconnection) which is associated with the increasing separation of the flare ribbons observed in Hα and the increasing height of post-flare loops located over the polarity inversion line (PIL) (Masuda *et al.*, 1995). Figure 1.10 shows multi-temperature intensity maps of flaring loops on the solar limb observed by *Hinode* EUV Imaging Spectrometer (EIS) on 2006 December 17. The hottest loops are the tallest since they have more recently reconnected whereas the smaller loops have had more time for cooling. In addition to downward and upward acceleration of particles along loops, reconnection produces shocks. See §1.6 for a discussion of magnetic reconnection, current sheets, plasma flows and shocks resulting from reconnection which are shown in Figure 1.9.

Historically, flares have been classified as either eruptive or confined. An eruptive flare is essentially described by the standard two-ribbon flare model discussed above. The fraction of flares that is considered to be eruptive i.e. associated with a CME, depends on the intensity and duration of flares and increases as the class of flare becomes larger (Burkepile *et al.* (1994) and Harrison (1995)). Sheeley *et al.* (1983) found a monotonic increase of CME probability with X-ray duration so that long duration flares are more eruptive. Harrison (1995) analyzed 674 events in 1986/87 and determined that there appeared to be a 6.4% chance of a flare of duration about one hour having an observed CME association but the chances increase to 50% of a flare of duration six hours having an observed CME association. Wang and Zhang (2007) found that 90% of X-class flares are eruptive and 10% are confined. Further,

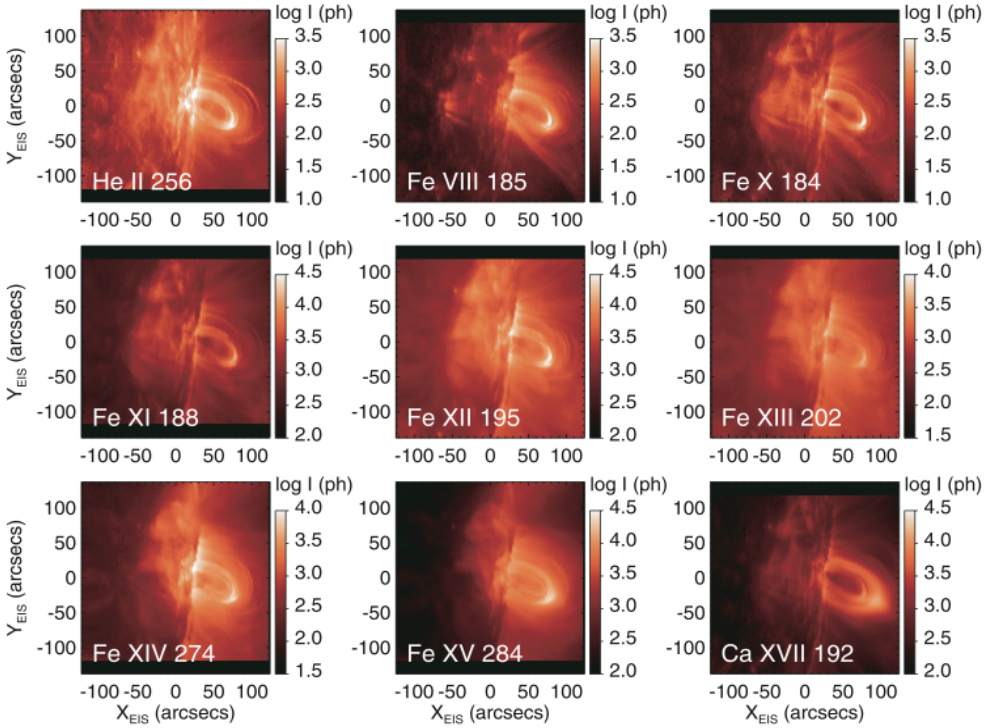

Figure 1.10: *Hinode* EIS intensity maps of nine emission lines at the peak time of a C-class flare observed on 2006 December 17. Temperatures span from 50,000 K (He II) to 5 MK (Ca XVII). From Hara *et al.* (2008).

results of Yashiro *et al.* (2005) are consistent with earlier work as they showed in a study of 1301 events that 80% of C3-9 flares are not associated with CMEs whereas 100% of flares above X3 are eruptive. However, Feynman and Hundhausen (1994) and Green *et al.* (2002b) reported cases of X-class flares with no observed CMEs.

A confined event occurs in a more compact region and lasts for a shorter period than eruptive flares. Kahler *et al.* (1989) reported confined events tend to be more impulsive with just 22% of a sample of flares of M-class and above associated with CMEs. Impulsive flares are linked to quadrupolar confined flares where there are four flare ribbons located at the footpoints of loops with four independent connectivities separating the overlying structure into four regions (Goff *et al.*, 2007). Mandrini *et al.* (1991) and Demoulin *et al.* (1993) showed that the locations of separatrices between the four regions are linked to the flare activity. Melrose (1997) developed a model of 3D quadrupolar reconnection in terms of two interacting current-carrying loops. The model does not include any 'open' field or opening of the two loops therefore, no CME is involved with this configuration.

Table 1.3: Typical CME properties.

Mass	10^{13} kg
Angular width	20 - 360°
Density (m^{-3})	
Front	10^{14}
Cavity	10^{13}
Core	10^{17}
Temperature	
Front	2 MK
Cavity	2 MK
Core	8,000 K
Magnetic Field Strength (T)	
Front	10^{-4}
Cavity	10^{-4}
Core	10^{-3}
Energy	10^{25} J
Velocity	< 200 to $> 2{,}000$ km s^{-1}
Frequency	
Solar minimum	1 per 2 days
Solar maximum	a few per day
Mass flow rate	10^{8} kg s^{-1}

1.4.6 CMEs

CMEs are dynamically evolving and expanding plasma structures carrying frozen-in magnetic flux into the heliosphere. Like flares, they are very energetic events associated with the release of magnetic energy into the corona, however, the cause-effect relationship between CMEs and flares is controversial. Broadly, they are distinctly different plasma processes but flares and CMEs are likely to be related by a common magnetic instability, reconnection, and a large-scale reorganization of magnetic fields.

Although CME observations present a rich variety of appearances, the classic CME is a three-part structure comprised of a bright frontal shell of material surrounding a dark cavity with a filament/prominence core. The structures are illustrated in Figure 1.11. 'Typical' CME physical properties and those of the individual structures are listed in Table 1.3. Hot loop arcades left on the Sun after eruption may be considered CME structures. Not all of the structures are visible in all CMEs.

In general, CME models are based on free energy stored in magnetic fields as other sources of energy including kinetic, gravitational, and thermal, are not sufficient to power CME eruptions (Forbes, 2000). Most models have a pre-eruptive configuration containing a stressed core-field and stabilizing overlying field. In Figure 1.12, top panels, a typical quadrupolar configuration with a sheared core is

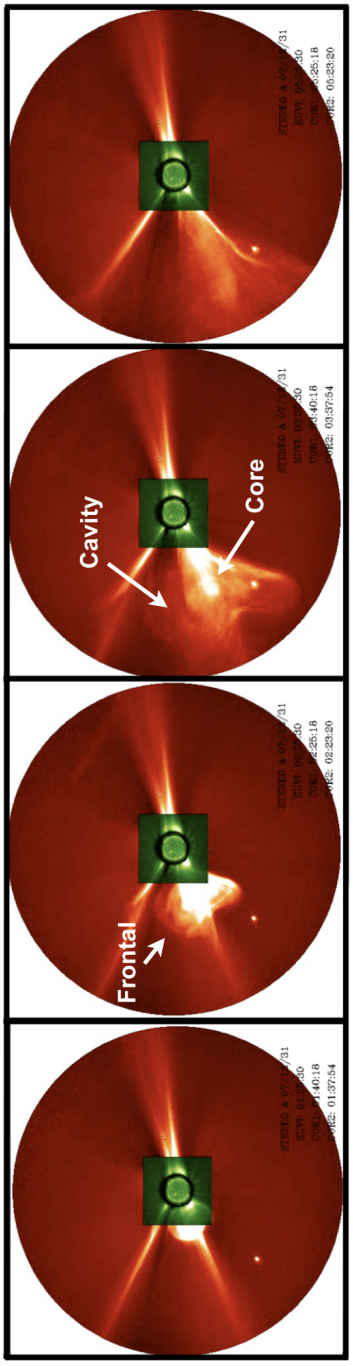

Figure 1.11: Composite images of STEREO EUVI 195 Å , COR1, and COR2 showing the three-part structure of a CME on 2007 December 31. Adapted from Liu *et al.* (2009)

used to demonstrate the three CME models discussed here though, only the breakout model requires such a configuration (Moore and Sterling, 2006). Each model has a twisted flux rope at some stage of an eruption and a vertical current sheet under the flux rope. Observations show that the eruption starts with a relatively long-lasting slow-rise phase (Figure 1.12, middle panels) having little acceleration which is then followed by an explosive fast-rise phase (Figure 1.12, bottom panels) of much stronger acceleration (Moore and Sterling (2006) and references therein). Where the models differ is in trigger and driving mechanisms. Trigger mechanisms slowly drive or dynamically perturb the pre-eruptive configuration such that the flux rope erupts. Examples of triggers include magnetic breakout, kink instability, converging and shearing flows, and flux emergence. Driving mechanisms are processes that can fully account for the observed expansion and exponential acceleration of the core flux rope. An example of a driver is the torus instability. A brief account of models involving some of the triggers and drivers are given below.

1. Internal tether-cutting/release model

   Magnetic configurations often involve a balance of forces between magnetic pressure (upward-directed) and magnetic tension (downward-directed). Field lines, or tethers, provide the tension force that opposes a rising eruption in the case of CMEs. As field lines are cut or released, the tension on the remaining field lines increases until they 'break' and the CME erupts. Moore *et al.* (2001) and others proposed this class of model where an arcade of loops overlays highly sheared field lines. When the footpoints of the arcade are driven close together by converging flows towards the PIL, the shear increases, thus enhancing the upward-directed magnetic pressure on the tethers. A flux rope is formed through reconnection within the sheared arcade (i.e. below the flux rope) during the slow-rise phase. The process accelerates to the explosive phase when reconnection occurs above the flux rope, weakening the overlying field, as indicated in the bottom panel of the left column of Figure 1.12. If the overlying field becomes sufficiently weak, the flux rope erupts. See §5.8 for more on this class of model and the role flux cancellation plays in a CME eruption.

2. External tether-cutting/magnetic breakout model

   This class of model is a variation of the internal tether-cutting model. The main differences are that the flux rope is built up during the eruption and that reconnection takes place above the flux rope. Figure 1.12, middle column, contains cartoons that illustrate the breakout model (Antiochos *et al.*, 1999). Footpoint motions shear the core field, increasing the magnetic stresses, and gradually inflating the central lobe. Expansion of the central lobe compresses

the overlying field at the null point and a current sheet forms there. When the current sheet is thin enough, reconnection begins above the expanding arcade and the field is opened above it as shown in the lower panel of the middle column of Figure 1.12. As the rising arcade 'stretches' the central lobe field, a current sheet eventually forms at the interface of the field below the core/filament and the removal of constraining field is accelerated, leading to the explosive phase and the forming, through reconnection, of a flux rope out of the highly sheared core field.

3. Flux rope MHD instability models

   Flux rope magnetohydrodynamics (MHD) instability models differ from tether-cutting models in that the beginning of the eruptive process does not involve reconnection either above or below in the core field of the flux rope. This model class includes two types - kink and torus instabilities. In a kink unstable configuration, a twist in the flux rope develops due to photospheric evolution of the field and the force-free equilibrium becomes unstable. This occurs if the twist exceeds a critical value of 2.5 turns (Hood and Priest, 1981), where twist is a measure of the end-to-end winding of the field lines around the flux rope axis. The loss of equilibrium leads to the formation of a current sheet and the eventual initiation of reconnection under the flux rope (Moore and Sterling (2006) and references therein). Török and Kliem (2005) modeled a confined eruption using MHD simulations with an ideal helical kink instability of a force-free flux rope anchored in the photosphere. They found very good agreement with observations in the development of the helical shape and the rise profile of the eruption. Torus instability models involve the expansion of the flux rope by the radially-directed hoop force as represented by the expansion instability of a toroidal current ring in a low plasma β environment. Eruption occurs when the overlying field drops sufficiently rapidly with height. Török and Kliem (2007) were able to replicate with one mechanism both fast and slow CMEs with the MHD simulations incorporating a torus instability with varying overlying field strength. Their result has implications for an eruption of a filament of an AR embedded in a CH covered in Chapter 5.

1.4.7 Measuring the Solar Magnetic Field

Direct measurement of the line-of-sight (LOS) photospheric field is straightforward using Zeeman splitting of spectral emission lines. Pieter Zeeman discovered that for laboratory gases, spectral emission lines split into polarized components in the presence of a magnetic field. In 1908, Hale used this concept to confirm the presence of strong magnetic fields in sunspots on the Sun. Zeeman's discovery is the basis

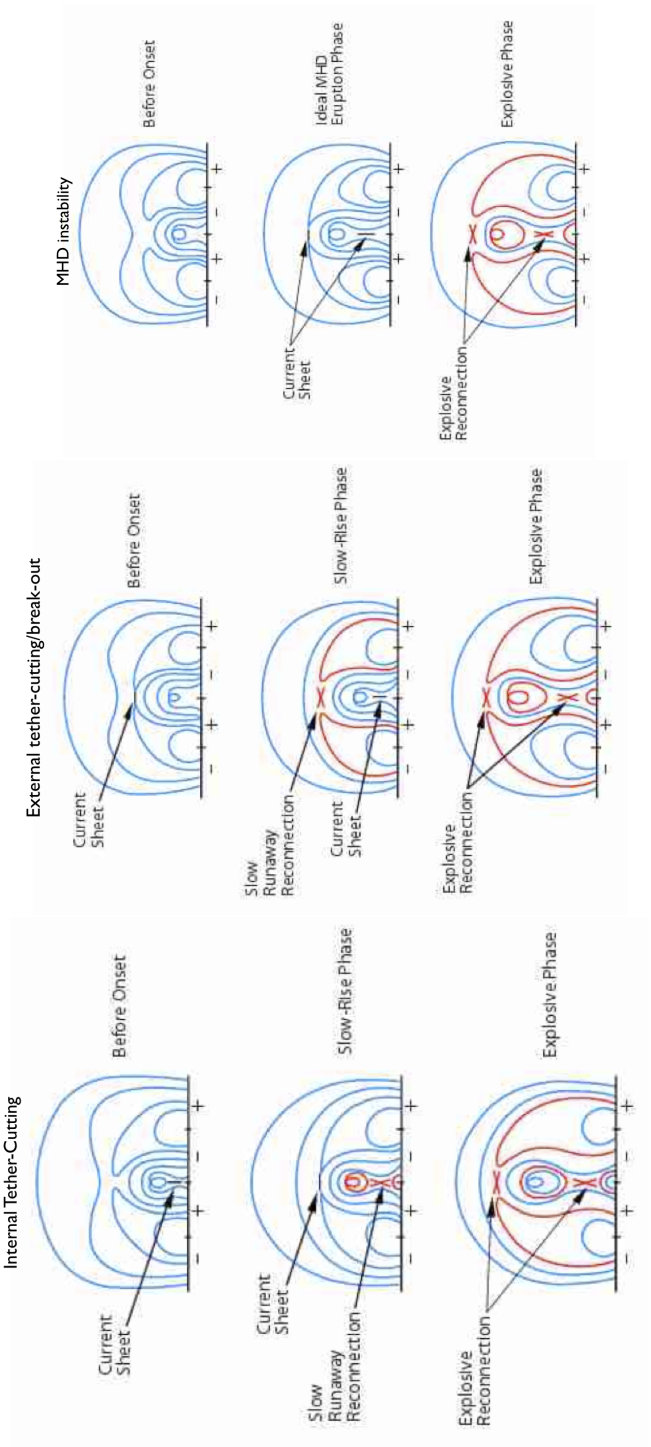

Figure 1.12: Before eruption onset (top panels), slow-rise phase of eruption (middle panels), and explosive phase of eruption (bottom panels) quadrupolar magnetic configurations for internal tether-cutting, external tether-cutting/breakout, and MHD instability CME models (left, middle, and right panels, respectively). From Moore and Sterling (2006).

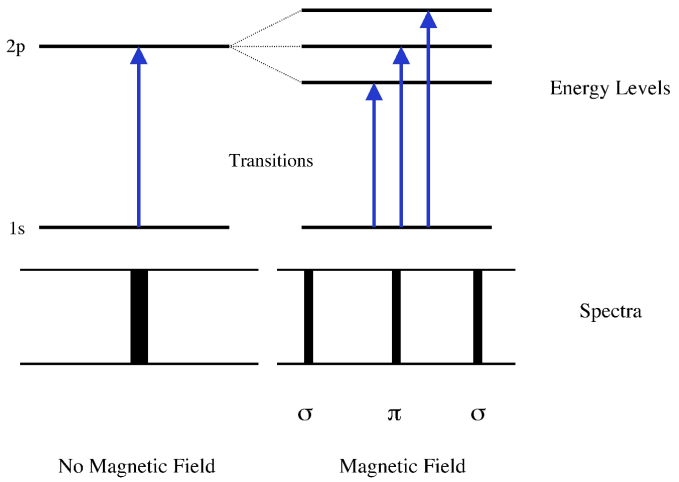

Figure 1.13: Illustration of Zeeman splitting. The spectral line splits into a Zeeman triplet in the presence of a magnetic field. The triplet consists of an unshifted π component and two shifted σ components. See text for a discussion of the polarizations of the components when the observer's LOS is along and perpendicular to the magnetic field direction.

for obtaining photospheric observations of the Sun's magnetic field. The amount of splitting is proportional to the magnetic field strength and the Landé factor. If the field is strong enough or the Landé factor large enough, then the Zeeman splitting is observable. The displacement of the split lines from their original position ($\Delta\lambda$) is

$$\Delta\lambda = 4.7 \times 10^{-8} g^* \lambda^2 B, \tag{1.8}$$

where wavelength, λ is measured in cm, magnetic field, B in gauss, g^* is the Landé factor for the particular transition. The Landé factor g for each state of the transition is given by

$$g = 1 + \frac{J(J+1) + S(S+1) - L(L+1)}{2J(J+1)}. \tag{1.9}$$

In the case of a weak magnetic field, L (total orbital angular momentum), J (total angular momentum), S (total spin momentum), and M_J (magnetic quantum number that determines the component of the total angular momentum in any one direction) are the quantum numbers which define the state of the atom.

Figure 1.13 shows a spectral line which has split into a Zeeman triplet in the presence of a magnetic field. The triplet consists of an unshifted component, π and two shifted components, σ. There are two so-called Zeeman effects, the longitudinal and transverse. In the case of the longitudinal Zeeman efect, the LOS is in the direction of the magnetic field so that the observer sees only the two σ-components. The two components have circular polarization in the opposite sense. When the observer's LOS is perpendicular to the magnetic field, the σ-components as well as the π-component are visible (transverse Zeeman effect). The σ-components are linearly polarized parallel to the magnetic field and the π-component is linearly

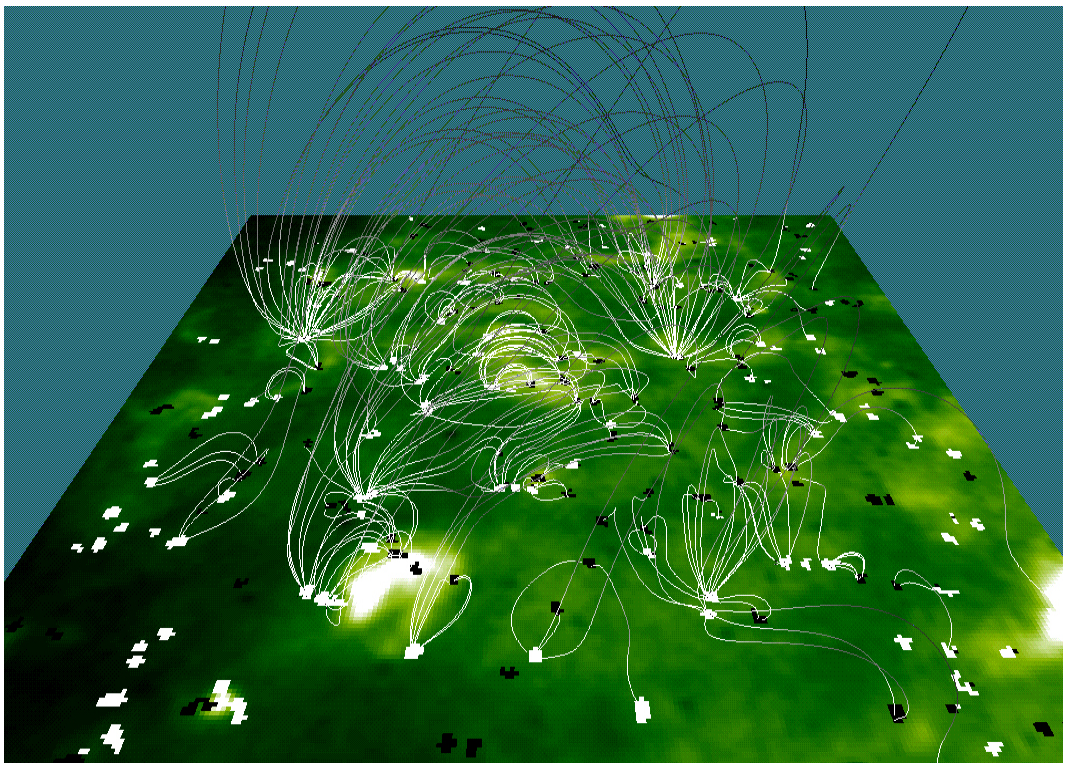

Figure 1.14: Magnetic field extrapolation of the magnetic carpet showing the small-scale magnetic field connecting the network with a spatial scale of supergranular cells.

polarized perpendicular to the magnetic field. These polarizations are valid for an absorption line. For an emission line, the polarizations change as follows: the circular polarizations are reversed for longitudinal Zeeman effect and parallel and perpendicular are exchanged for transverse Zeeman effect. Since the line splitting is proportional to λ^2, the Zeeman effect can be used for magnetic field measurements of the corona in the infrared.

SOlar Heliospheric Observatory (SOHO) Michelson Doppler Imager (MDI) measurements of the photospheric LOS magnetic field suggest the quiet Sun (QS) is comprised of small-scale mixed polarity magnetic fields that are interconnected in a highly complicated 'carpet'. Figure 1.14 shows a model of the magnetic carpet (Title and Schrijver, 1998; Schrijver *et al.*, 1998) based on MDI magnetograms (from `http://umbra.nascom.nasa.gov/ssu/magnetic_carpet.html`). Small-scale field motions force magnetic reconnections that continuously change the magnetic field topology, releasing energy in the process.

1.5 MHD

MHD is the study of the flow of an electrically conducting fluid such as a plasma in the presence of an electromagnetic field. With the MHD approximation, the coronal plasma can be treated as a magnetized fluid with bulk properties such as velocity, pressure, and density. In the next section, a plasma is defined and the three conditions for whether an ionized gas may be considered a plasma are given. This is followed by a brief discussion of the MHD equations governing the behavior of the plasma in §1.5.3.

1.5.1 What is a plasma?

A plasma is a quasi-neutral gas composed of positively and negatively charged particles. In the corona and solar wind (SW), the charged particles are usually ions and electrons which can generate and be affected by magnetic fields. Plasmas exhibit collective behavior such as bulk motions and oscillations. An ionized gas of number density n_0 and temperature T can be regarded as a plasma if the following criteria are met:

- Debye length

$$\lambda_D = \left[\frac{\varepsilon_0 k_B T}{e^2 n_0}\right]^{1/2} \ll L \tag{1.10}$$

  The Debye length, λ_D, is the distance over which there is a balance between the thermal particle energy and the electrostatic potential energy so that the plasma is able to screen out a charge imbalance within it. There is a collective shielding effect. λ_D is short compared to the scale length of the plasma system.

- Plasma parameter

$$N_D = \frac{4}{3}\pi\lambda_D^3 n_0 \gg 1 \tag{1.11}$$

  N_D is the number of particles within the Debye sphere whose radius is λ_D. A Debye sphere is a sphere of influence where the shielding effect is a result of the collective behavior of the plasma, therefore, it is necessary that the sphere contains a high number of particles. When the plasma parameter is greater than unity, the plasma is considered to be a weakly coupled, diffuse, and hot plasma.

- Plasma frequency

$$f_{CN} \ll f_{Pe} = \frac{1}{2\pi}\left[\frac{e^2 n_0}{m_e \varepsilon_0}\right]^{\frac{1}{2}} \tag{1.12}$$

f_{Pe} is the typical oscillation frequency of the electrons within the plasma. The electron plasma frequency must be large compared to the frequency of collisions of electrons with neutrals so that the plasma continues to exhibit its collective behavior.

Notation for the above equations: e and m_e are the electron charge and mass, k_B is Boltzmann's constant, ε_0 is the permittivity of free space, and L is the scale length of the plasma system. This section is based on Harra and Mason (2004).

1.5.2 Distribution Function of a Plasma

The distribution function, Equation 1.13, provides a description of a plasma that specifies the position and velocity of all the particles throughout a volume based on a Maxwellian distribution:

$$f(v) = n\left(\frac{m}{2\pi k_B T}\right)^{\frac{3}{2}} exp\left(-\frac{mv^2}{2k_B T}\right). \tag{1.13}$$

1.5.3 MHD Equations

MHD equations are comprised of the mass, momentum, and energy conservation principles as follows:

- Mass Continuity Equation

$$\frac{\partial \rho}{\partial t} + \boldsymbol{\nabla} \cdot (\rho \boldsymbol{v}) = 0 \tag{1.14}$$

  ρ is the plasma density, $\boldsymbol{v}$ is the flow velocity, t is the time.

- Motion Equation

$$\rho \frac{\partial \boldsymbol{v}}{\partial t} + \rho(\boldsymbol{v} \cdot \boldsymbol{\nabla})\boldsymbol{v} = -\boldsymbol{\nabla} p + \boldsymbol{j} \times \boldsymbol{B} + q\boldsymbol{E} + \rho \boldsymbol{g} + \boldsymbol{F} \tag{1.15}$$

  $\boldsymbol{\nabla} p$ is the plasma pressure gradient, $\boldsymbol{j}$ is the current density, $\boldsymbol{B}$ is the magnetic induction, $\boldsymbol{j} \times \boldsymbol{B}$ is the Lorenz force per unit volume, q is the charge density, $\boldsymbol{E}$ is the electric field strength, $\rho \boldsymbol{g}$ is the gravitational force, and $\boldsymbol{F}$ is an additional force including those associated with viscosity.

- Energy Equation

$$\frac{\partial p}{\partial t} + \boldsymbol{v} \cdot \boldsymbol{\nabla} p + \gamma p \boldsymbol{\nabla} \cdot \boldsymbol{v} = E_\ell \tag{1.16}$$

γ is the ratio of specific heat at constant pressure to specific heat at constant volume and E_ℓ is the total energy loss function.

1.5.3.1 Equation of State

An equation of state relating pressure, density, and temperature is required. The ideal gas law states:

$$p = R\rho T = nk_B T, \tag{1.17}$$

where R is the universal gas constant, n is the total number of particles per unit volume, and k_B is Boltzmann's constant.

1.5.3.2 Ohm's Law

Ohm's law expresses that the moving plasma in the presence of magnetic field is subject to an electric field $\boldsymbol{v} \times \boldsymbol{B}$ in addition to $\boldsymbol{E}$. This form of Ohm's law couples the electromagnetic equations to the plasma fluid equations through $\mathbf{v}$, the plasma velocity:

$$\boldsymbol{j} = \sigma(\boldsymbol{E} + \boldsymbol{v} \times \boldsymbol{B}). \tag{1.18}$$

1.5.3.3 Maxwell's Equations in MHD

Maxwell's equations form a set of equations governing the behavior of electric and magnetic fields. In MHD, the equations take the form as given below based on the following assumptions (Harra and Mason, 2004):

1. typical plasma velocities $\boldsymbol{v} \ll \boldsymbol{c}$, and
2. effects of local electric charge densities, displacement currents of viscosity, and radiation are neglected.

Maxwell's equations are:

- Faraday's Equation:

$$\boldsymbol{\nabla} \times \boldsymbol{E} = -\frac{\partial \boldsymbol{B}}{\partial t}, \tag{1.19}$$

- Gauss's Law for E (Poisson's equation):

$$\boldsymbol{\nabla} \cdot \boldsymbol{E} = 0, \tag{1.20}$$

- Ampere's Law:

$$\boldsymbol{\nabla} \times \boldsymbol{B} = \mu_0 \boldsymbol{j}, \tag{1.21}$$

- Gauss's Law for B:

$$\boldsymbol{\nabla} \cdot \boldsymbol{B} = 0. \tag{1.22}$$

  Gauss's law expresses that no net magnetic flux crosses the surface and there are no magnetic sources or monopoles.

1.5.3.4 Induction Equation

$$\frac{\partial \boldsymbol{B}}{\partial t} = \boldsymbol{\nabla} \times (\boldsymbol{v} \times \boldsymbol{B}) + \eta \boldsymbol{\nabla}^2 \boldsymbol{B} \tag{1.23}$$

The induction equation expresses the fact that the time evolution of the magnetic field can be due to advection ($\boldsymbol{\nabla} \times (\boldsymbol{v} \times \boldsymbol{B})$) and/or diffusion ($\eta \boldsymbol{\nabla}^2 \boldsymbol{B}$). Note, magnetic diffusivity, η, may be expressed in terms of electric conductivity, σ:

$$\eta = \frac{1}{(\mu_0 \sigma)}. \tag{1.24}$$

1.5.4 Magnetic Reynolds Number

Two regimes in which the magnetic field either diffuses or moves with the plasma are given by the ratio of the advection and diffusion terms of the induction equation, or the Reynolds number:

$$R_m = \frac{\boldsymbol{\nabla} \times (\boldsymbol{v} \times \boldsymbol{B})}{\eta \boldsymbol{\nabla}^2 \boldsymbol{B}} = \frac{\left(\frac{v}{l}\right)}{\left(\frac{\eta}{l^2}\right)} = \mu_0 \sigma v l, \tag{1.25}$$

where v and l are characteristic velocity and length values, μ_0 is magnetic permeability, σ is electric conductivity.

Table 1.4: Typical values for magnetic Reynolds numbers (R_m) for selected astrophysical objects. L is length-scale, v is velocity-scale, η is diffusivity. (Kivelson and Russell, 1995)

Astrophysical Object	L (m)	v (m s^{-1})	η (m^2 s^{-1})	R_m
solar corona	10^8	10^3	1	10^{11}
sunspot	10^7	10^3	8×10^2	1.3×10^7
Earth's magnetosphere	10^7	10^5	10	10^{11}
accretion disks in CVs	10^8	10^3	1	10^{11}
accretion disks in AGN	10^8	10^3	3×10^{-2}	3×10^{13}
jets in CVs	10^7	10^5	10^4	10^8

Case 1: $\mathrm{R}_m \ll 1$ (diffusion dominates):

$$\frac{\partial \boldsymbol{B}}{\partial t} = \boldsymbol{\nabla} \times (\boldsymbol{v} \times \boldsymbol{B}) + \eta \boldsymbol{\nabla}^2 \boldsymbol{B} \Longrightarrow \frac{\partial \boldsymbol{B}}{\partial t} = \eta \boldsymbol{\nabla}^2 \boldsymbol{B} \tag{1.26}$$

Case 2: $\mathrm{R}_m \gg 1$ (advection dominates - e.g. in the solar corona):

$$\frac{\partial \boldsymbol{B}}{\partial t} = \boldsymbol{\nabla} \times (\boldsymbol{v} \times \boldsymbol{B}) + \eta \boldsymbol{\nabla}^2 \boldsymbol{B} \Longrightarrow \frac{\partial \boldsymbol{B}}{\partial t} = \boldsymbol{\nabla} \times (\boldsymbol{v} \times \boldsymbol{B}) \tag{1.27}$$

Coronal values of the Reynolds number range from 10^8 to 10^{12}. Typical Reynolds numbers for other astronomical objects are shown in Table 1.4 for comparison. In general, Reynolds numbers are large for astrophysical objects therefore the advection term in the induction equation dominates and the magnetic field advects with or is 'frozen' into the plasma (case 2). Plasma moves along the field, not across it. On the other hand, when the diffusion term dominates, the magnetic field lines 'slip' through the plasma. This can occur in localized regions where the gradients of the magnetic field become sufficiently large, strong currents build, and length-scales shorten so that the localized reconnection takes place even in astrophysical objects with very large average magnetic Reynolds numbers.

1.5.5 Lundquist Number

The Lundquist number is the ratio of the Alfvén wave crossing timescale and resistive diffusion timescale:

$$S = \frac{v_A l}{\eta} = \mu_0 \sigma v_A l, \tag{1.28}$$

where v_A is the Alfvén speed:

$$v_A \equiv \frac{B}{(\mu_0 \rho)^{\frac{1}{2}}}. \tag{1.29}$$

The typical value of the Alfvén speed in the corona is about 1,000 km s^{-1} and typical coronal values of the Lundquist number range from 10^8 to 10^{12}. Such high Lundquist numbers indicate highly conducting plasmas.

1.5.6 Coronal Magnetic Field Extrapolations

In the corona, spectral lines are relatively broad and the magnetic field is weak therefore the Doppler width is much greater than the Zeeman splitting (§1.4.7). This fact makes direct observations of the coronal magnetic field extremely difficult. Other methods used to measure the coronal field, including radio brightness maps associated with optically thick harmonics of gyro-emission frequencies, measuring the Hanle effect where the presence of a magnetic field alters the linear polarization from resonance or coherent line scattering, and measuring Zeeman splitting of strong infrared lines (Régnier (2007), Liu (2009) and references therein), still require improved signal-to-noise ratio, spatial coverage and temporal resolution in order to provide definitive quantitative measurements of the coronal field. Thus, indirect methods are used to understand the coronal magnetic field structure. One such method is to model the coronal magnetic field by extrapolating from photospheric observations.

In a low plasma β environment, it is generally assumed that the coronal magnetic field is nearly force-free and any currents that might be present are nearly parallel to the field. Neglecting gas pressure and gravity, a magnetic field is defined to be force-free when the Lorentz force is zero,

$$\boldsymbol{j} \times \boldsymbol{B} = 0. \tag{1.30}$$

Combining Ampere's Law (Eq. 1.21) with Eq. 1.30 yields the condition for force-free magnetic fields expressed in terms of $\boldsymbol{B}$,

$$(\boldsymbol{\nabla} \times \boldsymbol{B}) \times \boldsymbol{B} = 0. \tag{1.31}$$

Eq. 1.31 leads to the force-free equation

$$\boldsymbol{\nabla} \times \boldsymbol{B} = \alpha \boldsymbol{B}, \tag{1.32}$$

where α is a free scalar parameter with the dimension of inverse length, typically

measured in radians per Mm. α identifies how much current flows along a given field line (De Rosa *et al.*, 2009) and $\alpha \neq 0$ characterizes a nonpotential field.

A number of extrapolation methods are based on the force-free assumption including potential field, linear force-free field (LFFF), nonlinear force-free field (NLFFF), and the Potential Field Source Surface (PFSS) extrapolations. Brief definitions of these first three models are as follows:

Potential: $\alpha = 0$. The field is current-free and in the lowest possible energy configuration.

LFFF: α is constant in the computational volume. Numerical methods based on Fourier transforms, Green functions, and spherical harmonics are commonly used in LFFF extrapolations (Schmieder and Aulanier, 2003; Aschwanden, 2005; Régnier, 2008). LFFF modelling requires as a boundary condition a LOS longitudinal magnetogram (B_z) such as from MDI.

NLFFF: α is a function of space α(x,y,z) and is constant along a given field line (Equation 1.33) but not throughout the computational volume. This can be shown by taking the divergence of Equation 1.32 and the result is

$$\boldsymbol{B} \cdot \boldsymbol{\nabla} \alpha = 0, \tag{1.33}$$

which means the gradient of α is always normal to the direction of $\boldsymbol{B}$ and α is unchanged along a given field line. This method requires a vector magnetogram (B_x, B_y, B_z) as a boundary condition.

Extrapolated field lines in the force-free configurations can be compared with loops observed in EUV and X-rays since coronal loops 'outline' magnetic field lines due to the frozen-in condition. The AR displayed in Figure 1.15 is a case in point. Bright loops observed in X-rays are modeled using the extrapolation methods described above. The magnetogram in Figure 1.15 provides the photospheric boundary for each extrapolation. A highly sheared AR is selected in order to illustrate some of the shortcomings of the various models. Figure 1.16 shows the potential, two LFFF, and NFFF model results. Potential extrapolations may capture the global structure of the corona e.g. coronal holes (CHs), large loops, streamers, however, comparison of the field lines computed from the potential model in the upper left panel of Figure 1.16 with the X-ray loops of the AR indicates a significant divergence between the model and the observation. LFFF extrapolations in the upper right and lower left panels of Figure 1.16 (α = 0.06 Mm^{-1} and -0.06 Mm^{-1}, respectively) are able to give a sense of the overall 'handedness' of the AR, but neither model is able to replicate the degree to which the AR is sheared. A single α value can not fit all

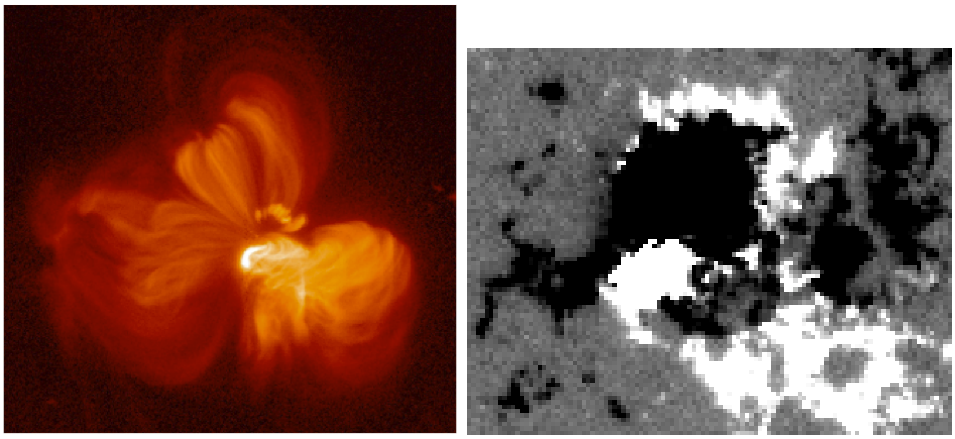

Figure 1.15: XRT thin Be filter image of AR 10930 loop system in December 2006 (left) and SOHO/MDI magnetogram (right) used to construct extrapolated coronal field in Figure 1.16. Courtesy of M. Murray.

.

of the loops of the AR as the complexity of the AR exceeds the point where the LFFF method is valid (Schmieder and Aulanier, 2003). Less sheared ARs, global field of the corona, magnetic topology of flaring ARs, filaments, and small scale flux emergence are some of the applications appropriate for LFFF modelling (Schmieder and Aulanier, 2003). Case studies of NLFFF extrapolations have shown good alignment between model field lines and the locations of EUV and X-ray loop structures, sigmoids and twisted flux ropes (De Rosa *et al.*, 2009), however, the NLFFF method is not the ultimate answer to 3D modelling of the coronal field (Régnier, 2008), as can be seen by comparing the model with the observations. De Rosa *et al.* (2009) concluded that improved NLFFF modelling requires: 1. vector magnetic field data covering larger areas, 2. accommodation by modelling algorithms of various uncertainties in the boundary data, and, 3. a more realistic physical model to approximate the photosphere-to-corona interface.

The PFSS model is the most commonly used model of the global corona. It provides the magnetic field between the photosphere and the source surface, a surface where coronal field becomes radial and 'open'. Between the source surface and the photosphere, the magnetic field is potential, therefore the corona is current-free. The PFSS model uses LOS radial Carrington synoptic MDI maps as input. The model compares well with large-scale X-ray and EUV loops and CH locations. Figure 1.17 shows a PFSS extrapolation for AR 10942 on 2007 February 20. Green field lines on the eastern side of the AR are connected with the source surface at 2.5 R_{sun} and are considered to be 'open', whereas, white field lines are connected to the solar surface and are closed. In Chapter 3, the PFSS extrapolation is used to demonstrate that AR outflows driven by magnetic reconnection along quasi-separatrix layers (QSLs) can be expelled along 'open' field lines and make up a component of the slow SW.

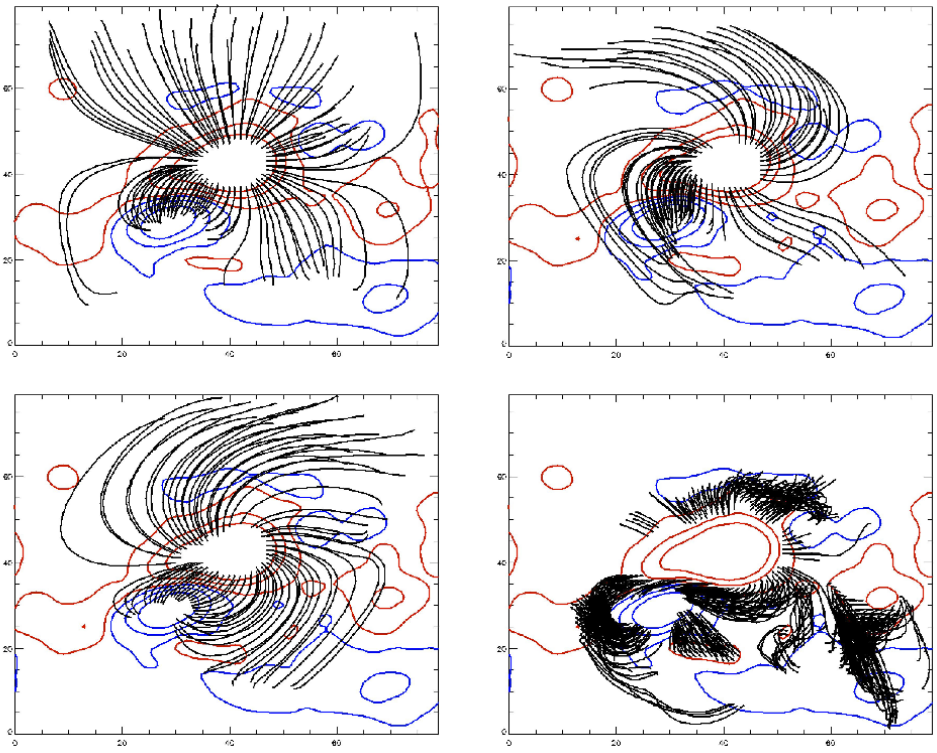

Figure 1.16: Examples of potential (upper left, $\alpha = 0$), LFFF (upper right, $\alpha = 0.06$ Mm^{-1} and bottom left, $\alpha =$ -0.06 Mm^{-1}), NLFFF (bottom right, $\alpha = \alpha$(x,y,z)) extrapolations. Extrapolations use the magnetogram in Figure 1.15 (right) as the lower boundary. Potential, LFFF and NFFF results are compared to the X-ray image of the AR in Figure 1.15. Blue/red contours: 100/-100 G, 500/-500 G, 1,000/-1,000 G. (Regnier Code for potential extrapolation and Wiegelmann Code for linear and non-linear extrapolations). Courtesy of Michelle Murray.

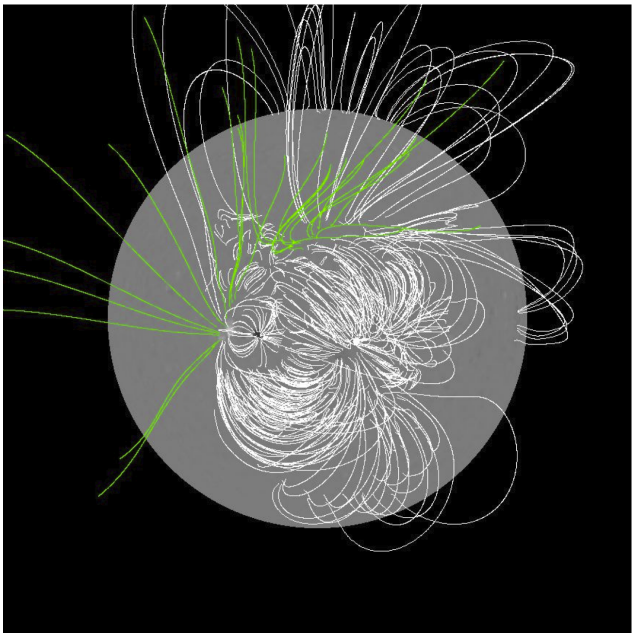

Figure 1.17: PFSS extrapolations for AR 10942 on 20 Feb 2007 (see §3.4.2). The plot was produced using IDL Software for Analyzing Solar Magnetic Fields - PFSS Extrapolation software in SolarSoft. Green field lines are 'open' and connect with the source surface at 2.5 R_{sun}. White field lines are closed and connect back to the solar surface.

1.6 Magnetic Reconnection - a Fundamental Plasma Physics Process

The coronal magnetic field is constantly stressed due to dynamic boundary (i.e. photospheric and chromospheric) conditions including new flux emergence, differential rotation, convective motions, and interplanetary field connectivity changes. When magnetic stress builds up, the large-scale coronal field is required to restructure via magnetic reconnection processes in order to release large amounts of energy and return to a relaxed state. Such topological changes provide an efficient transformation of non-potential (free) magnetic energy to kinetic energy. Reconnection leads to the heating of coronal plasma and acceleration of particles e.g. the SW. It is also thought to produce large electric currents and shock waves (Parnell, 2000). Observational evidence of reconnection includes reconnection inflows and outflows, jets, plasmoids, shocks, particle acceleration, chromospheric evaporation. Much of this evidence will be presented and discussed in subsequent chapters.

1.6.1 2D Steady Reconnection - the Basic Model

In a highly conductive plasma magnetic field lines are 'frozen in' the plasma therefore no reconnection can take place and magnetic topology is conserved. In this case, the magnetic Reynolds number, R_m, is $\gg 1$, and the induction equation (Equation 1.23) simplifies to Equation 1.27 so that the diffusion term is negligible. However, magnetic reconnection requires the dissipation of electric currents so R_m must be $\ll 1$. In order for $R_m \ll 1$, either the ohmic magnetic diffusivity, η, must increase or the scale length, l, must decrease, or both (see §1.5.4). The time evolution of the magnetic field of the induction equation, $\frac{\partial \boldsymbol{B}}{\partial t}$, is then dominated by the diffusion term (Equation 1.26). Under these conditions, magnetic field lines are no longer 'frozen in' the plasma and reconnection is able to occur.

Magnetic nulls are locations at which the magnetic field strength falls to zero. In 2D, magnetic reconnection occurs at an X-type null where two field lines with different connectivities, for example, $A \rightarrow A^{'}$ and $B \rightarrow B^{'}$ are reconnected to form two new field lines with connectivities $A \rightarrow B^{'}$ and $B \rightarrow A^{'}$ (Parnell *et al.*, 2010). Four distinct flux domains exist in the X-type null configuration. Separatrices, which intersect at the X-point, divide the topologically distinct regions. As a result of reconnection, flux moves across the separatrices from one flux domain to another.

Figure 1.18 shows the simplified magnetic configuration in the 2D steady reconnection model where all magnetic field quantities are time-independent. When anti-

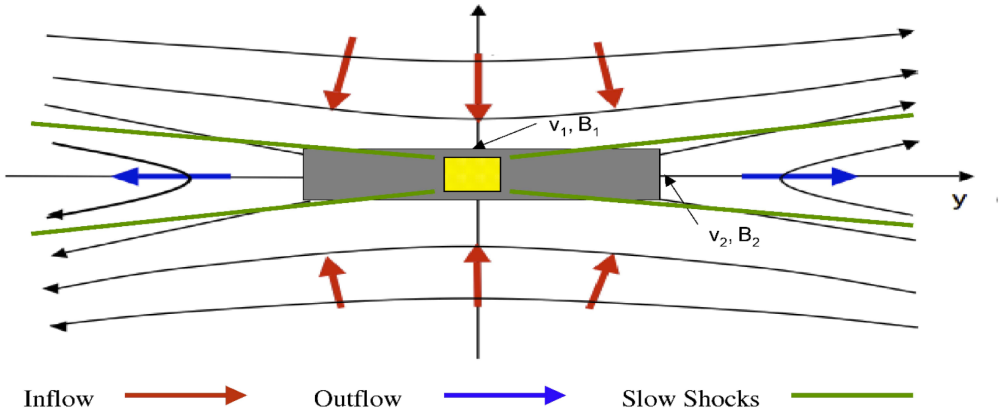

Figure 1.18: Standard 2D model of steady magnetic reconnection. A dynamic boundary is formed where anti-parallel magnetic field lines meet (along the Y-axis) and the magnetic field goes to zero. Inflows (red arrows) in the positive and negative X-directions create outflows (blue arrows) along the neutral line. Gray rectangle is the diffusion region for the Sweet-Parker reconnection model. Yellow rectangle is the small diffusion region and the green solid lines represent slow-mode MHD shocks in the outflow regions of the Petschek model. See text for a description of the models. Adapted from Schindler *et al.* (2000).

parallel field lines meet, a neutral boundary layer is formed along the Y-axis. The magnetic field vanishes at the boundary across which there is a continuous change from positive to negative field. The force balance across the neutral boundary layer can be expressed by:

$$\frac{B_1^2}{2\mu_0} + p_1 = p_{nbl} = \frac{B_2^2}{2\mu_0} + p_2, \tag{1.34}$$

where B_1 and p_1 are magnetic and thermal pressure on one side of the neutral boundary layer (parallel to the Y-axis in Figure 1.18), B_2 and p_2 are magnetic and thermal pressure on other side (parallel to the X-axis), and p_{nbl} is the thermal pressure in the neutral boundary layer where $B = 0$.

External forces (e.g. AR expansion) drive inflows which in turn create outflows along the neutral line located along the Y-axis. Red/blue arrows indicate inflows/outflows in Figure 1.18. In the diffusion region, as B_1 tends to zero, plasma $\beta \gg 1$ so that the plasma and magnetic field lines decouple. Plasma is directed along the neutral line into the outflow regions at the Alfvén speed where the magnetic field lines are experiencing a high magnetic tension force.

The Lorentz force creates an electric field, E_0, at the diffusion region in the direction perpendicular to the XY plane in Figure 1.18. A current sheet is associated with the electric field (via Ohm's Law, Equation 1.18) as follows:

$$E_0 = \frac{1}{c} v_1 B_1 = \frac{1}{c} v_2 B_2 = \frac{j_{nl}}{\sigma}. \tag{1.35}$$

Reconnection processes can be slow and quasi-static or fast and highly dynamic. Brief descriptions of an example of slow (Sweet-Parker) and fast (Petschek) reconnection models follow, however, there are many more realistic and complex reconnection models that are beyond the scope of this thesis.

1.6.2 Sweet-Parker Reconnection

The Sweet-Parker reconnection model (Sweet, 1958; Parker, 1957, 1963) is essentially described by the 2D steady reconnection model with a diffusion region that has length L along the Y-axis and width l along the X-axis. The region is indicated by a gray rectangle in Figure 1.18. $L \gg l$. Outflow speed, v_2, is approximately Alfvénic and is related to the inflow speed, v_1, via mass conservation:

$$v_1 L = v_2 l. \tag{1.36}$$

The reconnection rate, M, is defined as the ratio of the inflow speed, v_1, to the Alfvén outflow speed, and $v_2 = v_A$:

$$M = \frac{v_1}{v_A}. \tag{1.37}$$

The condition for steady state, where the inflow speed equals the diffusion speed, gives:

$$v_1 = \frac{\eta}{l}. \tag{1.38}$$

Substituting for l in Equation 1.36 using Equation 1.38,

$$M = (\frac{\eta}{L v_A})^{1/2} = \frac{1}{(S)^{1/2}}, \tag{1.39}$$

where S is the Lundquist number (Equation 1.28). Typical coronal Lundquist values yield $M \approx 10^{-4}$ - 10^{-6}. The Sweet-Parker reconnection rate is too slow to explain the magnetic dissipation in fast, highly dynamic events such as solar flares.

1.6.3 Petschek Reconnection

Petschek (Petschek, 1964) proposed a model with much faster reconnection rates than that of the Sweet-Parker model. Essentially, faster reconnection occurs because the length of the diffusion region, L, is much shorter, therefore, the propagation time across the diffusion region is shorter. The diffusion region is indicated by the yellow rectangle in Figure 1.18. Compared with the Sweet-Parker model, a

smaller amount of plasma flows through the diffusion region of the Petschek model. Consequently, slow-mode shocks (shown by the green lines in Figure 1.18) arise when a large fraction of the inflowing plasma encounters the Alfvénic plasma in the outflow regions. The slow-mode shock waves propagate from the ends of the diffusion region and play a key role in accelerating the plasma and converting magnetic energy into heat. The Petschek reconnection rate is given by (Petschek, 1964):

$$M \approx \frac{\pi}{8\ ln(S)}, \tag{1.40}$$

so for coronal Lundquist values, Petschek reconnection rate $M \approx 0.01$ - 0.02, three orders of magnitude faster than the Sweet-Parker reconnection rate (Aschwanden, 2005).

1.6.4 3D Reconnection

2D magnetic reconnection is limited in the variety of topologies that can approximate solar reality. Many magnetic reconnection models of more complex scenarios such as the unified flare model (§1.4.5), magnetic breakout model or the sheared arcade model (§1.4.6) require 3D magnetic topologies. As a result, during the 1990s research began to focus on 3D reconnection which is far less constrained than its 2D counterpart (Parnell, 2000). In 3D topologies, magnetic reconnection can occur at 3D nulls as well as in regions where there are no nulls present (Schindler *et al.*, 1988).

1.6.4.1 3D Reconnection in the presence of nulls

Priest and Titov (1996) investigated how reconnection can occur at a single 3D null by considering the global behavior of velocity, $\boldsymbol{v}$, and magnetic field, $\boldsymbol{B}$, in the vicinity of the null. They assumed that the system reaches a series of equillibria in a steady and ideal manner with $\boldsymbol{j} \times \boldsymbol{B} = 0$, therefore, Ohm's law can be simplified to:

$$\boldsymbol{E} + \boldsymbol{v} \times \boldsymbol{B} = 0, \tag{1.41}$$

and Faraday's law can be stated as:

$$\boldsymbol{\nabla} \times \boldsymbol{E} = 0. \tag{1.42}$$

The magnetic field is specified in a defined region where the boundary conditions of the velocity flow are given then Equations 1.41 and 1.42 are solved for $\boldsymbol{v}$ and singu-

larities are identified (Parnell, 2000). Singularities, or nulls, indicate the locations where the assumption of ideal MHD is not valid and reconnection may take place.

There are three different types of reconnection at a 3D magnetic null - spine, fan, and separator. Figure 1.19 contains a simple schematic of the magnetic field configuration or skeleton at a potential 3D null. The fan and spine of the null are the 3D equivalent to 2D separatrices (Priest and Titov, 1996). The spine consists of two fields lines that leave/enter the null from opposite directions (along the Z-axis in Figure 1.19) and the fan plane consists of a continuum of field lines which radiate out of/into the null and form a separatrix surface. Fans and spines are perpendicular at potential nulls (where the current is zero), however, current components perpendicular and parallel to the spine cause the fan plane to move and may alter the structure of the field lines in the fan (Parnell, 2000).

Separator reconnection occurs in far more complex magnetic topologies involving two or more nulls. For example, Figure 1.19, bottom panel, shows the topology of a quadrupolar region with two nulls. Such a configuration is a model of a new bipole which has emerged in the vicinity of a pre-existing bipole. The volume is divided into topologically separate regions by a separatrix surface which is a surface of field lines encompassing magnetic flux from a single source (i.e. one polarity of a bipole). At the intersection of the two separatrix surfaces embedding the two bipoles, a separator connects the pair of opposite polarity nulls.

Figure 1.20 shows the 3D null reconnection topologies for spine, fan, and separator reconnection in cylindrical and dome-like fan surface geometries. In the case of spine reconnection, the current is parallel to the spine (Priest and Titov 1996). A field line penetrates the fan surface or dome of the null, twists around the spine, and reconnects on the opposite sides of the fan and the spine. A rotational type of reconnection results within a flux envelope enclosing the diffusion region (Birn and Priest, 2007). See Figure 1.20, left panels, where the field line has moved through the fan surface in cylindrical geometry and through the fan dome in dome-like fan surface geometry. For fan reconnection, the current is along the fan. The field line does not penetrate the fan but merely twists around the spine in both geometries. Magnetic flux is advected through both the spine and the fan plane (Birn and Priest, 2007). In the case of separator reconnection, reconnection occurs preferentially along the separator where there are high parallel currents and, therefore, high parallel electric fields. It occurs over an extended region and might occur at multiple 'hot spots' along the separator, away from the nulls (Parnell *et al.*, 2010).

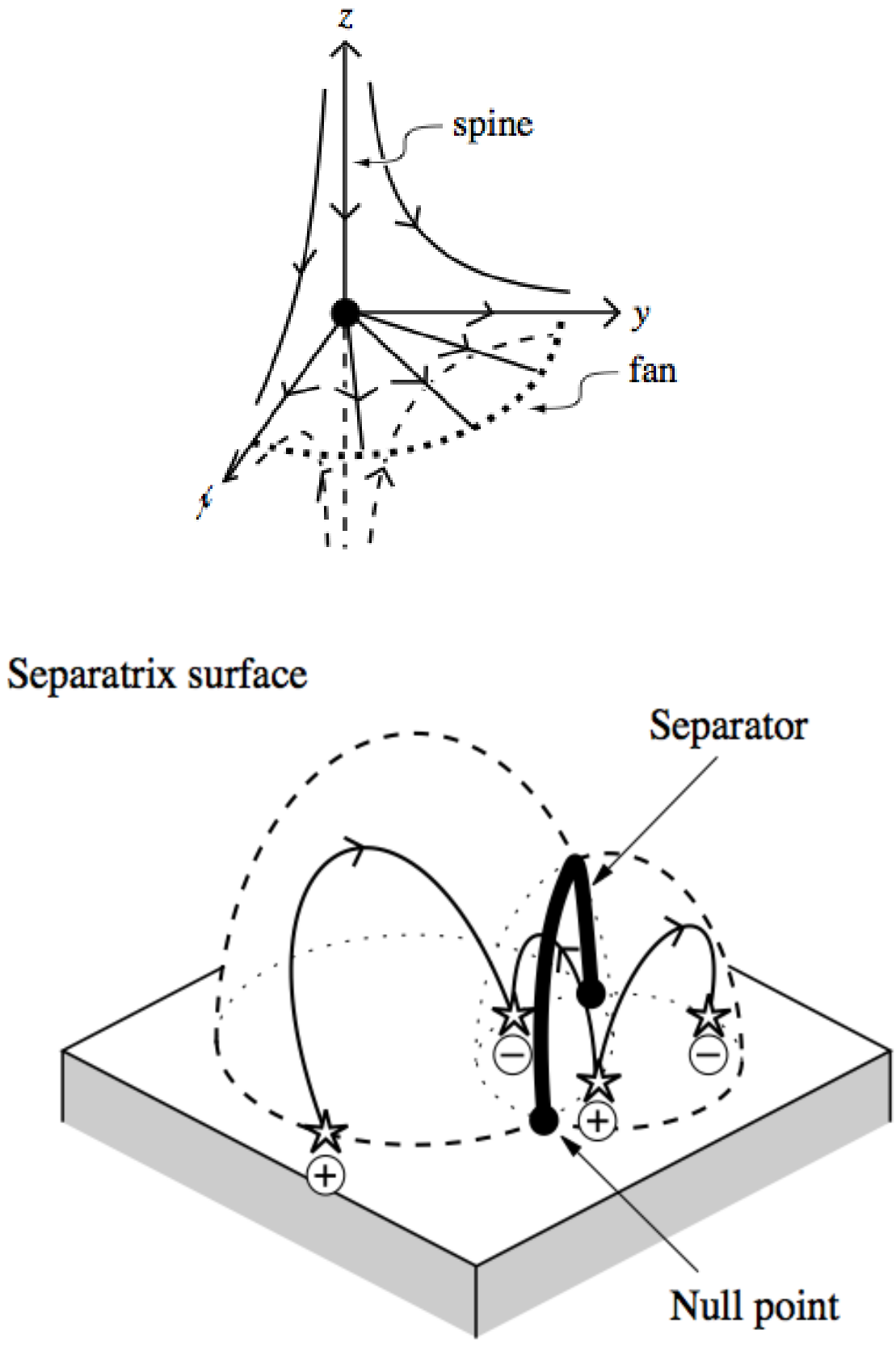

Figure 1.19: Magnetic configuration of a 3D null (top) and multiple nulls (bottom). From Priest (2001).

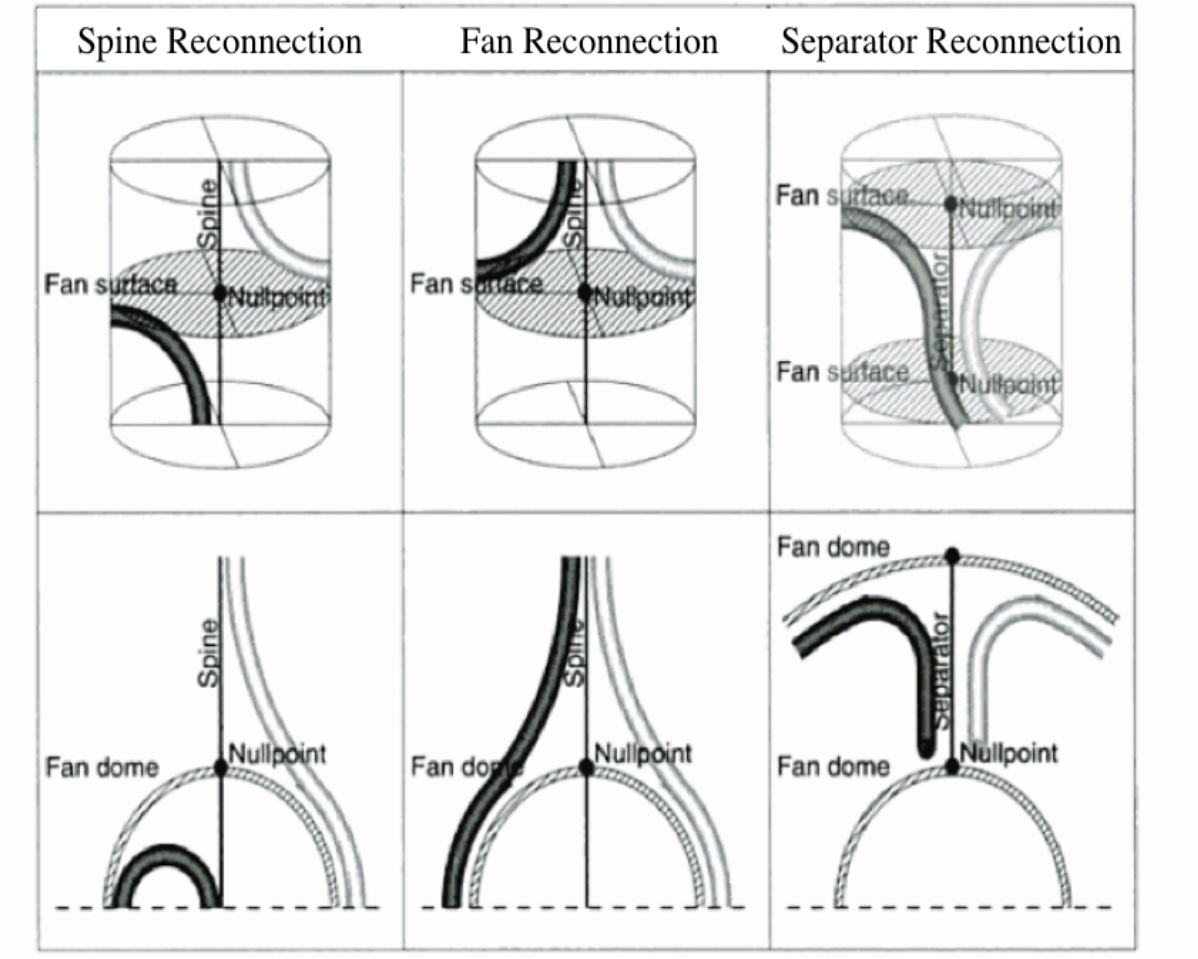

Figure 1.20: Spine (left), fan (middle), and separator (right) 3D null reconnection topologies. Top row shows the three reconnection regimes for a cylindrical geometry and the bottom row for a dome-like fan surface geometry. 3D nulls are designated by black dots, spine and separator curves by thick lines, fan surfaces and domes by hatched regions, pre-reconnection line by light gray color, and post-reconnection by dark gray color. From Aschwanden (2005).

1.6.4.2 3D Reconnection in the absence of nulls

So far, only 2D and 3D reconnection at nulls has been described. Further discussion of 3D reconnection in the absence of nulls will be reserved for §3.5.4 where it will be demonstrated that reconnection along QSLs is a plausible mechanism to drive AR outflows. However, some of the basic principles are covered here. QLSs are locations where continuous reconnection takes place. This is also known as component reconnection.

In the case of QSLs, the connectivity of the magnetic field is no longer defined by the skeletons with null points, as described above, but rather by thin volumes across which the mapping of the magnetic field displays strong gradients in connectivites (Priest and Démoulin, 1995; Demoulin *et al.*, 1996). Titov *et al.* (2002) proposed a function which characterizes the connectivity gradient by the squashing degree of the field lines/flux tubes (see §3.4.2 for the mathematical form of the squashing degree, Q). Figures 1.21 and 1.22 help to illustrate the concept of a strong gradient in magnetic connectivity. A typical example of computed field lines in a quadrupolar topology is found in Figure 1.21, top panel. Blue and magenta contours are opposite polarities of the two bipoles which make up the quadrupolar configuration and multi-colored field lines connect opposite polarities within and without of the bipoles. The yellow line delineates the polarity inversion line (PIL) of the configuration. Photospheric traces of the QSLs in the quadrupolar topology with arrows identifying QSLs at the boundaries are shown in the bottom panel of Figure 1.21. Figure 1.22 displays a cartoon series of a strong gradient in magnetic connectivity in the quadrupolar topology in Figure 1.21. The blue and yellow crescent-shaped regions are the QSL traces in Figure 1.21, bottom panel. As the thin, blue QSL trace is crossed, the connectivities to the opposite polarity shift spatially along the yellow QSL trace. The same occurs in reverse. A thin volume is formed.

Parnell (2000) summarizes Priest and Démoulin (1995) and shows more formally how the footpoint of a field line moves a distance $2x_0$ and the endpoint moves a much greater distance $2x_0\mathrm{e}^{1/l}$ where $l \ll 1$ (analogous to crossing the blue QSL trace and connectivities spreading out along the yellow QSL trace in Figure 1.22). For $l \ll 1$, the 3D, non-zero magnetic field is of the form:

$$\boldsymbol{B} = (x, y, -l). \tag{1.43}$$

A typical field line is:

$$(x, y, z) = (x_0 e^{z/l}, y_0 e^{-z/l}, z). \tag{1.44}$$

For a field line with a footpoint in the $z = 0$-plane and an endpoint in the $z = 1$-plane, the footpoint is (x_0, y_0, 0) and the endpoint is ($x_0\mathrm{e}^{1/l}$, $y_0\mathrm{e}^{-1/l}$, 1). If the

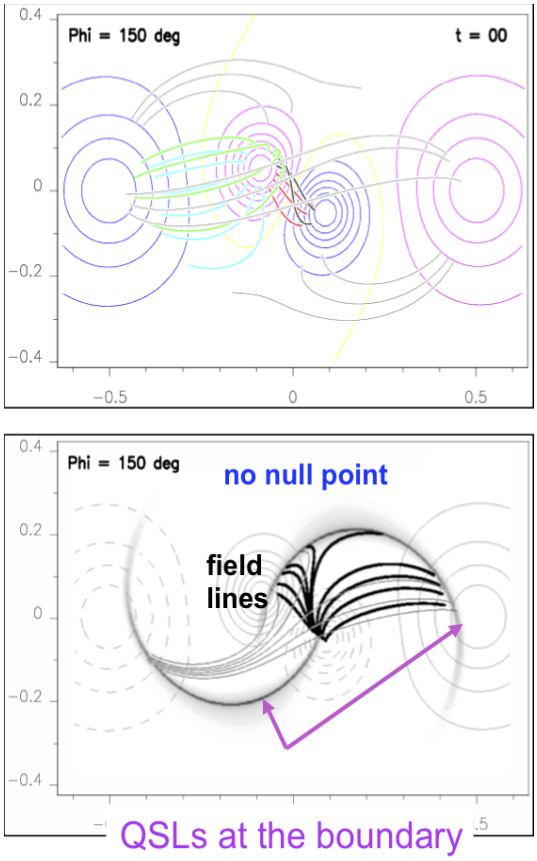

Figure 1.21: Top: Quadrupolar configuration showing connectivities between positive and negative polarities (blue and purple contours). Bottom: Photospheric traces of QSLs in the quadrupolar configuration. Current density is highest along the QSL traces in the photospheric plane. Courtesy of P. Démoulin.

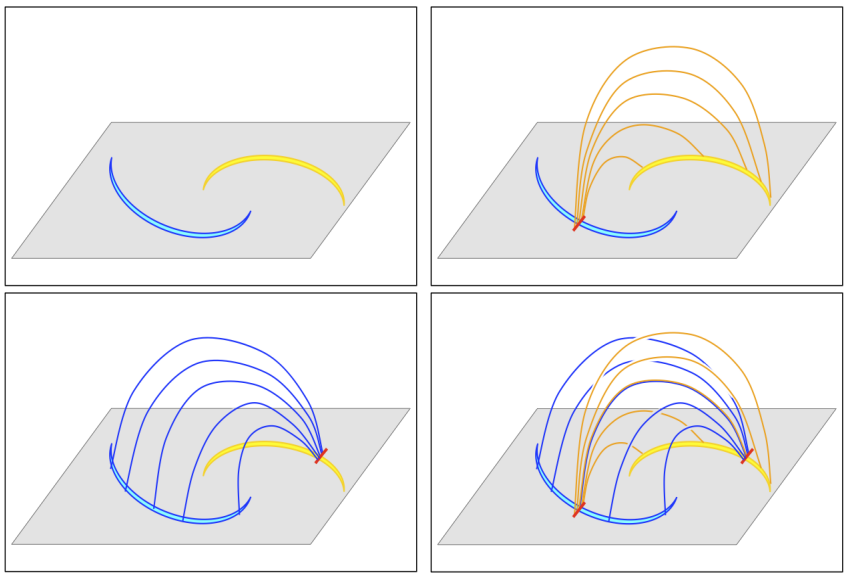

Figure 1.22: Yellow and blue photospheric traces of QSLs. Moving the short distance across the blue QSL trace results in connectivities spreading along the opposite polarity QSL trace and visa versa. Courtesy of P. Démoulin

Table 1.5: Comparison of 2D and 3D reconnection (Parnell and Haynes, 2009).

2D Reconection	3D Reconnection
1. Must occur at X-type null points	1. Can occur at null points or in the absence of null points
2. Occurs at a single point	2. Occurs continually and continuously throughout diffusion region volume -not at a single point
3. Pairs of field lines break and recombine into new two new pairs of field lines	3. Pairs of field lines or even pairs of surface break, but do not recombine into two new pairs of field lines or surfaces
4. Discontinuous field line mapping	4. Continuous or discontinuous field line mapping
5. Stagnation type flow	5. Counter-rotating flows

field line footpoint moves from

$$(x_0, y_0, 0) \rightarrow (-x_0, y_0, 0), \tag{1.45}$$

then the endpoint would move from

$$(x_0 e^{1/l}, y_0 e^{-1/l}, 1) \rightarrow (-x_0 e^{1/l}, y_0 e^{-1/l}, 1). \tag{1.46}$$

So the footpoint of the field line moves a distance of $2x_0$, whereas its endpoint moves a distance of $2x_0 \mathrm{e}^{1/l} \gg 2x_0$ since $l \ll 1$. Parnell (2000) suggests this implies that the field line may move at a speed in excess of the Alfvén speed thus the field line decouples from the plasma. The regions where this occurs are QSLs where reconnection takes place. MHD simulations have demonstrated QSL reconnection and in fact, recently QSLs have been identified in laboratory plasma experiments (Lawrence and Gekelman, 2009). §3.2.1.2 has further discussion of the characteristics and applications of QSLs.

In summary, Table 1.5 from Parnell and Haynes (2009) provides a brief comparison of 2D and 3D reconnection.

1.7 The Corona

The corona, or crown, is the extremely hot and tenuous outer atmosphere of the Sun that extends to heights of more than one R_{sun} above the photosphere (Figure 1.23). Its temperature exceeds 1 MK, thus it can be observed directly at EUV and X-ray wavelengths, however, there are four white-light components to the solar corona: K-

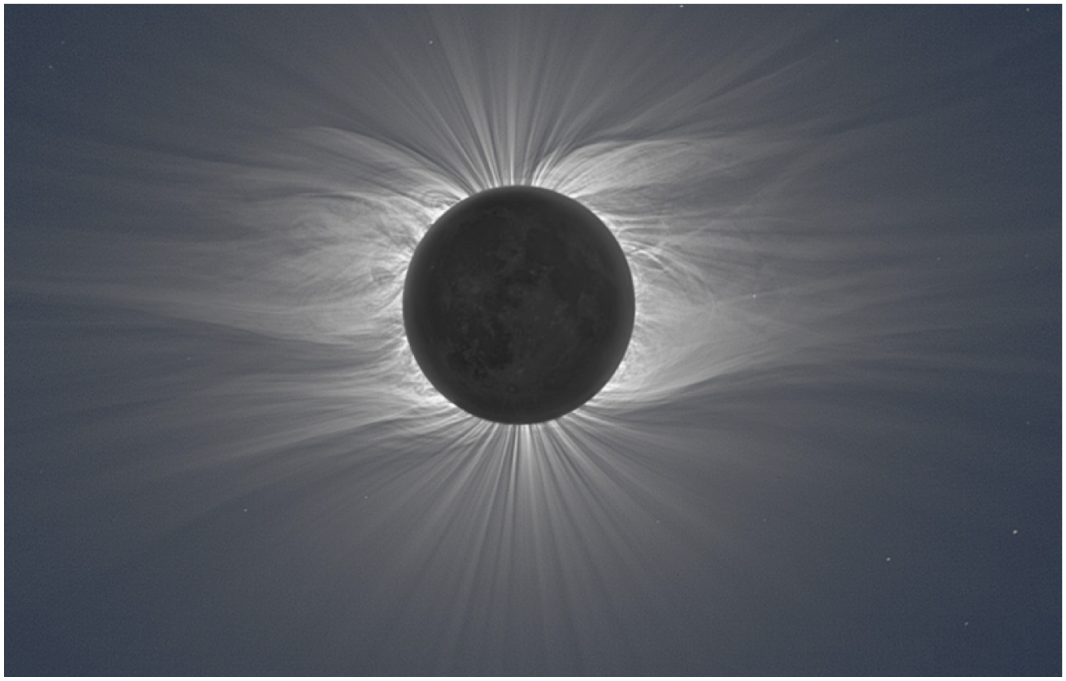

Figure 1.23: Solar corona at solar minimum on 2009 July 22. Credit: M. Druckmuller, Brno Observatory, Czech Republic.

(kontinuierlich), F- (Fraunhofer), E- (emission), and T- (thermal emission) corona.

The K-corona includes some of the classic coronal structures including streamers and CMEs. It is caused by the scattering of photospheric light by free electrons of the coronal plasma which produces a partially polarized continuous emission spectrum. The type of scattering process is Thomson scattering and the cross section is:

$$\sigma_T = \frac{8\pi}{3} \left(\frac{e^2}{m_e c^2} \right). \tag{1.47}$$

There is no wavelength dependence and the scattering rate is proportional to the electron density. Hydrogen Balmer series (n=2) emission lines (known as the Fraunhofer lines) are broadened or smeared due to the large thermal velocities of the scattering electrons. The F-corona, also known as the dust corona or zodiacal light, produces dark absorption lines of the photospheric Fraunhofer spectrum arising from scattering by interplanetary dust. The F-corona dominates raw images of coronagraphs and heliospheric imagers out to tens of degrees (see §2.2.2). Thermal emission of the dust, mainly in the infrared, causes the T-corona. Finally, isolated spectral line emission from highly ionized atoms of the coronal plasma forms the E-corona ($\geq$ 0.5 R_{sun}) spectrum. A narrow bandpass filter is required in order to detect the strong E-corona spectral lines against the local background K- and F-continuum.

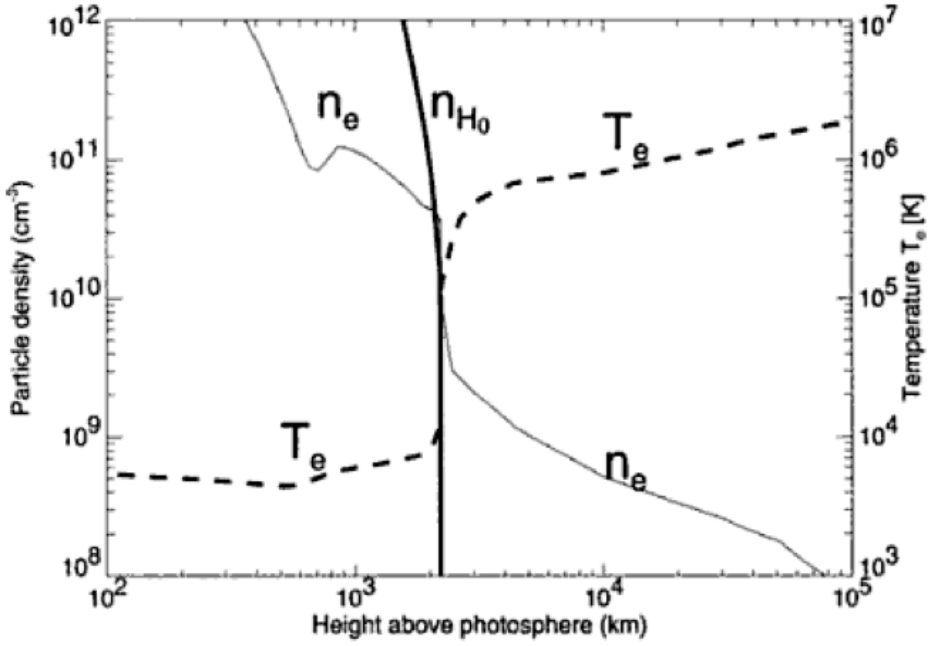

Figure 1.24: Electron density, n_e, and temperature, T_e, model of the chromosphere and lower corona (Fontenla *et al.*, 1990; Gabriel, 1976). Thick black line indicates the neutral hydrogen density, n_{H0}. Plasma is fully ionized in the corona and partially ionized in the chromosphere (Aschwanden, 2005).

1.7.1 Temperature Structure of the Corona

The electron temperature, T_e, vs. height of the solar upper atmosphere is shown in Figure 1.24. There is a rapid temperature rise from the top of the photosphere (T = 6000 K) to the corona (T > 1 MK) over a radial distance of approximately 1 R_{sun}. A positive temperature gradient throughout the solar atmosphere appears to violate the 2nd law of thermodynamics which loosely states that heat can not flow spontaneously from a region of lower to a region of higher temperature without a heat source. The problem of coronal heating has plagued astrophysics for over 70 years (see §1.7.1.2 for a brief discussion).

Hinode X-ray Telescope (XRT) temperature response spans 10^6 to $10^{7.5}$ K. XRT's 9 X-ray analysis filters make it possible to detect plasmas within this temperature range. Figure 1.25 shows a temperature map (right panel) constructed from filter ratio analysis for the entire solar disk. It is clear from the map that the temperature structure of the corona is far from homogeneous. Different structures have very different temperatures. Temperatures range from the cool plasma of two equatorial CHs at approximately 1×10^6 K to the hot AR loops at approximately 3.5×10^6 K, however, the map is dominated by QS with the temperature $\approx 2 \times 10^6$ K (blue).

The multi-temperature distribution of the corona can be classified using tem-

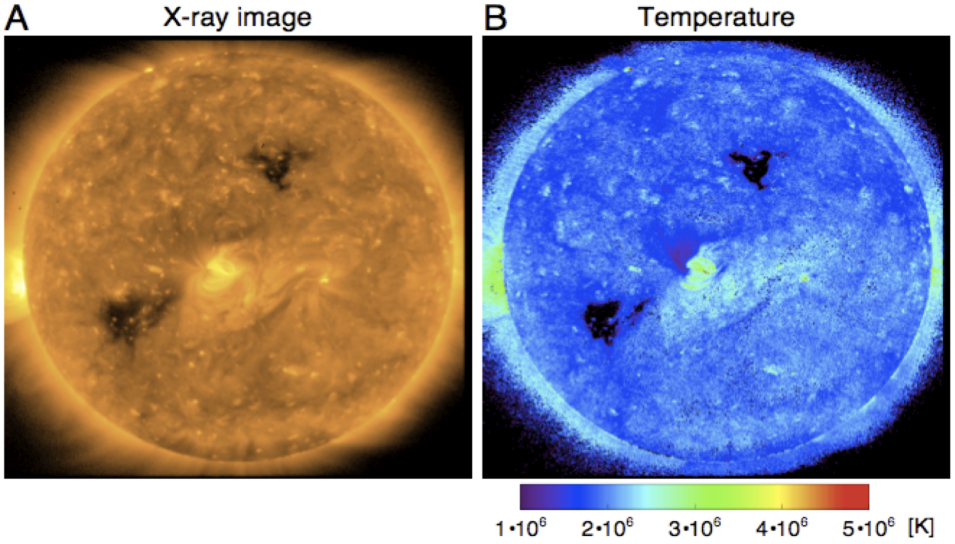

Figure 1.25: Left panel (A) - *Hinode* XRT full-disk X-ray image of the Sun. A bright AR is located very near to disk center. Two dark patches to the north and southeast of the AR are equatorial CHs. Right panel (B) - Coronal temperature derived from XRT multi-filter observations. Temperatures range from a low of approximately 1×10^6 K in CHs to 3.5×10^6 K in AR loops. Blue quiet Sun ($T \approx 2 \times 10^6$ K) dominates the image. Credit: N. Narukage, Hinode 1, Dublin (2007 August 24)

perature and emission measure (see §1.7.6) obtained by XRT filter ratio analysis. Figure 1.26 displays color-coded regions that correspond to various coronal structures: AR core - red, AR and X-ray bright points - orange, AR footpoint - brown, quiet Sun - blue, AR plasma outflow - green, and CH - purple. Figure 1.27 shows a (log-log) plot of emission measure vs temperature for the color-coded structures in Figure 1.26. It is surprising how well different structures fit into classification categories.

1.7.1.1 Energy Balance

In order to begin to understand the coronal heating problem, it is useful to look at the energy balance in the corona. Assuming a steady-state where the energy that flows into a unit volume of the corona is balanced by the energy that flows out, there are three mechanisms for energy flux loss: heat conduction (F_c), radiation (F_r), and SW transport (F_{sw}). Average coronal energy losses for each mechanism in different types of solar regions are indicated in Table 1.6 (Withbroe, 1981). These values should be compared to the total solar energy flux of 6.96×10^{10} erg cm^{-2} s^{-1}. Clearly, in each type of region the total flux loss is only a small fraction of the total solar flux, therefore, the amount of energy input required to sustain the corona, even in hot ARs, is only 10^{-4} of the solar energy flux (Golub and Pasachoff, 1997).

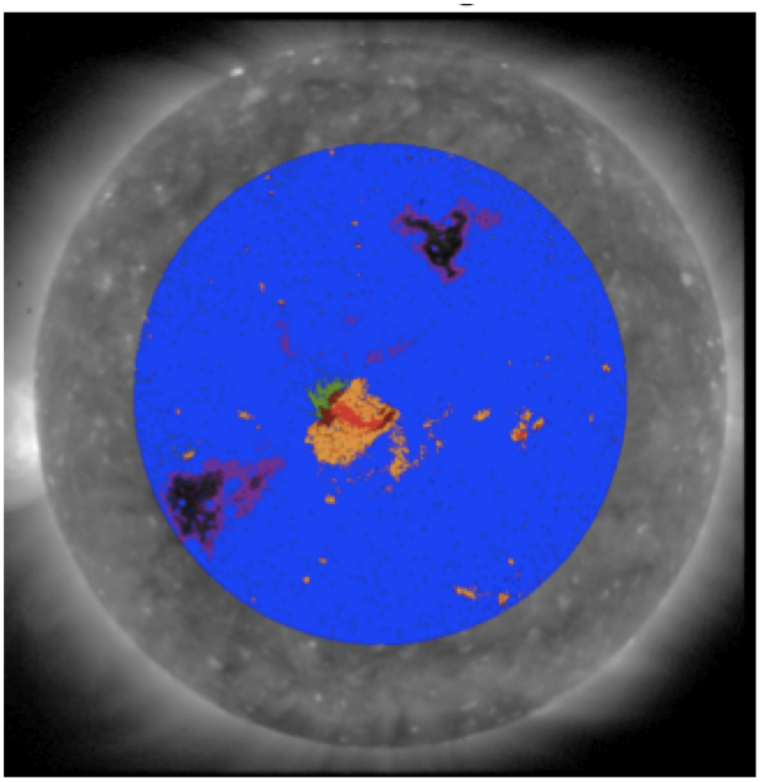

Figure 1.26: Coronal structures classified by temperature and emission measure. AR core - red, AR and X-ray bright point - orange, AR footpoint - brown, quiet Sun - blue, AR plasma outflow - green, CH - purple. Credit: N. Narukage, Hinode 1, Dublin (2007 August 24)

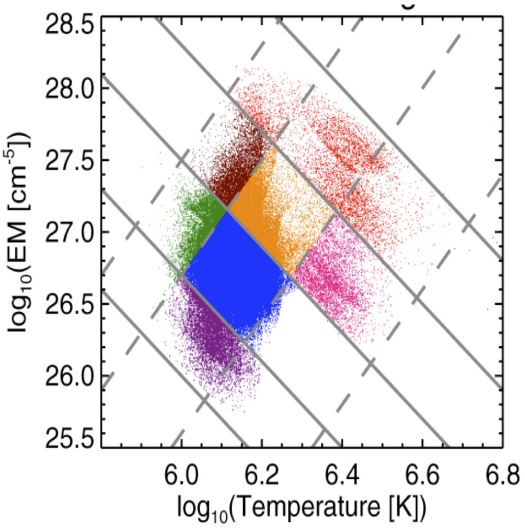

Figure 1.27: T-EM (emission measure) diagram showing classification of regions. Color code is the same as in Figure 1.26. (AR core - red, AR and X-ray bright point - orange, AR footpoint - brown, quiet Sun - blue, AR plasma outflow - green, CH - purple). Credit: N. Narukage, Hinode 1, Dublin (2007 August 24)

Table 1.6: Average coronal energy losses for quiet Sun, ARs, and CHs (erg cm^{-2} s^{-1}). Based on Withbroe (1981).

Loss mechanism	Quiet Sun	Active Region	CH
Conductive flux, F_c	2×10^5	10^5 - 10^7	6×10^4
Radiative flux, F_r	10^5	5×10^6 - 10^7	10^4
SW flux, F_{sw}	$< 5\times10^4$	10^7	8×10^5
Total flux loss, F_c+F_r+F_{sw}	3×10^5	10^7	8×10^5
Percent of total solar flux	<0.001	0.01	0.001

1.7.1.2 Coronal Heating

As discussed in §1.7.1, some form of heat source is needed to maintain coronal plasma temperatures in excess of 10^6 K. There is near-global agreement that the mechanical energy necessary to heat the corona is generated by the turbulent fluid motions of the convective zone (Golub and Pasachoff, 1997; Klimchuk, 2006; Schrijver and Siscoe, 2009). The footpoints of magnetic field lines or flux tubes are buffeted by these motions which leads to either the stressing of the field or the generation of waves, depending on time scales of the motions compared to the Alfvén travel times (Klimchuk, 2006). At least two key questions remain - how is the mechanical energy transported to the corona and how is it dissipated?

Broadly, heating mechanisms can be divided into two categories, direct current (DC) and alternating current (AC) mechanisms. For DC heating mechanisms, the 'energy carrier' is current sheets and dissipation occurs via reconnection and magnetic field stresses. Timescales of the photospheric velocity field which drives the footpoint shuffling or buffeting are longer than the Alfvèn travel time across the coronal structure in the case of DC mechanisms (Golub and Pasachoff, 1997; Mandrini *et al.*, 2000; Klimchuk, 2006; Schrijver and Siscoe, 2009). Nano-flare heating is a prime example of DC heating. For AC heating mechanisms, the 'energy carriers' are waves (including, but not limited to, fast and slow mode MHD waves, magnetoacoustic surface waves, and Alfvèn waves) and dissipation mechanisms include shock dissipation, damping, resonance heating, and MHD turbulence (Golub and Pasachoff, 1997; Mandrini *et al.*, 2000; Klimchuk, 2006; Schrijver and Siscoe, 2009). The timescales of the velocity field are shorter than the Alfvèn transit time for AC heating mechanisms. By no means is the coronal heating problem solved though it has been refined by substantial advances in modeling, observations, simulations, and data analysis. The lively debate is likely to continue for some time.

1.7.1.3 Why is the Coronal Temperature of Order 1 MK?

A plasma's temperature is determined by both the heat dissipated and by the plasma's ability to lose energy. There are at least three ways for coronal plasma to lose energy (Schrijver and Siscoe, 2009):

1. by optically thin radiation (e.g. oxygen and iron), Λ, described by

$$\Lambda(T_e) = n_e n_H f(T_e) \tag{1.48}$$

   where T_e is the electron temperature, n_e is the electron density, n_H is the hydrogen density, and $f(T_e)$ is a function of temperature dependent on line emission;

2. by thermal conduction along magnetic field lines with a conduction coefficient, $\kappa(T_e) \propto \mathrm{T}_e^{5/2}$; and,

3. by acceleration of the SW.

In a dense plasma environment, the $n_e n_H$ term in Equation 1.48 is large and variations in heat input can be accommodated by small changes in plasma temperature, which will remain at approximately photospheric temperatures where conduction is very inefficient. However, the efficiency of radiative losses drops off rapidly as density falls exponentially with height (see Table 1.2). This means any heat input will raise the plasma temperature until thermal conduction can balance energy input. As given in (2) above, thermal conduction varies with $\mathrm{T}_e^{5/2}$, so a balance of thermal conduction and energy input does not occur until the plasma temperature is of order 1 MK (Schrijver and Siscoe, 2009).

1.7.2 Density Structure of the Corona

Though the density of the corona is lower than that of a laboratory vacuum, it is still an inhomogeneous, highly structured plasma with the structure related to the Sun's magnetic field eg CHs and ARs. In general, density variations range from approximately 10^6 cm^{-3} in the highly tenuous upper corona to 10^{11} cm^{-3} in hot flare loops. Aschwanden and Acton (2001) used temperature tomography combined with *Yohkoh* SXT data to obtain density measurements in various coronal structures. Their results are compared with others in Figure 1.28. All density values decrease with increasing height in the corona. QS and streamer densities fall from approximately $10^{8.5}$ to 10^7 cm^{-3} over 0.8 R_{sun}. CHs densities fall at the steepest

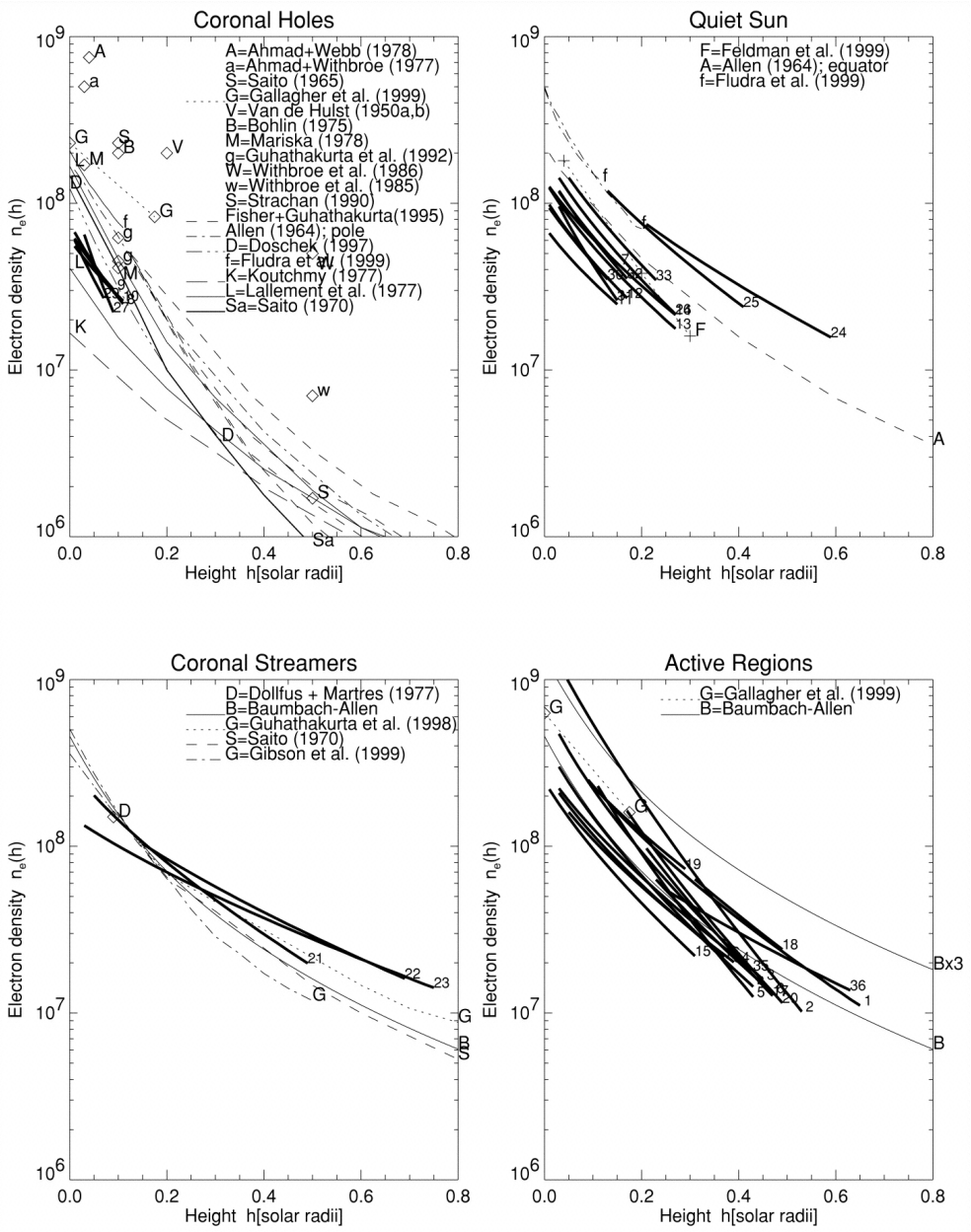

Figure 1.28: Comparison of electron density measurements for various structures in the corona obtained from a variety of measurements and modeling techniques. Clockwise from top left - CHs, QS, ARs and coronal streamers. The height ranges from 0.003 to 0.8 R_{sun} (Aschwanden and Acton, 2001).

rate from approximately 10^8 to 10^6 cm^{-3} over <0.8 R_{sun}. ARs remain the densest structures at all heights (10^9 to 10^7 cm^{-3}).

1.7.3 Chemical Composition - the FIP Effect

The chemical composition of the corona is broadly similar to that of the photosphere for most elements, however, some subtle yet crucial differences do exist. Elements with a low first ionization potential (FIP) of $\leq$ 10 eV such as silicon, magnesium,

and iron, are overabundant by 3 to 10 times relative to their abundances in the photosphere. Determination of relative abundances can be problematic due to the complete ionization of hydrogen in the corona. There are no hydrogen emission lines that can be used to measure absolute abundances, so emission lines from heavy elements are used for the measurement of relative abundances. This leads to an ambiguity as to whether the FIP fractionation effect is an increase of low-FIP elements into the corona or a draining of high-FIP elements from the corona.

Abundance variations based on the FIP effect are important because they can be used to probe source regions in the solar atmosphere of elements detected in the SW. Relative abundances in CHs and newly emerged ARs appear to be similar to that of the photosphere whereas they differ in the QS and in mature ARs (Sheeley, 1995, 1996). Feldman *et al.* (2009) evaluated the coronal composition and FIP effects of the QS, polar CHs and ARs above the limb and an AR on the disk using *Hinode* EIS. Laming (2004) used the FIP effect to distinguish plasma associated with 'open' and closed field. This is important for locating fast and slow SW in the solar atmosphere. For example, Young (2005) used the Mg/Ne abundance ratio to determine the FIP effect in the QS and concluded that only a small fraction of the QS can connect to the SW where this abundance ratio is 4-5 times greater than that of the photosphere.

1.7.4 Plasma β

Throughout the solar atmosphere, plasma and magnetic pressures compete for dominance. The plasma β is the critical parameter that describes the dominating force. It is the ratio of gas pressure to magnetic pressure (see Equation 1.49). When $\beta \gg 1$, the kinetic energy exceeds the magnetic energy therefore charged particles can escape their gyro-orbits and diffuse across the magnetic field. Under these conditions, gas pressure dominates the magnetic pressure as is the case in the photosphere and in the solar interior. In most of the corona, magnetic pressure fully dominates the gas pressure and $\beta \ll 1$. Table 1.7 shows typical values of plasma β in the photosphere and layers of the corona (Aschwanden, 2005). The cool and hot corona (T = 1 MK and 3 MK, respectively) have plasma β values $\ll 1$ whereas the photosphere and outer corona (acceleration region of the SW) have values $\gg 1$.

$$\beta \equiv \frac{p_{th}}{p_m} \equiv \frac{2\xi n_e k_B T_e}{\frac{\boldsymbol{B}^2}{2\mu_0}}, \tag{1.49}$$

p_{th} is plasma pressure, p_m is magnetic pressure, ξ is coronal ionization fraction, n_e is electron density, k_B is the Boltzmann constant, T_e is the electron temperature,

Table 1.7: Physical parameters and plasma β in the photosphere and corona (Aschwanden, 2005).

Parameters	Photosphere	Cool corona	Hot corona	Outer corona
Electron density (cm^{-3})	2×10^{17}	1×10^{9}	1×10^{9}	1×10^{7}
Temperature (K)	5×10^{3}	1×10^{6}	3×10^{6}	1×10^{6}
Pressure (dyne cm^{-2})	1.4×10^{5}	0.3	0.9	0.02
Magnetic field (G)	500	10	10	0.1
Plasma β	14	0.07	0.2	7

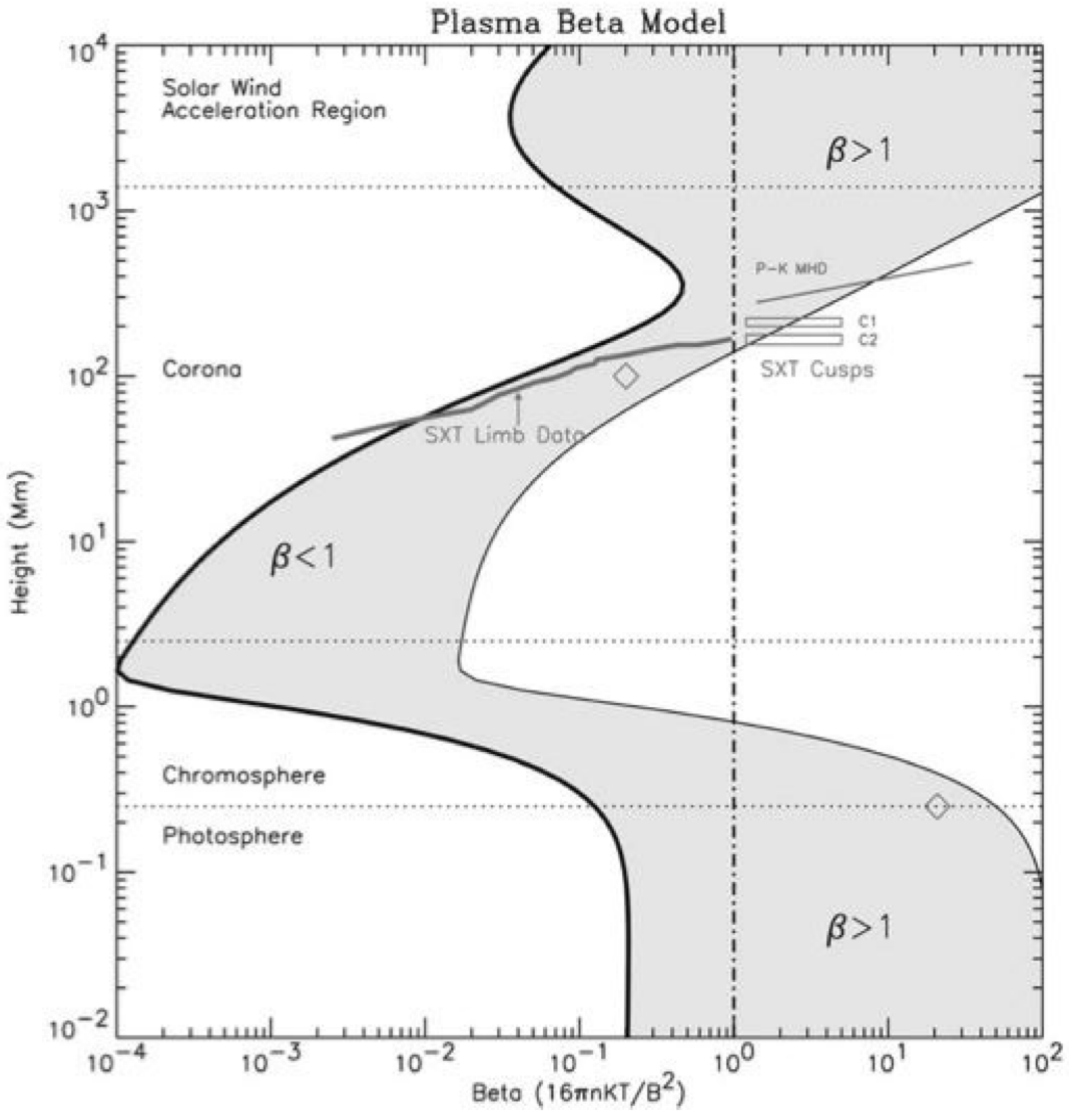

Figure 1.29: Plasma β in the solar atmosphere. The boundaries are 100 G and 2500 G magnetic field strengths. From Gary (2001)

μ_0 is the magnetic permeability in a vacuum.

Gary (2001) constructed a comprehensive model of the plasma β above an AR based on measurable physical parameters derived from EUV and X-ray observations such as electron density and temperature, however, the magnetic field is problematic above the photosphere due to lack of visible observations of Zeeman lines (see §1.4.7).

Figure 1.29 shows how β varies with height within the solar atmosphere. The results are based on a single pressure model and the boundaries of the shaded area are derived from plage and umbra magnetic models (100 and 500 G, respectively). The fact that the plasma β regime varies significantly with height along a magnetic field line routed in the photosphere and extending into the corona has implications for the force-free field assumption of most coronal magnetic extrapolation models.

If $\beta \ll 1$, the plasma pressure has virtually no influence, so the magnetic field is essentially force-free. In a force-free field, the gradient of the magnetic pressure is balanced by the curvature force, therefore, the condition for hydrostatic equilibrium applies along each field line when the velocity is less than the sound speed (see §1.5.6).

$$\boldsymbol{j} \times \boldsymbol{B} = -\nabla \frac{B^2}{2\mu_0} + \frac{(B \cdot \nabla)B}{\mu_0} = 0, \tag{1.50}$$

where $\boldsymbol{j} \times \boldsymbol{B}$ is the Lorenz force per unit volume, $\nabla(\mathrm{B}^2/2\mu_0)$ is the gradient of the magnetic pressure, and $(\mathrm{B} \cdot \nabla)\mathrm{B}/\mu_0$ is the magnetic tension force.

1.7.5 EUV and X-ray Emission from the Corona

None of the layers in the atmosphere are in global thermodynamic equilibrium where the intensity of the radiation or source function can be described by the Planck function associated with blackbody radiation. However, local thermodynamic equilibrium (LTE), defined by the local value of temperature, holds in the photosphere. There the temperature changes and radiation escapes, but slowly enough for LTE conditions to be assumed. Non-LTE (NLTE) conditions are associated with the chromosphere. In NLTE, the plasma has a kinetic temperature different to the temperature that characterizes the radiation passing through it and interacts with it. Coronal equilibrium is controlled entirely by the interactions of ions and electrons of corona and photospheric radiation passes through coronal plasma without interacting with it.

1.7.5.1 Ionization and Recombination Processes in the Corona

Radiation from hot plasmas like the corona involves the interaction of a hot, tenuous gas with electromagnetic radiation. Atoms with electrons in any of the available quantized energy levels are continually perturbed by the surrounding electromagnetic radiation field or one or more free electrons or other ions. Ionization and

recombination processes that contribute to the X-ray and EUV spectrum of the corona involve:

- interaction with the electromagnetic radiation field by:
  - induced absorption when a photon from the ambient radiation field excites an electron in an atom to a higher energy level in a bound-bound transition which produces absorption lines in the corona;
  - stimulated emission when a photon from the ambient radiation field stimulates an electron to move to a lower energy level emitting a second photon in the process;
- spontaneous emission when an atom in a higher energy state may spontaneously emit a photon without a photon from the surrounding radiation field and move to a lower energy level;
- collisions with free electrons above and below the ionization threshold of an ion;
- transfer of an electron from one ion to another.

Ionization-recombination processes can be paired as follows:

- Photo-ionization + radiative recombination
- Collisional ionization + three-body recombination
- Auto-ionization + dielectronic recombination

Photo-ionization is a bound-free transition where a bound electron becomes free from the atom because the photon from the radiation field has more energy that the ionization energy of the atom. The 'excess' energy is the kinetic energy of the free electron. Collisional ionization occurs by collision of free electrons and ions. The ion is left in a higher ionization state when an outer electron is removed. In the solar atmosphere, the most important processes that cause a transition from one level to another in an ion are collisional processes between ions and free electrons. Collisional processes are involved in the formation of nearly all spectral lines below 2000 Å (Phillips *et al.*, 2008). Auto-ionization occurs when an ion spontaneously ionizes without the perturbation of a photon from the radiation field. If an inner-shell electron is removed then an electron from a higher energy level must fill the inner-shell vacancy.

Radiative recombination is the reverse process of photo-ionization. A free electron is captured by the ion into an available energy state and the 'excess' energy is removed by the emission of a photon. This transition produces Balmer (transitions to n=2 in the hydrogen series) and Lyman (transitions to n=1 in the hydrogen series) continua. Three-body recombination occurs in relatively high density plasma when two electrons or an electron and ion interact with the ion resulting in recombination of one or both electrons. Dielectronic recombination involves two electrons - a free electron is captured by the ion and becomes excited as does a bound electron. The doubly excited ion stabilizes with the electrons falling into the lowest available energy states. Dielectronic recombination is an important process for the energy levels above the ionization potential of an ion. Dielectronic satellite line emission is prominent in the X-ray range.

Forbidden line transitions produce line emission by atoms undergoing energy transitions prohibited by quantum mechanics selection rules. There is a small probability that an atom will make the transition from a meta-stable state to a lower energy state by spontaneous emission. Such transitions are observed in the low-density plasma of the corona as atomic collisions are unlikely and forbidden line emission will probably occur before collisional de-excitation. Forbidden transitions account for a significant portion of the photons emitted by the corona.

For a given temperature, the balance of atomic process rates for a particular element in the corona is complex as there is a continuous competition between the various processes described above. In general, the ionization balance in the corona is given by: collisional ionization + auto-ionization = radiative recombination + dielectric recombination. The ionization state of the coronal plasma is directly related to the temperature so that the higher the temperature, the higher is the ionization state.

1.7.5.2 Transition Probabilities - Einstein Coefficients

In order to understand the EUV and X-ray emissions lines that dominate the spectrum of the corona, the atomic transition probabilities between the quantized energy levels must be examined in some detail. Einstein (in 1917) calculated transition probabilities between higher energy level m (with energy state E_m) and lower energy level n (with energy state E_n) in a system that settles into an equilibrium at temperature T. Einstein's postulates are:

- the electromagnetic radiation is in equilibrium at temperature T and has a black-body spectrum defined by the Planck function;

- the rate for induced absorption is proportional to the energy density, U_ν;
- the total number of atoms in an energy state does not change;
- the Boltzmann probability distribution describes the statistical distribution of energy level populations.

Einstein defined a coefficient A_{mn} for spontaneous emission from a higher energy state E_m to a lower energy state E_n and a coefficient B_{mn} for stimulated emission between the same energy states.

The atomic transition probability per unit time, P_{mn}, between higher energy state, E_m and lower energy state, E_n is:

$$P_{mn} = A_{mn} + B_{mn}U_\nu \tag{1.51}$$

and the probability, P_{nm}, for the reverse process via induced absorption between a lower energy state, E_n and a higher energy state, E_m, is:

$$P_{nm} = B_{nm}U_\nu. \tag{1.52}$$

This is the mathematical formulation of Einstein's second assumption given above. The energy density, U_ν at temperature T is given by the Planck function:

$$U_\nu = \frac{8\pi h\nu_{nm}^3}{c^3}\frac{1}{e^{h\nu_{nm}/k_BT} - 1}, \tag{1.53}$$

where h is the Planck constant, ν_{nm} is the frequency of transition nm, c is the speed of light, and k_B is the Boltzmann constant. The Boltzmann distribution for population density of excited state E_m at temperature T is:

$$N_m = \frac{g_m}{g_0}N_0 \; exp\left(\frac{-\chi_m}{k_BT}\right), \tag{1.54}$$

where N_m is the number of electrons in higher energy level m, N_0 is the number of electrons in the ground state, g_m is the statistical weight of state m, g_0 is the statistical weight of the ground state, and χ_m is the excitation energy of energy level E_m. The relative population of energy states E_n and E_m is given by:

$$\frac{N_n}{g_n} = \frac{N_m}{g_m} \; exp\left(\frac{-E_n - E_m}{k_BT}\right). \tag{1.55}$$

Combining Equations 1.51, 1.52, and 1.53:

$$\frac{g_n}{g_m} \; exp\left(\frac{-E_n}{k_BT}\right) \; B_{nm}U_\nu = exp\left(\frac{-E_m}{k_BT}\right) \; (A_{mn} + B_{mn}U_\nu) \tag{1.56}$$

gives a relationship for the Einstein coefficients. If a photon has energy of $h\nu_{nm} = \mathrm{E}_m$ - E_n then the ratio of transition rates between induced absorption and spontaneous emission is:

$$A_{mn} = \frac{8\pi h\nu_{nm}^3}{c^3} B_{mn} \tag{1.57}$$

and

$$g_m B_{mn} = g_n B_{nm}. \tag{1.58}$$

(The preceding subsection is based on Aschwanden (2005)).

1.7.5.3 Transfer Equation

Radiation emitted by a source such as the Sun passes through the extended volume of the Sun itself and the intervening matter such as the interplanetary medium. The intensity of the beam is the specific intensity, I_ν, with units ergs s^{-1} cm^{-2} sr^{-1} Hz^{-1}. Two other quantities are important, the optical depth and the source function. The optical depth is a measure of the amount of radiation absorbed or scattered along a path from the source at s_0 to s:

$$\tau_\nu(s) = \int_{s_0}^{s} \alpha_\nu(s^{'})\, ds^{'}, \tag{1.59}$$

where α_ν is the absorption coefficient. The source function, S_ν, is the ratio of the emission coefficient to the absorption coefficient and can be expressed in terms of the Einstein coefficients A and B. The radiative transfer equation mathematically expresses the propagation through intervening matter affected by absorption, emission, and scattering:

$$\frac{dI_\nu}{d\tau_\nu} = -I_\nu + S_\nu. \tag{1.60}$$

The solution of the radiative transfer equation can be written in a convenient form assuming a constant source function:

$$I_\nu(\tau_\nu) = S_\nu + exp^{-\tau_\nu}\ (I_\nu(0) - S_\nu). \tag{1.61}$$

When $\tau_\nu \to \infty$, $\mathrm{I}_\nu = \mathrm{S}_\nu$ and the source is considered to be optically thick. On the other hand, when $\tau_\nu \to 0$, either $\mathrm{I}_\nu = \mathrm{I}_\nu(0)$ if the intervening matter is negligible, or $\mathrm{I}_\nu(0) = 0$ and the emitting source is optically thin. In the latter case, intensity is proportional to the optical depth:

$$I_\nu(\tau_\nu) = S_\nu\ \tau_\nu. \tag{1.62}$$

The corona is optically thin and shows a center-to-limb variation because the optical path increases by a factor of $1/\cos(l$ - $l_0)$ as a function of longitude l from disk center

($l = l_0$). (The preceding was based on Golub and Pasachoff (1997) and Aschwanden (2005)).

1.7.5.4 Calculating Coronal Emission - Line Radiation

At coronal temperatures and densities, major contributions to coronal emission come from a small number of elements that dominate the radiative emission. These elements include Fe and Si among others. The corona is considered to be optically thin, therefore the number of photons in a single spectral line is the sum of all contributions along the LOS. Emission in a single spectral line in element X for one transition from j to i (bound-bound emission) is:

$$X_j^{+m} \longrightarrow X_i^{+m} + h\nu_{ij}, \tag{1.63}$$

where X_j^{+m} is an atom of element X with m electrons removed and $\mathrm{h}\nu_{ij}$ is the energy difference between levels j and i. The fact that the spectral line is not infinitely sharp requires a function for an emission profile, ψ_ν, in order to obtain the emissivity of the plasma, P_ν (ergs cm^{-3} s^{-1} Hz^{-1}):

$$P_\nu = N_j(X^{+m})\ A_{ji}\ h\nu_{ij}\ \psi_\nu, \tag{1.64}$$

where $\mathrm{N}_j(\mathrm{X}^{+m})$ is the number density of atoms of the element X in the higher level j, A_{ji} is the Einstein coefficient for spontaneous emission from the higher energy level j to i, $\mathrm{h}\nu_{ij}$ is the energy per photon, and ψ_ν is the emission profile. Total power emitted in the transition j $\rightarrow$ i per unit volume (ergs cm^{-3} s^{-1}) is:

$$P_{ij} = N_j(X^{+m})\ A_{ji}\ \frac{hc}{\lambda_{ij}}, \tag{1.65}$$

(λ_{ij} is the wavelength of the photon). Power P_{ij} is obtained by integrating emissivity of the plasma over all frequencies. Next, flux detected at 1 AU in the emission line over a volume element in the corona (ergs cm^{-2} s^{-1}) is given by:

$$F_{ij} = \frac{1}{\pi R^2} \int_{\Delta V} P_{ij}\ dV. \tag{1.66}$$

The coronal spectrum for a given temperature and density is $\sum \mathrm{F}_{ij}$, however, the crucial unknown quantity is the number density of atoms of the element X^{+m} in higher level j, $\mathrm{N}_j(X^{+m})$, which is embedded in P_{ij}. A number of ratios are used with the observable electron density (N_e) to determine its value:

$$N_j(X^{+m}) = \frac{N_j(X^{+m})}{N(X^{+m})}\ \frac{N(X^{+m})}{N(X)}\ \frac{N(X)}{N(H)}\ \frac{N(H)}{N_e}\ N_e, \tag{1.67}$$

where $\frac{N_j(X^{+m})}{N(X^{+m})}$ is the fraction of atoms of element X in ionization stage $+m$ in level j, $\frac{N(X^{+m})}{N(X)}$ is the fraction of element X in ionization stage $+m$, $\frac{N(X)}{N(H)}$ is the abundance of element X relative to hydrogen, and $\frac{N(H)}{N_e}$ is the hydrogen abundance relative to electron density ($\approx$0.83 in regions of the solar atmosphere with T $> 10^5$ K) (Mason and Fossi, 1994).

1.7.6 Coronal Approximation

In general, the relative population of two successive stages of ionization is given by the ratio of the ionization upward from and downward to X^{+m}:

$$\frac{N_j(X^{+(m+1)})}{N(X^{+m})} = \frac{Q(X^{+m})}{\alpha_{tot}(X^{+m})}, \tag{1.68}$$

where Q(X^{+m}) is the total rate coefficient for ionization from X^{+m} to $X^{+(m+1)}$ and α_{tot}(X^{+m}) is the total rate coefficient for recombination from $X^{+(m+1)}$ to X^{+m}.

The coronal approximation assumes that higher level j is populated from ground level g by collisions with thermal electrons and is depopulated by radiative decay. Collisional de-excitation, radiative excitation, and collisional excitation from levels higher than ground level g are ignored. These simplifying assumptions are appropriate for typical coronal temperatures and densities but they breakdown in higher temperature and density regimes such as during solar flares. If upward and downward rates are equated:

$$N_g(X^{+m})\ N_e\ C^e_{gj} = N_j(X^{+m})\ \sum_{k<j}\ A_{jk}, \tag{1.69}$$

where $N_g(X^{+m})$ is the ground state population, N_e is the electron density, C^e is the electron collisional rate coefficient for transition $g \rightarrow j$, N_j is the upper level population density and $\sum_{k<j}\ A_{jk}$ is the summation over spontaneous emission coefficients A_{jk}. Solve for $N_j(X^{+m})$ in Equation 1.69 and substitute into Equation 1.65:

$$P_{gj} = 0.8 A_x\ \frac{N(X^{+m})}{N(X)}\ C^e_{gi}\ \frac{hc}{\lambda_{gj}}\ N_e^2\ B_{jg}, \tag{1.70}$$

where A_x is the abundance of element X relative to hydrogen, 0.8 is the hydrogen abundance relative to electron density, and B_{jg} is the radiative cascade coefficient taking into account the branching ratio. Typically, temperature terms are grouped together in the contribution function, G(T), which is a sharply peaked function around the temperature of maximum formation of X^{+m}. The peak temperature is unique to each ion species. G(T) contains all of the atomic physics involved in the

formation of the spectral line and is given by:

$$G(T, \lambda_{gj}) = \frac{N(X^{+m})}{N(X)} \; C^{e}_{gi} \; B_{jg}. \tag{1.71}$$

P_{gj} can be restated using the contribution function:

$$P_{gj} = 0.8 A_x \; G(T, \lambda_{gj}) \; \frac{hc}{\lambda_{gj}} \; N_e^2. \tag{1.72}$$

Emissivity P_{gj} depends on N_e^2 and $\int N_e^2$ dV is the definition of emission measure of the volume element dV (units cm^{-3}). The emission measure depends on the physical conditions of the emitting plasma in the corona as it is proportional to the number of free electrons and to the electron density within the volume element. Differential emission measure (DEM), Q(T), is defined by:

$$I(\lambda_{ij}) = \frac{1}{4\pi R^2} A_x \; \int G(T, \lambda_{ij}) \; \frac{hc}{\lambda_{gj}} \; Q(T) \; dT \tag{1.73}$$

and is a measure of the amount of emitting material as a function of temperature. DEM is a fundamental observable, however, $I(\lambda_{ij})$ is integrated along the LOS which may include contributions from coronal structures with varying temperature and density. As a result, DEM curves are model dependent. (The preceding was based on Phillips *et al.* (2008) and Golub and Pasachoff (1997)).

Figure 1.30 shows the isothermal emission measure loci for silicon emission lines observed by *Hinode* EIS (Warren and Brooks, 2009). The authors found the best fit temperature to be log $T = 6.05$ assuming a constant density of log $n_e = 8.35$. If the atomic data, assumed density, and observed intensities are mutually consistent then the loci curves would lie close together as indicated by the red dot in Figure 1.30. This suggests isothermal plasma since an isothermal DEM model was used to calculate the emission measure loci curves.

1.7.7 Line Broadening

Spectral emission lines are not infinitely thin. Instead, their profiles extend over limited wavelength intervals. The line profile describes the flux distribution, *F(ν)*, which is peaked at the central frequency, ν_{ij}, and is given by:

$$F(\nu) = F_0 \; \psi(\nu), \tag{1.74}$$

where

$$\int_0^\infty \; \psi(\nu) \; d\nu = 1. \tag{1.75}$$

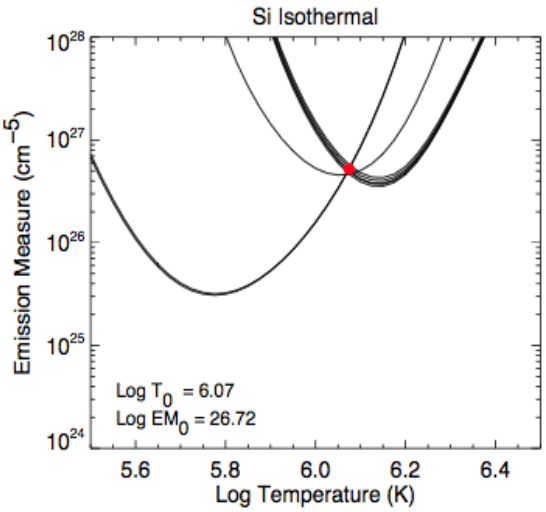

Figure 1.30: Emission measure loci for silicon emission lines observed by *Hinode* EIS using an isothermal model. The best fit temperature is log T = 6.05. Density is assumed to be log n_e = 8.35. There is generally good agreement among the silicon lines using the isothermal DEM calculations (Warren and Brooks, 2009).

Two common profiles shapes are Gaussian and Lorentzian profiles. Figure 1.31

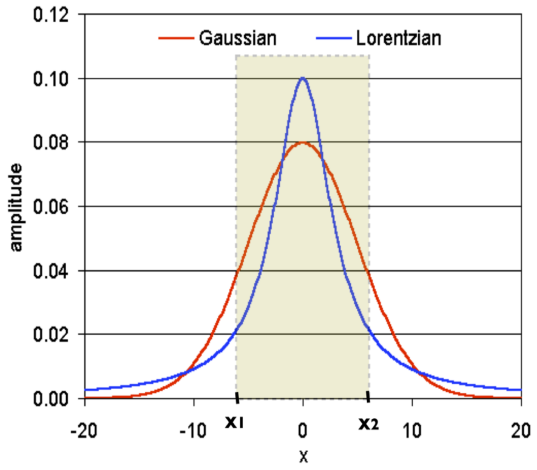

Figure 1.31: Typical line profile shapes - Lorentzian is blue and Gaussian is red. Full width half maximum is the interval X1 to X2 where the Gaussian profile amplitude is 0.4, half of the peak value of 0.8.

displays plots of both profiles, Lorentzian in blue and Gaussian in red.

The width and shape of spectral line profiles are influenced by the detecting instrument's characteristics and the physical properties of the emitting plasma.

- Instrumental spectral line profile

  The instrument observing the emitting source will broaden the spectral line profile. Such broadening is a function of the optical system, including the finite

resolution of the detector. Pre-launch laboratory and observed line widths are used to determine or infer the instrumental width and profile. It is not a trivial matter to establish the instrument profile as it may not be Gaussian, symmetric at the line peak, and/or there may be wavelength dependence (Phillips *et al.*, 2008). In the case of *Hinode* EIS, instrumental line width was inferred to vary between the short and long wave detectors, 0.054 Å and 0.057 Å, respectively (Brown *et al.*, 2008). In addition, it is likely that the instrumental width is different for the 1" and 2" slits. Figure 1.32 shows the instrumental widths for both slits (1" - solid line and 2" - dashed line). The 2" slit width is 7 mÅ larger than that for the 1" slit for the short wave detector. EIS's instrumental width varies in the Y-direction therefore the difference in the sizes of the FOVs of the two rasters may contribute to the 7 mÅ difference between the instrumental widths of the two slits (see EIS WIKI: `http://msslxr.mssl.ucl.ac.uk:8080/eiswiki/Wiki.jsp?page=InstrumentalWidthOfEIS`).

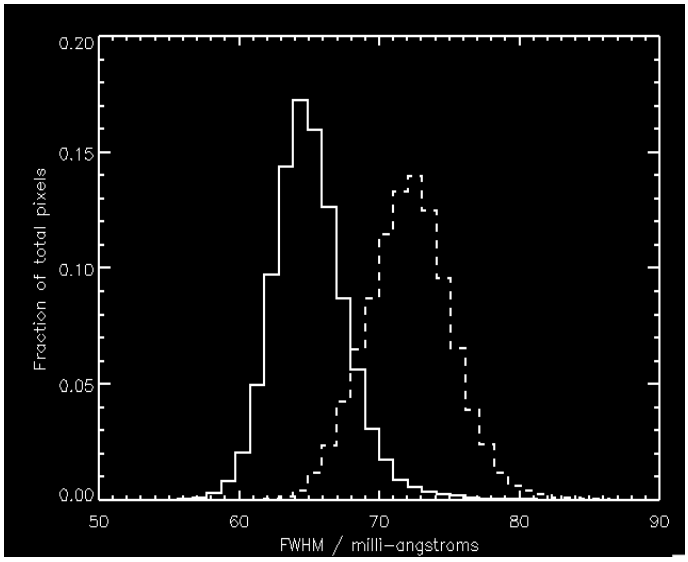

Figure 1.32: *Hinode* EIS FWHM instrumental widths for 1" and 2" slits. The 2" slit width is 7 mÅ larger than that for the 1" slit.

- Natural line profile

  The natural line profile is attributable to the intrinsic energy width of atomic energy levels in the atom (Phillips *et al.*, 2008). Uncertainty in the energy quantum emitted due to an electron transition depends on 1. how long the electron has been in its excited state, and 2. how long the electron will remain in its de-excited state (Harra and Mason, 2004). Excited states of allowed transitions have a lifetime of about 10^{-8} s which is equivalent to a few tenths of a nanometer (in the optical wavelength range), hence the intrinsic narrowness of the natural line profile. Forbidden transitions have longer lifetimes, typically milliseconds to seconds, and much narrower profiles compared with those of

allowed transitions. The profile of a naturally broadened line is Lorentzian (Figure 1.31) given by:

$$\psi(\nu) = \frac{1}{\pi} \frac{\frac{\Gamma}{4\pi}}{(\nu - \nu_0)^2 + (\frac{\Gamma}{4\pi})^2}, \tag{1.76}$$

where

$$\nu_0 = (E_j - E_i)/h \tag{1.77}$$

and

$$\Gamma = \sum_{k<j} A_{jk} + \sum_{k<i} A_{ik}. \tag{1.78}$$

- Doppler line profile

  Significant line broadening is due to the temperature dependent Doppler motions of the emitting source in the coronal plasma along the LOS. Doppler-broadened profiles may be caused by random thermal motions, rotation, turbulence, waves, and bulk plasma motions along the LOS (Phillips *et al.*, 2008). The broadening is inhomogeneous since not all of the ions in the plasma behave in the same way which usually results in a Gaussian line profile. This type of broadening dominates the solar atmosphere. The Doppler effect is defined for an ion moving at velocity v along the LOS as:

$$\nu = \nu_0 \left(1 + \frac{v}{c}\right), \tag{1.79}$$

  where ν is the observed frequency relative to the rest frequency of the radiation, ν_0, and c is the speed of light.

  For spectral emission lines that are not very strong, profiles can be approximated with a Gaussian function. $\psi(\nu)$ then gives

$$\psi(\nu) = \frac{1}{\sqrt{\pi}\Delta\nu} \, exp^{-\left(\frac{(\nu-\nu_0)}{\Delta\nu}\right)^2}. \tag{1.80}$$

  Typically, $\psi(\nu)$ is characterized by the full width half maximum (FWHM) of the profile. Figure 1.31 shows the FWHM in the interval X1 to X2 where the amplitude of the Gaussian profile is at half of the peak value. FWHM is:

$$FWHM = \frac{\nu_0}{c} \sqrt{4 \; ln \; 2 \; \frac{2k_B T_i}{M_i}}. \tag{1.81}$$

  Expressed as functions of wavelength, $\psi(\nu)$ and the FWHM, respectively, are:

$$\psi(\lambda) = \frac{1}{\sqrt{\pi}\Delta\lambda} \, exp^{-\left(\frac{(\lambda-\lambda_0)}{\lambda\nu}\right)^2} \tag{1.82}$$

and

$$FWHM = \frac{\lambda_0}{c}\sqrt{4\ ln\ 2\ \frac{2k_BT_i}{M_i}}, \tag{1.83}$$

where

$$\Delta\lambda = \frac{\lambda_0}{c}\sqrt{\frac{2k_BT_i}{M_i}}. \tag{1.84}$$

In the solar atmosphere, measured line widths are broadened above the level that is indicated by the electron kinetic temperature i.e. from Doppler broadening. The excess broadening is non-thermal in origin and is due to plasma turbulence. Non-thermal velocities are evident throughout the active Sun - in ARs and flares - as well as the QS. Taking in account non-thermal broadening ($v = v_{NT}$), the FWHM becomes:

$$FWHM = \frac{\lambda_0}{c}\sqrt{4\ ln\ 2\ \left(\frac{2k_BT_i}{M_i} + v_{NT}^2\right)}. \tag{1.85}$$

- Collisional or pressure line profile

  Collisional broadening occurs in higher density plasmas where the rate of collisions between the emitting ion and other particles in the plasma is greater. During collisions there is an exchange of energy which leads to the broadening of the energy levels. Broadening is inversely related to the mean time between collisions resulting in a transition between two energy levels. This form of broadening is likely to have more effect in the photosphere where the density is 4 to 5 orders of magnitude greater than that of the corona.

- Opacity

  Opacity can affect the line profile shape since more photons will be removed by absorption when the line profile is wider (Phillips *et al.*, 2008).

In summary, the thermal Doppler broadening and plasma turbulence are the most dominant broadening mechanisms in the corona (Phillips *et al.*, 2008) and the FWHM that characterizes total line broadening (thermal, non-thermal and instrumental) is:

$$FWHM = \frac{\lambda_0}{c}\sqrt{4\ ln\ 2\ (v_{th}^2 + v_{NT}^2 + v_{inst}^2)}. \tag{1.86}$$

1.7.8 Coronal Diagnostics

Spectroscopic diagnostic techniques provide information about the dynamic phenomena in the corona. Some of the techniques are presented here. Further discussion of turbulence and abundances can be found in previous sections.

1.7.8.1 Spectral Line Doppler Shifts

The velocity of an emitting plasma along the LOS can be determined by measuring the Doppler shifts of the spectral lines. Bulk plasma flows are considered to be red-shifted when the spectral line is shifted to longer wavelengths (λ) as the emitting source is moving away from the observer. Conversely, plasma moving toward the observer is blue-shifted and the spectral line is shifted to shorter wavelengths relative to the rest wavelength (λ_0). In the context of solar observations, red-shifted plasma flows are downflows and blue-shifted plasma flows are upflows in closed loops or outflows in 'open' field or very extended, 'open'-like loops. The Doppler shift stated in terms of wavelength is (c.f. §1.7.7):

$$\lambda = \lambda_0 \left(1 - \frac{v}{c}\right), \tag{1.87}$$

where λ is the observed wavelength, λ_0 is the rest wavelength, v is velocity, and c is the speed of light.

1.7.8.2 Density

Coronal electron densities can be determined directly from the observed intensities of spectral lines as intensity is proportional to emission measure (§1.7.6) which in turn is proportional to the square of the electron density for a given temperature, however, this method requires knowledge of the emitting region's volume, the use of the contribution function which covers a broad temperature range, temperature determination from filter ratios, and implicit assumptions of ionization equilibrium. Forbidden transitions of coronal lines, with relatively small spontaneous decay probabilities to lower levels, provide an alternative method to directly determine electron density in the corona without any assumptions of the emitting region's volume. In addition to having levels which are depopulated by allowed transitions, an ion may have so-called metastable levels, which are populated by collisions but depopulated by both collisions and low-rate/low-probability radiative decay (Golub and Pasachoff, 1997). Populations of metastable levels are relatively large in low density environments such as the corona since depopulation by low-rate radiative decay dominates and line intensities are proportional to the square of electron density. However, for collisional depopulation of a metastable level, line intensities are proportional to electron density, therefore, the ratio of lines formed from allowed and metastable levels provides a direct method for determining electron densities in the corona.

1.7.8.3 Temperature

The approximate temperature of coronal plasma may be determined by assuming ionization equilibrium where ion levels depopulate by electron impact and populate by radiative and dielectronic recombination. Atomic models such as CHIANTI provide theoretical calculations for ionization equilibrium that show for a given temperature which ionization stage is predominant. The existence of a particular ion spectral line indicates the plasma temperature, assuming ionization equilibrium.

1.7.8.4 Turbulence

As discussed in §1.7.7, non-thermal broadening of an emission line profile is a measure of turbulence in a plasma.

1.7.8.5 Abundances

The strength of an element's spectral line depends directly on the abundance of the element in the emitting region. Typically, ion abundances are specified relative to so-called heavier elements in the corona since hydrogen is fully ionized. The relative abundance of an element in the plasma can be determined by the ratio of the intensity of two different ions if their emissivities are similar. See §1.7.3 for a discussion of relative abundances in the corona.

1.7.9 Structures in the Corona

As discussed in previous sections, the solar magnetic field is responsible for the structures and dynamics observed in the corona. In the following sections, a brief account is provided of some of the structures identified in Figure 1.33, however, more detailed discussions of ARs, CHs, and X-ray jets can be found in the appropriate science chapters.

- Active regions

  The morphological appearance of ARs in the corona is vastly different to what is observed in the photosphere (c.f. §1.4.3). In the corona, ARs are characterized by their highly structured loops. As a result of constant magnetic activity, plasma heated in the chromosphere are upflows into coronal loops. The hot, ionized plasma outlines the closed, Ω-shaped magnetic field lines along which

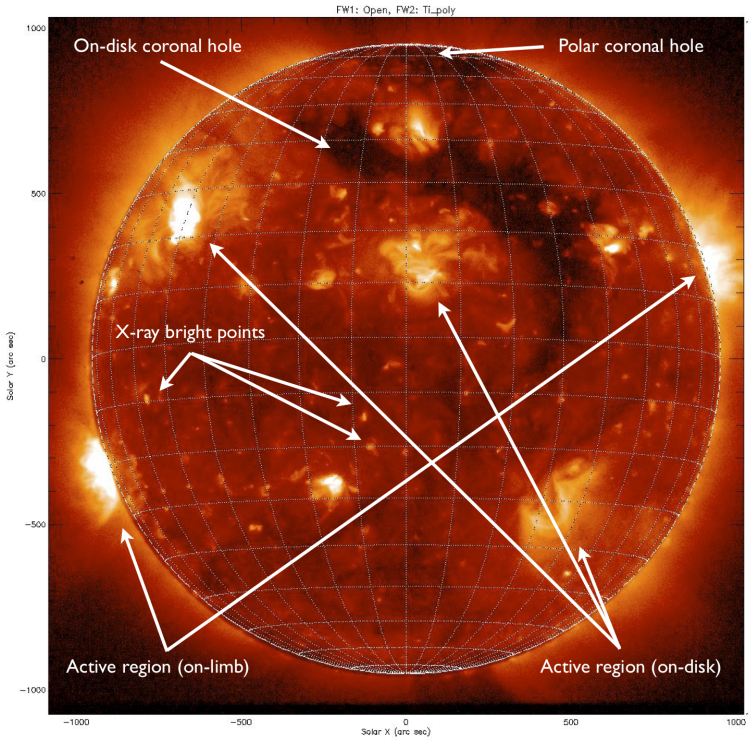

Figure 1.33: Ti poly filter X-ray image of the solar corona observed with *Hinode* XRT on 03 May 2010. Image adapted from Hinode Science Data Centre Europe.

it is confined. Filled loops are hotter and denser than the background corona and produce bright emission in EUV and soft X-ray wavelengths (see Figure 1.33). Brightness is closely linked to the strength of the magnetic field in the AR.

A filament is a dark and elongated structure when observed on the solar disk. Filament material consists of dense, cool plasma (temperature 5 - 15,000 K), hence, its dark appearance against the bright coronal background. Its counterpart on the solar limb is a prominence. All filaments are found above the PIL separating regions of opposite polarity whether in an AR or in the QS. They form in filament channels which are regions in the chromosphere where the magnetic field is aligned with the PIL. The main body of the filament is suspended by magnetic field lines above the PIL. Mass flow occurs along the magnetic field oriented along the filament axis. The underlying field may be magnetic flux ropes that support the dense plasma against gravitational forces in their magnetic 'dips'. If the overlying field can no longer contain the rising, expanding field then the filament may erupt as a CME (c.f. §1.4.6)

Helmet streamers are observed in white-light or EUV as bright, dome-shaped structures that extend 2 - 3 R_{sun} into the corona. Figure 1.23 has examples of radially aligned helmet streamers located in the equatorial region of the Sun. They are associated with ARs and are especially prominent at solar minimum.

Helmet streamer magnetic topology is both 'open' and closed. The base region contains closed field lines crossing a neutral line along which a filament may be found. A cavity of low density and brightness is located over the filament just beneath the cusp-shaped helmet-like feature. Cusp-shaped loops are indicators of dynamical processes as a result of reconnection. The region above the cusp is characterized by the presence of a current sheet embedded in a plasma flow, or stalks, that extend radially for 10 -12 R_{sun} into the heliosphere. Plasma flows occur as the thermal pressure starts to dominate the magnetic field as plasma $\beta \geq 1$. One of the sources of the slow SW is believed to be in and around the solar streamer belt.

When an AR is highly sheared then the loops may form a bright forward or inverse S-shaped sigmoid, generally observed in soft X-ray emission. The topological structure of a sigmoid is highly complex. It consists of differently oriented loops that form two opposite J-shapes that form the distinctive S-shape. Sigmoids are associated with eruptive activity. Canfield *et al.* (1999) found that ARs with sigmoids are 68% more likely to erupt. This is related to the non-potentiality of the sigmoidal magnetic field and its significant excess free energy (see Chapter 5).

- Quiet sun regions

  The QS comprises all areas outside ARs and CHs on the solar surface. However, the QS is a misnomer as there are many ongoing dynamical processes from small scale phenomena such as network heating events, blue-shifted outflows associated with QS network boundaries, mini-CMEs, and coronal bright points (BP), to large scale prominences and trans-equatorial loops. Temperature sensitive line ratios give temperatures ranging from 1.0×10^6 to 2.1×10^6 K and density sensitive line ratios give electron density of $10^{9.03}$ cm^{-3} (Golub and Pasachoff, 1997). QS magnetic topology is dominantly closed. In Figure 1.33, BPs are the obvious feature in the QS as they are characterized by enhanced emission in X-ray and EUV. They tend to be found at network boundaries, away from ARs. BPs are associated to small bipolar magnetic regions which are emerging or canceling.

- Coronal holes

  The defining physical characteristic of a CH is its dominant unipolar 'open' magnetic field. The 'open' field connects the solar surface to the heliosphere and provides efficient conduits for outflowing plasma and accelerated particles. CHs are thought to be the source of the fast SW. In EUV and X-rays, CHs are relatively well-defined features devoid of emission due to lower temperatures and electron density compared to the QS (for density comparison see Figure 1.28). Habbal *et al.* (1993) found the average temperature to be

significantly lower, 0.78 - 0.93 MK between 1.02 - 1.07 R_{sun}, than in the surrounding QS (0.94 - 1.2 MK). EUV temperature and density diagnostics are difficult because of contamination from hotter plasma along the LOS.

Hinode SOT observations of polar CH magnetic fields revealed vertically oriented flux tubes with field strength as strong as 1kG (Tsuneta *et al.*, 2008). Field vectors diverged from the center of flux elements which Tsuneta *et al.* (2008) interpreted to be consistent with magnetic flux tubes that are expanding and fanning out with height. In the magnetic environment of polar CHs, vertical flux tubes should undergo a large expansion between the photosphere and the lower corona as a result of their high field strength. The radial expansion factor *A(h)* of a flux tube can be expressed as:

$$A(h) = A(0)\left(1 + \frac{h}{R_{sun}}\right)^2 f(r), \tag{1.88}$$

where distance (r) = R_{sun} + (h) from the Sun center and $f(h)$ is a super-radial expansion factor for polar magnetic field (Aschwanden, 2005).

A characteristic transient feature of CHs are jets visible in soft X-rays and EUV. They are a consequence of reconnection between 'open' and closed fields in CHs. Heated plasma is accelerated and flows along the 'open' field. See §4.2 for further discussion on jets.

1.8 The Extended Corona - the Solar Wind and the Heliosphere

Enclosed by the interstellar medium (ISM), the heliosphere is the volume of space formed by the outflowing SW and the Sun's magnetic field. Its size is determined by the balance between the dynamic pressure of the SW and the pressure of the ISM. The heliosphere is thought to extend beyond 100 AU to the boundary between the SW and ISM plasmas known as the heliopause.

The SW consists mainly of ionized coronal plasma (ionized hydrogen and helium with traces of heavier elements such as partially ionized Fe, Si, Mg, Ca, present in solar abundances) and solar magnetic fields. The high temperature and high thermal conductivity of the corona ensure that the SW is continually expanding outward, reaching supersonic speeds and extending far into the heliosphere. Before discussing the standard SW model and its results, it is appropriate to provide a

brief overview of SW properties based on observations from a number of spacecraft including *Ulysses*.

SW streams are divided into two distinct categories, the fast SW, with polar CHs as its source region and the slow SW with its less well understood origins in the streamer belt around the solar equator, ARs, and CH boundaries. Figure 1.34 shows the spatial distribution, velocities, and IMF magnetic field direction of both streams obtained by *Ulysses* over three orbits (McComas *et al.*, 2008) during Solar Cycle 23 and the beginning of Solar Cycle 24. In general, the slow SW has high density and is variable in composition and temperature whereas the fast SW is more uniform. Table 1.8 summarizes the SW properties at 1 AU.

Table 1.8: SW properties at 1 AU. Courtesy of R. Forsyth.

Property at 1 AU	Fast SW	Slow SW
Speed (v)	$\sim$750 km s^{-1}	$\sim$400 km s^{-1}
Number density (n)	$\sim$3 cm^{-3}	$\sim$10 cm^{-3}
Flux (nv)	$\sim 2\times10^8$ cm^{-2} s^{-1}	$\sim 3\times10^8$ cm^{-2} s^{-1}
Magnetic field (B_r)	$\sim$3 nT	$\sim$3 nT
Proton temperature (T_p)	$\sim 2\times10^5$ K	$\sim 4\times10^4$ K
Electron temperature (T_e)	$\sim 1\times10^5$ K	$\sim 1.3\times10^5$ K
Composition (He/H)	$\sim$5%	$\sim$1 to 30%

1.8.1 The Standard Model for the SW

The presence of a tenuous solar corona with a temperature that exceeds 10^6 K has two implications: the high thermal conductivity of the corona means that it will extend into the interplanetary space (IPS) and the corona can not be in hydrostatic equilibrium in order for IPS pressure values to be reached. The corona must be continuously expanding. Chapman and Zirin (1957) and Parker (1958) first predicted the existence of the expanding corona, or SW, several years before it was observed. Parker formulated the first SW model which is often referred to as the standard model.

For Parker's model, the expanding plasma of the SW is assumed to be steady, isothermal, and an ideal gas. Further, the system is considered to be spherically symmetric so there is a dependence on the radial distance r only i.e. the SW flows radially away from the Sun. The governing MHD equations that reflect these simplifying assumptions are:

$$\boldsymbol{\nabla} \cdot (\rho \boldsymbol{v}) = 0, \tag{1.89}$$

$$\rho(\boldsymbol{v} \cdot \boldsymbol{\nabla})\boldsymbol{v} = -\boldsymbol{\nabla} p + \rho \boldsymbol{g}, \tag{1.90}$$

$$p = \rho R T, \tag{1.91}$$

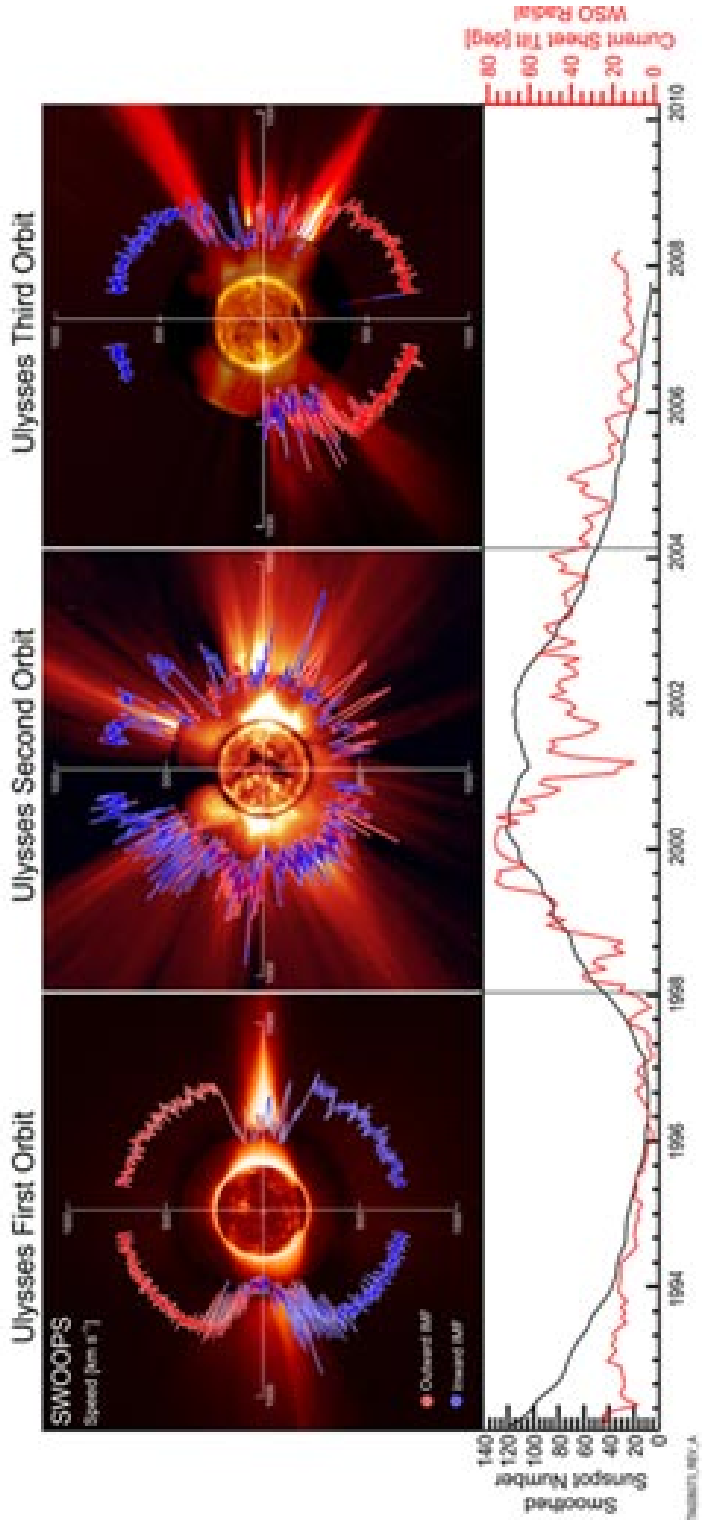

Figure 1.34: SW spatial distribution, velocities, and magnetic polarities (blue/red indicates negative/positive polarity) from three orbits of *Ulysses*. Bottom panel shows sunspot number during each orbit. Solar minimum occurred during the 1st and 3rd orbits and solar maximum during the 2nd orbit. (McComas *et al.*, 2008).

$$T = T_0, \tag{1.92}$$

$$g = \frac{GM_{sun}}{r^2}, \tag{1.93}$$

$$c_s^2 = \frac{p}{\rho} = constant, \tag{1.94}$$

ρ is density, v is radial velocity, p is pressure, g is gravitational acceleration in the radial direction, R is the gas constant, T is temperature, G is the gravitational constant, M_{sun} is the mass of the Sun, r is the radial distance from the Sun's center, and c_s is the speed of sound. Differential operators in a spherical coordinate system with a dependence on radial distance r only are of the form:

$$\boldsymbol{\nabla} a = \frac{da}{dr}, \tag{1.95}$$

$$\boldsymbol{\nabla} \cdot A = \frac{1}{r^2}\frac{d}{dr}\left(r^2 A_r\right). \tag{1.96}$$

Utilizing Equations 1.95 and 1.96 and substituting into Equation 1.90, the momentum equation becomes:

$$\rho v\frac{dv}{dr} = -\frac{dp}{dr} - \frac{GM_{sun}\rho}{r^2}, \tag{1.97}$$

and the equation for mass continuity (Equation 1.89) becomes:

$$\frac{d}{dr}\left(r^2\rho v\right) = 0. \tag{1.98}$$

Substituting for pressure and dividing through by ρ, Equation 1.97 becomes:

$$v\frac{dv}{dr} = -c_s^2\frac{1}{\rho}\frac{d\rho}{dr} - \frac{GM_{sun}}{r^2}. \tag{1.99}$$

Eliminate ρ using Equation 1.98,

$$\frac{d}{dr}\left(r^2\rho v\right) = \rho\frac{d}{dr}\left(r^2 v\right) + r^2 v\frac{d\rho}{dr} = 0 \tag{1.100}$$

to get

$$\frac{1}{\rho}\frac{d\rho}{dr} = -\frac{1}{r^2 v}\frac{d}{dr}\left(r^2 v\right). \tag{1.101}$$

Use Equation 1.101 and substitute into Equation 1.99 to obtain:

$$\left(v - \frac{c_s^2}{v}\right)\frac{dv}{dr} = 2\frac{c_s^2}{r} - \frac{GM_{sun}}{r^2}. \tag{1.102}$$

Equation 1.102 can be rewritten using the critical radius r_c:

$$r_c = \frac{GM_{sun}m}{4kT}, \tag{1.103}$$

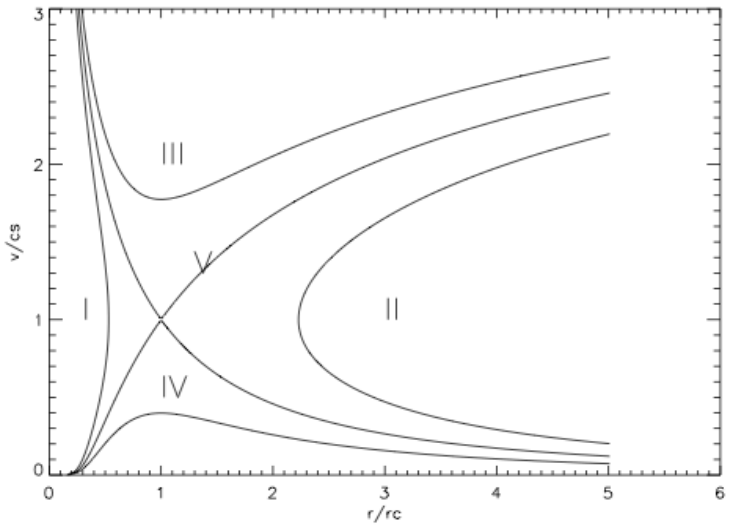

Figure 1.35: Classes of solutions to the Parker standard model. Types IV and V are physically possible.

which is the position where the SW speed v is equal to the sound speed, c_s, to get

$$\left(v - \frac{c_s^2}{v}\right)\frac{dv}{dr} = 2\frac{c_s^2}{r^2}(r - r_c). \tag{1.104}$$

Equation 1.104 is a separable ordinary differential equation,

$$\int \left(v - \frac{c_s^2}{v}\right) dv = \int 2\frac{c_s^2}{r^2}(r - r_c)\ dr \tag{1.105}$$

that has a solution

$$\left(\frac{v}{c_s}\right)^2 - log\left(\frac{v}{c_s}\right)^2 = 4\ log\left(\frac{r}{r_c}\right) + 4\frac{r_c}{r} + C. \tag{1.106}$$

Solutions to Equation 1.106 can be divided into five classes shown in Figure 1.35. Types I and II have two velocity values for the same distance and do not describe continuous SW flows from the the Sun to large distances from Sun. These solutions can be eliminated since only single-valued continuous solutions are physically valid. Type III solutions have supersonic velocities near the Sun which are not observed.

Types IV and V are physically possible. Type IV solutions are known as solar 'breeze' solutions because they predict subsonic SW velocities everywhere and reach the order of 1 km s^{-1} at 1 AU. Type V solutions start subsonically near the Sun, pass through the critical point where the SW speed is equal to the sound speed, and reach supersonic speeds at large distances (between 5 to 10 R_{sun}). *In situ* measurements in the early 1960s showed SW velocities of the order predicted by Type V solutions.

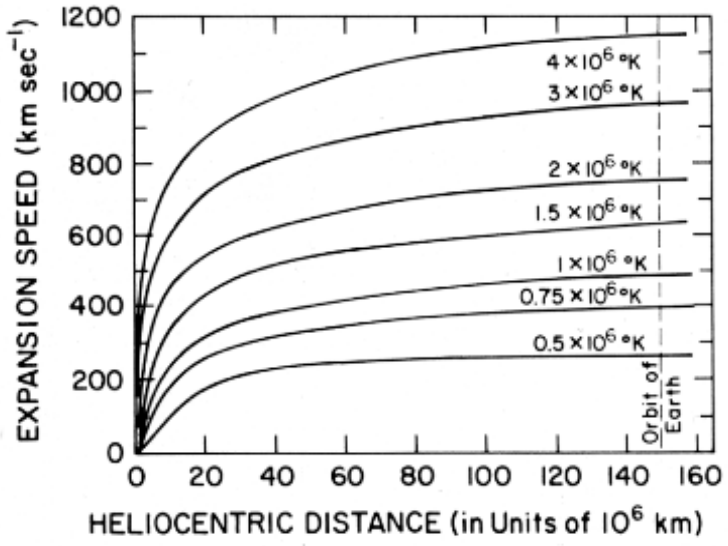

Figure 1.36: SW velocity of an isothermal corona vs heliocentric distance adapted from (Parker, 1958).

1.8.2 Current Generation of SW Models

Figure 1.36 shows the velocity of the SW as a function of the corona's temperature for the Parker model. The model predicts that the SW speed is based primarily on the corona's temperature so that high speed winds would have to originate in the hotter regions of the corona. This result contradicts observations of cooler CHs as the fast SW source region. A purely thermally driven SW is not sufficient to drive fast SW nor to explain two speed SW streams. Over time, two broad classes of theoretical models for SW acceleration have been proposed - wave/turbulence-driven (WTD) models and reconnection/loop-opening (RLO) models (Cranmer (2010); Cranmer and van Ballegooijen (2010) and references therein). In WTD models, the main energy is injected at the footpoints of flux tubes. 'Open' flux tubes rooted in the photosphere are perturbed by convection which produces Alfvèn waves that propagate into the corona. The waves are supposed to partially reflect back towards the solar surface and develop into MHD turbulence. These models have reproduced SW conditions with wave amplitudes of order as those observed in the corona (Cranmer, 2010). In RLO models, 'open' SW flux tubes reconnect with closed field regions. The mass, momentum, and energy of the SW is provided by loops of varying properties in the low corona (Cranmer, 2010).

1.8.3 The Structure of the Heliosphere

The expanding SW has a strong effect on the magnetic field configuration of the heliosphere as the magnetic field is 'frozen-in' so that it is transported with the

SW. Within the low plasma β environment of the corona, the magnetic field forces dominate the plasma forces, however, as the field strength decreases with distance, the plasma flow becomes dominant, and the magnetic field is constrained to move with the SW. Due to solar rotation, the magnetic field adopts an Archimedean spiral configuration and the angle of the field depends on the distance, latitude, and SW velocity. The magnetic field angle is approximated by:

$$tan\ \phi = \omega \frac{r}{v_r}, \tag{1.107}$$

where ϕ is the field angle at distance r, ω is solar rotation angular velocity, and v_r is the radial SW velocity. The spirals are referred to as Parker spirals.

As shown in Figure 1.34, left panel, the SW from polar CHs tends to be high speed, while the SW from the lower latitude activity belt is lower speed. Constrained by the magnetic field, the polar SW stream bends towards the ecliptic plane and merges with the equatorial SW stream. The fast SW may start to ram into the slower SW ahead of it, creating high-pressure regions called co-rotating interaction regions (CIRs). Figure 1.37 shows an illustration of fast and slow SW streams, the high compression region of a CIR, and the Parker spiral. At the edges of the CIR, a forward-reverse shock pair forms. The forward shock propagates outwards and the reverse shock propagates towards the fast SW stream. CIR-related shocks are important locations for the acceleration of particles throughout the heliosphere (Balogh *et al.*, 2008). Rarefaction regions are regions of low particle density located behind CIRs.

At solar minimum, the heliospheric magnetic field is relatively simple as it is dominated by the solar magnetic dipole. A heliospheric current sheet (HCS) forms where outward field lines from one hemisphere meet the inward field lines from the other hemisphere in the vicinity of the ecliptic plane. The tilt of the solar dipole field, and therefore the HCS, is smallest near solar minimum. Figure 1.38 shows the modeled HCS for CR 2053 from the Wilcox Observatory (`http://wso.stanford.edu/synsourcel.html`). The solid black line represents the neutral line separating the dark-shaded negative field of the northern hemisphere and the light-shaded positive field of the southern hemisphere. As the magnetic axis precesses around the rotation axis, the HCS also rotates with the Sun, resulting in a warped structure that is shaped like a ballerina's skirt. Spacecraft in the ecliptic plane are located first in one magnetic hemisphere then the other. This change in field structure is known as sector structure. It is the result of the tens of degrees offset of the magnetic dipole from the Sun's rotation axis (Balogh *et al.*, 2008).

As the Sun approaches solar maximum, the magnetic structure of the Sun is

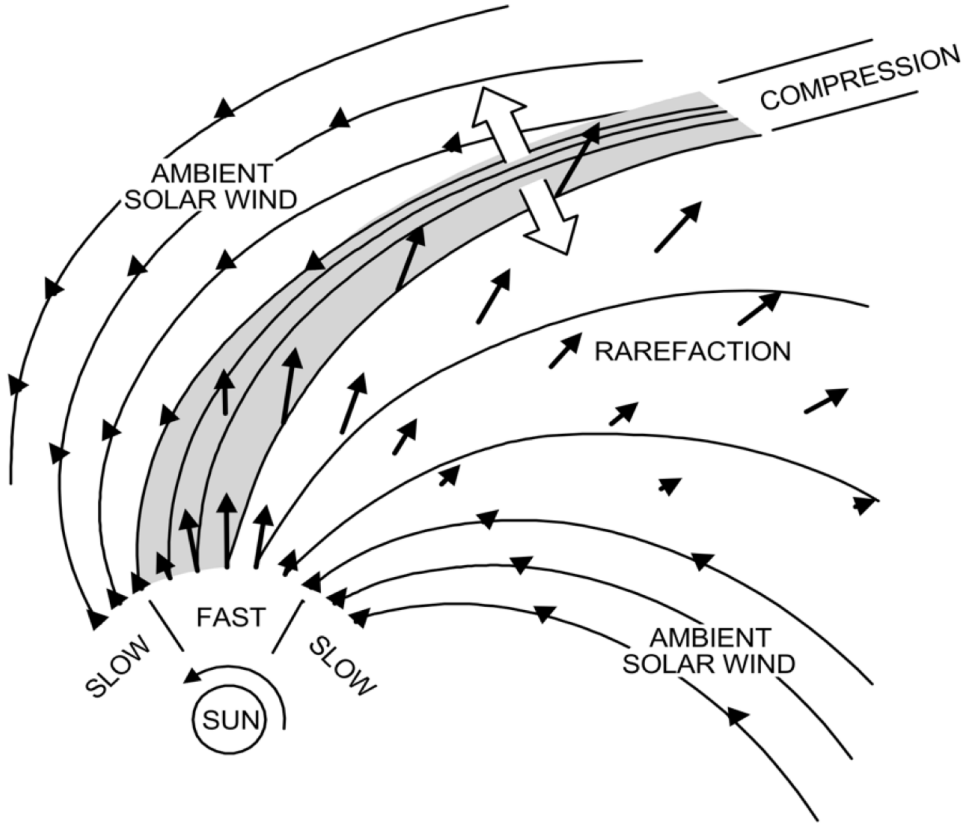

Figure 1.37: Cartoon of fast SW stream ramming or 'catching up' to the slow SW stream creating a region of high compression or a CIR. Forward-reverse shocks are indicated by the large arrows. Behind the CIR is the rarefaction region of very low density. The Parker spiral is the Archimedean spiral of magnetic field lines 'bending' due to solar rotation. From Pizzo (1986).

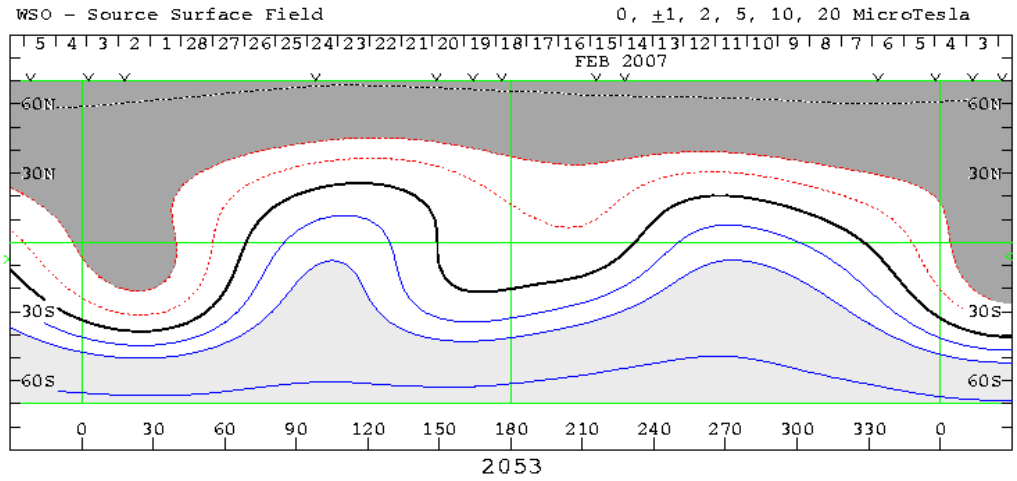

Figure 1.38: HCS for CR 2053. The solid black line represents the neutral line separating the oppositely directed magnetic field lines of the different hemispheres. The dark-shaded negative field of the northern hemisphere and the light-shaded positive field of the southern hemisphere are indicated. From the Wilcox Observatory.

increasingly more complex. In Figure 1.34, a comparison of the middle panel with the left and right panels demonstrates the changes in the SW source regions at solar maximum vs the previous and following solar minimum periods. The slow SW is no longer confined to equatorial regions. Streamers appear at high latitudes, producing streams of slow wind at these latitudes. Polar CHs are reduced in size. The HCS becomes more warped during maximum.

The current solar cycle (24) began in December 2008 during the 3rd orbit of *Ulysses*. Observations showed that the fast SW from the large polar CHs was slightly slower, much less dense, cooler, and had less mass and momentum flux than during the previous solar minimum which began in May 1996 (McComas *et al.*, 2008). This has implications for the size of the heliosphere as lower dynamic pressure means the heliopause may be receding. Further, the onset of Solar Cycle 24 occurred much later than predicted and the number of sunspots is expected to be lower that of the previous cycle.

1.8.4 ICMEs

The slow and fast SW streams are often permeated by transient phenomena such as interplanetary coronal mass ejections (ICMEs), the heliospheric counterparts of CMEs. Whereas CMEs are easily identified in white light with coronagraphs, the identification of their interplanetary counterparts is far from a trivial matter. Forsyth and Gosling (2001) and Zurbuchen and Richardson (2006) (and references therein) discuss signatures of ICMEs including:

- Counterstreaming suprathermal electrons (> 60eV),
- Counterstreaming energetic protons,
- Helium abundance enhancements,
- Declining velocity profile/expansion,
- Ion and electron temperature decreases,
- Magnetic field enhancement,
- Low plasma β,
- Low magnetic field variance,
- Characteristic smooth field rotations ($\gg 30^\circ$) consistent with flux ropes,
- Extreme density decrease,

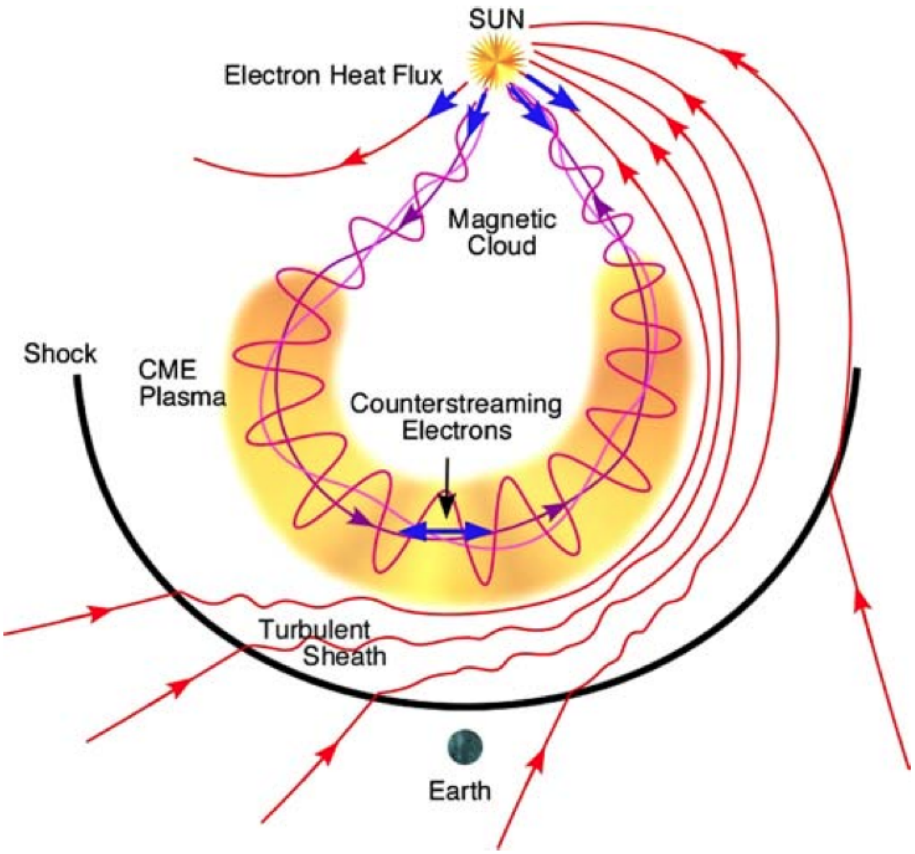

Figure 1.39: Cartoon of an ICME with a magnetic flux rope structure. Zurbuchen and Richardson (2006).

- Heavy ion composition that differs from that of the SW.

Not all ICMEs exhibit all of these signatures. Figure 1.39 is a schematic showing the flux-rope structure of an ICME and upstream shock relating some of the ICME signatures listed above. ICMEs and magnetic clouds are discussed in more detail in §4.4.

Chapter 2

Instrumentation

The data used in the work presented in this thesis come from both remote sensing and *in situ* particle and field instruments. The remote sensing instrumentation includes an EUV imaging spectrometer, two EUV imagers, an X-ray imager, a white-light heliospheric imager, and a magnetograph. The *in situ* instrumentation includes a SW electron analyzer, a suprathermal electron telescope, a magnetometer and an ionic composition and charge state distribution experiment. Such a wide range of instruments covering the solar magnetic field, solar atmosphere and the SW is required for a full understanding of coronal dynamics and any possible consequences.

2.1 *Hinode*

On 2006 September 23, the *Hinode* (or sunrise) (Kosugi *et al.*, 2007) satellite was launched from the Uchinoura Space Center in Japan. The satellite observatory consists of three solar telescopes, the SOT, the XRT, and the EIS, the latter two of which are extensively used in this work. *Hinode* is positioned in a Sun-synchronous polar orbit and provides virtually continuous observations for $\frac{2}{3}$ of the year. The scientific aims of the mission include determining the mechanisms responsible for coronal heating and transient events such as flares and CMEs and investigating physical processes of energy transfer throughout the solar atmosphere (Kosugi *et al.*, 2007).

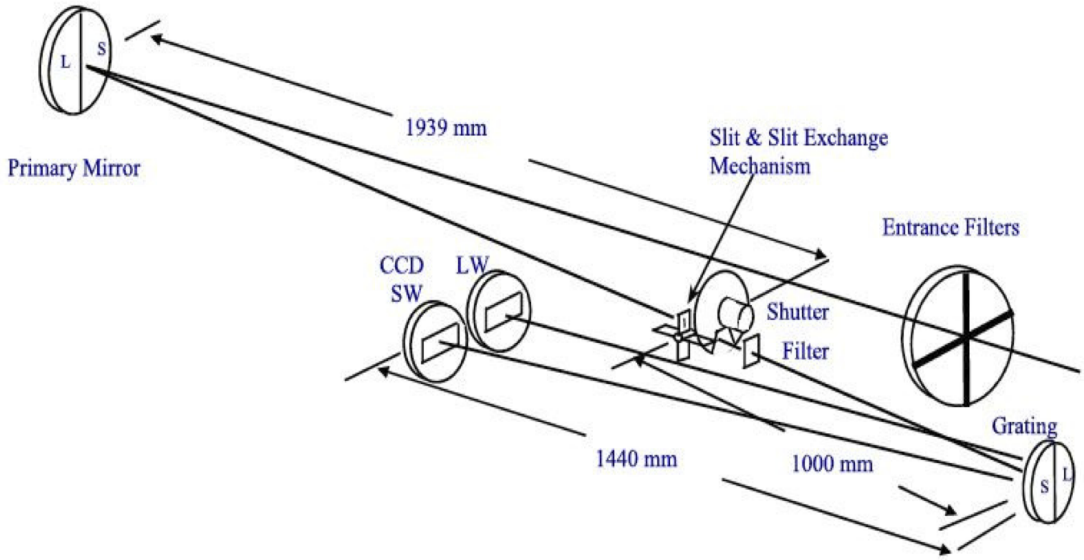

Figure 2.1: Hionde/EIS spectrometer optical layout with dimensions in mm. Short wavelength CCD detector (SW) covers 170 - 210 Å and long wavelength CCD detector (LW) covers 250 - 290 Å . From Culhane *et al.* (2007a).

2.1.1 Extreme Ultra-Violet Imaging Spectrometer (EIS)

EIS is a normal incidence multilayer-coated imaging spectrometer designed to observe the solar atmosphere from the transition region to the corona in the temperature range from < 0.1 MK to > 10 MK. It takes high resolution spectra in the wavelength ranges 170 - 210 Å and 250 - 290 Å, referred to as the short (SW) and long wavelength (LW) bands, respectively. The optical layout of the spectrometer is shown in Figure 2.1. Photons enter through a thin 1500 Å aluminum filter and are focused by the primary mirror onto a slit or slot then on the toroidal concave gratings. The gratings disperse diffracted photons onto a pair of thinned back-illuminated 1024×2048 (in dispersion direction) pixel CCD detectors. The use of such CCDs to register the diffracted photons significantly improves quantum efficiency. Mo/Si (molybdenum/silicon) multilayer coatings have been applied to both the primary mirror and the gratings in order to provide large effective areas in the SW and LW spectral bands. Figure 2.2 shows the AR spectra obtained just after launch in December 2006 (Young *et al.*, 2007). The dashed lines in the figure indicate the effective areas in each wavelength band. EIS core lines are Fe XII 195 Å, Fe XV 284 Å, and He II 256 Å (blue boxes in Figure 2.2). Key EIS instrument parameters are summarized in Table 2.1.

Four possible apertures can be selected using the slit/slot exchange mechanism - 1" slit, 2" slit, 40" slot and 266" slot. Slot observations provide high-cadence images of relatively large FOVs. In addition, the 40" slot can provide spectrally

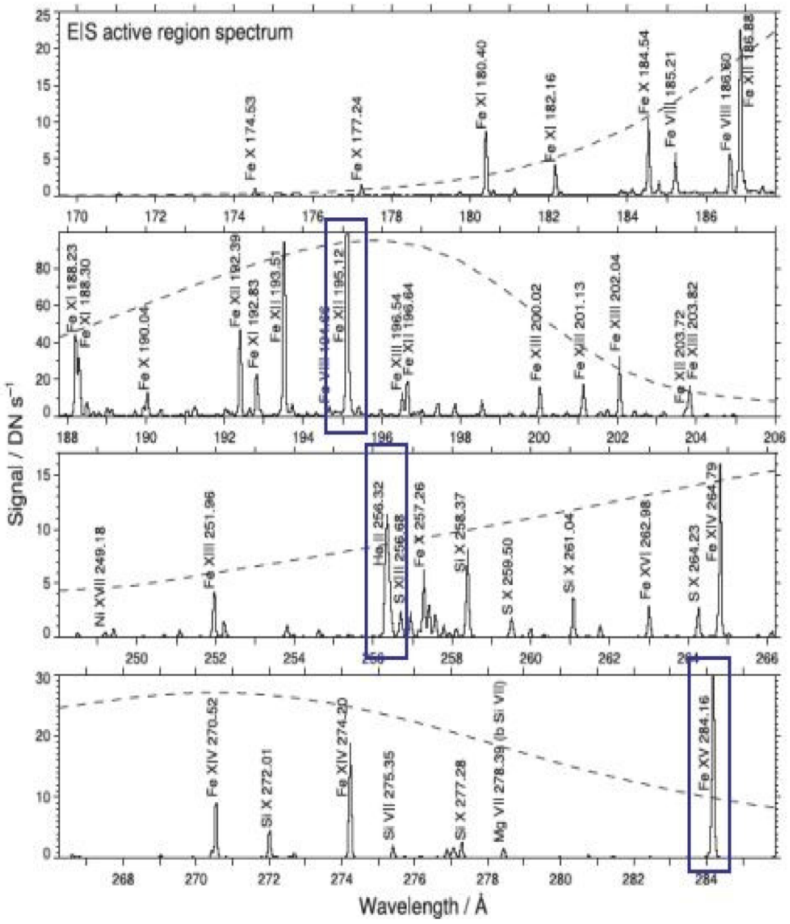

Figure 2.2: Hionde/EIS AR spectrum identifying key lines. EIS core lines, Fe XII 195 Å, Fe XV 284 Å, and He II 256 Å, are identified by the blue boxes. Effective areas are indicated by the dashed lines. Adapted from Young *et al.* (2007)

Table 2.1: EIS parameters adapted from Culhane *et al.* (2007a).

Wavelength bands	SW 170 - 210 Å ; LW 250 - 290 Å
Effective area	SW 0.30 cm^{-2}; LW 0.11 cm^{-2}
CCD detectors	2048 × 1024 × 13.5 μm pixels
Field of View	6 arc min × 8.5 arc min
Exposure time	2 - 5 sec for ARs
Spatial resolution	2 arc sec
Spectral resolution	47 mÅ FWHM at 185 Å ; 1 pixel is 22.3 mÅ
Velocity resolution	3 km sec^{-1} for Doppler velocities; 20 km sec^{-1} for line widths

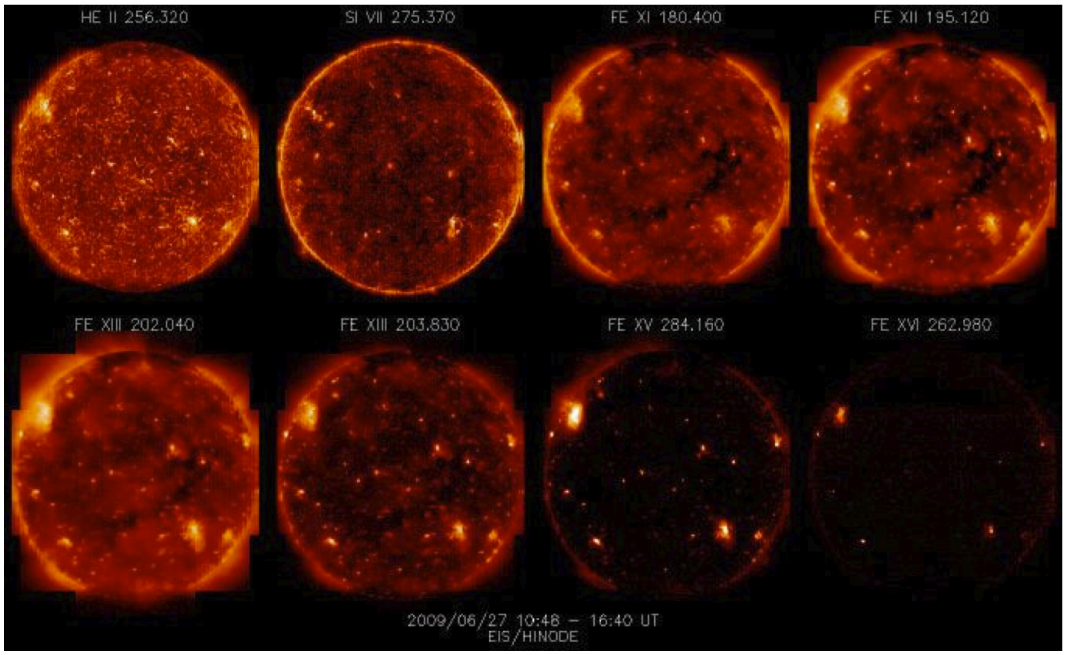

Figure 2.3: Sequence of EIS images taken for a selected range of spectral lines. Full-disk slot raster images from observations made on 2009 June 27 (HOP 130) were obtained in eight spectrally pure lines covering temperatures from 0.05 to 2.5 MK. Each image is constructed using the 40" slot. There are 15 fixed spacecraft pointing positions. At each position, 2 raster scans are made (except at the limb) for a total of 26 exposures in approximately 4 hours. Courtesy of Ignacio Ugarte-Urra.

pure images in a number of strong lines e.g. Fe XV 284 Å (Culhane *et al.*, 2007a). Slit observations provide Doppler and line width velocities with velocity resolution of 3 km s^{-1} for and 20 km s^{-1}, respectively (Culhane *et al.*, 2007a).

Two modes of observation can be selected, sit-and-stare and scanning. Sit-and-stare observations have FOVs that are the same as the slit/slot in the X-(dispersion) direction and primary mirror/spacecraft pointing remains fixed on a specified target. Spectroheliograms (raster images) with larger FOVs can be constructed by raster scanning either the slot or slit within a scan range of 6 arc min in the X-direction and 8.5 arc min in the Y-direction along the slot/slit height. A coarse mirror allows for ±15 arc min offset from spacecraft pointing in the E-W direction. A rotating shutter controls exposure times.

Figure 2.3 shows examples of full-disk raster images taken at eight different temperatures using the 40" slot that were constructed using a combination of primary (spacecraft) and coarse mirror positioning. Figure 2.4 shows Fe XII 195 Å emission line Doppler velocity, intensity, and calibrated non-thermal line-width maps obtained on 2007 October 17. The total FOV, 360"×512", was built up by raster scanning the 2" slit west to east in steps of 2" at 180 positions and taking an exposure at each position.

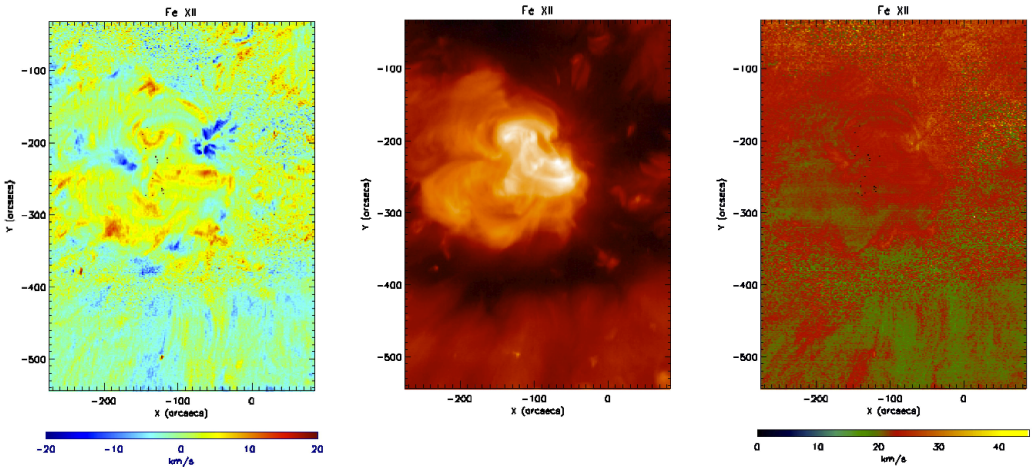

Figure 2.4: Example of EIS slit raster scan. EIS observation of a mature AR embedded in an equatorial coronal hole (CH) on 2007 October 17. Fe XII 195 Å Doppler velocity map (left), intensity map (middle), and calibrated non-thermal line-width map (right). The images were made using the 2" slit moving in 2" steps 180 times.

2.1.2 EIS Instrumental Effects

A number of instrumental effects must be taken into account when preparing, reducing, and interpreting EIS data. These effects include the following:

- Grating tilt - The grating and CCD axes are not exactly aligned leading to an offset of less than one pixel between for example Fe XII 186.88 Å and 195.12 Å spectral images.

- Slit tilt - None of the four EIS slits, 1", 2", 40", and 266" are perpendicular to the CCD dispersion axes. The 1" slit tilt is 1.18×10^{-5} Å per pixel and the 2" tilt is 1.09×10^{-4} Å per pixel.

- Orbital variation - A spectral line's position shifts throughout the orbit of *Hinode* due to the thermal changes occuring across the EIS instrument. This amounts to approximately 35 km s^{-1} for Fe XII 195 Å but the velocity amplitude varies with wavelength so that Fe XV is 24 km s^{-1}.

- Detector offset - There is an offset of 15 to 20 pixels in the Y-direction between the SW and LW detectors.

- EIS Point Spread Function (PSF) - For solar features with significant intensity gradients, it appears that regions of the strongest redshift/blueshift are spatially offset from regions of the highest intensity. In Figure 2.5, left panel, three crosses in the intensity map indicate the intensity peaks, however, their locations do not correspond to the greatest redshift in the ve-

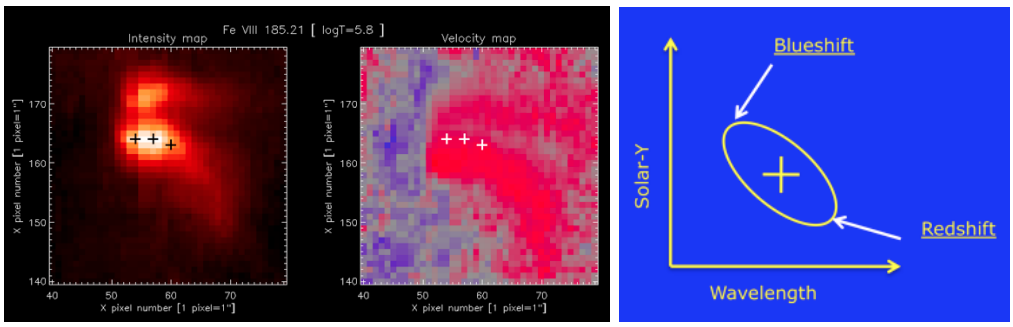

Figure 2.5: Offset between regions with the highest intensity (left) and strongest redshift (middle) and elliptical spot on detector spreading over a number of pixels (right). From EIS WIKI.

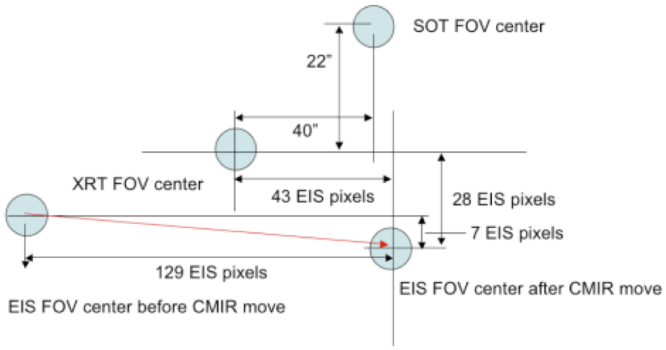

Figure 2.6: Instrumental offsets between EIS, XRT, and SOT.

locity map (middle panel). When there is a decreasing/increasing intensity gradient from north to south then the centroid position will be redshifted/blueshifted and visa versa. A similar effect was observed in SOHO CDS data and was attributed to an elliptical, tilted PSF as shown in the right panel of Figure 2.5 (from EIS WIKI: `http://msslxr.mssl.ucl.ac.uk:8080/eiswiki/Wiki.jsp?page=TestPage2`). Whether the PSF function is responsible for the observed effect is still under investigation.

- Line width variations - Instrumental width varies between the SW and LW detectors and between the 1" and 2" slits. Instrumental width is 0.054 Å and 0.057 Å for the SW and LW detectors, respectively. The 2" slit instrumental width has been measured to be 0.007 Å more than the 1" slit width.

- *Hinode* instrumental offsets - The three instruments onboard *Hinode* are offset from each other. Figure 2.6 shows the offsets which must be taken into account when coaligning EIS, XRT and SOT data (from EIS WIKI: `http://msslxr.mssl.ucl.ac.uk:8080/eiswiki/Wiki.jsp?page=InterInstrumentOffsets`).

All of the instrumental effects are well-documented on EIS WIKI, from where the above list was adapted. Most of the standard SolarSoft EIS data preparation

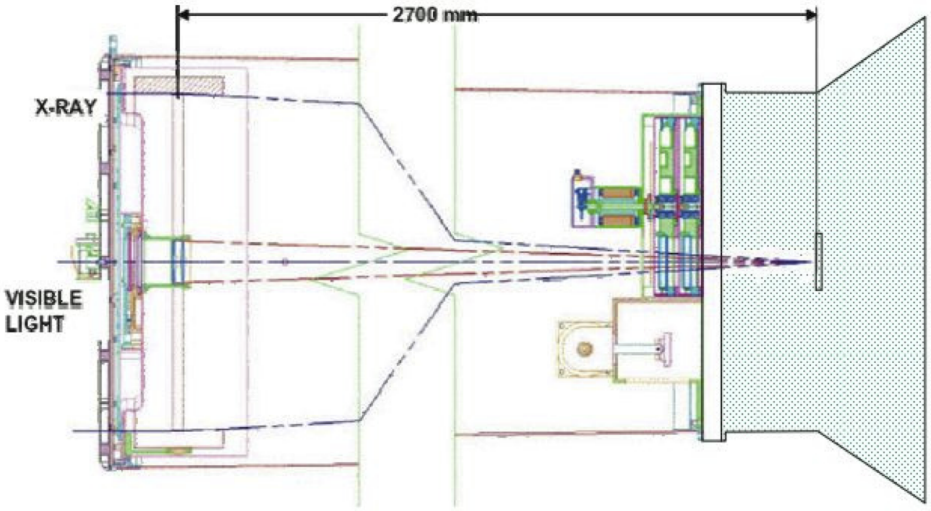

Figure 2.7: Schematic of grazing-incidence XRT. The optics are located on the left, inside the entrance aperture door. The CCD detector is at the back of the telescope on the far right. From Golub *et al.* (2007).

and reduction routines include some form of correction for the instrumental effects with the exception of the PSF.

2.1.3 X-ray Telescope (XRT)

The XRT (Golub *et al.*, 2007) provides a combination of spatial, spectral, and temporal coverage of the Sun's primary emission in the soft X-ray spectral range. Its capabilities exceed those of previous coronal X-ray imagers and allow for a number of key science questions to be investigated including (Golub *et al.*, 2007): How are CMEs and flares triggered? How do coronal structures brighten? Where and how does reconnection take place in the corona? XRT plays a key role in the overall *Hinode* mission objective of understanding how magnetic energy is transferred throughout the solar atmosphere (Kosugi *et al.*, 2007).

XRT is a high-resolution grazing-incidence (GI) telescope that focuses soft X-rays onto a 2048 $\times$ 2048 pixel array CCD detector. Grazing-incident optics are used to overcome the difficulty in focusing X-rays. An X-ray beam passes through a mirror at normal incidence, however, when the beam hits the mirror at a very shallow glancing angle, it is reflected at the same angle and only a small portion of the X-ray beam passes through. Figure 2.7 is a schematic of the grazing-incidence XRT. X-rays enter the telescope at an oblique angle from the left. A modified paraboloid-hyperboloid design provides surfaces which are optimized such that magnification is

Table 2.2: Physical characteristics of analysis filters (top) and telescope parameters (bottom) adapted from Golub *et al.* (2007).

Filter	Material	Thickness (Å)
Al-mesh	Al	1600
Al-poly	Al	1250
C-poly	C	6000
Ti-poly	Ti	3000
Be-thin	Be	9×10^4
Al-med	Al	1.25×10^5
Be-med	Be	3.0×10^5
Al-thick	Al	2.5×10^5
Be-thick	Be	3.0×10^6
Field of view		2048"×2048"×1.0"
X-ray wavelength		2 - 200 Å
G-band wavelength		4305 Å
Temperature range (K)		1×10^6 to 30×10^6

constant over the full aperture (Golub *et al.*, 2007). Thin filters at the front of the telescope reduce the entrance of visible light. Two filter wheels are located in front of the back-side illuminated CCD detector, near the focal plane. In addition to the X-ray GI optics, XRT is equipped with visible optics. Visible light used with the G-band filter provides a method of coalignment for XRT and SOT images.

There are nine analysis filters that provide varying X-ray passbands. Filter thickness differs by a factor of 10^4 (Golub *et al.*, 2007). Thinner filters are used for faint, lower temperature targets and the thickest filters are used for flare observations. Table 2.2 gives the physical characteristics of the analysis filters. Figure 2.8 shows full-disk XRT images taken with Al-mesh, Ti-poly, Al-poly, and C-poly filters (from `http://solar-b.nao.ac.jp/QLmovies/index_e.shtml`). These are the 4 thinnest filters and are best suited to observe QS and an equatorial CH as the series of images taken on 2007 October 17 clearly demonstrate.

XRT's temperature response for all filters is provided in Figure 2.9. The temperature response is calculated assuming constant columnar emission measure as a function of temperature of 1×10^{30} cm^{-5} (from ATOMDB/APEC coronal plasma emission model) (Golub *et al.*, 2007).

2.2 STEREO

The *Solar TErrestrial RElations Observatory* (STEREO) (Kaiser *et al.*, 2008) consists of twin spacecraft, one follows (referred to as STEREO-B) the Earth while the

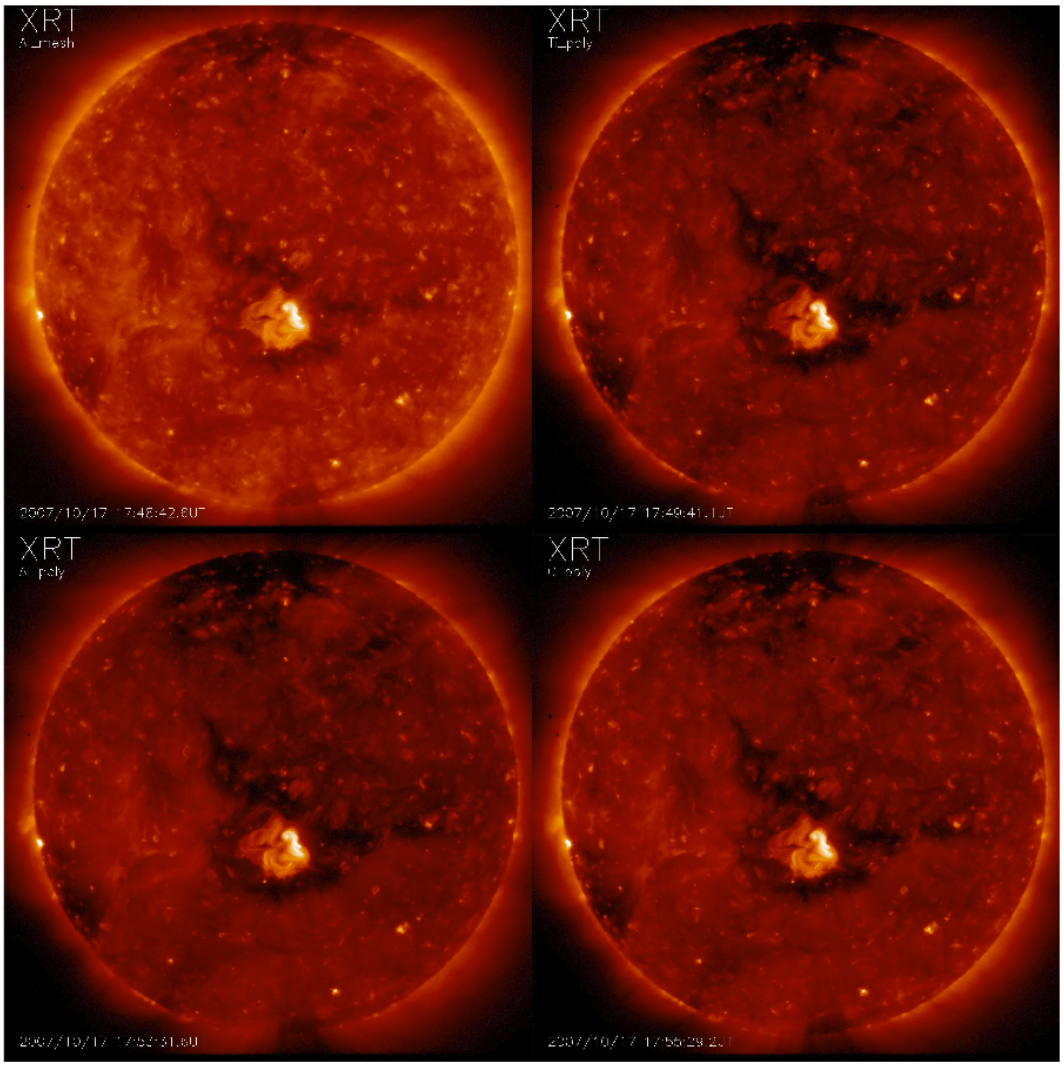

Figure 2.8: Clockwise from upper left: *Hinode* XRT full-disk images taken 2007 October 17 with the Al-mesh, Ti-poly, Al-poly, and C-poly filters, respectively. These thin filters are suitable for QS and CH observations.

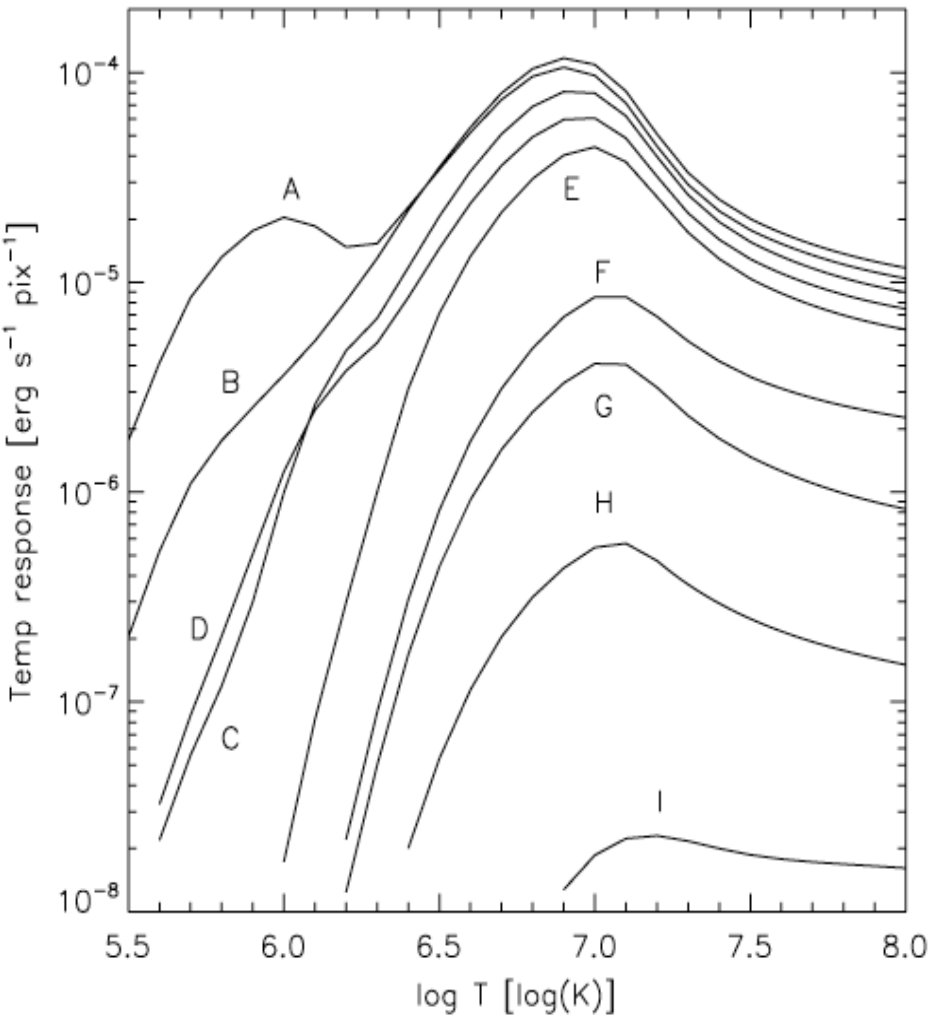

Figure 2.9: *Hinode* XRT temperature response of the different filters. The labels designate the filters as follows: A: Al-mesh, B: Al-poly, C: C-poly, D: Ti-poly, E: Be-thin, F: Be-med, G: Al-med, H: Al-thick, and I: Be-thick. From Golub *et al.* (2007).

other leads (referred to as STEREO-A). Each STEREO spacecraft is equipped with remote sensing and *in situ* particle and field instruments for the main purpose of understanding CME initiation processes on the solar disk and to follow the propagation of CMEs into the heliosphere in three dimensions. The spacecraft, launched on 2006 October 26 from Cape Canaveral, Florida, USA, orbit the Sun in the ecliptic plane at a heliocentric distance close to 1 AU. STEREO A is somewhat closer and STEREO B is further away from the Sun. The angle of separation between each spacecraft and the Earth increases by 22.5° per year (Kaiser *et al.*, 2008). Figure 2.10, left panel, shows the drifts and separation of the two spacecraft in years 1 - 5 of the mission.

The STEREO mission has four distinct phases (Kaiser *et al.*, 2008) that are dependent upon the spacecraft separation angle as no single angular spacing is best for all of the instruments on the identical spacecraft. Initially the drift rates of STEREO A and B (leading to the 22.5° per year increase in separation angle) were selected as a compromise between competing remote sensing and *in situ* requirements (Driesman *et al.*, 2008). Phase 1 occurred when the spacecraft separation angle was less than 50° (up to 400 days after launch). This separation is ideal for making high-cadence 3-D images of structures in the corona, before, during and after CMEs. In addition, stereoscopic measurements of small structures visible in the EUVI telescopes can be made with angular spacing of less than 20°. Phase 2 is when the spacecraft are at quadrature (50° to 110°, 400 to 800 days) which is required to optimize CME triangulation. Phase 3 will have a separation angle up to 180° and CMEs will be observed by both spacecraft in the plane of the sky. Phase 4 will provide direct full-disk viewing of the far side of the Sun.

Some of the work presented in Chapters 4 and 5 uses STEREO instruments (the EUVI and the white-light heliospheric imager) when the spacecraft separation angle between the spacecraft was 36.6° (during Phase 1). Figure 2.12, top and middle rows, shows pairs of full-disk images (STEREO A and B) in each spectral channel on 2007 October 17 (from `http://stereo-ssc.nascom.nasa.gov/`). Figure 2.10, right panel, is a plot of spacecraft positions on that date.

2.2.1 STEREO/Extreme Ultra-Violet Imager (EUVI)

Each STEREO spacecraft carries a suite of imagers - the Sun-Earth Connection Coronal and Heliospheric Investigation (SECCHI) package (Howard *et al.*, 2008). SECCHI comprises five telescopes, one of which is an EUV Imager (EUVI) (Wuelser *et al.*, 2004). The EUVI observes the chromosphere and low corona out to 1.7 solar radii in EUV emission lines at 171, 195, 284, and 304 Å (Fe IX, Fe XII, Fe XV, and

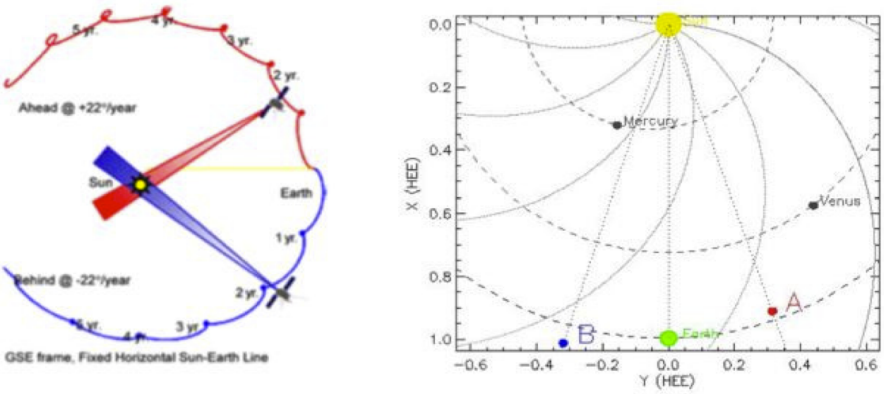

Figure 2.10: Left: The orbits of both STEREO spacecraft, projected onto the ecliptic plane. The drifts of the spacecraft and yearly separation angle are shown. From Driesman *et al.* (2008). Right: Positions of STEREO A (red) and B (blue) on 2007 October 17 (at the time of the observations in Figure 2.12). Separation angle of STEREO A and B is 36.6°. Mercury, Venus and estimated Parker Spiral positions are included in the plot (produced using the STEREO Orbit Tool).

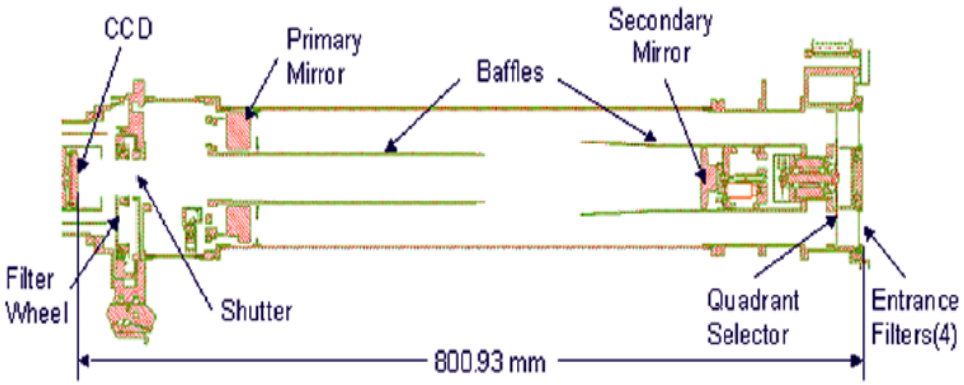

Figure 2.11: STEREO EUVI telescope optical layout. From Howard *et al.* (2008).

He II, respectively), spanning a temperature range of 1×10^5 K to 2×10^6 K. The four spectral channels were chosen to match those of SOHO EIT (§2.3.1).

Figure 2.11 shows the EUVI optical layout. Photons enter the normal incidence EUV telescope through a 1500 Å aluminum filter which stops the transmission of UV, visible, and infrared radiation. The EUV radiation then passes through the quadrant selector to one of the four quadrants of the telescope optics, bouncing off the primary and secondary mirrors before reaching the back-thinned 2048×2048 pixel CCD detector. All mirrors have been treated with a narrow passband reflective multilayer Mo/Si coating. Exposure time is controlled by the rotating blade shutter. Table 2.3 summaries EUVI parameters.

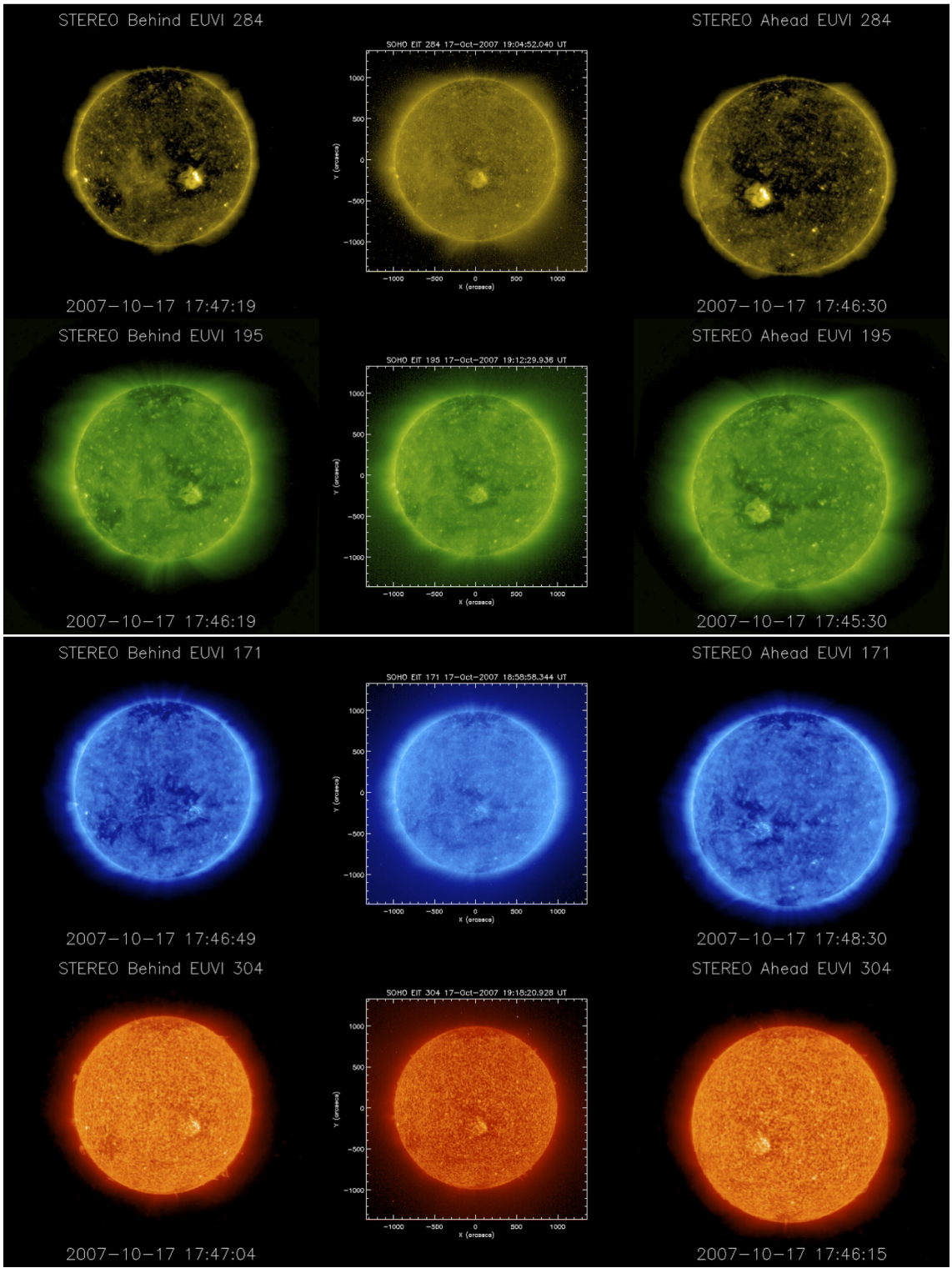

Figure 2.12: First (top) row, left to right: STEREO EUVI B (behind), SOHO/EIT, and STEREO EUVI A (ahead) 284 Å Fe XV full-disk images; second row: STEREO EUVI B, SOHO/EIT, and STEREO EUVI A 195Å Fe XII full-disk images; third row: STEREO EUVI B, SOHO/EIT, and STEREO EUVI A 171 Å Fe IX/X full-disk images; fourth row: STEREO EUVI B, SOHO/EIT, and STEREO EUVI A 304 Å He II full-disk images All observations were made on 2007 October 17 during Phase 1.

Table 2.3: EUVI telescope properties. Adapted from Howard *et al.* (2008).

Ion	Fe IX	Fe XII	Fe XV	He II
Wavelengths	171 Å	195 Å	284 Å	304 Å
Central wavelength	173 Å	196 Å	285 Å	307 Å
Bandwidth	14 Å	16 Å	19 Å	30 Å
CCD detector (pixels)		2048×2048		
Field of View		± 1.7 radii		

Table 2.4: HI key parameters. Adapted from Howard *et al.* (2008).

	HI-1	HI-2
FOV Center (deg)	13.98	53.68
Angular FOV (deg)	20	70
Image array (pixels)	1024×1024	1024×1024
Image pixel size	70 arcsec	4 arcmin
Spectral bandpass (nm)	630 - 730	400 - 1000

2.2.2 STEREO Heliospheric Imager (HI)

In addition to the EUVI, the SECCHI instrument packages on board STEREO A and B include two heliospheric white light imagers, HI-1 and HI-2 (referred to as HI-1A and HI-2A, HI-1B and HI-2B; Harrison *et al.* (2008)). HI is designed to observe the inner heliosphere from 12 to 215 solar radii, looking back towards the Sun-Earth line. HI-1 has an angular FOV of 20° set to 13.98 ° from the Sun along the ecliptic plane and HI-2 has an angular FOV of 70° set to 53.68°. The combined HI FOV is large enough to cover a radially expanding CME within a 45° cone in the ecliptic plane (see Figure 2.13). Figure 2.14 shows the extent of the combined HI FOV (Harrison *et al.*, 2008). Table 2.4 lists key HI parameters. See §4.4.3 for more discussion of the HI instrument.

One of the challenges presented by white light observations with this particular FOV is detecting the weak CME signal against the background. The CME signal strength relative to the background is a function of the elongation angle and within the HI FOV, the background level varies from 10^{-7} to 10^{-14} of solar disk brightness. Figure 2.13 shows the CME signal profile (blue) and the sum of the electron (K) corona and dust (F) corona (black, K + F) plotted on a scale of the ratio of natural background (B) to solar disk brightness (B_0) vs elongation angle, ε.

The HI instrument design uses a baffle system (forward, perimeter and internal baffles) and occultation to reject light from reaching the CCD detectors with 2048×2048 pixels of 13.5 microns. A forward baffle is positioned to reject solar disk and inner corona light. The Sun remains below the forward baffles at all times. The function of the perimeter baffle is to reject stray light from the spacecraft and

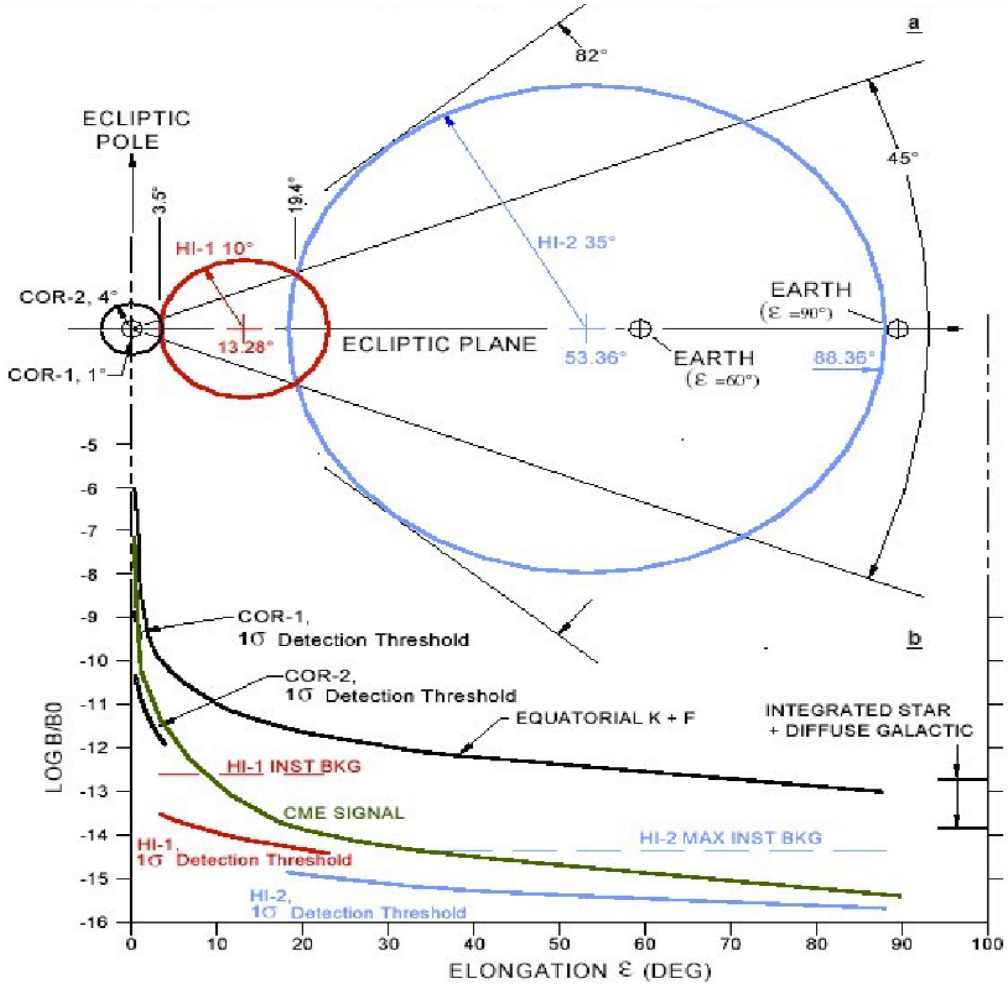

Figure 2.13: HI-1 and HI-2 FOVs and the major contributions to the observed intensities - F-corona and K-corona. Adapted from Howard *et al.* (2008).

the internal baffles are designed to reject light from the Earth, planets, stars and F-corona (Eyles *et al.*, 2009).

While the weak CME signal vs the background signal normally requires long duration exposures, cosmic ray contributions pose a significant problem. HI uses a sum of many images of shorter duration exposures each of which are cleaned on the spacecraft. 1024×1024 pixel synoptic science images are routinely downloaded. A base-frame or recent image is then subtracted from the summed image in order to extract the CME signal. Figure 2.15 presents a time-elongation map (or J-map) derived by plotting strips from HI-1A and HI-2A running difference images, extracted along a particular position angle which intersects the latitude of the target when crossing the plane of the sky as viewed from STEREO B, as a function of elongation (along the ordinate) and time (along the absissa). The use of difference images minimizes the contribution of the stable F-corona and is a very useful technique for highlighting faint propagating features. (From STEREO Science Center website - `http://stereo-ssc.nascom.nasa.gov/beacon/secchi_jplot.shtml`).

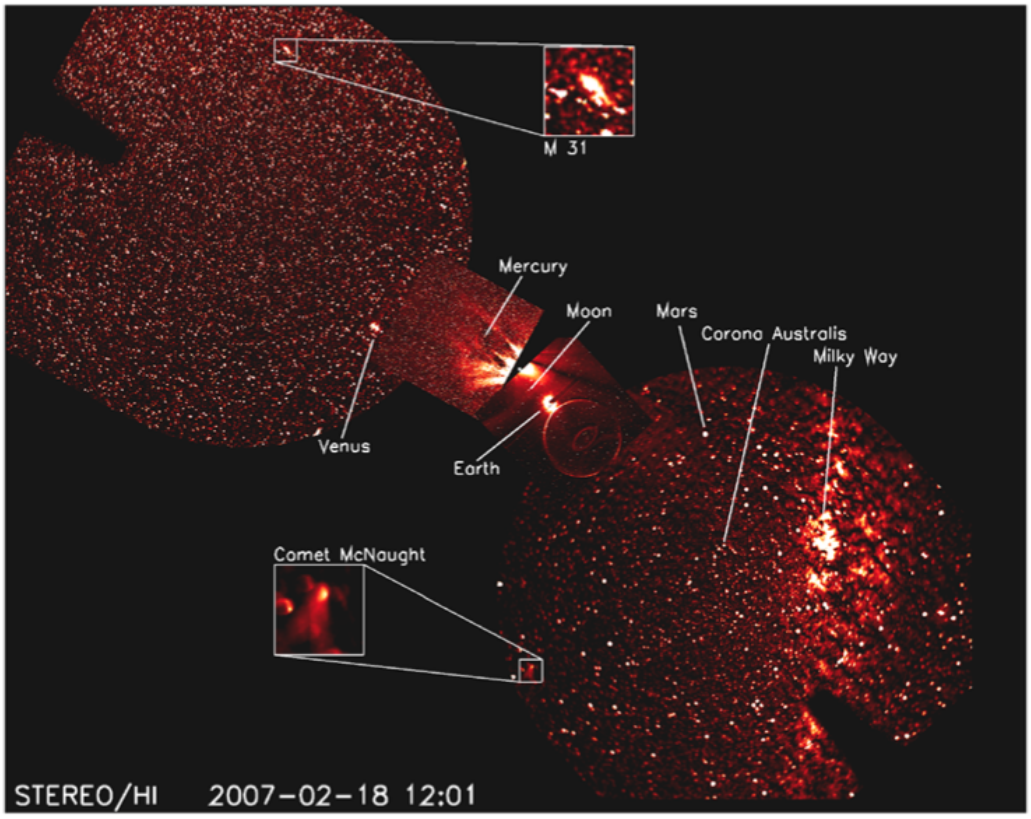

Figure 2.14: A composite of HI images on 2007 February 18. From Harrison *et al.* (2008).

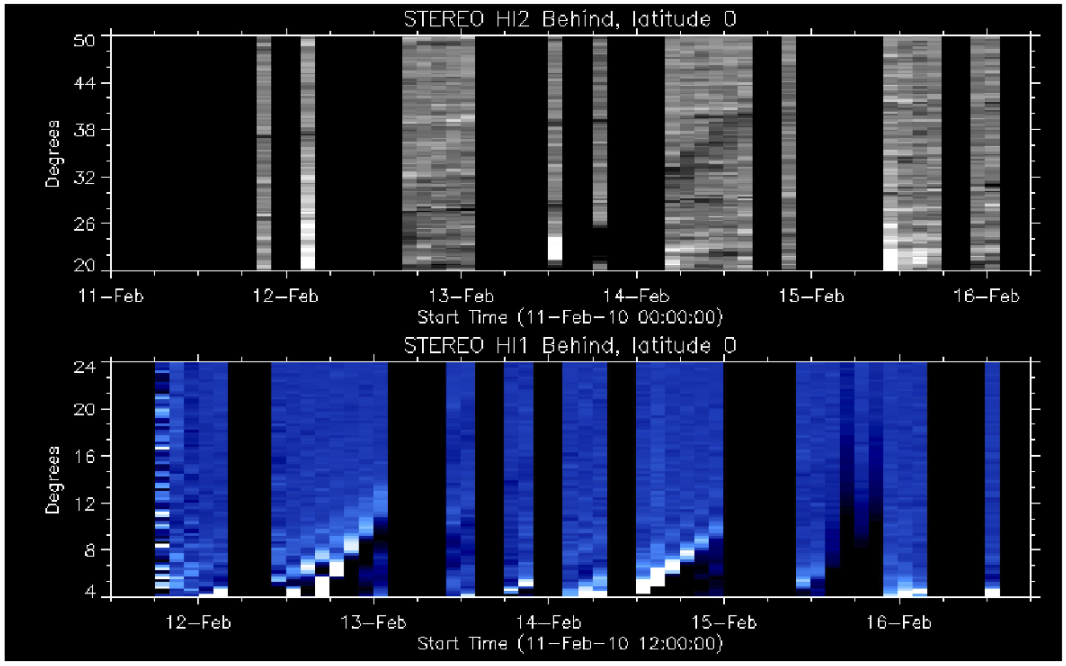

Figure 2.15: Sample of HI time-elongation plots (j-maps or j-plots).

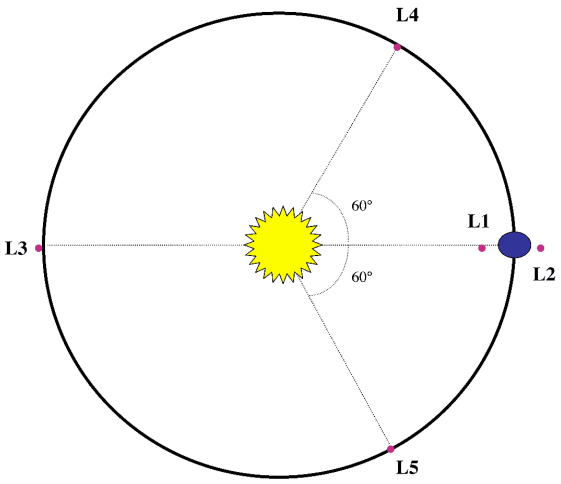

Figure 2.16: Lagrangian points L1 to L5 in the Sun-Earth system. SOHO is located at L1.

2.3 SOlar Heliospheric Observatory

The Extreme-ultraviolet Imaging Telescope (EIT) (Delaboudinière *et al.*, 1995) and the Michelson Doppler Imager (MDI) (Scherrer *et al.*, 1995) are two of the 12 instruments onboard the SOlar Heliospheric Observatory (SOHO) which was launched from Cape Canaveral Air Station on 2 December 1995. The scientific objectives of the SOHO mission include the investigation of the structure and dynamics of the solar interior using helioseimology and the physical processes that heat the solar corona (Domingo *et al.*, 1995).

SOHO's position at the L1 Sun-Earth Lagrangian point approximately 1.5 $\times 10^6$ km from the Earth provides uninterrupted coverage of the Sun. At L1, SOHO is not subjected to Earth occultation which would be the case in low Earth orbit. Lagrangian points are locations in space where a satellite with negligible mass under the gravitational influence of two large bodies, here the Sun and the Earth, will remain at rest relative to the larger ones. In a two-body rotating system, Lagrangian points are gravitational 'null' points. Figure 2.16 shows the position of the five Lagrangian points in the Sun-Earth system.

2.3.1 EIT

Like STEREO's EUVI (2.2.1), EIT is designed to provide full-disk images of the Sun in four bandpasses, 171, 195, 284, and 304 Å (Fe IX, Fe XII, Fe XV, and He II, respectively), spanning a temperature range of 6×10^4 K to 3×10^6 K (Delaboudinière *et al.*, 1995). Table 2.5 contains EIT's bandpasses and their observational objectives.

Table 2.5: EIT parameters adapted from Delaboudinière *et al.* (1995).

Wavelength	Ion	Peak T	Observational Objective
304 Å	He II	8.0×10^4 K	chromospheric network; CHs
171 Å	Fe IX	1.3×10^6 K	corona/transition region boundary; structures inside CHs
195 Å	Fe XII	1.6×10^6 K	quiet sun corona
284 Å	Fe XV	2.0×10^6 K	ARs
CCD detector			1024×1024 pixels
Field of View			45×45 arcmin×2.6 arcsec; ± 1.5 radii
Spatial resolution			5 arcsec

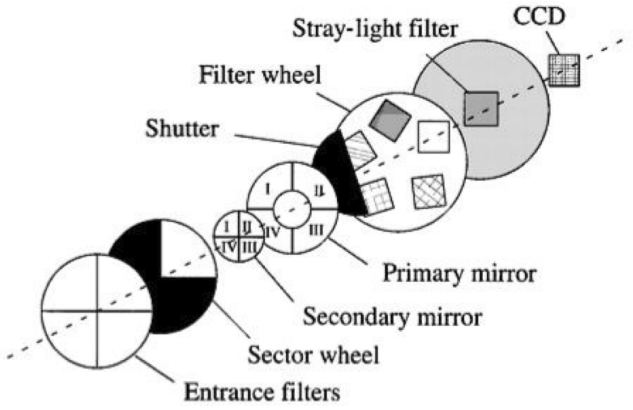

Figure 2.17: Schematic of the EIT telescope from Delaboudinière *et al.* (1995).

EIT is a normal incidence telescope with a FOV 45 arcmin square and a spatial resolution of approximately 5 arcsec (Delaboudinière *et al.*, 1995). The optical layout is shown in Figure 2.17. After incident photons enter the telescope via the entrance filter (a heat rejection filter made of layers of 1500 Å Al/700 Å cellulose/1500 Å Al), a rotating mask is used to select the bandpass quadrant. The telescope's primary and secondary mirrors are divided into matched quadrants, one for each bandpass. A bandpass is defined by interference effects arising in the multilayer coatings of Mo/Si used within the quadrant. Photons are then focused on a 1024×1024 pixels back-illuminated CCD that is protected by a stray-light filter.

Examples of full-disk images from SOHO EIT and STEREO EUVI corresponding bandpasses are shown in Figure 2.12. A comparison of images clearly demonstrates the difference in spatial resolution and viewing angle between the two satellite observatories. Figure 2.18 shows how the EIT broad-passband filter image at 284 Å compares to the spectrally pure EIS image at the same wavelength. The EIT passband includes contribution from the much cooler Si VII line.

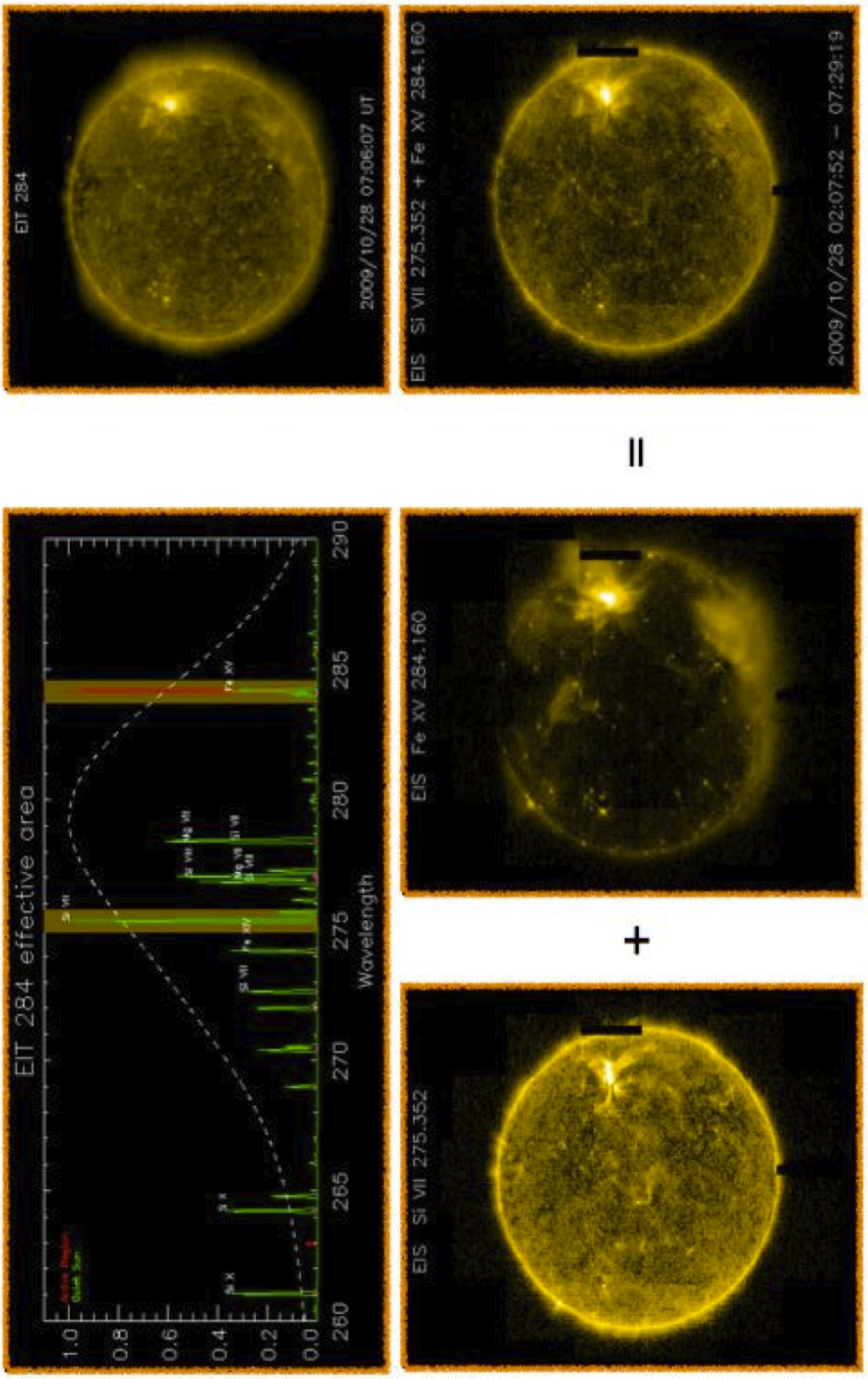

Figure 2.18: Comparison between EIT broad-passband filter image and EIS spectrally pure images. Upper left: EIT 284 Å effective area showing emission lines in the range 260 to 290 Å. Si VII and Fe XV are high-lighted in gold. Upper right: EIT 284 Å full disk image. The EIT passband includes two lines formed at very different temperatures. Lower panel, left to right: Individual EIS Si VII and Fe XV images and combined image. The combined EIS image is very similar to the EIT Fe XV image. Courtesy of Ignacio Ugarte-Urra.

Table 2.6: MDI parameters adapted from Scherrer *et al.* (1995).

CCD	1024×1024 21 μm pixels
Full-disk field of view	34×34 arcmin
High resolution field of view	10.5×10.5 arcmin
Resolution	4 arcsec (full-disk), 1.25 arcsec (high resolution)
Spectral range	6768 Å± 190 mÅ
Spectral bandwidth	94 mÅ
Selectable polarization	S-wave, P-wave, RCP, LCP

2.3.2 MDI

Probing the Sun's interior using the techniques of helioseismology is one of the three main areas of scientific investigation of the SOHO mission. The Solar Oscillations Investigation (SOI) uses the Michelson Doppler Imager (MDI, Scherrer *et al.* (1995)) instrument to make the required measurements including LOS velocity, LOS magnetic field, line and continuum intensities, and high-resolution transverse velocity (Scherrer *et al.*, 1995). Here, only the general instrument layout and LOS magnetic field measurements are discussed.

MDI has a 12.5 cm refracting telescope that feeds light through a system of filters onto a 1024×1024 CCD camera. A dual, tunable Michelson interferometer imaging system defines a narrow passband (94 mÅ) along the Ni I 6768 Å absorption line formed in the mid-photosphere. MDI can observe in two modes, selected by the shutter, full-disk mode with a FOV of 34'×34' with 4" resolution and high-resolution mode with a FOV of 10.5'×10.5' with 1.25" resolution. The high-resolution FOV is positioned at the central meridian, 160" north of the solar equator. Table 2.6 lists the key parameters of the MDI instruments.

Light enters the objective and enlarging lenses and is folded by the ISS tilt mirror. Wave plates in the polarization analyzer wheel convert right and left circularly polarized (LCP and RCP, respectively) light into vertically plane polarized light. This is accomplished by using quarter-wave plates that change circularly to linearly polarized light by shifting the phase 90° between two perpendicular polarization components and half-wave plates that retard one component of the polarized light by 180°. The converted output is then split by a polarizing beam splitter, sending the vertically polarized (longitudinal) component through the instrument and the orthogonal (transverse) component to the limb sensor assembly which is used to determine the instrument's relative pointing. For magnetic measurements, the polarization analyzer wheel is used to alternatively select LCP and RCP positions. Figure 2.19 shows a schematic of the instrument's light path and primary optical components. Green elements identify the telescope, filter wheels, and Imaging Sta-

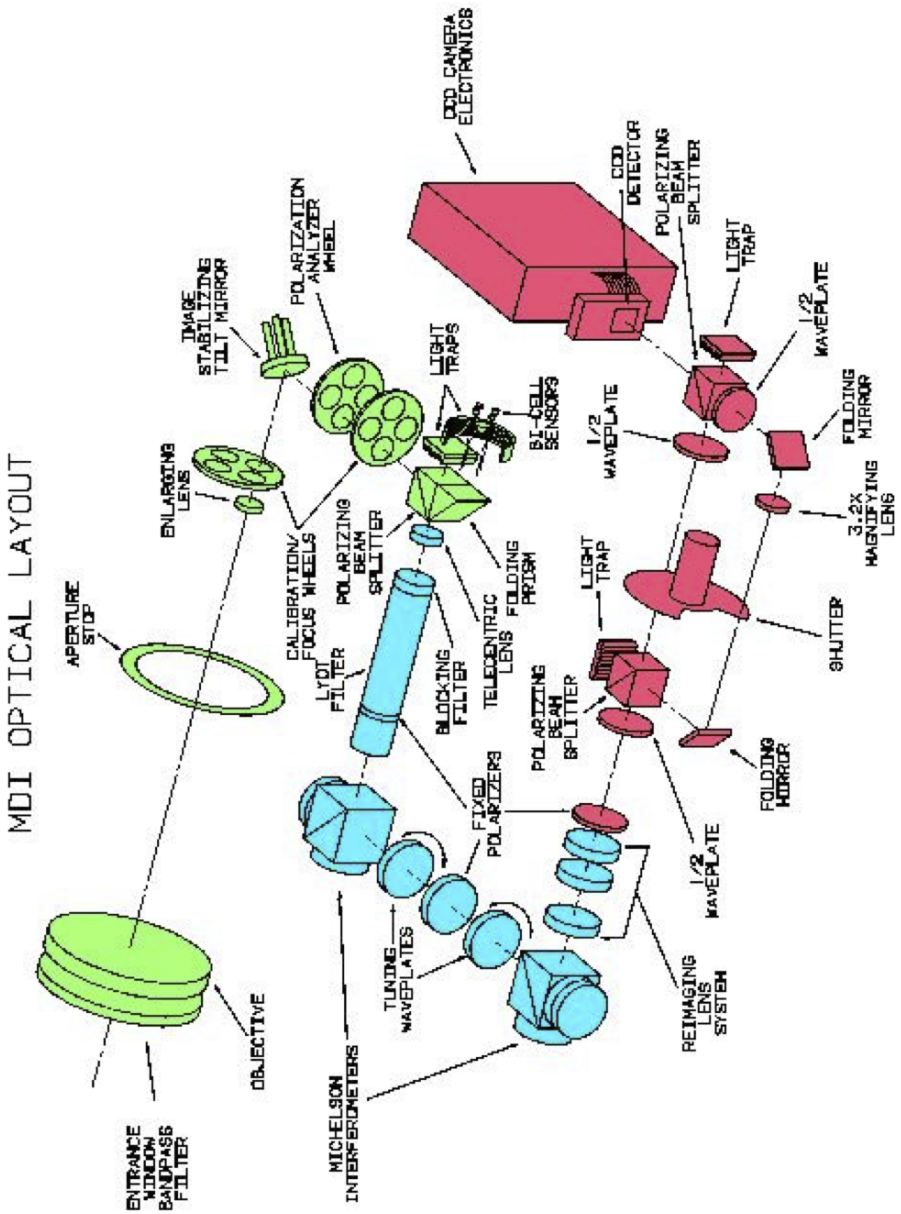

Figure 2.19: MDI optical layout. From Scherrer *et al.* (1995).

bilization System (ISS). Blue elements contain the filters and re-imaging optics. The beam distribution system and CCD camera are red (Scherrer *et al.*, 1995).

The filter system, consisting of the Lyot filter and two tunable Michelson interferometers which define the instrument transmission profile, enables filtergrams to be made near the Ni I 6768 Å line by tuning the Michelsons' peak transmis-

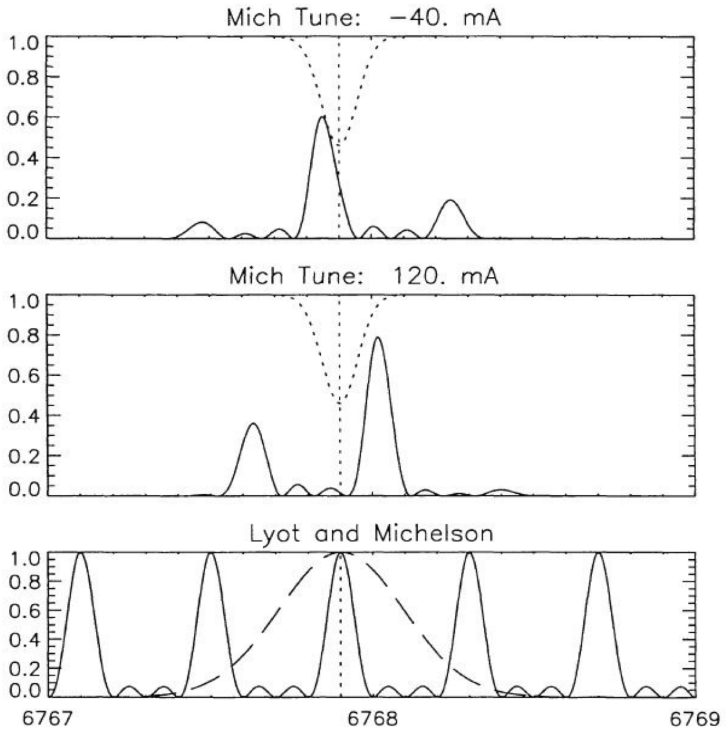

Figure 2.20: MDI Lyot filter (dashed lines) and Michelson interferometer (solid lines) instrument transmission profiles (bottom panel) around the Ni I 6768 Å line (dotted lines). Upper panels show the resulting instrument transmission profiles for Michelson tuning positions at -40 mÅ and 120 mÅ with respect to the Ni I 6768 Å line profile. From Scherrer *et al.* (1995).

sion. Filtergrams are obtained at five tuning positions 75 mÅ apart spanning a tuning range of 377 mÅ. Doppler velocity and continuum intensity are then computed from the filtergrams. The Doppler velocity is estimated from a ratio of the filtergrams which is then compared to an onboard lookup table constructed from synthetic line profiles and measured filter transmission profiles (Green *et al.* (2003) and references therein). Figure 2.20, bottom panel, shows the individual profiles of the Lyot filter (dashed lines) and the Michelson interferometers (solid lines) with the Ni I 6768 Å line profile (dotted lines). The upper panels show the transmission profiles for two of the tuning positions. MDI's LOS longitudinal magnetograms are constructed by measuring separately the Doppler shifts of the LCP and RCP light. The longitudinal magnetic flux density (i.e. the LOS component of the magnetic field averaged over the pixel FOV) is given by the difference in the Doppler shift between these two polarizations as it is a measure of the Zeeman splitting (see §1.4.7). A typical MDI full-disk magnetogram is shown in Figure 2.21 (from: `http://soi.stanford.edu/production/mag_gifs.html`).

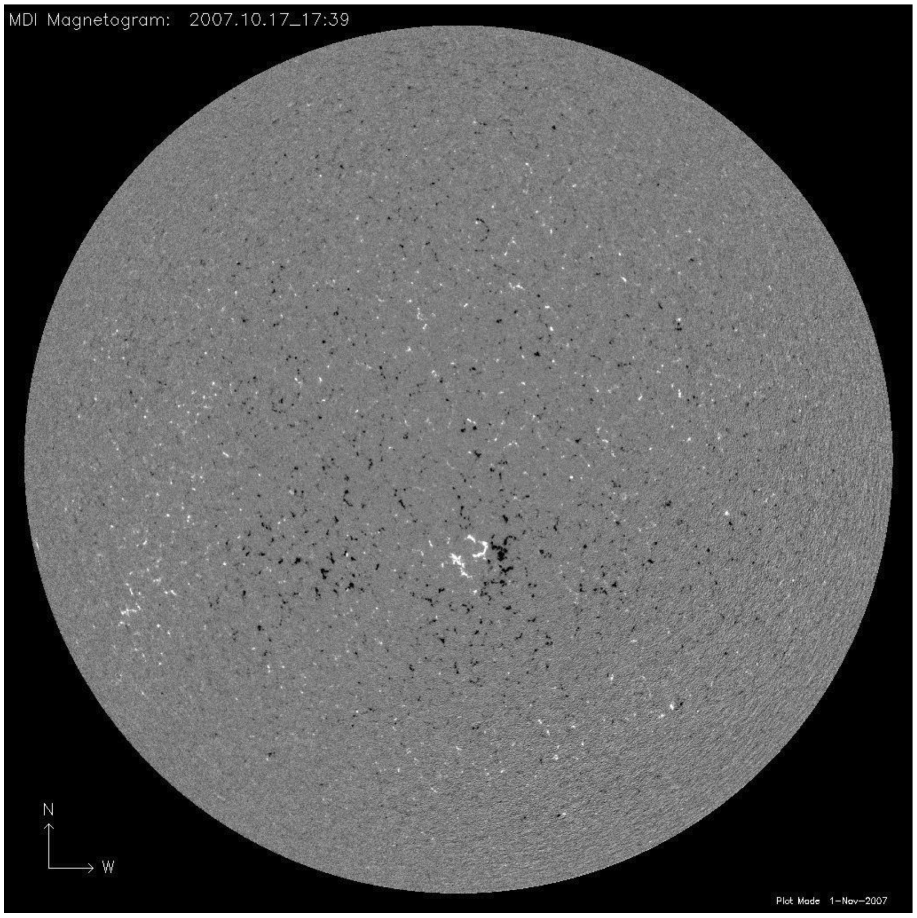

Figure 2.21: MDI magnetogram for 2007 October 17. Black/white is negative/positive polarity. Concentrations of negative and positive magnetic field surrounded by fragments of negative polarity (in image center) correspond to the AR and surrounding CH viewed in EUV (see Figure 2.12) and X-ray (see Figure 2.8).

2.4 *In situ* Instruments

In situ measurements provide information about the state of the ambient SW and energetic particles in the near-Earth environment. Combining the *in situ* measurements with remote sensing observations enables the flow of energy and matter to be traced from the source regions on the Sun to the Earth. The coupling of *in situ* and remote sensing observations is necessary to develop an understanding of the fundamental nature and origin of outflows, the SW, flares, and CMEs. Data from the following *in situ* instruments onboard STEREO and ACE are utilized in Chapter 4 to track an eruption of a CME from an AR in a CH to 1 AU and to analyze the heliospheric consequences of interchange reconnection.

2.4.1 STEREO Instruments

Among STEREO's particle experiments are the In situ Measurements of Particles and CME Transients (IMPACT) and PLAsma and Suprathermal Ion Composition (PLASTIC). STEREO A and B contain nearly identical sets of *in situ* instruments.

2.4.1.1 IMPACTS's SWEA

IMPACTS's SWEAs (Sauvaud *et al.*, 2008) are top-hat SW electron analyzers that measure the electron fluxes of SW thermal and suprathermal electrons from 1eV to 3keV over a solid angle of 360° × 120°. Electrons enter the electrostatic analyzer at a range of azimuthal angles and are focused on to microchannel plate detectors. Each SWEA has a wide FOV which provides the capability to determine the directionality of suprathermal electrons when the interplanetary magnetic field rotates out of the ecliptic plane. Each SWEA instrument is located at the end of the boom in Figure 2.22.

2.4.1.2 IMPACTS's MAG

IMPACTS' MAGs (Acuña *et al.*, 2008) magnetometers measure the vector magnetic field in two ranges up to ±65,536 nT and ±500 nT. MAG's nominal time resolution is eight vectors s^{-1}. The sensitivity and dynamic ranges of the instruments allow for the measurement of time-variable, large-scale structure of the IPS as well as the local sources for *in situ* acceleration mechanisms such as shocks and discontinuities. The

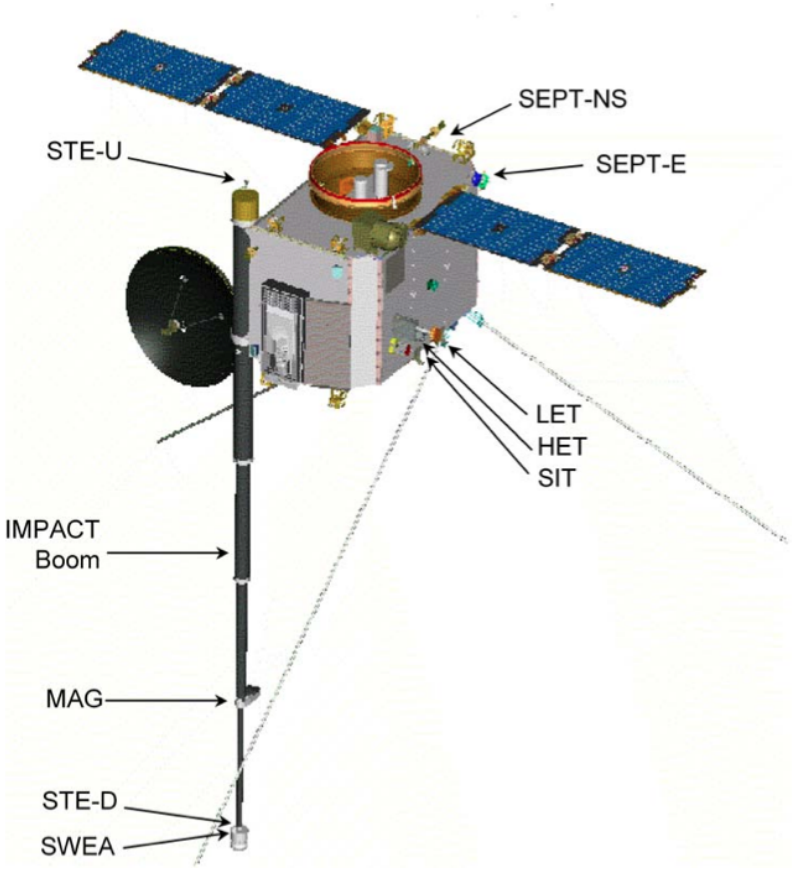

Figure 2.22: Location of IMPACT instruments on the deployable STEREO boom (Acuña *et al.*, 2008).

location of the magnetometers at close to the end of the IMPACT boom minimizes the effect of any spacecraft magnetic fields on MAG measurements (see Figure 2.22).

2.4.1.3 PLASTIC

The Plasma and Suprathermal Ion Composition (PLASTIC) instruments provide *in situ* SW and low-energy ion measurements (Galvin *et al.*, 2008). Each instrument is a mass spectrometer that is used to determine the elemental composition, ionic charge states, and bulk flow parameters of SW ions up to the mass of Fe. PLASTIC also measures suprathermal ions in the energy range from 0.3 to 80 keV and has nearly complete angular coverage in the ecliptic plane. PLASTIC consists of:

- The Solar wind sector (SWS) Small Channel measures the distribution function of protons and alpha particles, providing proton density, velocity, thermal speed, and proton/alpha ratios (Galvin *et al.*, 2008).
- The SWS Main Channel measures the elemental composition, ionic charge state distribution, and bulk and thermal speeds of C, O, Mg, Si, and Fe (Galvin

et al., 2008).

- The Suprathermal Ions Wide-Angle Partition Sector (WAP) covers FOVs exceeding 200° for each STEREO A and B (Galvin *et al.*, 2008).

2.4.2 ACE Instruments

The Advanced Composition Explorer (ACE) has six high-resolution spectrometers that measure the elemental, isotopic, and ionic charge-state composition of nuclei from H to Ni from SW energies to galactic cosmic-ray energies (about 1 keV to 500 MeV) (Stone *et al.*, 1998). Figure 2.23 shows the instruments onboard ACE. Three of the instruments have been used for work in this thesis. They are:

- SWICS - The Solar Wind Ion Composition Spectrometer measures the chemical and ionic-charge composition of the SW and the thermal and mean speeds of SW ions from H through Fe at SW speeds above 300 km s^{-1} for protons and 170 km s^{-1} for Fe^{+16} (Gloeckler *et al.*, 1998).

- SWEPAM - The Solar Wind Electron, Proton, and Alpha Monitor are electron and ion curved-plate electrostatic analyzers that measure the three-dimensional characteristics of the SW and suprathermal electrons from 1 to 900 eV and ions/alpha particles from 0.26 to 35 keV, respectively (McComas *et al.*, 1998).

- MAG - The magnetometer measures the dynamic behavior of the vector magnetic field in eight ranges: ± 4 nT, ± 16 nT, ± 64 nT, ± 256 nT, ± 1024 nT, ± 4096 nT, ± 16384 nT, and ± 65536 nT (Smith *et al.*, 1998).

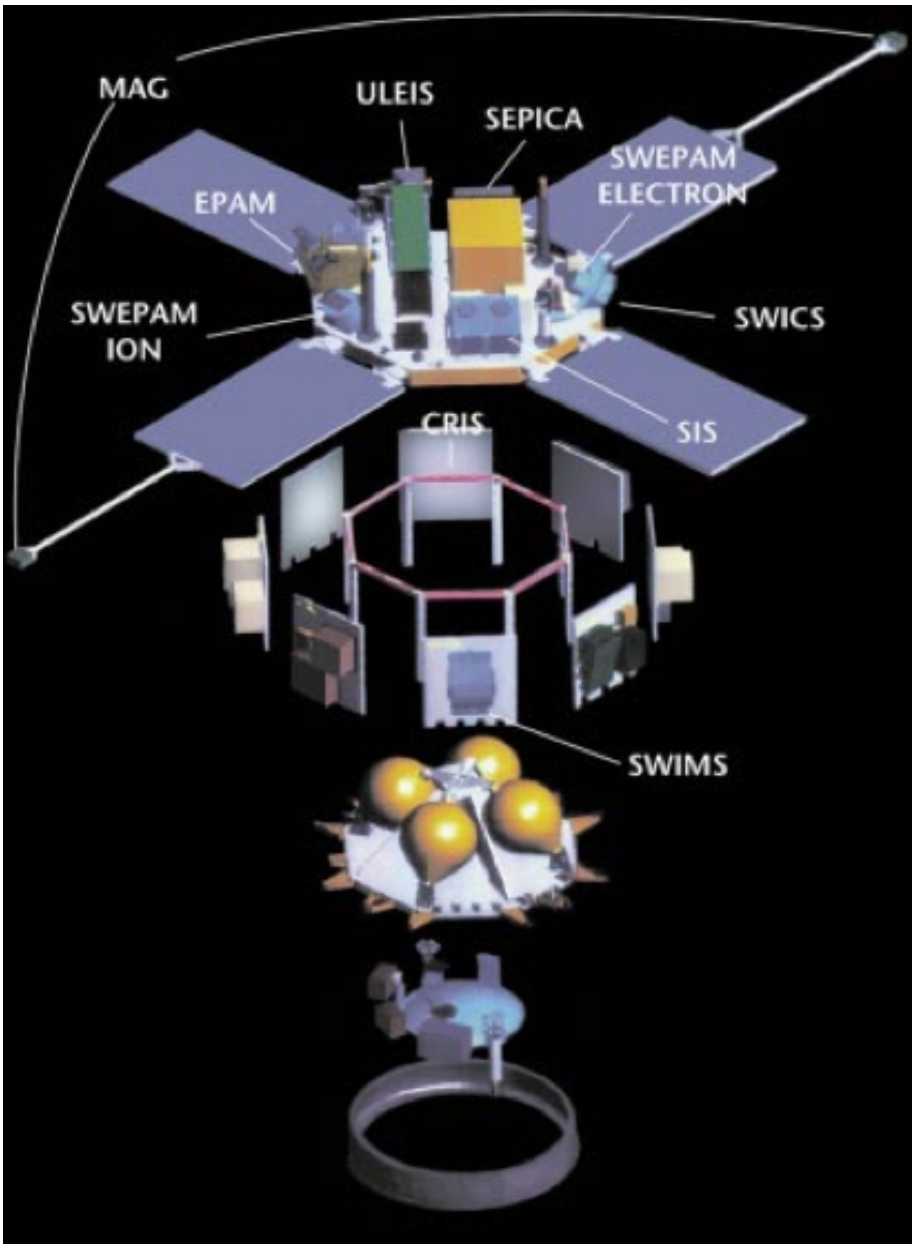

Figure 2.23: Instruments onboard ACE (Stone *et al.*, 1998).

Chapter 3

Magnetic Reconnection along QSLs - A Major Driver of Active Region Outflows

The main results of the work presented in this chapter were published in Baker *et al.* (2009b). The paper was presented at the 3rd Hinode Science Meeting in Tokyo in December 2009. The analysis is the outcome of the author's own work, while collaborations with the paper's co-authors are acknowledged as follows: L. van Driel-Gesztelyi acted in the capacity of academic supervisor; C. Mandrini computed the magnetic extrapolations and modeling; P. Démoulin contributed with very helpful discussions. The paper has 8 citations to date. Preliminary results discussed in §3.6 were presented at COSPAR in Bremen in July 2010.

3.1 Abstract

Hinode EIS has discovered ubiquitous outflows of a few to 50 km s^{-1} from ARs. These outflows are most prominent at the AR boundary and appear over monopolar magnetic areas. They are linked to areas of significant non-thermal line broadening and are stronger in hotter EUV lines. The outflows persist for at least several days. Using *Hinode* EIS and XRT observations of AR 10942 coupled with magnetic modeling, it is demonstrated that the outflows originate from specific locations of the magnetic topology where field lines display strong gradients of magnetic connectivity, namely QSLs, or in the limit of infinitely thin QSLs, separatrices. It was found that the strongest AR outflows are in the vicinity of QSL sections located over areas of strong magnetic field. Magnetic reconnection at QSLs separating closed field lines

of the AR and either large-scale externally connected or 'open' field lines is a viable mechanism for driving AR outflows which are likely contributors to the slow SW.

3.2 Active Region Outflows

An extensive body of literature exists discussing AR plasma motions and Doppler shift measurements of chromospheric, TR, and to a lesser extent, coronal emission lines from the spectrometers aboard rocket flights, *Skylab*, Solar Maximum Mission (SMM) Ultraviolet Spectrometer and Polarimeter (USVP), and the SOHO Coronal Diagnostic Spectrometer (CDS) and Solar Ultraviolet Measurements of Emitted Radiation (SUMER), among others.

Gurman and Athay (1983) obtained Doppler velocity measurements in the chromospheric C IV resonance line (T = 10^5) for eight sunspots using SMM USVP. Mean flow velocities over the umbra of the eight sunspots relative to the mean flow velocity in large areas of the quiet network were determined to be a mean upflow of 1.2 $\pm$ 5.6 km s^{-1}. Qiu *et al.* (1999) reported counter-streaming mass flows in AR loops observed in Hα blue and red wings and posed that the flows occur in filamentary magnetic field structures located at the base of AR loops. Achour *et al.* (1995) measured AR redshifts in TR and coronal lines using the High Resolution Telescope and Spectrograph (HRTS). LOS velocities increased with temperature to peak before reversing. O IV (T = 1.35 $\times$ 10^5 K) is the turning point where redshifts peaked at 17 km s^{-1}. Velocities dropped off at higher temperatures to $\sim$2.4 to 14.8 km s^{-1}. Spadaro *et al.* (2000) detected siphon-like flows along compact coronal loops in AR 7978 by analyzing SUMER data.

Brynildsen *et al.* (1998) studied the dynamics in the TR of sunspots (AR 7981) using CDS and SUMER. A comparison of relative LOS velocities of O V, a TR line, and Mg IX, a lower corona line, showed the flow fields differed. Downflow regions were predominantly observed in the TR and directly above, outflows were found in the lower corona such that there was a marked difference in the flow fields between the two layers in the solar atmosphere. Measured relative velocities ranged from 30 km s^{-1} to -30 km^{-1}. Similar results were obtained by Teriaca *et al.* (1999) using SUMER to measure Doppler shifts as a function of temperature between 10^4 to 10^6 K in AR 7946. Red-shifted velocities for a number of emission lines increased from zero s^{-1} at 2 $\times$ 10^4 K to 15 km s^{-1} at 10^5 K (chromospheric temperature). At higher temperatures in the TR and corona, the opposite flow direction was observed. Blue-shifted velocities in the TR were measured to be -8 km s^{-1} at 6.3 $\times$ 10^5 K (Ne VIII) and -10 km s^{-1} at 10^6 K (Fe XII) in the corona. Marsch *et al.* (2004) combined

magnetograms (MDI and NSO/KP) and SUMER spectroscopic measurements with magnetic modeling of the corona for three ARs. They found blueshifts in N V, O VI, and Ne VIII TR emission lines (temperatures ranging from $10^{5.3}$ to $10^{5.8}$ K) above the ARs and sharp red-blue boundaries between closed and 'open' field at the periphery of the three ARs.

Winebarger *et al.* (2001) reported brightness variations along dense bundles of coronal field lines of an AR observed by the Transition Region and Coronal Explorer (TRACE) in the Fe IX/X channel. The apparent outflow is frequently observed in TRACE data. Brightness fluctuations were detected as transient, localized emission traveling along loops. The projected velocities of the apparent outflows is between 5 and 17 km s^{-1}. They concluded that the fluctuation events are in fact mass flows after comparing the observed emission to quasi-static loop model predictions. Winebarger *et al.* (2002) detected steady flows in fan-like loops in ARs using TRACE and SUMER co-aligned observations. In the past decade, the so-called flows in TRACE observations have fueled a lively debate as to whether the brightness fluctuations are indeed mass flows or waves (De Moortel *et al.*, 2002; De Pontieu *et al.*, 2003).

Previous measurements of AR plasma flows have been limited by spectral, spatial and temporal resolution of spectrographs. Since its launch on-board the *Hinode* satellite (Kosugi *et al.*, 2007) on 2006 September 23, EIS (Culhane *et al.*, 2007a) has produced routine measurements of Doppler shifts and broadening in lines formed at TR and coronal temperatures. In particular, EIS, with its large FOV and excellent spectral resolution, has provided opportunities to investigate plasma flows in all solar environments from CH to ARs. One of the most intriguing EIS results is the discovery of ubiquitous hot plasma outflows seen in all ARs (Doschek *et al.*, 2007; Del Zanna, 2008; Harra *et al.*, 2008; Hara *et al.*, 2008; Doschek *et al.*, 2008). AR outflows are especially important because they are considered to be a possible source of the slow SW (Sakao *et al.*, 2007; Harra *et al.*, 2008).

Sakao *et al.* (2007) reported *Hinode* XRT (Golub *et al.*, 2007) observations of continuous outflows from the edge of AR 10942. The XRT observations were supported by EIS observations of AR blue-shifted flows reported by Doschek *et al.* (2007), Del Zanna (2008), Harra *et al.* (2008), Hara *et al.* (2008), Doschek *et al.* (2008) and Marsch *et al.* (2008). All authors describe the physical characteristics of the AR outflows and it is very clear that such outflows are distinct from the impulsive plasma flows that result from fast reconnection events such as X-ray jets. These persistent AR outflows are located in regions of low electron density and low radiance (Del Zanna, 2008; Harra *et al.*, 2008; Doschek *et al.*, 2008) at the edges or periphery of ARs (Sakao *et al.*, 2007) and over monopolar areas (Doschek *et al.*,

2008). They have been observed to persist at nearly the same location within ARs during their transit across the solar disk (Sakao *et al.*, 2007; Doschek *et al.*, 2008; Bryans *et al.*, 2010). Blue-shifted LOS velocities for Fe XII 195.12 Å typically range from a few to 50 km s^{-1} (Del Zanna, 2008; Harra *et al.*, 2008; Hara *et al.*, 2008; Doschek *et al.*, 2008) and are faster in hotter coronal emission lines (Del Zanna, 2008).

3.2.1 Active Region Outflows and Line Profile Asymmetries

Understanding the dynamics of the plasma in ARs is crucial to understanding the processes that produce and drive AR outflows. Analysis of emission line profiles is an important diagnostic tool for probing the thermal and dynamic structure of outflow plasma, especially as an asymmetric line profile contains much more information than a symmetric, or Gaussian profile. Peter (2010) suggests that line profile asymmetry can be due to

- two or more spatial components,
- opacity effects,
- non-Maxwellian velocity distribution of ions,
- line blends,
- asymmetric instrument profile.

Prior to the advent of *Hinode* EIS, spatial and spectral resolutions were insufficient for investigating the profiles of emission lines formed in the corona at temperatures exceeding 10^6 K. Recent work, based on EIS observations, by Hara *et al.* (2008), De Pontieu *et al.* (2009), McIntosh and De Pontieu (2009), Peter (2010), and Bryans *et al.* (2010) among others, has provided new insight into the nature of emission line profiles of hotter coronal lines, especially EIS's core Fe XII line, Fe XIV, and Fe XV. Hara *et al.* (2008) first reported that significant deviations from a single-Gaussian profile were found in the blue wings of the Fe XIV and Fe XV line profiles for outflows near AR footpoints. Blue-shifted velocity outflows from AR 10938 observed on-disk contained a high-velocity component of more than 100 km s^{-1} in the blue wing. Hara *et al.* (2008) conclude that there are unresolved high-speed outflows which has implications for coronal heating mechanisms.

De Pontieu *et al.* (2009) used maps of blue-red (B-R) asymmetry in the Fe XIV emission line to isolate outflows from the bright line core, with typical velocities of

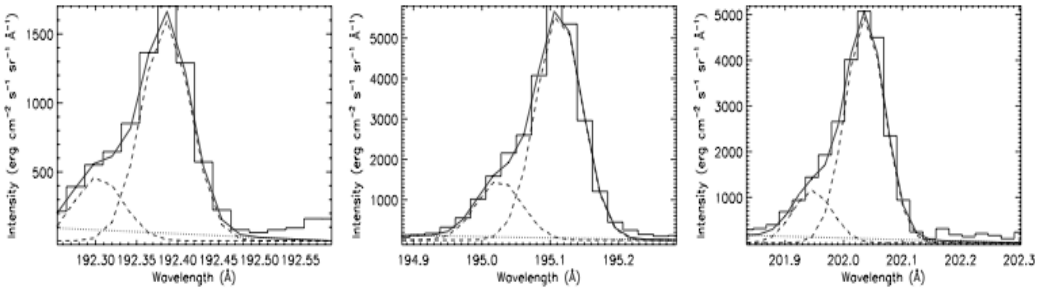

Figure 3.1: Observed EIS Fe XII 192.39 Å (left), Fe XII 195.12 Å (middle), and Fe XIII 202.02 Å (right) spectra from a single pixel located at the base of AR 10978 outflow regions. The profiles are modeled with a double-Gaussian fit (solid curve) comprised of primary and secondary components (dashed lines). (From Bryans *et al.* (2010)).

10 - 20 km s^{-1}, from the faint outflows in the blue wings that have velocities of 50-100 km s^{-1}. They found the blue wing outflows are predominantly observed in the moss region at AR footpoints. The sites of the pervasive and universal faint outflows at coronal temperatures are well correlated with chromospheric activity and have similar upward velocities to Type II spicules. De Pontieu *et al.* (2009) suggest that the mass supplied by the spicules can play a significant role in supplying the corona with hot plasma.

Of particular interest to Bryans *et al.* (2010) is the correlation between line shift and line width reported by Doschek *et al.* (2008) and Hara *et al.* (2008). Bryans *et al.* (2010) suggest that emission lines showing the largest non-thermal velocities and linewidths indicate that the outflows may result from multiple flow sites. They model the outflowing plasma as a blend of outflow sites with different flow speeds by imposing a double-Gaussian fit to the asymmetric line profiles using 10 sets of EIS observations of AR 10978 in the period 2007 December 9 to 15. The asymmetric line profiles of Fe XII and Fe XIII, typical of line emission in outflow regions, were modeled as the sum of two Gaussians with the same width and using a linear background (see Figure 3.1). Over 10 rasters, they found primary component median velocities of 0 - 10 km s^{-1} for the eastern outflow region and 5 - 13 km s^{-1} for the western outflow region. Secondary component median velocities were 90 - 120 km s^{-1} on the east and 100 - 130 km s^{-1} on the west, with over 200 km s^{-1} observed. Significant contribution from the secondary components occurred in isolated regions at the base of the outflows on both sides of the AR and were observed throughout the entire seven day period (see the red contours in Figure 3.2). Even though a double-Gaussian fit of the Fe XII and Fe XIII emission line profiles gives a more accurate fit compared to a single-Gaussian fit, Bryans *et al.* (2010) still found a correlation between velocity and width for the primary component. This suggests that a double-Gaussian fit does not fully describe the outflow regions. Lower temperature lines including Si VII and Fe VIII were found to have symmetric line profiles that are well

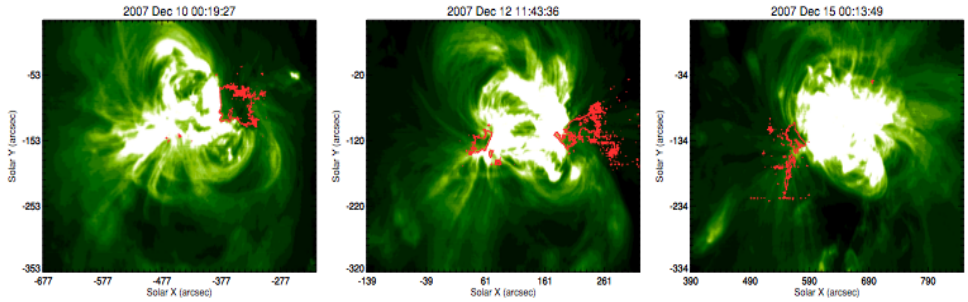

Figure 3.2: Fe XII total intensity (sum of primary and secondary components) images of AR 10978 overlaid with red contours that show where the secondary component intensity is 5% of the primary component intensity. The secondary component is located primarily at the footpoints of the AR where the outflows are observed. (From Bryans *et al.* (2010)).

modeled by a single Gaussian.

Peter (2010) set out to detect additional components accounting for small excesses in the line wings of EIS Fe XV emission by comparing profiles modeled by single-Gaussian, constrained double-Gaussian, and free double-Gaussian fitting procedures. For AR 10938, they found the spectra are best fit by a narrow line core and a broad minor component as determined by a free double-Gaussian model. Blue wing/minor component Doppler shifts are 115 - 130 km s^{-1} at the footpoint regions of loops i.e. at the base of the outflow regions. The location and blue wing velocities are consistent with those of Bryans *et al.* (2010).

3.2.1.1 Potential Mechanisms for Driving Outflows

Whereas red-shifted (cooling) down flows observed in AR closed loops are well understood, to date there is no general consensus for the mechanism(s) driving blue-shifted AR outflows. Among the mechanisms proposed are:

- Coronal plasma circulation -

  Marsch *et al.* (2008) combine coronal magnetic field extrapolations and spectroscopic data to argue that the blueshifts and redshifts observed in TR and coronal emission lines correspond to outflows and downflows of plasma on 'open' and closed magnetic field lines. The magnetic field lines confine large-scale plasma flows in the low-β plasma of the corona as it continuously circulates in separate coronal structures. The flow pattern appears to be long-lasting on large scales indicating quasi-steady flows throughout the corona. Marsch *et al.* (2008) interpret coronal plasma circulation as mass supply to and loss from the corona. They assume that the origin and driver of the circulation of flows lies in the magnetoconvection below the photosphere in the

solar convection zone.

- Impulsive heating at AR footpoints -

  Hara *et al.* (2008) propose that the hot plasma outflows observed near the base of the corona is direct evidence for impulsive heating at the footpoints of AR loops. High velocity components of blue-shifted outflows in the blue wings of the Fe XIV and Fe XV line profiles are consistent with the nanoflare heating model of Patsourakos and Klimchuk (2006).

- Chromospheric evaporation -

  Del Zanna (2008) refers to some similarities between AR outflow patterns and CDS observations of the gradual phase of two ribbon flares. Arcades of cooling plasma are forming while 'gentle' outflows seen in hotter lines occur along the sharp boundaries outside of the arcade (del Zanna *et al.*, 2006). The outflows are attributed to chromospheric evaporation due to reconnection. Del Zanna (2008) speculates that continuous flux emergence and braiding by photospheric motion leading to reconnection driven chromospheric evaporation may drive AR outflows.

- Expansion of large-scale reconnecting loops -

  Harra *et al.* (2008) use a large-scale magnetic field model of the corona and EIS observations to show that strong outflows on the eastern side of AR 10942 occur in the vicinity of expanding large-scale reconnecting loops or 'open' field.

- Continual AR expansion -

  Three-dimensional simulations of an AR embedded in a CH carried out by Murray *et al.* (2010) show that outflows are accelerated along the 'open' field simply as a result of the AR expanding horizontally as it develops. Murray *et al.* (2010) propose that the only necessary elements for this mechanism to operate are a horizontally expanding AR and a nearby compressible magnetic field with a vertical component. In the case of nearby closed field, plasma flows will be confined by the magnetic field and would be siphon flows. Outflow velocities are consistent with measurements of AR expansion (Uchida *et al.*, 1992), therefore, AR expansion is a plausible mechanism to drive outflows in all ARs whether the surrounding field is closed and/or 'open'.

- Waves -

  A number of oscillations and waves have been observed in a variety of solar structures including plumes, prominences, and loops. Ofman *et al.* (1997) first reported quasi-periodic variations in the polarized brightness in polar CHs due to density fluctuations along plumes. This was followed by observations using SOHO EIT and *Yohkoh's* SXT (see de Moortel (2009) and references

there in). The perturbations were found to travel along the plumes at the local sound speed suggesting propagating slow magneto-acoustic waves. Similar disturbances have been observed in coronal loops by TRACE. With the advent of TRACE, it became clear that intensity perturbations are a common phenomenon, often found in large, quiescent loops or fan-like structures, at the edges of AR over plage areas and above sunspot umbra (de Moortel, 2009). The quasi-periodic nature of the perturbations observed in TRACE share similar properties including an oscillation period of 284.0 ± 10.4 s, relative amplitude of 3.7% ± 0.2%, and propagation speed of 99.7 ± 3.9 km s^{-1} (McEwan and de Moortel, 2006). Theoretical MHD modeling by Nakariakov *et al.* (2000) and others confirms the interpretation that the propagating disturbances in EUV emission observed in coronal loops are likely to be slow magneto-acoustic waves. The driver of the waves is thought to be the 'leakage' of the global solar surface p-modes (de Moortel, 2009). de Moortel (2009) states that it is not immediately obvious how AR outflows relate to the propagating intensity perturbations but there are notable similarities especially the location at AR edges and apparent velocities.

3.2.1.2 Applications of QSLs

When viewing the plethora of EIS velocity maps containing ARs, it is quite striking that the outflows appear to occur at locations where magnetic field lines with drastically different connectivities are rooted or meet. At such locations outflows are concentrated at boundaries that mark the change in magnetic topology from 'open' to closed field or appear over a monopolar area between loops connecting to different regions of opposite polarity (see Figure 3.3). Such locations are called separatrices or, in the general case, QSLs (Demoulin *et al.*, 1996). In three-dimensional magnetic field configurations, separatrix surfaces separate topological volumes with different magnetic connectivities, while QSLs are defined as thin volumes in which field lines display strong gradients of magnetic connectivity (for a recent review, see Démoulin (2007)). When these gradients become infinitely large a QSL becomes a separatrix. Specifically, separatrices are present in 'open'-closed magnetic topology. QSLs are preferential locations for current layer development and magnetic reconnection in the absence of magnetic nulls and 'bald patch' separatrices (Demoulin *et al.*, 1997; Milano *et al.*, 1999; Aulanier *et al.*, 2005b; Titov *et al.*, 2008). At QSLs, field lines continuously slip across each other during the reconnection process, leading to successive rearrangements of the connections between neighboring field lines along the QSLs, as was shown by MHD simulations (Aulanier *et al.*, 2006) and inferred from *Hinode* XRT observations (Aulanier *et al.*, 2007).

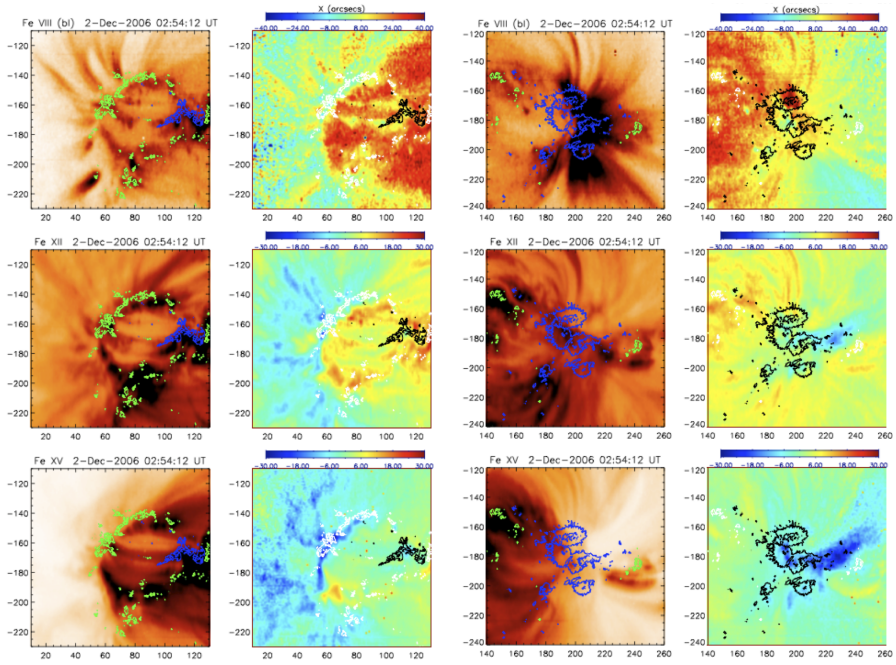

Figure 3.3: Zoomed views of the eastern (columns 1 and 2) and western (columns 3 and 4) sections of AR 10926. From the top, Fe VIII, Fe XII, and Fe XV intensity and velocity maps overlaid with *Hinode* SOT Stokes-V data (green/blue and white/black contours are positive/negative polarity). Velocity maps show outflows concentrated at the edges of AR 10926 where there is a change in magnetic topology from 'open' to closed field or loops connecting to different regions of opposite polarity. From Del Zanna (2008).

The relationship between separatrices and QSLs in three dimensions and observations has been explored in many different solar magnetic configurations in recent years, from small-scale X-ray bright points (XBP) to large-scale X-class flares. Mandrini *et al.* (1996) concluded that the brightness evolution of an XBP was linked to magnetic reconnection at QSLs. Fletcher *et al.* (2001) associated TR brightenings with both QSLs and 'bald-patch' separatrices.

When flares have been studied and related to magnetic reconnection at QSLs, Hα and UV flare brightenings were found along or next to QSLs (Demoulin *et al.*, 1997). In an X1 flare, Gaizauskas *et al.* (1998) reported that plage brightenings and flare kernels were located at the intersection of QSLs with the photosphere. Flare kernels have been successfully compared to the photospheric and chromospheric traces of QSLs. In addition, Demoulin *et al.* (1997) and Mandrini *et al.* (1997) found concentrated electric currents along the boundaries of QSLs where magnetic energy is believed to be stored in the magnetic field associated with these currents. The release of free magnetic energy may occur when the thicknesses of QSLs, and their associated current layers, are small enough for reconnection to take place. Mandrini *et al.* (1997) calculated the thickness of a QSL located over a single polarity, where an XBP was observed, to be less than 100 m during the lifetime of the XBP. Recently, a combination of slip-running reconnection along QSLs before and after

reconnection at a null-point embedded within the QSLs was shown to explain the observed dynamics of flare ribbons (Masson *et al.*, 2009). Note, Schrijver *et al.* (2010) investigated the formation of EUV 1 - 2 MK loops that fan out from the periphery of ARs in association with strong flux concentrations. For eight ARs with largely potential field configurations, they found that the loop fan structures occur in the vicinity of QSLs within the strong-field regions of magnetic plage. Schrijver *et al.* (2010) builds on and cites the work on AR 10942 presented in this chapter.

In summary, theoretical magnetic field topology studies based on QSLs have withstood the test of solar flare observations in the recent past and have confirmed that reconnection is the main physical process in solar flares. With new instruments such as *Hinode* EIS, the role of QSLs in association with AR outflows is tested. It is proposed here that the answer to what drives the persistent and ubiquitous AR outflows lies in the AR magnetic field topology. The AR outflows are observed near or along QSLs. In the following sections this idea is applied to AR 10942 by computing its magnetic topology and comparing the location of QSLs with outflow regions identified in the EIS data.

3.3 Data Reduction

3.3.1 AR 10942

AR 10942 appeared at the Sun's eastern limb on 2007 February 16. As it crossed the solar central meridian on the 22nd, the AR was measured to have a magnetic flux of approximately 4×10^{21} Mx. Oriented east-west with a leading negative polarity, it was observed by the *Hinode* satellite at various times between February 19 and 26. Here the focus is on EIS observations on February 20 and 21.

No single EIS observation covered the full extent of AR 10942 so multiple data sets and, hence, EIS studies were used to analyze both the eastern and western sections of the AR. Approximately 24 hours separated the observations. A raster scan using the 2" slit and consisting of 120 pointing positions with exposure time of five seconds per position was performed with EIS from 23:45 to 23:55 UT on 2007 February 20 (Study ID 37). The EIS FOV was 240"×240" and covered most of the AR. A different raster scan using the 1" slit with exposure time of 30 seconds per position was performed from 11:16 to 11:37 UT on February 20 (Study ID 57). The FOV was narrower (41"×400"), however, it covered the core eastern outflow region of the AR. On the western side of the AR, a raster scan with a FOV of 128"×512" included the outflow region that was not fully covered in the raster timed at 23:45

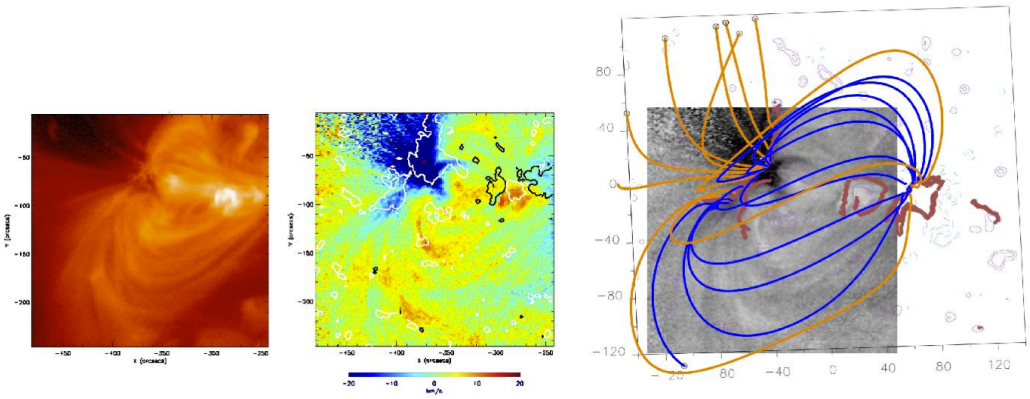

Figure 3.4: Left panel - EIS Fe XII emission line intensity map of AR 10942 at 23:45-23:55 UT on 2007 February 20. Middle panel - EIS Fe XII emission line velocity map overlaid with ± 50 G MDI magnetic contours. White/black is positive/negative polarity. Right panel - photospheric trace of QSLs (thick red lines) and field lines originating in the QSLs are overlaid on a grayscale EIS Fe XII emission line velocity map. Orange/blue field lines are drawn from the western/eastern side of the eastern QSL over the positive polarity and lines with circles leave the computational box and are considered to be 'open' or large extended loops. The coordinate system is centered on the AR instead of the Sun and both axes have units of Mm. Magnetic field isocontours are shown in continuous pink/dashed blue lines for positive/negative values of the field (± 20, ± 50, and ± 500 G). The overlay image clearly shows strong AR outflows along 'open' field lines computed from the eastern side of the QSL located over the positive polarity. Note, the size of the computational box for this figure and Figures 2, 3, 4, and 6 is 400 Mm in all directions.

UT on the 20th. This raster scan, using the 1" slit with 60 seconds exposure time, ran from 11:40 to 13:48 UT on February 21 (Study ID 45). EIS Fe XII intensity maps of each scan are shown in the left panels of Figures 3.4, 3.5, and 3.6 (23:45 UT and 11:16 UT on the 20th and 11:40 UT on the 21st, respectively).

EIS data reduction was carried out using standard SolarSoft EIS procedures. Raw data were corrected for dark current, hot, warm and dusty pixels, and cosmic rays. Relative Doppler velocities were determined by fitting a single-Gaussian function to the calibrated spectra in order to obtain the line center for each spectral profile. A fitted line center was further corrected by removing instrumental effects including slit tilt and orbital variation. Blueshifts (redshifts) seen in the final velocity maps in the middle panels of Figures 3.4 to 3.6 correspond to negative (positive) Doppler velocity shifts along the LOS.

In general, the EIS line profiles are found to be well represented by a single-Gaussian function with no line asymmetries or enhanced wings. For a single-Gaussian fit, the standard EIS fitting routine 'eis_auto_fit' automatically calculates the initial parameters by locating the pixel within the data cube with the maximum intensity in the spectrum. This is used as a 'first guess' for the amplitude and centroid of the emission line (typically the Fe XII core line). The minimum intensity value in the spectrum is used as the 'first guess' for the spec-

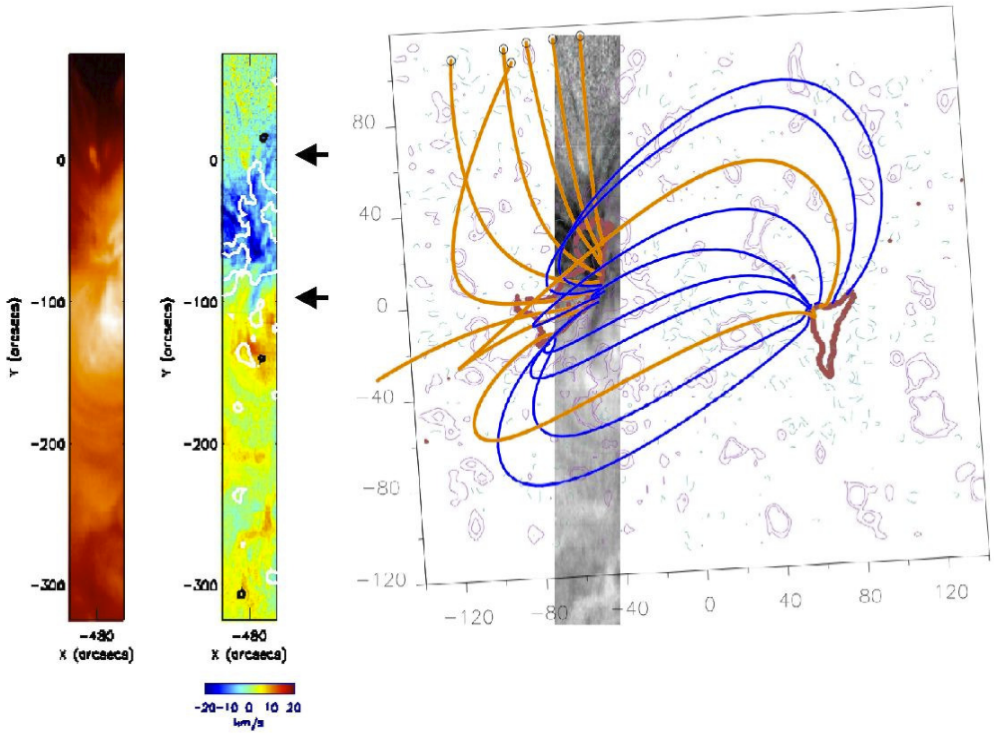

Figure 3.5: EIS Fe XII emission line intensity (left panel) and velocity (middle panel) maps and photospheric trace of QSLs and field lines originating in the QSLs (right panel) at 11:16-11:37 UT on 2007 February 20. The drawing convention is the same as that used in Figure 3.4. The image in the right panel shows AR outflows along 'open' field lines computed from the eastern side of the QSL. (Black arrows indicate the zoomed FOV shown in Figure 3.12).

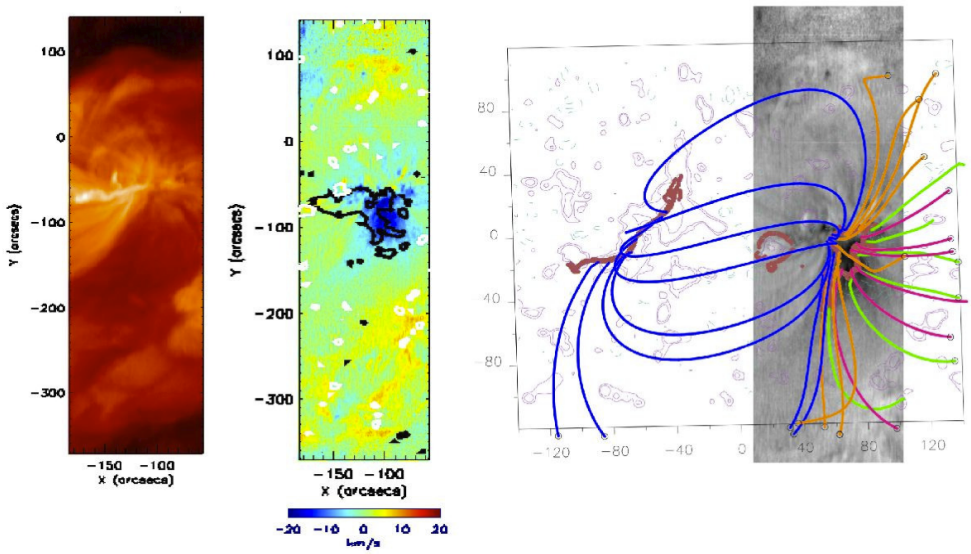

Figure 3.6: EIS Fe XII emission line intensity (left panel) and velocity (middle panel) maps and photospheric trace of QSLs and field lines originating in the QSLs (right panel) at 11:40-13:48 UT on 2007 February 21. The drawing convention is the same as that used in Figure 3.4, with the addition of green/pink field lines computed from the east/west side of the western part of the QSL trace. The AR negative polarity is connected to the AR positive polarity and to the positive polarity of a neighboring bipole to the west. The overlay image shows AR outflows along 'open' field lines computed from the inner side of the closed QSL trace. Note that the MDI magnetic map used as boundary condition for the modeling was taken at 08:03 UT, 3.5 hours prior to the start of the EIS scan, due to patchy magnetic data coverage.

trum background. The initial width is assumed to be the instrumental width of 70 mÅ. Under certain circumstances, there are significant deviations from single-Gaussian profiles, as was discussed in §3.2.1. Anomalous line widths in the Fe XII 195.12 Å EIS core line were discovered for a small but significant number of pixels in the observation on 2007 February 20 at 11:16 UT. This necessitated a double-Gaussian fitting of the core line profile using Peter Young's documents entitled 'Gaussian fitting for the *Hinode*/EIS mission' and 'Gaussian fitting examples using eis_auto_fit' (both documents are available on the EIS WIKI website: `http://msslxr.mssl.ucl.ac.uk:8080/eiswiki/Wiki.jsp?page=054a`). In the case of double-Gaussian fitting, the initial parameters such as the location and amplitude of each of the lines are manually specified using the EIS 'eis_fit_template' routine. See §3.6.1.1 for a complete discussion of the results of the double-Gaussian fitting.

Evaluation of the Fe XII emission line profile called for density diagnostics of the eastern side of AR 10942 on 2007 February 20 at 11:16 UT. The CHIANTI v6.0 atomic model which contains atomic data and analysis software to derive a density value from a measured line ratio value was used to produce a Fe XIII λ203.82/λ202.04 emission line ratio density map. CHIANTI's database consists of energy levels, radiative decay rates, electron excitation/de-excitation coefficients, and proton excitation/de-excitation (see Young *et al.* (2008) and references within) for Fe XIII lines, among others. As an aside, Fe XII λ186.88/λ195.12 line ratios were preferred, however, the 186.88 line did not have sufficient statistics. The two Fe XIII data sets were prepped, fitted with single-Gaussians, and instrumental effects were removed as described above. Fitted data structures were input into CHIANTI which was then used to obtain the theoretical curve that relates the emission line ratio to electron density for the pair of lines. Figure 3.22 is the CHIANTI output. The plot shows the strong sensitivity of the lines to density as the ratio varies by a factor of 43 from 10^8 to 10^{10} cm^{-3} (Young *et al.*, 2008). Finally, the CHIANTI output density structure is converted to a map structure. See §3.6.1.1 for the Fe XIII λ203.82/λ202.04 emission line ratio density map.

Co-alignment of EIS data with the underlying photospheric magnetograms, from which magnetic field extrapolations are made and QSLs are calculated, is a crucial step in determining whether the blue-shifted outflows observed at the periphery of the AR are located at or near QSLs. First, full-disk XRT images were co-aligned with full-disk SOHO MDI (Scherrer *et al.*, 1995) magnetograms using the solar limb location, after which on-disk features were matched. Then, EIS Fe XII and Fe XV 284.16 Å images were co-aligned with XRT images. MDI magnetic field data were overlaid on all images for final confirmation of alignment. Standard SolarSoft procedures were applied to data from XRT and MDI. Additional descriptions of the

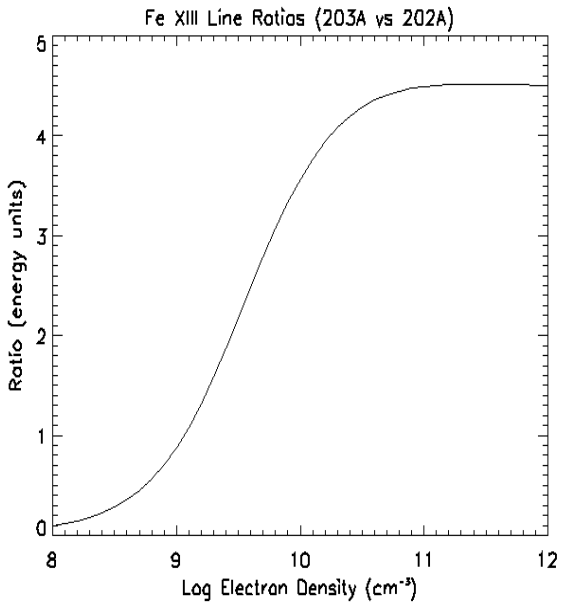

Figure 3.7: Theoretical variation of emission line ratio versus electron density for EIS Fe XIII λ203.82/λ202.04 from CHIANTI atomic model in SolarSoft IDL.

AR and its surrounding coronal field can be found in Sakao *et al.* (2007) and Harra *et al.* (2008).

In the analysis of AR 10942, only those data sets which have sufficient photon counts for fitting line profiles have been selected. EIS exposure times ranged from 5 to 60 seconds, thus data quality was affected for some weaker lines. In addition, MDI data cadence was not ideal with only four magnetograms spanning the EIS data period. Data quality can affect how well outflows observed in EIS velocity maps match QSL locations. This will be discussed in §3.5

3.3.2 AR at Disk Center

EIS also observed a mature, dispersed AR at 18:07 UT on 2008 January 10 when it was at disk center. It will be more fully discussed in §3.6. The AR was measured to have a magnetic flux of approximately 1×10^{21} Mx. A raster scan using the 2" slit and consisting of 90 pointing positions with exposure time of 25 seconds per position was performed with EIS from 18:07 to 18:45 UT. The FOV is 180" $\times$ 512" and covers all of the positive polarity and part of the nearby equatorial CH. Study ID 236 consists of 24 emission lines, however, the signal-to-noise (S/N) ratio is insufficient in a large number of weaker lines as the study is designed for fast cadence observations of AR footpoints. Intensity and velocity maps in §3.6 are made from the slit raster observations.

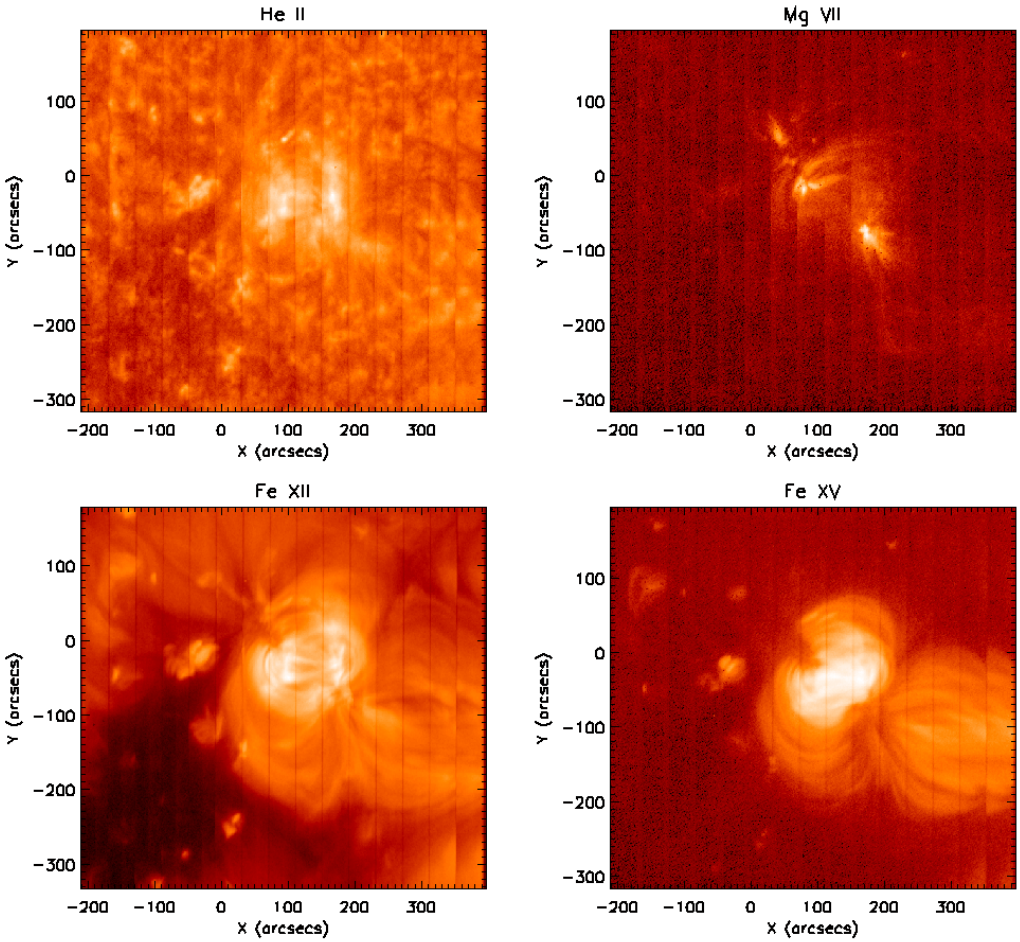

Figure 3.8: EIS 40 ” slot raster images of AR at disk center on 2008 January 10 at 16:02 UT. Clockwise from top left: He II T = $10^{4.7}$ K, Mg VII T = $10^{5.8}$ K, Fe XII T = $10^{6.1}$ K, and Fe XV T = $10^{6.3}$ K. The AR is visible in all lines, however, the CH is clear only in the Fe XII emission line.

The 40” slot (Study ID 235) was employed to construct large FOV images of 600” × 512”. Figure 3.8 shows 40” slot images for He II T = $10^{4.7}$ K, Mg VII T = $10^{5.8}$ K, Fe XII T = $10^{6.1}$ K, and Fe XV T = $10^{6.3}$ K. The large FOV is well suited for providing context, coaligning with MDI magnetograms, and matching magnetic model field lines. Reduction procedures used for this AR are the same as those described in the previous section for AR 10942 (§3.6).

3.4 Magnetic Field Modeling and Topology

The Quasi-Separatrix Layers Method (QSLM) and the properties of QSLs have been discussed in detail by Demoulin *et al.* (1996) and reviewed by Démoulin (2006, 2007). Here only a brief description of the magnetic field modeling technique and the application of the QSLM including recent improvements and some modeling limitations are provided. The focus then shifts to the specific results obtained for

AR 10942.

3.4.1 The Magnetic Field Model

To compute the magnetic field topology of AR 10942, first the coronal field is modeled. The LOS magnetic field of AR 10942 is extrapolated to the corona using the discrete fast Fourier transform method under the LFFF hypothesis ($\boldsymbol{\nabla} \times \boldsymbol{B} = \alpha \boldsymbol{B}$, where $\boldsymbol{B}$ is the magnetic field and α is a constant). As AR 10942 is not at disk center on February 20 and 21, a transformation of coordinates from the observed to the local frame is done, as discussed in Demoulin *et al.* (1997).

The MDI magnetogram closest in time to each EIS map is used as the boundary condition for the coronal magnetic model. Therefore, since there are three different EIS scans, three different models are computed. The value of the free parameter of each model, α, is set to best match the loops observed either by EIS in Fe XII or by XRT depending on whether the EIS FOV is large enough to identify the global shape of loops. The procedure followed is discussed in Green *et al.* (2002a). The best matching values of α are $9.4{\times}10^{-3}$ Mm^{-1} for the EIS maps starting at 11:16 UT and 23:45 UT on February 20 and $6.3{\times}10^{-3}$ Mm^{-1} for the EIS map at 11:40 UT on February 21.

In all of the magnetic field models, there are a number of field lines which leave the computational box, particularly, those field lines rooted in the vicinity of a QSL. The LFFF hypothesis is not well suited for modeling 'open' field lines because the field is forced to be balanced within the box. It is noted that the original imbalance in the magnetic field data was approximately 2.2 G uniformly distributed in a FOV shown in all model figures (i.e., extending 240 Mm in the east-west and 240 Mm in the north-south directions).

The fast Fourier-transform method used in the LFFF extrapolations may lead to artifacts due to the periodic nature of the solution. By enlarging the computational box, the effect of the periodicity is decreased so the weak influence of the box size on the stability of the QSLs locations indicates that the periodicity is not a major issue. This was further tested using a potential field extrapolation where there is no intrinsic limitation of the box size ($\propto 1/\alpha$). The QSLs remained at the same locations as the box was increased in size. These potential extrapolations were qualitatively compared to the spherical source-surface extrapolations of the same AR in Sakao *et al.* (2007). They show field lines originating in the vicinity of the outflows on the eastern side of the AR as is the case in Figure 3.4, supporting the veracity of the existence of 'open' or large-scale field lines in the models.

3.4.2 Brief Description of the Quasi-Separatrix Layers Method

QSLs are defined as regions where there is a drastic change in field line connectivity (see e.g. Demoulin *et al.*, 1996), as opposed to the extreme case of separatrices where the connectivity is discontinuous. Consider the mapping from one photospheric polarity to the opposite one, denoted by $\boldsymbol{r}_+(x_+, y_+) \mapsto \boldsymbol{r}_-(x_-, y_-)$, and the reversed mapping $\boldsymbol{r}_-(x_-, y_-) \mapsto \boldsymbol{r}_+(x_+, y_+)$. These mappings can be represented by the vector functions $[X_-(x_+, y_+), Y_-(x_+, y_+)]$ and $[X_+(x_-, y_-), Y_+(x_-, y_-)]$, respectively. For example, a QSL is present at (x_+, y_+) when $X_-(x_+, y_+)$ and/or $Y_-(x_+, y_+)$ depend strongly on x_+ and/or y_+. The strong variation of these functions, X_- and/or Y_-, is found when computing the norm of the connectivity gradient as described below. The norm $N(\boldsymbol{r}_+)$ of the Jacobian matrix in Cartesian coordinates is

$$N_+ \equiv N(x_+, y_+) = \sqrt{\left(\frac{\partial X_-}{\partial x_+}\right)^2 + \left(\frac{\partial X_-}{\partial y_+}\right)^2 + \left(\frac{\partial Y_-}{\partial x_+}\right)^2 + \left(\frac{\partial Y_-}{\partial y_+}\right)^2}. \quad (3.1)$$

In a similar way, in the negative polarity the matrix is

$$N_- \equiv N(x_-, y_-) = \sqrt{\left(\frac{\partial X_+}{\partial x_-}\right)^2 + \left(\frac{\partial X_+}{\partial y_-}\right)^2 + \left(\frac{\partial Y_+}{\partial x_-}\right)^2 + \left(\frac{\partial Y_+}{\partial y_-}\right)^2}. \quad (3.2)$$

A QSL was first defined by the condition $N_+ >> 1$ and $N_- >> 1$ in both photospheric polarities (Demoulin *et al.*, 1996). However, for a field line linking photospheric locations (x_+, y_+) and (x_-, y_-), both of which have different normal field components B_{z+} and B_{z-}, the definition of a QSL given by Equations (3.1) and (3.2) implies that $N(x_+, y_+) \neq N(x_-, y_-)$ if $B_{z+} \neq B_{z-}$. Titov *et al.* (2002) defined another function to characterize QSLs which is independent of the mapping direction, the squashing degree Q. It was shown that Q can be simply defined by the product of the values of N determined when starting the mapping of field lines from both of their photospheric footpoints, therefore

$$Q \equiv N_+ N_- . \quad (3.3)$$

Then, a QSL is defined to exist when $Q >> 2$; the value $Q = 2$ being the lowest possible value. This value is found when, for example, $x_+ = -x_-$ and $y_+ = y_-$ (as present in a simple potential arcade oriented along the y direction). On the other hand, Q becomes infinitely large when the field line mapping is discontinuous, *i.e.* when there are separatrices. By definition, Q is uniquely defined along a field line by $(\boldsymbol{B} \cdot \boldsymbol{\nabla})Q = 0$.

The physical meaning of this new definition can be explained as follows. Consider an elementary flux tube rooted in an infinitesimal circular region with a given polarity sign, Q measures the aspect ratio of the distorted ellipse defined by the mapping of this flux tube footpoint in the other polarity sign. That is, Q measures how much the initial elementary region is squashed by the mapping. MHD simulations have shown that the thickness of a QSL is related to the current density that develops in it, such that the thinner the QSL, the higher the current density (Aulanier *et al.*, 2007). More specifically, the thickness is defined as the full width at half maximum of the Q profile that is computed along a one-dimensional segment that crosses the photospheric QSL trace.

Q can be computed only for field lines reaching the lower boundary at both ends (*i.e.* the field lines are closed). A fraction of the lower boundary is magnetically connected to one side or to the top of the computation box. Such field lines either extend into interplanetary space or they have long connections outside the AR. They are refered to as 'open' field or large-scale loops. In-between truly 'open' and closed field lines a separatrix is present. Moreover, in-between the closed field lines of the AR and large-scale externally connected field lines, a QSL is generally expected since one footpoint of the connection depends drastically on the position of the other footpoint which stays inside the AR. With this extrapolation procedure, the two cases cannot be distinguished and only the transition between closed and 'open' (box-reaching) field lines are computed. This transition is kept by imposing an arbitrarily high value of Q (larger than the minimum value of Q used in the figures shown). How the transition is affected by the size of the computational box is discussed in §4.2.

The finite size of the computational box does not allow for the ability to distinguish between truly 'open' and large-scale field lines. Indeed, some of the field lines leaving the computational box remain 'open' in spherical source-surface (at R_{sun}) computations as indicated by the 'open' green field lines located on the eastern side of the AR in Figure 3.9. The model was produced using the LMSAL PFSS package in IDL which is distributed via SolarSoft. The package enables the user to access a database of potential field models of the solar corona that are based on an evolving surface-flux transport model of photospheric magnetism. LMSAL's software produces spherically gridded vector fields based on MDI LOS magnetograms. Sakao *et al.* (2007) show similar 'open' field lines in their potential field calculations modeling the same AR (see Figure 4B of Sakao *et al.* (2007)). Other field lines are truly large-scale connecting to a neighboring AR as verified by the white closed field lines in Figure 3.9 or far quiet Sun regions (also see Harra *et al.* (2008)), therefore, it is reasonable that the high-Q dominant QSLs are not artifacts resulting from the methodology.

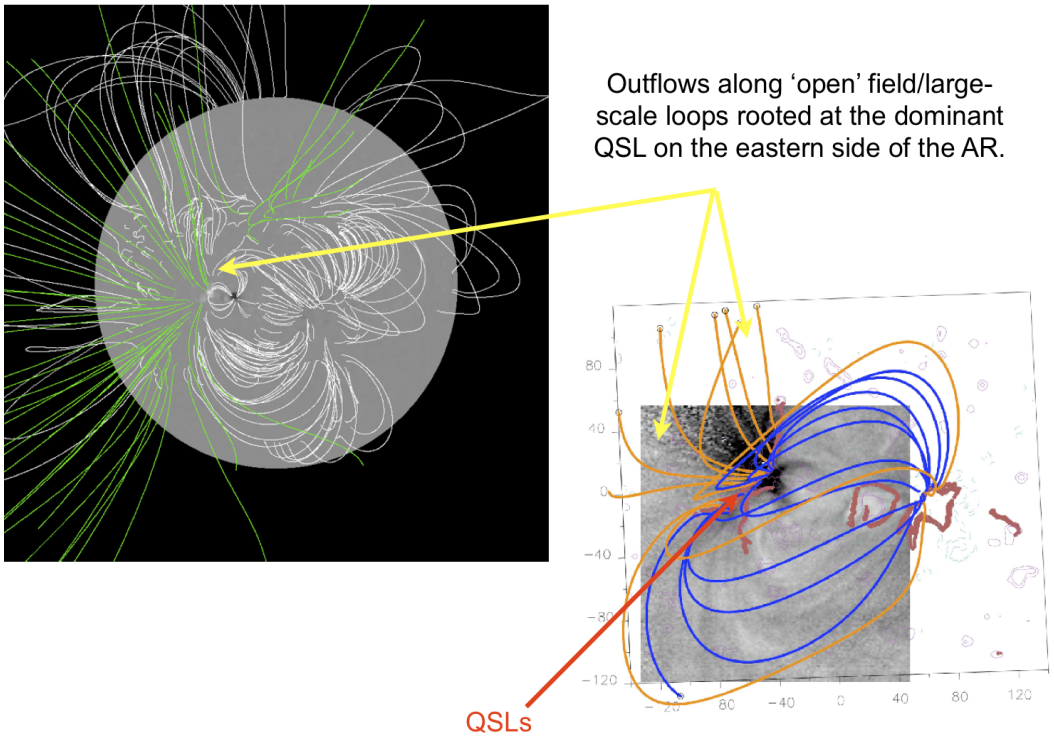

Figure 3.9: Left - PFSS model of the solar corona on 2007 February 20. Green lines are positive 'open' field extending to the source surface at 2.5 R_{sun} and white lines are closed field. The model was produced using the LMSAL PFSS package in IDL which is distributed via SolarSoft. Right - photospheric trace of QSLs (thick red lines) and field lines originating in the QSLs are overlaid on a grayscale EIS Fe XII emission line velocity map from Figure 3.4. Green 'open' field lines in the PFSS model are located in the vicinity of the strongest outflows over the dominant QSL where the orange 'open'-like field lines are rooted. 'Open' field provides the means by which AR outflows are able to access the SW.

The numerical procedure used to determine the values of Q in this work has been thoroughly discussed by Aulanier *et al.* (2005b). The magnetic field model takes observed magnetograms as the boundary condition, therefore, the presence of parasitic polarities in the configuration (e.g. see MDI magnetogram at 11:16 UT on February 20 in Figure 3.5) results in multiple QSLs. However, only those corresponding to the highest values of Q, in other words, the thinnest QSLs lying on both main positive and negative AR polarities are considered. The magnetic models together with the QSL locations are shown in the right panels of Figures 3.4 to 3.6. This is only the second time (see Masson *et al.* (2009)), that the QSLM using the definition given by Equation 3.3 has been applied to observed magnetic field data, though there are some differences in the methodology between the approach used here and that of Masson *et al.* (2009).

3.5 Results

3.5.1 Locations of Dominant QSLs

Before comparing the locations of the QSLs calculated by the QSLM with the locations of the observed AR outflows, the correctness of the extrapolations by comparison with coronal observations of AR 10942 was first considered. Figure 3.10, left panel, shows the large-scale topological structure of the AR and its surroundings based on the MDI magnetogram closest to the EIS observation time of 23:45 UT on February 20. There is a global agreement between the coronal magnetic field model with the XRT observations in Figure 3.10 and with the EIS Fe XII intensity map in Figure 3.4, left panel. Though not shown, the global structure is similar to the large-scale coronal magnetic field model calculated at the time of each EIS observation, 12 hours earlier on the east side (Figure 3.5) and 12 hours later on the west side (Figure 3.6).

Figure 3.10, right panel, shows the photospheric trace of the dominant QSLs (indicated by thick red lines) overlaying SOHO MDI magnetic field isocontours. The most extended QSL (labeled as a) is located over the following positive polarity of the AR (eastern side) where the strongest outflows are seen in the EIS observation on February 20 at 23:45 UT (Figure 3.4). A major QSL (labeled as d) is found over the leading negative polarity and is associated with outflows visible in the EIS velocity map in Figure 3.6. In the following sections, QSLs with values of $\log_{10} Q$ above ≈ 10, will be referred to as dominant QSLs.

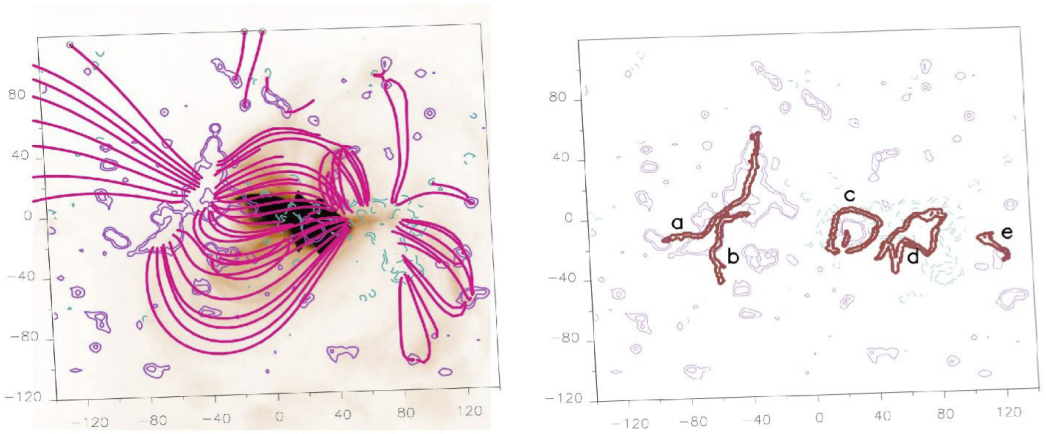

Figure 3.10: Left panel - Linear force-free magnetic field model of AR 10942 with $\alpha = 9.4{\times}10^{-3}$ Mm^{-1} over *Hinode* XRT image. There is a global agreement between the coronal magnetic field model with the XRT observations and with the EIS Fe XII intensity map in the left panel of Figure 3.4. Right panel - Photospheric trace of dominant QSLs (thick red lines) in AR 10942 with SOHO MDI magnetic field contours. The magnetogram and magnetic model correspond to Figure 1, as does the drawing convention. The photospheric traces of QSLs have been labeled as *a*, *b*, *c*, *d*, and *e*. Though the shapes of QSLs and the photospheric field distribution change, this labeling is used to refer to the equivalent QSLs at different times.

3.5.2 Stability of QSL Locations

The limited size of the computation box can influence the extrapolated field, and in particular the limit between closed and 'open' or 'box-reaching' field lines. How the locations of dominant QSLs depend on the computational box size was tested and it was found the QSL locations on the positive polarity were stable. The limit between closed and 'open' or 'box-reaching' field lines was also stable. The QSL on the negative preceding polarity somewhat decreased in extension, however, the QSL section associated with the core outflows did not change. Figure 3.11 shows a side-on view of the enlarged computational box and the resulting photospheric traces of the dominant QSLs overlaid on the same large FOV EIS velocity map from Figure 3.4. Dominant QSLs (Figure 3.11, right panel) are similar to those shown in Figure 3.10 before the computational box was enlarged.

3.5.3 Fe XII Flows

In the velocity map of the large FOV (Figure 3.4, middle panel), there is a series of loop structures connecting the positive and negative magnetic field concentrations of the AR. These loops are red-shifted, indicating downflows within the loop structures. LOS downflow velocities range from a few km s^{-1} up to a maximum of 32 km s^{-1}. The eastern and western region velocity maps shown in Figures 3.5 and 3.6, respectively, are dominated by outflows with small patches of downflows up to 14

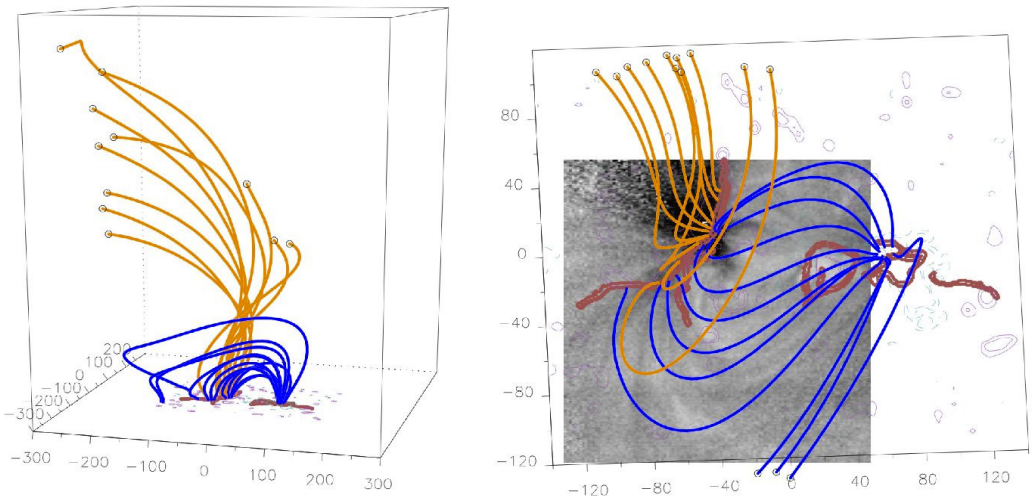

Figure 3.11: Magnetic field model and high-Q QSL locations computed using the same MDI magnetogram as a boundary condition and α as in Figure 3.4, but a larger computational box (600 Mm in both east-west and north-south directions and 700 Mm in height). Drawing conventions are similar to those used in Figures 3.4 to 3.6. Left panel - shows field lines in the full box from an arbitrary point of view. Orange and blue field lines are drawn from the newly computed QSLs in the same way as in Figure 3.4. Right panel - photospheric trace of QSLs and the same field lines as in the left panel from the observer's point of view overlaid on a grayscale EIS Fe XII emission line velocity map (c.f. Figure 3.4). The eastern dominant QSLs (labeled as a and b in Figure 3.10) are wholly stable with the enlargement of the computational box whereas the western QSL (labeled as d in Figure 3.10) shrinks slightly towards the south.

km s^{-1}.

Blue-shifted outflow regions are observed at the periphery of the AR in all velocity maps. In addition, outflows are located over the monopolar magnetic field concentrations of the AR. Outflows are strongest over each of the strongest magnetic field concentrations, especially to the east. This is shown in the middle panels of Figures 3.4 to 3.6 where MDI magnetic field isocontours of ± 50 G are overlaid on each velocity map. Maximum LOS velocity for the eastern side of the AR is -49 km s^{-1} in the raster scan at 23:45 UT on February 20. Outflows observed in the maps starting at 11:16 UT on the 20th and at 11:40 UT on the 21st have velocities of -14 and -13 km s^{-1}, respectively. These values and properties of the AR outflows are consistent with analysis carried out by previous authors studying this particular AR (Sakao *et al.*, 2007; Harra *et al.*, 2008).

3.5.4 Relationship between Fe XII Outflows and QSLs

The right panels in Figures 3.4 to 3.6 illustrate the relationship between QSLs and the blue-shifted outflows observed in EIS Fe XII velocity maps of both the eastern and western main AR polarities. Across all of these panels, the outflows consistently

occur in the vicinity of QSLs. Unlike QSLs and flare kernels, the relationship is more subtle since kernels are formed in a relatively thin layer of the atmosphere whereas outflows are observed over a broad range of coronal heights. A direct comparison for coronal flows is further complicated by the fact that the two-dimensional velocity maps result from the integrated, optically thin emission along the LOS over a large depth. Presently, it is not possible to deconvolve these two-dimensional maps in order to obtain the three-dimensional locations of the observed flows. Moreover, for an AR observed away from the solar central meridian, the LOS integration is significantly different from integration along the local vertical, thus creating projection (foreshortening) effects.

Though the precise three-dimensional structure of the velocities cannot be determined, the projection of the expected locations of the outflows with the observed velocity maps can be compared. Outflows are expected in the vicinity of QSLs where reconnection can transform closed loops into 'open' field or large-scale loops. The dense plasma of the initial closed loop is no longer confined along the reconnected magnetic field and is accelerated by a plasma pressure gradient and a magnetic tension force. Then, as in previous flare studies, both the photospheric trace of QSLs and the field lines rooted on both sides of QSLs are shown. For velocities observed in hot lines (e.g. Fe X 184.54 Å and Fe XII), it is the spatial extension of the 'open'/large-scale field lines which is the most relevant to compare with the spatial distribution of the observed outflows. Indeed, it is found that such a set of field lines greatly spreads out from the QSL photospheric trace and they fill a spatial region which is comparable to the observed outflows, as explained below.

Figure 3.4 shows the largest map obtained of this AR. Two QSLs are present on the main positive (following) polarity at this time (see Figure 3.10 for a better view of the photospheric trace of the QSLs). In the right panel of Figure 3.4, orange (blue) colored field lines have been computed with integration starting on the east (west) side of the QSL labeled as *a* in Figure 3.10. Field lines ending in a black circle have reached the computational box and are considered to be 'open' or large-scale loops. These 'open' field lines are found to overlay relatively well the observed strongly blue-shifted outflows. Since projection effects are taken into account in the magnetic model, this indicates that the strong outflows are plausibly coming from the vicinity of this QSL.

Figure 3.5 shows the magnetic field structure and outflows associated with the eastern (following) polarity of the AR, ≈ 12 hours before that shown in Figure 3.4. At that time, it is found that the shape of the photospheric trace of the QSL over the positive polarity is closed rather than the two open QSL traces found in Figure 3.4 and labeled as *a* and *b* in Figure 3.10. However, this difference is not important for

the present study since the extension of the QSL trace shown depends on the choice of the minimum value of $\log_{10} Q$, *i.e.* a QSL trace can appear to be closed or not depending on this minimum value. EIS outflows are associated with the westernmost section of the closed QSL trace from where field lines starting from both sides (Figure 3.5) have been computed. This is basically the same configuration shown in Figure 3.4. On the easternmost section of the closed QSL trace, a drastic change of connectivity is also present between 'open'/large-scale field lines and small-scale ones connecting small negative polarities on the east side of the AR. These field lines are not shown so that Figure 3.5 is not overcrowded, however, similar connectivities with a mirrored symmetry are shown in Figure 3.6 at the westernmost side of the AR.

On the western side of the AR shown in Figure 3.6 the photospheric trace of the QSL is similar to that labeled as *d* in Figure 3.10. For this observation, field lines all around the QSL are indicated using a different color for field lines computed from the eastern and western QSL sections (Figure 3.6). The western side has similar connectivities to those of the eastern side of the following polarity, *i.e.* the QSL separates short field lines (green, connecting the main polarity to network-like polarities) from 'open' ones (pink). Similarly, the blue and orange field lines are analogous to those found in Figures 3.4 and 3.5 for the following polarity. Again, the blueshifts are mainly found along 'open' field lines located in the vicinity of the QSL.

3.5.5 Relationship between Si VII Outflows and QSLs

To complement the EIS Fe XII observation in Figure 3.5, data in the cooler Si VII 275.35 Å spectral line with a S/N large enough to detect well the velocities over the AR are analyzed. This allows a closer comparison of outflows with the calculated QSLs as the emission comes from a less spatially extended region. It is possible to determine which section of the QSL is related to the strong coronal outflows. In Figure 3.12, zoomed velocity maps from two cooler emission lines, Si VII and Fe X ($\log_{10} T_{max}$ = 5.8 and 6.0, respectively), are shown with the corresponding zoomed EIS Fe XII map ($\log_{10} T_{max}$ = 6.1). All maps are overlaid with the positive polarity magnetic contours (white = 100 G and red/blue = 500 G) and the (black) photospheric trace of QSL (labeled 'a' and 'b' in Figure 3.10) at 11:16 - 11:37 UT on February 20 (c.f. Figure 3.5, right panel). Figure 3.12 provides evidence that the strongest outflows occur in the vicinity of the strongest magnetic field concentrations along the dominant QSLs with values of $\log_{10} Q$ above ≈ 10.

The EIS Si VII velocity map is also shown alone (Figure 3.12, panel A) so that

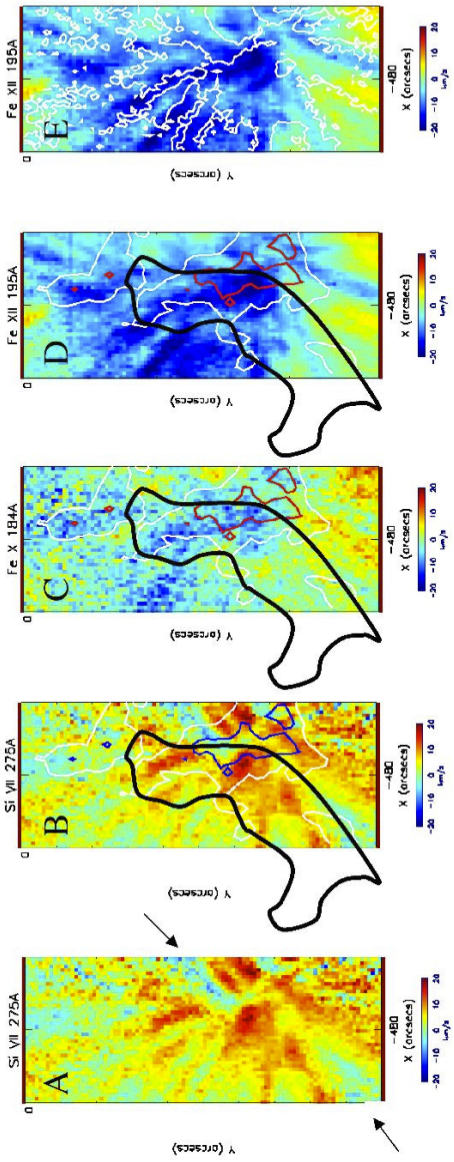

Figure 3.12: Zoomed EIS Si VII, Fe X, and Fe XII emission lines ($\log_{10} T_{max}$ = 5.8, 6.0, and 6.1, respectively) velocity maps of AR 10942 at 11:16-11:37 UT on 2007 February 20. Panel A - Si VII. Panel B - Si VII overlaid with contours of 100 G (white) and 500 G (blue) magnetic field isocontours. Panels C and D - Fe X and Fe XII, respectively, overlaid with contours of 100 G (white) and 500 G (red) magnetic field isocontours. Thick black contours are photospheric traces of the dominant QSL from Figure 3.5, right panel. Panel E - Fe XII overlaid with contours (white) of Si VII downflows (5 km s^{-1}). The strongest outflows in the hotter Fe lines occur in the vicinity of the strongest magnetic field concentrations on the western side of the QSL. Red-shifted downflows evident in Si VII appear to 'end' on the same side of the QSL. The pattern of the downflow structures in Si VII (panel E) appears to 'outline' the slightly displaced outflows in the hotter Fe lines (see panel E). The narrow outflow lanes in Si VII (indicated by black arrows in panel A) appear to be the base of outflow regions fanning out in EIS Fe X and Fe XII velocity maps (panels C and D). See §3.5.5 for a detailed discussion of this figure.

the blue outflow lanes (marked by arrows) can be better seen. These weak blue outflow regions are narrow and elongated, as would be expected if the outflows are a result of reconnection along a QSL or separatrix. Indeed, these narrow blue regions lie close to the western part of the closed QSL and appear to be the base of the extended blueshifts seen fanning out in the velocity maps of the hotter Fe X and Fe XII emission lines. There is a slight difference in position between the QSL and the northern narrow blue-shifted region observed in Si VII (Figure 3.12, panel A), though the core of the strongest outflows does lie close to the strongest magnetic field and a small section of the western QSL. Slight differences in position of the QSL are most likely due to the fact that the LFFF model includes only a global magnetic shear through a unique value of α. Typically, α is non-uniform in ARs and a significant departure from the mean value is found in vector magnetograms. Furthermore, due to unusually scarce MDI magnetic field maps coverage, the magnetic map used as a boundary condition for the modeling was taken at 08:03 UT, 3.5 hours prior to the start of the EIS scan, and magnetic evolution during this period may result in some differences between the computed QSL and observed flow locations.

The Si VII velocity map (Figure 3.12, panels A and B) is dominated by red-shifted downflows, showing strong resemblance to the pattern of upflows observed in the higher-temperature Fe lines (Figure 3.12, panels C, D), while being not exactly co-spatial with them. Stronger downflow lanes (deep red in Figure 3.12, panels A and B) are separated by weak downflow lanes (green) and by two upflows lanes (indicated by the two arrows). In Figure 3.12, (panel E), a contour (white) of Si VII downflows (= 5 km s^{-1}) is overlaid on the Fe XII velocity map (the offset between the two EIS CCDs has been taken into account). The contour is consistent with the outline pattern of the hotter upflows. The red-shifted loop-like features (Figure 3.12, panels A and B), which are visually better defined than the blue-shifted structures in the hot Fe X and XII lines, appear to converge towards the QSL, most of them ending on its western side. The pattern of the downflow structures in Si VII 'trace' the slightly displaced outflows in the hotter Fe lines. Since QSLs indicate regions where reconnection can transform closed loops into 'open' field or large-scale loops, it is suggested that the red-shifted structures in Si VII represent cooling downflows of previous outflows resulting from earlier reconnection events, and thus they provide further evidence that the outflows originate from the vicinity of QSLs and fan out with height.

3.5.6 Are outflows observed over all QSLs?

No. Outflows are *not* observed over all QSLs. This was already seen on the following polarity for the eastern part of the QSL (Figure 3.12). In order to drive outflows, a

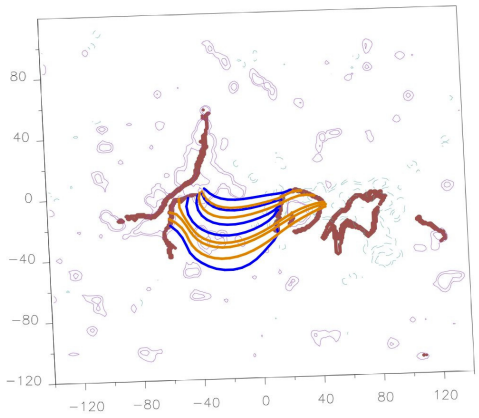

Figure 3.13: Field lines originating from internal QSLs represent low lying loops. Orange/blue field lines are drawn from the eastern/western side of the QSL trace located on the positive magnetic polarity. The magnetogram, magnetic model, and drawing convention correspond to Figure 3.4.

QSL separating 'open' or large-scale field lines from closed ones is required. But this alone is not sufficient. An evolution of the magnetic configuration is needed to first build up significant currents along the QSL and the current layer thickness must become small enough to induce magnetic reconnection. Conversely, not all QSLs can drive outflows, even with the just mentioned field evolution, since the presence of large-scale or 'open' field lines is required only on one side of the QSL. QSLs are typically present inside ARs (see the references on flares in §1) and are present in the case of AR 10942 as shown in Figure 3.13. No significant upflows are associated with this internal QSL.

Reconnection at QSLs in closed, small-scale loops can drive siphon flows by an asymmetric deposition of energy in the reconnected loops. So closed loops can have upflows dominant in one leg of the reconnected loops. However, such upflows in coronal lines are expected to be mixed up with downflows from other loops, in particular, those coming after a heating episode when coronal loops are cooling down. Since many heating processes are expected to occur in the neighboring closed loops, without any significant phase synchronisation, the downflows are likely to be mixed with upflows, so that no clear upflow pattern is observed in closed loops outside flaring times (Figures 3.4-3.6, 3.12, and references to spectroscopic studies, in particular using EIS results, §3.2.1.2).

Additionally, it is possible that flows will not be instigated along the whole length of a QSL. Work done by Demoulin *et al.* (1997) on flare ribbon-QSL association showed that the presence of a QSL is not sufficient by itself for flare activity. As previously stated in this section, the evolution of the magnetic field must be such that it builds intense current layers (e.g. via twist or shear) which become thin

enough for reconnection to take place. A strong magnetic field is also required to provide enough magnetic energy. Moreover, not all QSLs are in the appropriate state to become flare-active (e.g. thin enough to reconnect). This is also a plausible scenario in the context of QSLs and AR outflows. The energy required would be less but an evolving and strong magnetic field are likely conditions for sections of a QSL with a high Q to become flow-active. The resulting outflows are a direct consequence of the reconnection. It can be confirmed that the strongest flows occur in the vicinity of the QSL sections that overlie the strongest magnetic field (see Figure 3.12), however, due to less than ideal data coverage, the proper study of the evolution of the QSLs was not possible and, therefore, how and why certain sections of the QSLs become flow-active could not be determined with more certainty. This is the basis for future work with a wider sample set and better data coverage.

3.6 Discussion

Hinode EIS and XRT observations of AR 10942 coupled with magnetic field modeling are used to analyze and explain AR outflows. QSL locations were computed from observed magnetic data using the new definition given by Titov *et al.* (2002). The strongest outflows are associated with portions of QSLs located over regions of strong magnetic field. The area and velocity of the outflows increase with temperature. It was found that a narrow blue-shifted outflow lane is present along some QSLs in the lowest temperature Si VII EIS velocity map where the exposure time is sufficient to have a significant velocity S/N level. The outflow area is larger in hotter Fe X and even larger in Fe XII, indicating that the outflows fan out and accelerate with height (Figure 3.12). Hot outflow regions are not well defined areas, therefore, determining their origin is non-trivial. The bases of the blue-shifted outflows were further constrained by red-shifted downflows seen in the Si VII velocity map bearing strong resemblance to the pattern of upflows observed in the higher-temperature Fe lines, while being not entirely co-spatial with them. These red-shifted structures can be interpreted as cooling plasma flows along loops of previous hot upflows. Since the red-shifted loop-like features appeared to converge towards the QSL, most of them ending in its vicinity, they provided further evidence that the outflows do originate from the vicinity of QSLs and fan out with height.

The eastern outflow region of AR 10942 was 25-32 degrees in distance from the central meridian leading to projection effects especially in the higher temperature loops along which outflows are fanning out from the vicinity of the QSLs. This effect, coupled with an intrinsic optically thin spectral line formation, masks, at least in part, the spatial origin of the outflows. In particular, it is difficult to clearly

separate two intrinsically different origins such as a shell-like source around QSLs from a volume-like source such as outflows coming from the full 'open'/large-scale field region. The clearest distinction between different spatial origins, so different physical mechanisms, can be best understood from spectral lines formed at the top of the TR where there are both relatively high velocities and a vertical localization of the line formation. This requires long exposure times to have a sufficiently high S/N ratio. Such data were available only once in the studied AR, however, it was sufficient to confirm the QSL origin of outflows.

Since QSLs have distinctive characteristics in coronal images, for example clearly separating loops indicating a change in connectivity, the general validity of the relationship between QSLs and AR outflows was verified visually in EIS maps from other publications (Hara *et al.*, 2008; Marsch *et al.*, 2008; Doschek *et al.*, 2008; Murray *et al.*, 2010). Figure 3.3 (Del Zanna, 2008) shows the clearest example observed so far with multi-line EIS velocity maps of an AR observed close to Sun center so that there are practically no projection effects. The strongest blue shifts are seen along narrow lanes separating closed AR loops from large-scale loops which appear 'open' or connect to distant magnetic polarities. Outflow regions in this AR demonstrably increase in strength and breadth with temperature and height, similar to what was observed in AR 10942.

3.6.1 Looking Directly into the Source of AR Outflows

The impact of projection effects preventing an unambiguous visual interpretation of the source at QSLs of outflows at higher temperatures deserves further investigation as a number of questions remain open including: Can the spatial origin of the outflows be constrained conclusively? In order to answer this question, an AR at the solar central meridian with a wide temperature coverage and sufficiently high S/N ratio in cooler lines is required.

Figure 3.14 shows the AR that was selected. The mature, dispersed AR is located very close to the solar disk center on 2008 January 10. The EIS FOV designated by the yellow box in Figure 3.14 is 180" × 512" and does not extend to the leading negative polarity on the western side of the AR. This is not crucial to the analysis of the AR's outflows as QSLs are defined by the global properties of the magnetic field and the coronal extrapolation is calculated using a full-disk MDI magnetogram as the boundary condition.

All of the data reduction and modeling methods described in §3.3.1 and §3.4, respectively, are utilized here. Figure 3.15, left, shows the LFFF extrapolation of

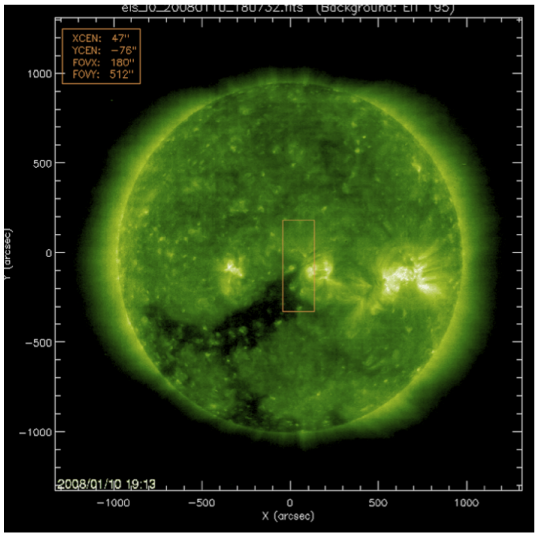

Figure 3.14: EIS FOV (yellow box) overlaid on a full-disk SOHO EIT 195 Å image. The positive polarity on the eastern side of the mature, dispersed AR is contained within EIS's FOV.

the coronal field superimposed on an Fe XII slot raster image. Good agreement between the modeled loops and the coronal observations of the AR is achieved with an α value of 3.1×10^{-3} Mm^{-1}. The low α value implies that the AR is not highly sheared. This is confirmed by inspection of images containing both polarities.

Figure 3.15, right, shows the photospheric trace of the dominant QSLs with SOHO MDI magnetic field isocontours of 50 G and 300 G. The most extended QSL is located over the positive polarity of the AR within the EIS FOV. Two other QSLs are found over the AR's negative polarity, just outside of the EIS FOV. It should be noted that the identification of dominant QSLs was more difficult in this case because the AR is more fragmented and dispersed, therefore, creating numerous small QSLs that comprise so-called background noise in the QSL plots. Only QSLs with Q exceeding a minimum threshold of 10^4 are designated as dominant QSLs.

The Fe XII intensity and velocity maps of the following positive polarity are displayed in the left and middle panels of Figure 3.16, respectively. The right panel of Figure 3.16 illustrates the relationship between the dominant QSLs and the blue-shifted outflows by overlaying photospheric traces of dominant QSLs and the field lines rooted in those QSLs over the EIS Fe XII velocity map. Drawing convention is the same as that is used for AR 10942. Here, the source of the outflows and the results for this AR are very similar to those in AR 10942. Once again, the outflows occur along field lines rooted in the dominant QSLs over the AR's positive polarity.

The PFSS model of the AR and the bordering equatorial CH is shown in Figure 3.17. It gives a plausible indication of the magnetic field configuration outside of the QSL computational box. 'Open' green field lines are located at the positive

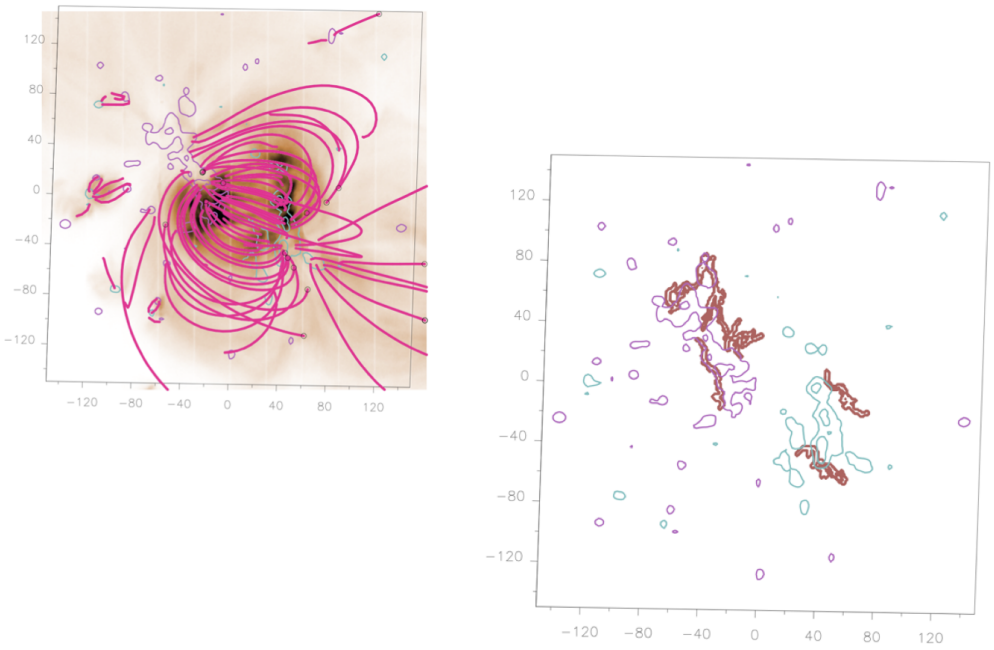

Figure 3.15: Left panel: Linear force-free magnetic field extrapolation of the AR with $\alpha = 3.1{\times}10^{-3}$ Mm^{-1} over *Hinode* EIS Fe XII slot raster image. There is global agreement between the model and the observations. Right panel: photospheric trace of dominant QSLs indicated by the thick red lines overlaid on MDI magnetogram (green/magenta is negative/positive, -50/50 G, and -300/300 G contours). The main QSL is located over the positive polarity of the AR within the EIS FOV.

polarity of the AR and in the CH to the east and appear to be spatially coincident with the orange field lines originating from the main QSL in Figure 3.16. White closed field lines connecting the AR's opposite polarities are similar to the blue field lines of the LFFF model in the right panel of Figure 3.16.

Figure 3.18 provides the connectivities of the dominant QSLs in the AR (as indicated by thick red photospheric traces of QSLs). Where field lines originating at the QSLs connect within and outside of the AR are indicated by the green/orange/blue color scheme around the red QSL traces. Field lines starting along the 'outside' of the QSLs marked by thick green lines are short loops that connect to the small dispersed magnetic fragments of surrounding network field. These field lines are not displayed in the right panel of Figure 3.16 as they are too numerous and would dominate the plot. Thick orange lines over the positive polarity show where the 'open' field or 'open'-like large-scale loops of the field lines drawn in Figure 3.16 are rooted on the 'inside' of the main QSL and connect outside of the computational box. Finally, field lines starting on the 'blue' side of the QSLs are closed within the AR and connect the AR's opposite polarities. The QSL locations and field line connectivities are important to understanding the outflows that originate in the vicinity of the QSLs and extend into the corona. The steepest connectivity gradient will be between the 'open'-like field and the field closing either in the AR or the surrounding

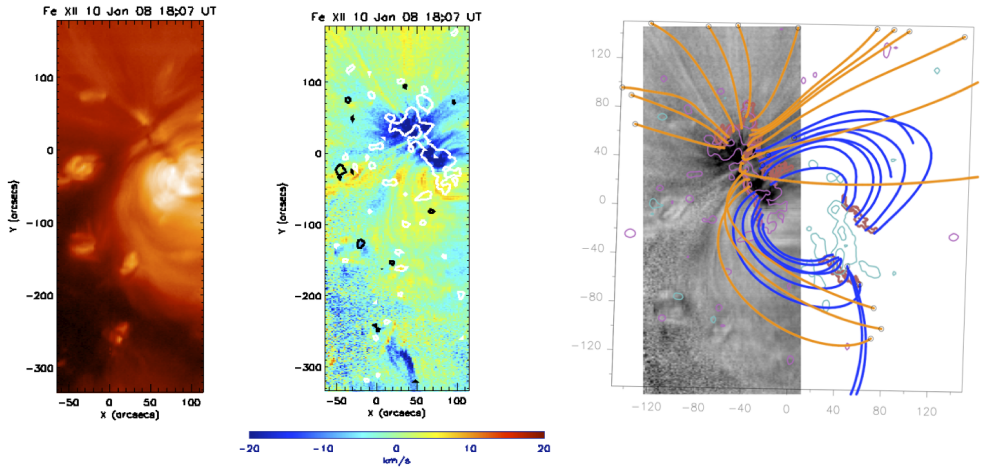

Figure 3.16: Left panel - EIS Fe XII emission line intensity map of the AR at 18:07 UT on 2008 January 10. Middle panel - EIS Fe XII emission line velocity map overlaid with ± 50 G MDI magnetic contours. White/black is positive/negative polarity. Right panel - photospheric trace of QSLs (thick red lines) and field lines originating in the QSLs are overlaid on a grayscale EIS Fe XII emission line velocity map. Orange/blue field lines are drawn from the 'inside' of the eastern QSL over the positive polarity. Lines with circles leave the computational box and are considered to be 'open' or large extended loops. The coordinate system is centered on the AR instead of the Sun and both axes have units of Mm. Magnetic field isocontours are shown in continuous pink/dashed green lines for positive/negative values of the field (± 50 G and ± 300 G). The overlay image clearly shows strong AR outflows are spatially coincident with field lines computed from 'inside' the QSL located over the positive polarity.

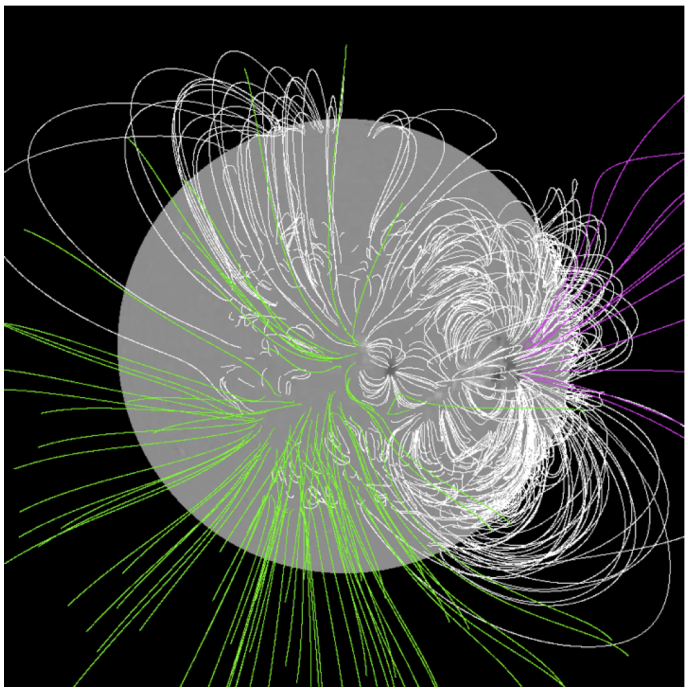

Figure 3.17: PFSS model of the solar corona on 2008 January 10. White lines are closed field and pink/green lines are negative/positive 'open' field lines which reach the source surface at 2.5 solar radii where the magnetic field is assumed to be radial. From LMSAL PFSS package in IDL.

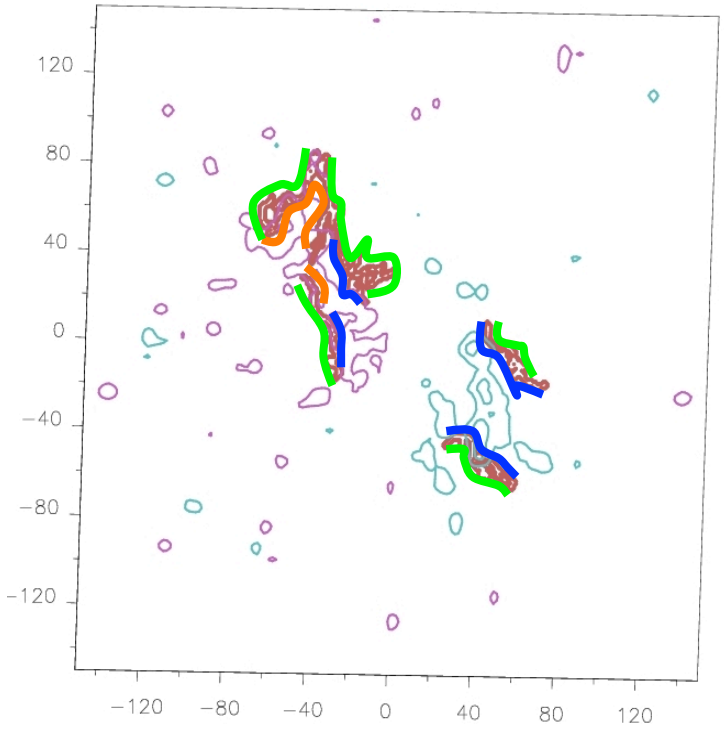

Figure 3.18: Plot from the right panel of Figure 3.15 showing the photospheric traces of QSLs (thick red lines) and the connectivities of the dominant QSLs. Orange and blue thick lines correspond to the field lines in Figure 3.16 and thick green lines indicate connectivites with the surrounding field comprised of small patches of network field. See text for discussion. Courtesy of C. Mandrini.

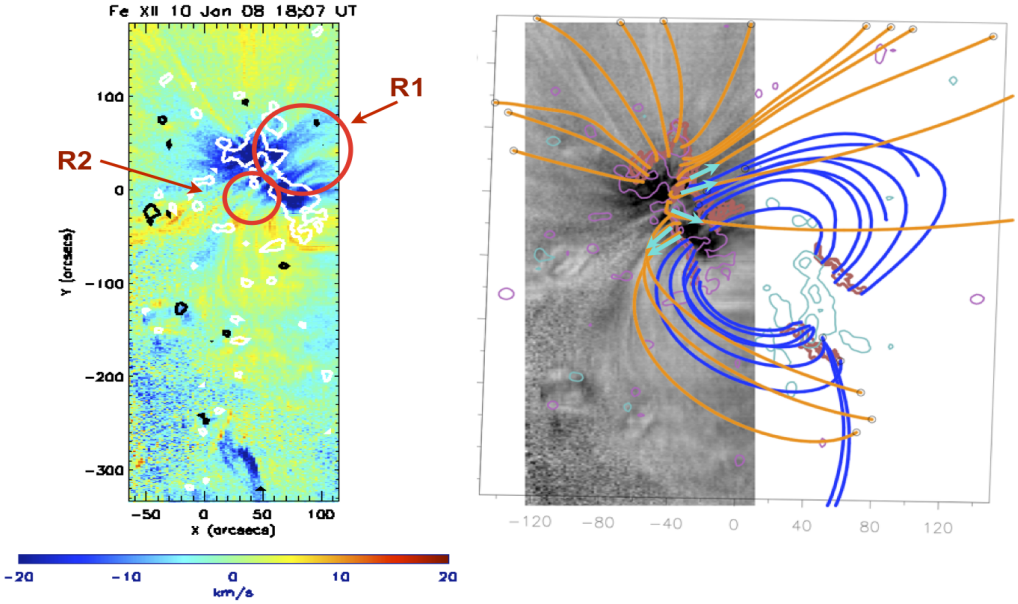

Figure 3.19: Left - EIS Fe XII emission line velocity map overlaid with ± 50 G MDI magnetic contours. White/black is positive/negative polarity. Outflow regions R1 and R2 are discussed in the text. Right - photospheric trace of QSLs (thick red lines) and field lines originating in the QSLs are overlaid on a grayscale EIS Fe XII emission line velocity map. The drawing convention is the same as that used in Figure 3.16. Light blue arrows indicate the expected direction of plasma flows as a result of QSL reconnection between AR loops (blue field lines) and 'open'-like field (orange field lines).

network field.

A detailed analysis of the outflows and their relationship to QSLs is possible in this case study because any projection effects due to the location of the AR on the solar disk have been minimized or in fact eliminated with the selection of the AR very close to disk center. Figure 3.19 focuses on the outflows viewed in the core EIS Fe XII emission line.

In Figure 3.19, right panel, the light blue arrows indicate where flows are expected as a result of QSL reconnection between the AR loops (in blue) and the very large scale loops or 'open'-like field (in orange). Outflows in region R1 (top of left panel) follow the fanning out of the 'open' field as expected when comparing the outflow pattern with the field lines. However, in region R2, outflows are weaker than in R1. This could be due to the mixing of outflows and downflows in the optically thin corona along the LOS. The top right panel of Figure 3.19 shows light blue arrows that indicate where outflows are to be expected with QSL reconnection between loops connecting the surrounding network (green connectivities in Figure 3.18) and very large-scale loops as footpoints are moving apart in Figure 3.20. Region R3 contains

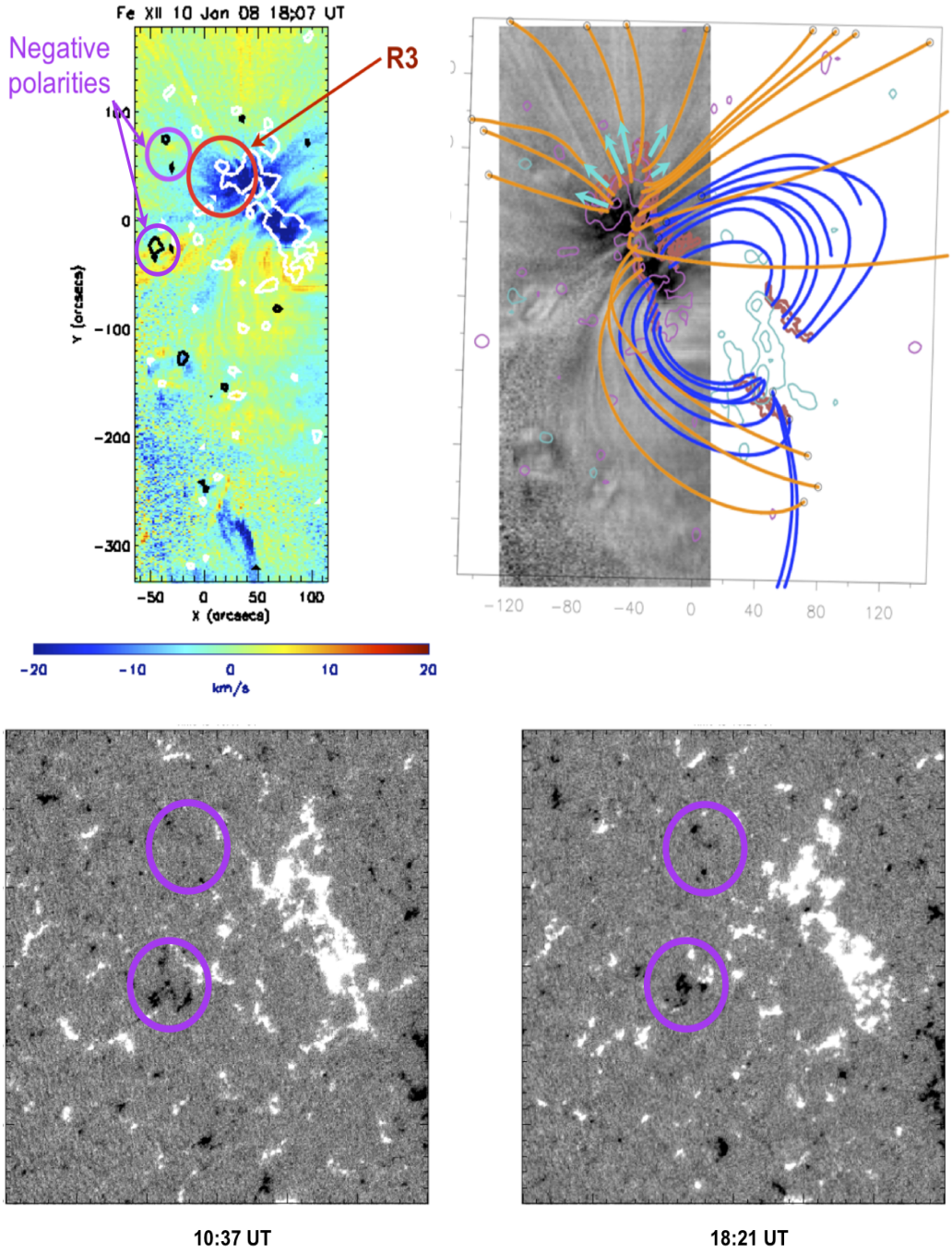

Figure 3.20: Top left - EIS Fe XII emission line velocity map overlaid with ± 50 G MDI magnetic contours. White/black is positive/negative polarity. Outflow region R3 is discussed in the text. Light blue arrows indicate the expected direction of plasma flows as a result of QSL reconnection between AR loops and the surrounding network field. Top right - photospheric trace of QSLs (thick brick red lines) and field lines originating in the QSLs are overlaid on a grayscale EIS Fe XII emission line velocity map. The drawing convention is the same as that used in Figure 3.16. Bottom panels: High resolution MDI magnetograms timed at 10:17 UT and 18:21 UT. Magenta circles correspond with negative polarity patches in the left panel of Figure 3.19. The negative polarity patches change before/after EIS velocity map timed at 18:07 UT resulting in the evolution of the dominant QSL and outflows on this side of the ARs.

strong outflows towards the northeast but not directly north as indicated by the flow arrows in the upper right panel. A possible explanation for the stronger flows towards the northeast in R3 could be the changes in the magnetic field on this side of the AR leading up to the time of the EIS observation, especially changes in the small negative polarities encircled in magenta in Figure 3.20. High resolution MDI observations show that the two small-scale negative polarity patches in the upper circles appear approximately at the time of the EIS observation. The negative polarity in the lower circles coalesce within the same time frame. Magnetic field evolution on the north-eastern side of the positive polarity changes the QSL and, thus, the flow pattern.

It was possible to partially constrain the origin of AR outflows in AR 10942. This was done by showing that the narrow lanes of outflows observed in Si VII velocity maps were aligned with the western side of the dominant QSL and by comparing the location and pattern of Si VII downflows with the Fe XII outflow pattern. Further, the Si VII downflow structure appears to converge towards the QSL. Though these arguments are strong, the origin of the outflows at the dominant QSLs can not be conclusively constrained because the inclination angle of AR 10942 to the LOS is too large to fully discount projection effects. Projection effects should be removed from the analysis of AR outflows at disk center and the origin of outflows in the vicinity of dominant QSLs can be confirmed. For the disk center AR, comparison of velocity maps of different emission lines provides reasonable evidence that this is the case. Figure 3.21 contains velocity maps for Mg V (T = $10^{5.5}$ K), Fe X (T = 10^{6} K), and Fe XII (T= $10^{6.1}$ K) overlaid with MDI magnetic field contours (white/black +50/-50 G).

Blue arrows in Figure 3.21 indicate the 'main' blueshift region which is a distinctive feature in the Mg V velocity map. This blueshift region is located in close proximity to the dominant QSLs, including separatricies, that separate 'open'-like field from AR loops where the magnetic field is strongest (c.f. Figure 3.18). Indeed, the magnetic field strength exceeds 300 G here. In the hotter Fe X and Fe XII lines, the blueshift pattern (indicated by red arrows in Figure 3.21) appears to be very different to the sheet-like region visible in the Mg V line. It is volume-like and expands with increasing temperature. A plausible interpretation for this outflow pattern is the acceleration of plasma along 'open' field as is the case in CHs. The base of the outflows is located above the 'open' part of the following polarity. At higher temperatures, the outflows extend their volume by following the fanning out of the 'open' field. In this case, the spatial extent of the outflows can be traced from their origin at QSLs in the lower solar atmosphere out through the corona.

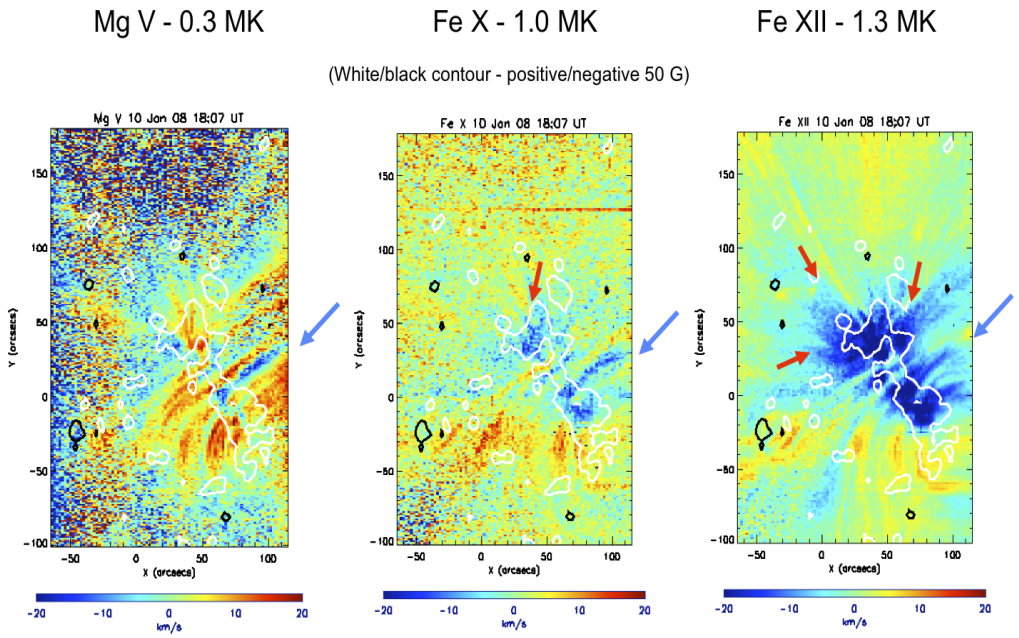

Figure 3.21: Mg V ($T = 10^{5.5}$ K), Fe X ($T = 10^{6}$ K), and Fe XII ($T = 10^{6.1}$ K) EIS velocity maps overlaid with MDI magnetic field contours (white/black +50/-50 G). Blue arrows indicate sheet-like main blueshift region at the QSLs - including separatrices separating 'open-like field from AR loops over strong magnetic field (>300 G) region. Visible in all lines. Red arrows indicate volume-like blueshift regions along open field lines found in LFFF extrapolation. The broad, extended blueshift pattern is not seen in Mg V but visible at higher temperatures as outflows follow fanning of open field rooted near QSLs over the 'open' section of the positive polarity.

3.6.1.1 Blue Wing Asymmetries in Fe XII Emission Profile of AR 10942

Line profile asymmetries have been observed in AR outflows in very specific locations at the footpoints of AR loops or the bases of AR outflow regions (Hara *et al.*, 2008; Peter, 2010; Bryans *et al.*, 2010). The presence of multiple component outflows in either of the two ARs discussed in this chapter may provide further insight into magnetic reconnection along QSLs as a driver of AR outflows. The Fe XII line profiles are modeled with a double-Gaussian fit in order to measure the secondary component velocities if multiple component outflows are present in the ARs.

The Fe XII emission line at 195.12 Å is the core line for *Hinode* EIS observations. It has high count statistics and is universally used to derive velocities and non-thermal widths from EIS observations. However, this line is blended with Fe XII at 195.18 Å (Young *et al.*, 2009), therefore care must be taken when analyzing the core EIS line. The presence of the blend can result in an increase in the observed line width and a redshift in the line center, depending on the density (Young *et al.*, 2009; Bryans *et al.*, 2010). In an analysis of this blend, Young *et al.* (2009) conclude that it is necessary to account for the Fe XII 195.18 Å when interpreting the intensity of EIS's core line at densities that exceed 10^{10} cm^{-3}. In the case of AR 10942, the maximum density was measured to be approximately $10^{9.3}$ cm^{-3} so that the Fe XII line at 195.18 Å is ignored in fitting the line profiles. See Figure 3.22 for a density map of the Fe XIII emission line for the eastern side of AR 10942 at 11:16 UT on 2007 February 20 (c.f. Figure 3.5).

The procedures described in §3.3.1 were used to perform the double-Gaussian fits. Emission from the primary component is dominant and significant contribution from the secondary component is only seen in a few small patches in the raster scan of the eastern side of AR 10942 at 11:16 UT on 20 February 2007. Figure 3.23 contains intensity and velocity maps along with profiles of primary and secondary components for a pixel located at the base of the outflows (indicated by the white cross in both maps) and Figure 3.24 shows a similar set of maps and profiles for a pixel located away from the outflows. The secondary component is visible in the blue wing of profiles from the base of the outflow region (bottom panels in Figure 3.23). Figure 3.25 shows the velocity distribution of the line core (top) and wings (bottom) within the EIS FOV. Outflow velocities in the line core are less than 22 km s^{-1} whereas the blue wing velocities exceed 90 km s^{-1}. High velocities at the base of outflow regions may be in the vicinity of QSLs with a sharp, highly localized connectivity gradient where faster reconnection outflows such as jets can occur. For example, high velocities may be the observational signature of reconnection between drastically different density loops thus creating a steep pressure gradient and accelerating the plasma. The asymmetric line profile could be comprised of flows

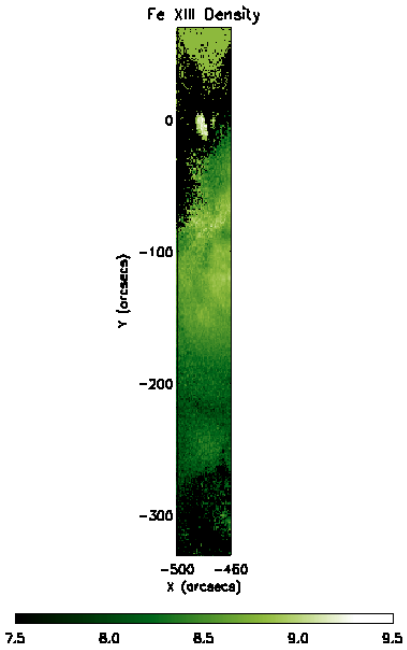

Figure 3.22: Electron density map (cm $^{-3}$ using the line ratios Fe XIII 202 and 203 Å for the eastern section of AR 10942 at 11:16 UT on 2007 February 20. Maximum measured electron density is $10^{9.5}$ cm^{-3}.

resulting from variable QSL reconnection in the optically thin corona along the LOS. Alternatively, different components of flow velocities may be observed, depending on the inclination angle of the magnetic field lines along which the plasma is confined.

3.6.2 Reconnection-related Mechanisms Driving AR Outflows at QSLs

There have been different proposals for the mechanisms driving the outflows and nearly all of them published so far fit within the QSL scenario. The major reasons why AR outflows fit well with the QSL scenario are as follows:

- QSLs (including separatrices) naturally explain the most puzzling characteristic of outflow regions which is their occurrence over monopolar areas (Doschek *et al.*, 2008). The computations show that QSL locations over the AR polarities are in good agreement with the outflow regions. By definition, QSLs divide drastically different connectivities over a magnetic polarity (see any of the papers analyzing flare observations cited in §3.2.1.2).
- The strongest outflows are seen at the periphery of ARs. As suggested by Marsch *et al.* (2004, 2008), the sharp boundaries found in Doppler velocity maps between blue and red-shifted features mark the change in magnetic

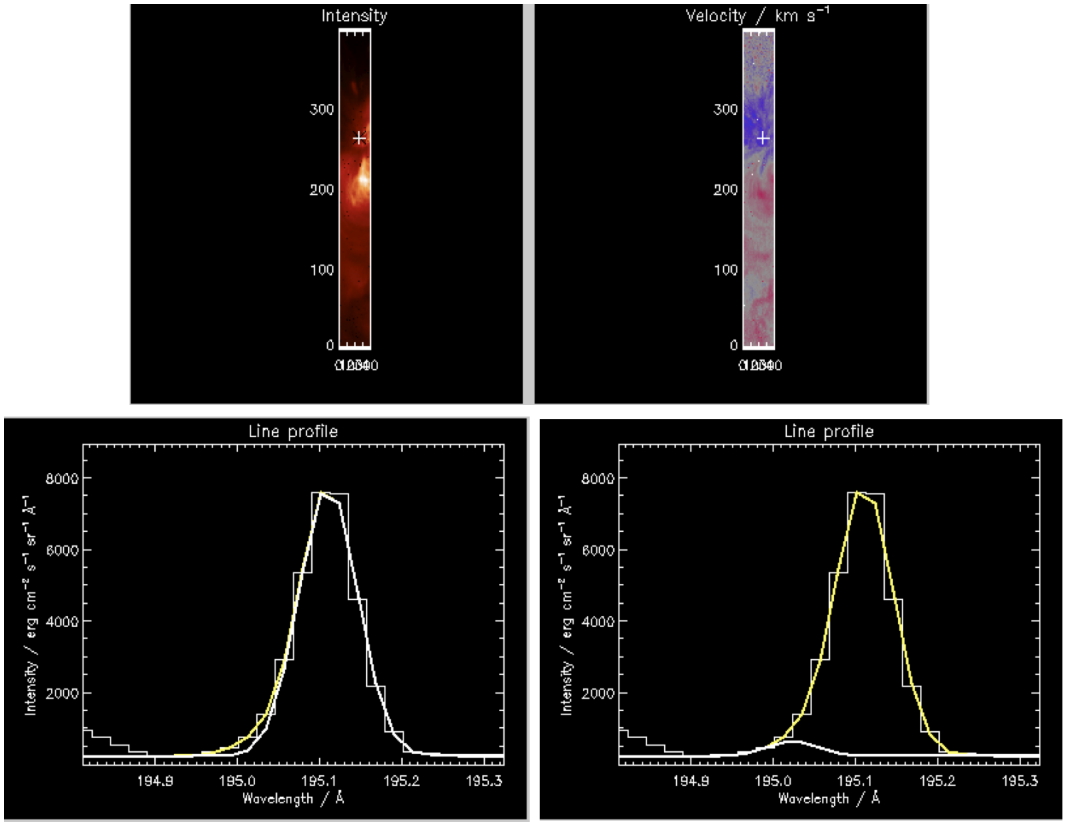

Figure 3.23: Top - EIS intensity and velocity maps for the eastern side of AR 10942 at 11:16 UT on 2007 February 20. Bottom - Line profiles for the pixel designated by the cross located at the base of the outflow region in the intensity and velocity maps. White lines show the primary (left) and secondary (right) component line profiles fitted with a double-Gaussian. The secondary component is the high velocity, blue wing component discussed in the text.

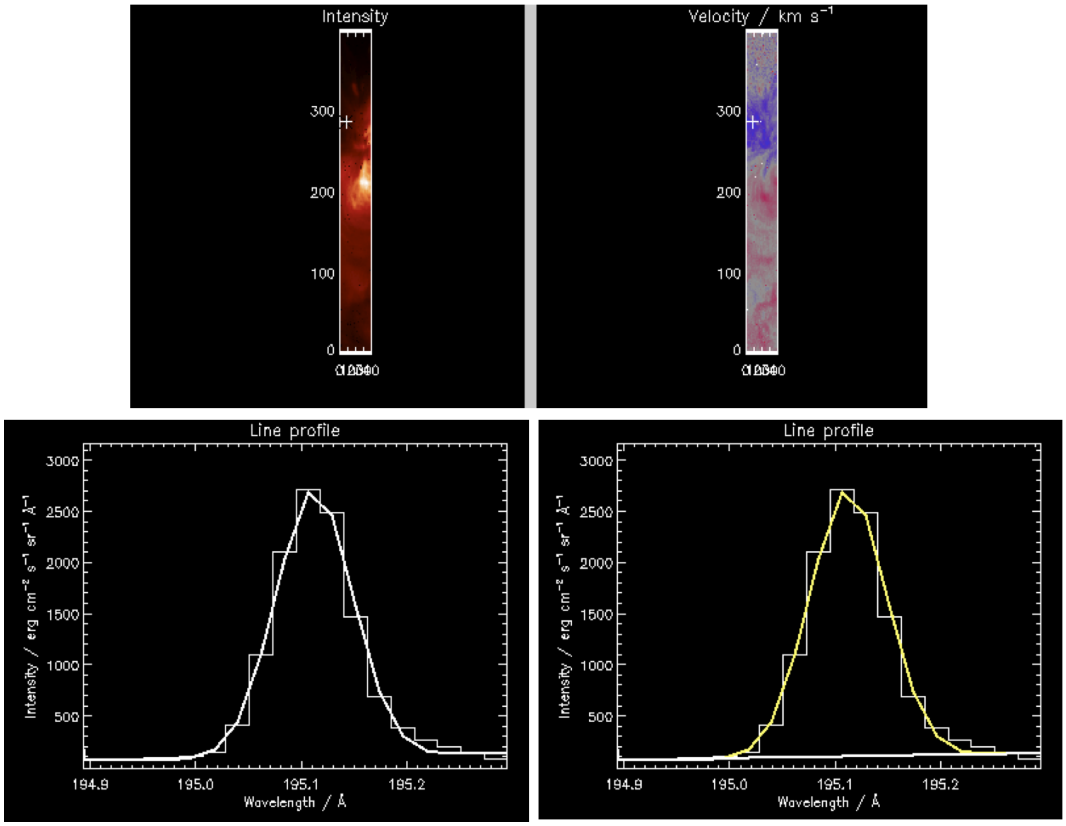

Figure 3.24: Top - EIS intensity and velocity maps for the eastern side of AR 10942 at 11:16 UT on 2007 February 20. Bottom - Line profiles for the pixel designated by the cross located in the extended section of the outflows in the intensity and velocity maps. The line profiles in the bottom panels show no secondary component in the blue wing of the Fe XII.

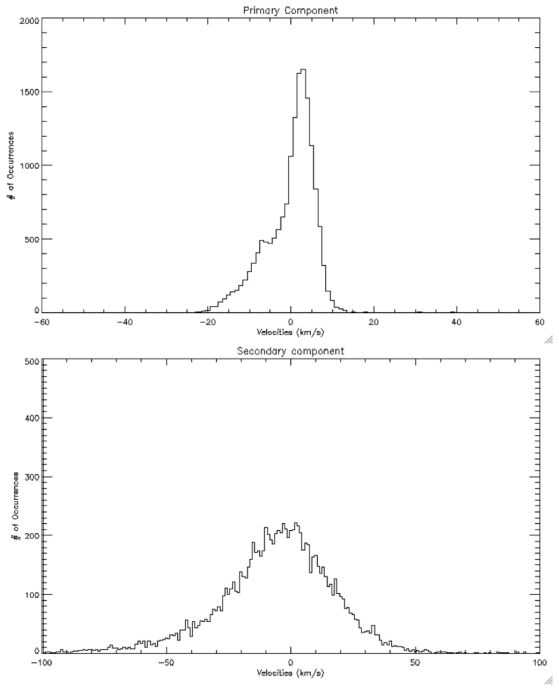

Figure 3.25: Histograms of the primary (top) and secondary (bottom) components velocities within the EIS FOV in Figures 3.21 and 3.24. Primary component velocities range from -23 to +20 km s^{-1} whereas the secondary component velocities exceed 50 km s^{-1} and exceeding over 90 km $^{-1}$.

topology from 'open' or large-scale to closed field.

- Another enigmatic characteristic of the AR outflows discovered by EIS is their longevity. Outflows persist at approximately the same locations for time scales of at least several days (Sakao *et al.*, 2007; Doschek *et al.*, 2008). The longevity of the outflows can be explained by the very nature of QSLs. They are defined by the global properties of the magnetic configuration which evolve slowly. More precisely, they are dominantly defined by the photospheric magnetic flux distribution with the exception of highly sheared configurations occurring in the core of ARs and related to large flares (see the reviews by Démoulin (2006, 2007) and references therein).

QSLs are locations where ideal MHD breaks down and reconnection takes place. This reconnection is rarely fast unless the current layer thickness is small enough and/or there is a strong driving force such as an ideal instability of the magnetic field. In three dimensions, reconnection occurs simultaneously at multiple locations along the length of a QSL involving many field lines over an extended area (Aulanier *et al.*, 2006, 2007; Parnell and Haynes, 2009), so outflows do not appear intermittent and patchy but rather smooth and extended. Of course, small-scale events with low reconnection rates are also expected to happen along QSLs, especially where they are initially broad. In these cases the accumulation of magnetic stress is needed to build a thin enough current layer to later start reconnection impulsively with a sufficiently fast rate. It is suggested that the reconnection-driven plasma flows observed on one side of a QSL are the result of the spatial and temporal superposition of nearly-continuous reconnection together with many small-scale events. These reconnections are driven by the almost permanent shuffling of footpoints.

Reconnection and consequent energy release lead to particle acceleration followed by heating of plasma. The heating of the plasma occurs through gentle chromospheric evaporation. Acceleration of particles results in enhanced non-thermal line broadening. Doschek *et al.* (2007), Del Zanna (2008), Hara *et al.* (2008) and Doschek *et al.* (2008) found a strong correlation between Doppler velocities of outflows and non-thermal velocities. Del Zanna (2008) proposed chromospheric evaporation as a possible mechanism for the origin of the AR outflows. Further, Hara *et al.* (2008) invoked 'the hot plasma upflow near the base of the corona is direct evidence for impulsive heating'. Reconnection over QSLs can naturally include these results.

There are at least five reconnection-related mechanisms that can drive AR outflows at QSLs:

1. impact of accelerated particles in denser lower layers leading to gentle chro-

mospheric evaporation;

2. pressure gradient generated after the reconnection of two loops;
3. small-scale reconnection jet-like outflows;
4. siphon flows along closed loops (see §3.5.6); and,
5. waves generated by reconnection.

None of the mechanisms currently put forward in the literature is contradictory to reconnection occurring at QSLs as proposed here, however, it is not the complete picture. An additional outflow mechanism proposed by Murray *et al.* (2010) is not based on reconnection. Continuous AR expansion compresses the neighboring magnetic field driving flows along 'open' field or long loops. These outflows appear at the boundary of ARs in the vicinity of QSLs, therefore, it is suggested that AR outflows are caused by a combination of reconnection along QSLs and AR expansion in the vicinity of QSLs. See Chapter 5 for more details on AR expansion as a driver of AR outflows.

3.7 Conclusion

Sakao *et al.* (2007) and Harra *et al.* (2008) suggested that the AR outflows are a possible source of the slow SW. Liewer *et al.* (2004) and Ko *et al.* (2006), analyzing AR sources of the slow SW using *in situ* and remote sensing data, linked the AR sources of the SW to separatrices between loops connecting two different opposite polarity regions. This is consistent with the suggestion of the relationship between QSLs and AR outflows.

In fact, QSLs are present everywhere in many magnetic structures. The values of the squashing degree Q have a wide range - as Q increases the QSL thickness decreases and reconnection becomes more prevalent. Specific characteristics of the QLSs may be linked to the magnitude of outflow velocities produced not only in ARs but also in helmet streamers around them and CH boundaries. QSLs are believed to be present in all of these structures which have been suggested as sources of the slow SW.

Chapter 4

Interchange Reconnection

In this chapter, work and results presented in each case study have been published separately. They are included here in §4.2, §4.3, and §4.4 with appropriate updates. A brief statement precedes each case study.

4.1 Abstract

IR is an important process that occurs on all scales within the heliosphere. Essentially it is an exchange of footpoints between 'open' and closed field lines which results in no net change in the total amount of 'open' and closed flux. The closed field lines are interchanged and the 'open' field lines are transported over distances comparable to the span of the reconnecting closed field lines (Crooker *et al.*, 2002). It was initially recognized (Nash *et al.*, 1988; Fisk and Schwadron, 2001; Wang and Sheeley, 2004) as a process for maintaining quasi-rigid rotation of CHs on the Sun in the face of differential rotation. More recently, IR has become a cornerstone for understanding a wide range of solar and heliospheric phenomena including but not limited to the opening of magnetic fields in ICMEs (Gosling *et al.*, 1995; Crooker *et al.*, 2002), the triggering of coronal X-ray jets (Shibata *et al.*, 1992; Wang and Sheeley, 2002), the supply of energy to and acceleration of the SW (Parker, 1991; Einaudi *et al.*, 1999; Fisk and Schwadron, 2001; Suess and Nerney, 2004), and the regulating of the interplanetary magnetic field strength (Crooker *et al.*, 2002; Owens and Crooker, 2006; Crooker and Owens, 2010). In this chapter, the coronal and heliospheric consequences of the process in three different scenarios across a range of scales are examined. In the first case study, enhancement in emission from relatively cool plasma after the main phase of X-ray jets in CHs is discussed. X-ray jets are an example of the small scale consequences of IR on the solar disk. The second case

study demonstrates how IR has significant impact on the evolution of CH boundaries when flux emerges within the vicinity of a CH. Finally, large scale heliospheric consequences of IR are tracked from the solar surface to 1 AU by combining remote and *in situ* observations of a filament eruption.

4.2 Case Study 1: Coronal X-ray Jets

The results of case study 1 were published in Culhane *et al.* (2007b) and Baker *et al.* (2008). For Culhane *et al.* (2007b), the author performed all EIS slot data preparation, reduction, and analysis including producing the multi-wave jet and bright point light curves as well as contributed towards the overall construction and direction of the paper. For Baker *et al.* (2008), the analysis is the outcome of the author's own work and L. van Driel-Gesztelyi acted in the capacity of academic supervisor. The paper has four citations to date.

4.2.1 Abstract

X-ray jets have been detected in the EUV and soft X-ray observations of *Hinode* EIS and XRT instruments. Both instruments were used to observe the jets in polar and on-disk CHs. Here, a multi-wavelength study of an X-ray jet and its associated BP found in an equatorial CH on 2007 June 19 is presented. Light curves (LCs) in 22 different emission lines were compared to that of *Hinode* XRT. As was found in a previous study of two polar X-ray jets, this jet shows a post-jet increase in its EUV LCs. The post-jet enhancement appears cooler than the jet. It is suggested this feature arises because the hot plasma of the jet, having failed to reach escape speeds, cools and falls back along the near vertical paths expected to be created by reconnection with 'open' field lines of CHs. In addition to the increase in post-jet EUV intensity, there is tentative evidence of impact heating possibly caused by the fall-back of plasma.

4.2.2 Introduction

Coronal X-ray jets were discovered by Shibata *et al.* (1992) and Strong *et al.* (1992) using *Yohkoh* SXT (Ogawara *et al.* (1991), Tsuneta *et al.* (1991)). The jets are associated with X-ray BPs and emerging flux regions (Shibata *et al.*, 1992, 1994, 1996; Shimojo *et al.*, 1998). Some jets appear to have a helical structure and others

are identified as being Hα surges (Shibata *et al.*, 1992). Based on observations of 20 jets, Shibata *et al.* (1992) suggested that X-ray jets are generated by magnetic reconnection. Shimojo *et al.* (1996) carried out a statistical study of 100 jets over a six month period. They found the following:

- Most jets are associated with small flares at their footpoints.
- Typical lengths are in the range of a few $\times$ 10^4 - 4 $\times$ 10^5 km.
- Apparent velocities are 10 - 1,000 km s^{-1} with an average velocity of about 200 km s^{-1}.
- Jet lifetimes extend up to approximately 10 hours.
- X-ray intensity distribution along a jet may exhibit an exponential decrease with distance from the footpoint.

Like Shibata *et al.* (1992), their systematic study of jet morphology was in good agreement with the magnetic reconnection model. Further, Shimojo and Shibata (2000) determined the physical parameters based on a study of 16 X-ray jets. Temperatures ranged from 3 - 8 MK and densities ranged from 0.7 - 4.0 $\times$ 10^9 cm^{-3}, both of which are similar to those of their associated BPs. Thermal energies of the jets were 10^{27} - 10^{29} ergs which is about 15% - 25% of that of the BPs. They suggested that X-ray jets are evaporation flows produced by reconnection heating.

Observations of coronal X-ray jets were limited to the EUV for a few years after the demise of *Yohkoh* in 2001. SOHO EIT, CDS, and SUMER provided detailed observations of jet-like eruptive events detected in the EUV. Harrison *et al.* (2001) discuss a complex event related to a CME. A high-temperature (1 MK) fan-like jet appears at the onset of a narrow CME. It is followed by a jet of cool ($\leq$ 0.25 MK), rotating plasma adjacent to a small, bright loop. Other EUV jets associated with the event are visible only in the cool lines of CDS. Harrison *et al.* (2001) did not find magnetic reconnection models compatible with the variety of structures in the event. Instead, they propose an Alfvèn wave model to describe all of the jet activity. Scullion *et al.* (2009) used SUMER to analyze small-scale jets in polar CHs at TR and lower corona temperatures. The multi-line observations show fast, repetitive plasma outflows with velocities of about 145 km s^{-1} in the lower atmosphere that are thought to be a precursor to macrospicule formation.

Patsourakos *et al.* (2008) analyzed a polar jet observed by both STEREO EUVI instruments. The spacecraft separation was about 11.7° so the 3D dynamics and morphology of an EUV coronal jet could be inferred. Initially the jet rises slowly at

< 20 km s^{-1} and then accelerates impulsively to velocities exceeding 300 km s^{-1}. A helical jet structure is evident from both vantage points thereby confirming the shape does not result from possible projection effects of single-viewpoint observations. A comprehensive study of 79 jet events using STEREO EUVI identified 31 jets as having a helical structure (Nisticò *et al.*, 2009). Further, Nisticò *et al.* (2010) discuss the observational features of 15 equatorial CH jets observed by STEREO EUVI and COR1 instruments. For one event, kinematics were determined in detail. The jet speed was almost 200 km s^{-1} and the downward acceleration of plasma from the emitting region was determined to be 0.11 km s^{-2} which is less than the solar gravitational force. Jet lifetimes were found to be comparable to those of polar jets. Based on their sample, Nisticò *et al.* (2010) tentatively conclude there are no substantial differences in origin or basic characteristics between polar and equatorial CH jets.

Hinode XRT and EIS are providing new insights into coronal X-ray jets. Cirtain *et al.* (2007) reported on the study of X-ray jets in polar CHs using *Hinode* XRT. Two distinct velocity classifications are observed in 100 hours - one close to the Alfvèn speed of about 800 km s^{-1} and the other near the sound speed of about 200 km s^{-1}. Jet events are far more frequent than previously thought. Cirtain *et al.* (2007) detected 10 h^{-1} instead of a few per day. Also, they frequently occur from the same BP. The jets are about 2×10^3 to 2×10^4 km wide and 1×10^5 km long and have lifetimes lasting from 100 to 2500 seconds. Savcheva *et al.* (2007) expanded the study of jets in polar CHs using 104 jet events in 44 hours of observations. Jets occurred at very high frequency of about 60 jets d^{-1}. In their sample, physical parameters show peaked distributions with maxima at 160 km s^{-1} for the outward velocity, 5×10^4 km for the height, 8×10^3 km for the width, and about 10 minutes for the duration of the jets. Raouafi *et al.* (2010) used XRT observations to study X-ray BPs in polar CHs. X-ray jets were found to have erupted in 28 of 33 events where the BP had an sigmoidal or 'S' shape. The authors of the study argue that the presence of micro-sigmoids at the base of jets can explain several of their properties including jet helical structure, transverse motions, and shapes.

Hinode EIS observations complement those of XRT. Kamio *et al.* (2007) derived the velocity structure of jets in a polar CH for the first time. Elongated jets above bright loops are blue-shifted by 30 km s^{-1} and the footpoints of the loops are red-shifted by 15 km s^{-1}. The amount of red shift decreases and crosses zero velocity near the loop top. In Kamio *et al.* (2009), SOHO SUMER and *Hinode* SOT and EIS are combined to better understand the magnetic connectivity and the formation of jets in CHs. Coronal jets are classified into two categories - persistent and transient. Persistent jets are associated with a stable BP and coronal upflows, whereas transient jets are short-lived events with upflows in the TR and corona. Footpoints of coronal

jets were correlated with vertical kG magnetic field patches in the photosphere which are 'open' field in CHs (Tsuneta *et al.*, 2008). Cool upflows ($\leq$ 0.16 MK) with velocities of 100 km s^{-1} were found in the TR but had no coronal counterpart. These flows are correlated with low-lying network fields and are interpreted to be the result of reconnection in the TR (Kamio *et al.*, 2009). Doschek *et al.* (2010) discuss temperatures and densities in BPs derived from EIS observations. They found the maximum temperature of BPs does not exceed 2 - 3 MK and below 1 MK, the BP morphology is highly complex. Electron densities were about 0.5 - 1.0 $\times$ 10^{9} cm^{-3}. Temperature and density analysis of an X-ray jet revealed that both parameters decrease with height, suggesting heat input from chromospheric evaporation characteristic of the Shimojo *et al.* (2001) jet model. Finally, a study of an AR jet by Chifor *et al.* (2008) showed a strong blue-shifted component, exceeding 150 km s^{-1}, and a weak red-shifted component at the base of the jet. Density of the high velocity upflow component was found to be greater than 10^{11} cm^{-3} and increasing with velocity. Jet emission was associated with magnetic flux cancellation.

Numerical simulations of coronal X-ray jets have been carried out for many years, first in 2D and more recently in 3D. Initially, Shibata *et al.* (1992) proposed a phenomenological model for X-ray jets in which emerging closed magnetic field reconnects with the overlying 'open' CH field. Reconnection heats the plasma to X-ray temperatures by Joule dissipation, which is the heat produced when a current is passed through an electrically resisting medium. The hot plasma is immediately transferred to both 'open' and reconnected closed field. Plasma flowing upward along the 'open' field is the X-ray jet, whereas plasma transferred downward forms a hot flare loop or the so-called BP. Yokoyama and Shibata (1995, 1996) carried out a 2D MHD numerical simulation based on the model in Shibata *et al.* (1992) and they were able to reproduce observed properties of X-ray jets including a cool jet (also referred to as an Hα surge) that forms next to the hot jet and is accelerated by magnetic tension force. However, the 2D simulation did not include the effect of conduction, therefore evaporation is omitted and observed densities could not be explained. Shimojo *et al.* (2001) conducted a 1D hydrodynamical simulation of chromospheric evaporation along the BP loop that included the effect of radiative cooling, heat conduction, and gravity. Shimojo *et al.* (2001) found that the physical parameters of the evaporation flow are similar to the observed properties of the X-ray jets, especially X-ray intensity along jets, unlike Yokoyama and Shibata (1995, 1996). They concluded that an X-ray jet is the evaporation flow produced by a flare at the footpoint of a large loop.

Miyagoshi and Yokoyama (2003) extended the work of Yokoyama and Shibata (1995, 1996) and Shimojo *et al.* (2001) by including thermal conduction and chromospheric evaporation processes in the 2D MHD magnetic reconnection simulations.

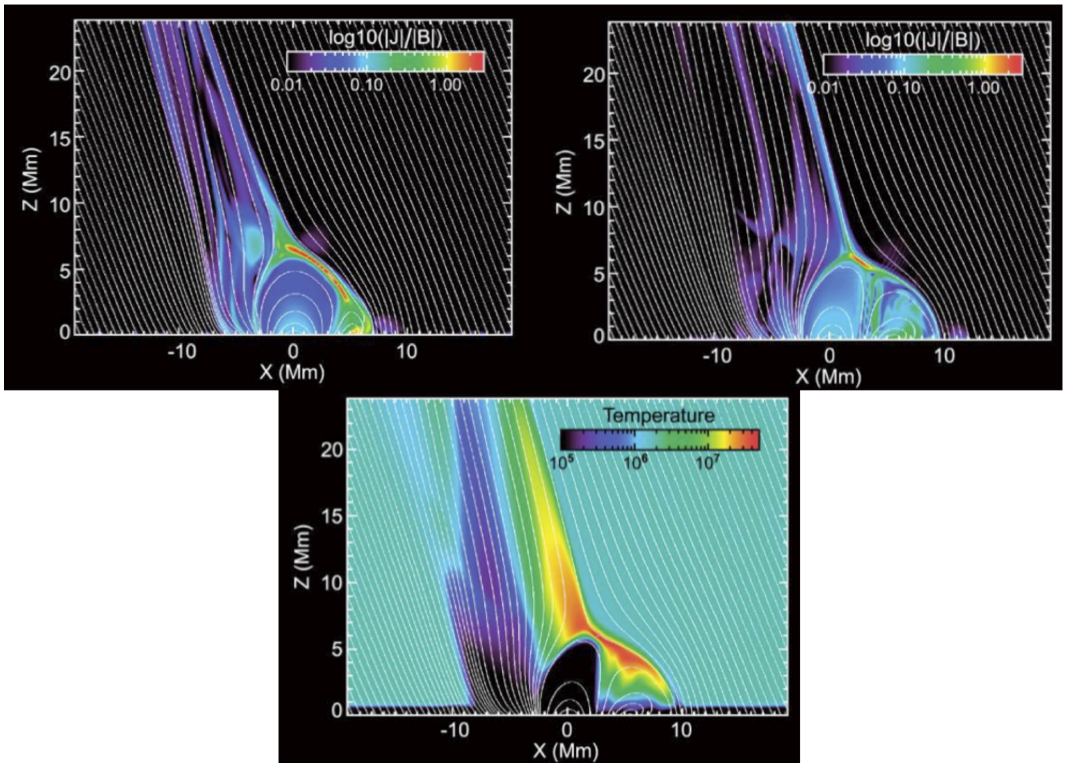

Figure 4.1: Vertical cuts of 3D MHD simulation of Moreno-Insertis *et al.* (2008). Top left panel shows velocity and field line projections at an early stage of evolution. A thin current sheet (in red) has formed above the emerged volume to the right and diffuse, elongated current perturbations corresponding to previously reconnected field lines are to the left. Top right panel shows the evolution of the configuration 7 minutes later. The relative sizes of the volumes within the double-chambered vault have changed in this time period. Bottom panel is the temperature distribution for the same time period as the plot in the top right panel. The reconnection site and jet contain the hottest plasma.

Initially magnetic flux rises as a result of magnetic buoyancy instability and evolves to form loops in the atmosphere. A current sheet forms when the loops reach the coronal field but reconnection does not take place immediately since there is dense gas carried up with the rising loops from the chromosphere and the threshold for anomalous resistivity is not satisfied. Eventually the current sheet becomes thinner and current density increases so that Petschek-type reconnection starts with a spatially localized diffusion region and high temperature plasma is produced by slow shocks (Petschek, 1964; Yokoyama and Shibata, 1994). Magnetic energy is converted to thermal energy through the shocks then heat conduction transports the thermal energy to the chromosphere along magnetic field lines. Dense gas from the chromosphere rises along the reconnected field lines and two types of jets are ejected, evaporation and low-density jets. High-density evaporation jets were successfully reproduced in the simulations.

Recently, Moreno-Insertis *et al.* (2008) developed a 3D MHD X-ray jet model of flux emergence into a CH with the density, temperature and magnetic field strength consistent with *Hinode* EIS and XRT observations. The magnetic configuration

consists of null-point and fan-separatrix topology. A twisted magnetic flux tube endowed with buoyancy in its center emerges and expands into the solar atmosphere. The pressure of the CH field opposes the expansion. At the location where the field of the rising plasma is oppositely aligned to the CH field, a current sheet forms as a thin red stripe in Figure 4.1, top left panel. Reconnection takes place across the current sheet resulting in 'open' field lines at the top edge of the current sheet and closed loops at the lower edge. Outflows ejected from the upper edge of the current sheet reach peak speeds of 400 km s^{-1} before being deflected into two secondary jets propagating in both directions along the field lines (Figure 4.1, top right). These jets are analogous to those described by the model of Yokoyama and Shibata (1995, 1996). The upward propagating jet reaches a velocity of 200 km s^{-1}. High temperatures are attained in the jet and reconnection site as is evident in the temperature distribution plot shown in the bottom panel of Figure 4.1. As reconnection proceeds, a double-chambered vault is formed, a shrinking one containing the original closed loops and another growing one containing the new set of high-temperature closed loops. In the early stages of reconnection, cool, high density plasma is loaded on the 'open' field to the left of the jet in the bottom panel of Figure 4.1. There is excellent agreement between the model results and EIS and XRT observations of an inverted Y-shaped jet in an equatorial CH.

Pariat *et al.* (2009) viewed the primary challenge for modeling X-ray jets is reproducing reconnection that occurs in a short-duration energetic burst, rather than quasi-continuously as is implied in long-lived structures such as plumes. They proposed a model where reconnection is forbidden for an axisymmetrical null-point and spine topology in order for magnetic stress to build up to high enough levels until an ideal instability breaks the symmetry and triggers a fast energy release via 3D reconnection. A significant portion of the energy liberated by reconnection is converted to non-linear torsional Alfvèn waves that compresses, heats, and accelerates the jet. The Moreno-Insertis *et al.* (2008) model showed that evaporation flows can explain many of the observed properties of X-ray jets, however, the mechanism cannot account for helical structure (Shibata *et al.*, 1992) and Alfvènic velocities of some X-ray jets. Pariat *et al.* (2009) are able to account for both jet properties though the assumption of axisymmetry is an idealized condition in the Sun.

4.2.3 Background to Post-Jet Enhancement in Cool Plasma

In a previous study of X-ray jets observed in the southern polar CH on 2007 January 20, Culhane *et al.* (2007b) found post-jet enhancement in EUV intensity in LCs of two jets shown in Figure 4.2. The 40" slot was used to obtain images in 14 emission lines for the polar jets and their associated BPs. Table 4.1 lists the EIS emission

lines used in the study with the corresponding wavelength, temperature, and other ions within the slot range. EIS and soft X-ray LCs for each jet and BP are plotted in Figures 4.3 and 4.4. X-ray LCs for both jets and BPs show impulsive behavior which then decays. EIS LCs for Jets 1 and 2 show similar behavior in hotter lines (e.g. Fe XV) and He II, whereas the LCs of cooler lines show markedly different behavior. The cooler Fe VIII, X, XI, and XII LCs rise 3 - 5 minutes after the main phase of the jets, especially in the case of Jet 2 where the post-jet enhancement is significantly pronounced. BP LCs exhibit similar impulsive behavior in a range of emission lines during the main phase but the BP of Jet 2 shows a post-jet enhancement in cooler lines which is not obvious in the LCs of Jet 1's bright point.

Culhane *et al.* (2007b) proposed a possible explanation for post-jet enhancement in cooler lines may be the falling back of hot plasma which fails to reach the Sun's escape speed. The hot, accelerated plasma leaves the contour region. Having failed to reach escape speed, the plasma then falls back some minutes later in a cooler state along the 'open' field lines of the surrounding CH. Rough estimates of the plasma apparent velocity were well below the solar escape speed of 618 km s^{-1}. Ko *et al.* (2005) found cool and hot components in a prominent jet observed on the limb by satellite and ground based instruments including SOHO CDS. The hot component was maintained for about 20 minutes and the cool components for about an hour. Ko *et al.* (2005) concluded their observations fit well the falling-back plasma scenario.

The 40" wide slot has a dispersion of about 0.023 Å per acrsec per pixel which corresponds to a total wavelength of ± 0.46 Å on either side of the nominal central wavelength of a particular emission line. Table 4.1 shows the ion blends for a number of emission lines. Due to this line blending, spectral velocities are not available when observing with the wide slot. Observation of jets in the equatorial CH using the 2" slit provides an opportunity to test the hypothesis for post-jet EUV enhancements in cooler ion lines.

4.2.4 Observations

The jet was observed in an equatorial CH on 2007 June 19 by *Hinode* EIS and XRT instruments (Culhane *et al.*, 2007b) employing the 2" slit (EIS Study #173). Data were obtained with the high data rate scanning raster consisting of 20 pointing positions with exposure time of 10 sec per postion. The study is composed of 22 emission lines from ions formed over a wide range of coronal temperatures from 0.3 MK to 12 MK in addition to lower temperature emission from He II. In this coordinated campaign, XRT high cadence observations (≈ 30 sec) employed the Ti/Poly filter. XRT's large FOV (512" × 512") provided context images for the

Table 4.1: Emission lines used in EIS jet study in Culhane *et al.* (2007b).

Ion	λ (Å)	T_e (MK)	Other ions with transitions in the 40" slot	LC color code
He II	256.32	0.079	Si X, Fe XII, Fe XIII Ni XVI, S XIII	Black - solid
Si VII	275.35	0.63	Si VII lines	Purple - solid
Si X	261.04	1.26	No other lines	Yellow - solid
Fe XII	195.12	1.26	Fe VIII, Ni XVI, Ni XV	Red - solid
Fe XIII	202.04	1.58	Ar XIII	Green - solid
Fe XIV	274.20	2.00	Si VII	Royal Blue - solid
Fe XV	284.16	2.00	Al IX	Light Blue - solid
Fe XI	188.23	1.26	Fe XI, Fe XII	Black - dotted
Ca XVII	192.82	5.01	Fe XI, O V	Black - dashed
Fe XVI	262.98	2.51	No other lines	Black - dash/dot
Fe X	184.54	1.00	Ar XI, Fe XI	Red - dashed
Fe VIII	185.21	0.40	Ni XVI	Green - dashed
Si X	258.37	1.26	Si IX	Royal Blue - dashed
Fe XIV	264.79	2.00	Fe XVI	Light Blue - dashed

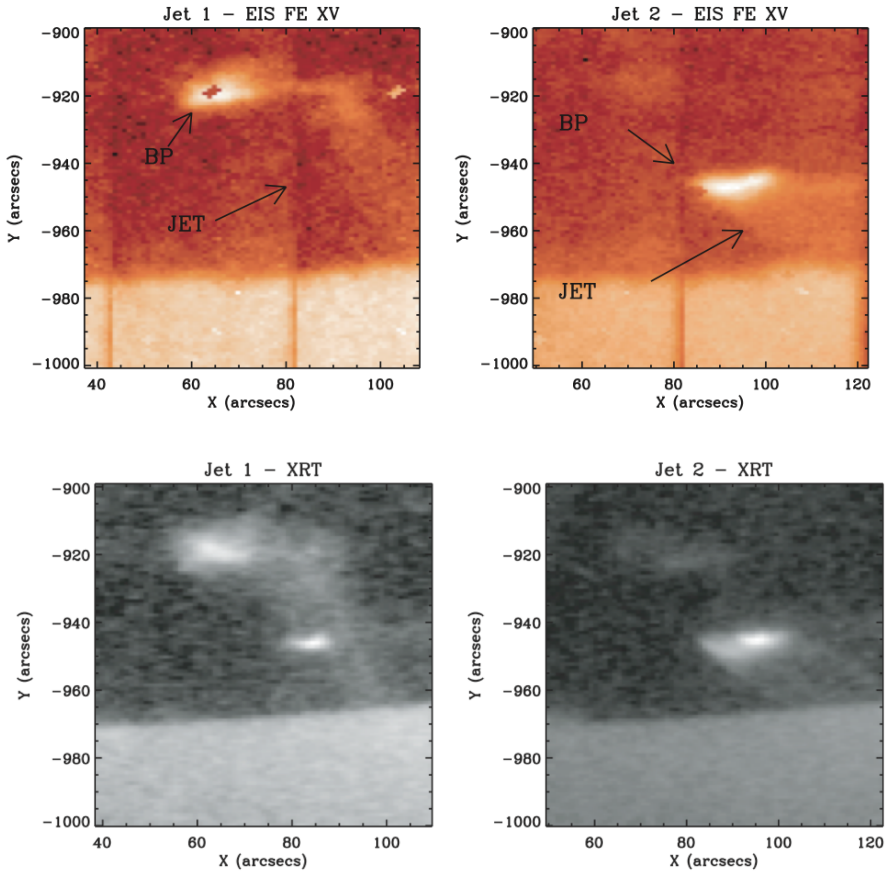

Figure 4.2: EIS Fe XV (top) and XRT soft X-ray (bottom) intensity maps for Jet 1 (left) and Jet 2 (right). Jets and BPs are indicated by arrows. From Culhane *et al.* (2007b).

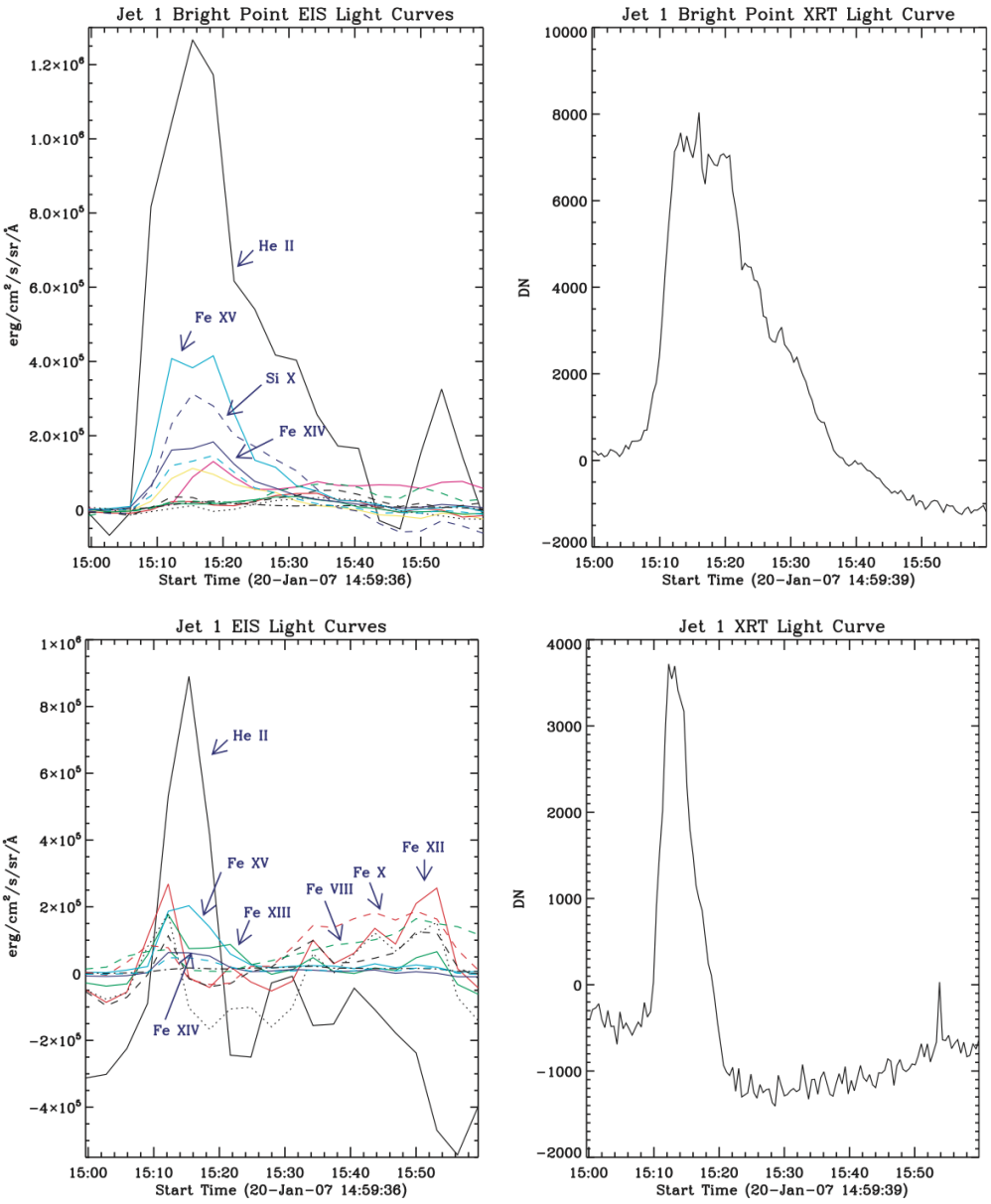

Figure 4.3: EIS multi-line (left) and XRT soft X-ray (right) LCs of Jet 2 BP (top) and Jet 2 (bottom). See Table 4.1 for details of EIS spectral lines used in the EIS plots. From Culhane *et al.* (2007b).

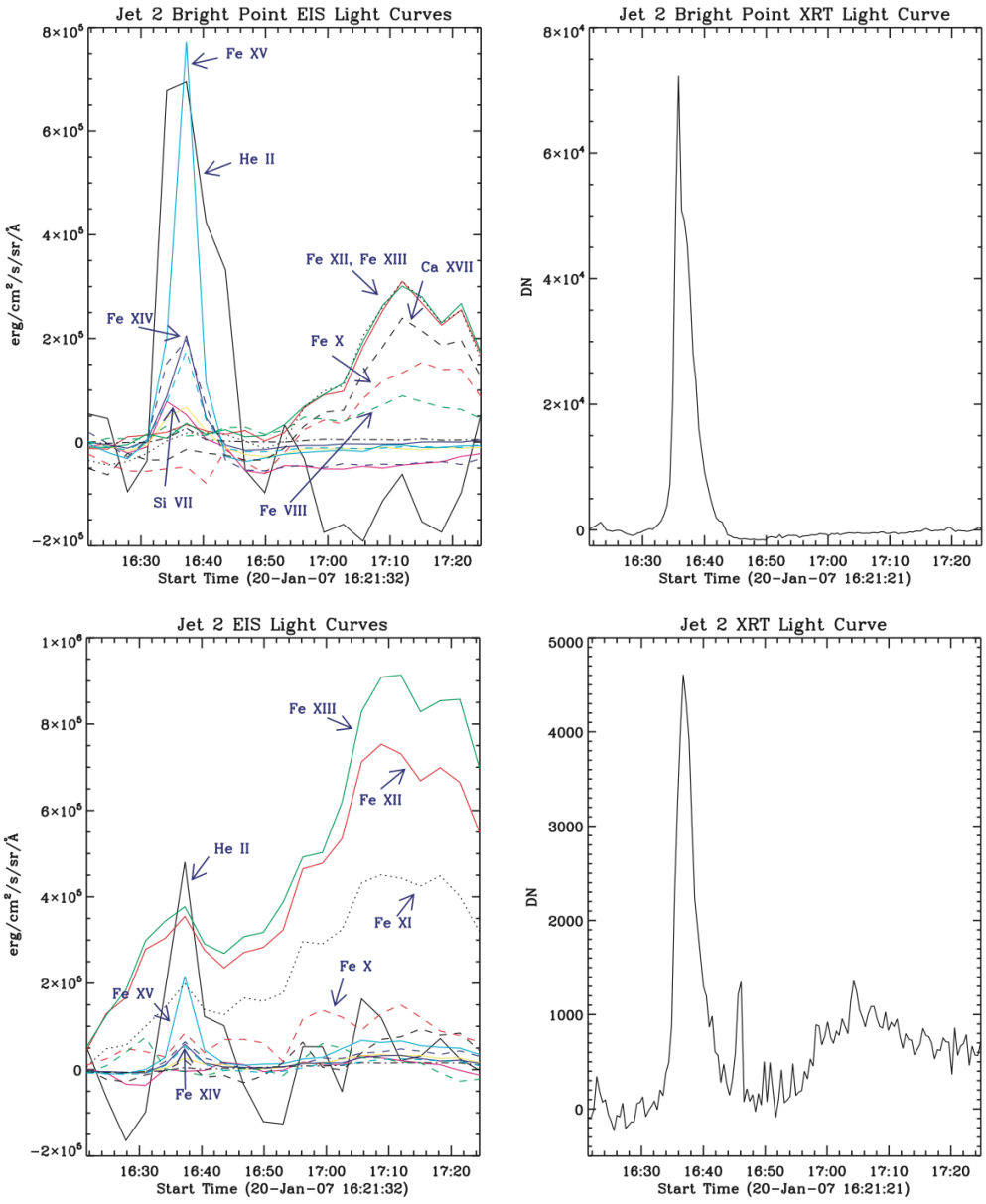

Figure 4.4: EIS multi-line (left) and XRT soft X-ray (right) LCs of Jet 1 BP (top) and Jet 1 (bottom). See Table 4.1 for details of EIS spectral lines used in the EIS plots. From Culhane *et al.* (2007b).

observing campaign.

Standard SolarSoft routines, including EIS_prep and XRT_prep, were used to create derotated map structures after correcting for instrument pointing, EIS's detector offset, and orbital variation.

LCs for each of the ions in EUV and soft X-ray images were constructed by fitting a contour around the jet and BP. Flux was summed and background subtracted within the contour region for each EIS line and XRT image over the lifetime of the jet. Ion ratios were calculated from the background adjusted flux. Jet and BP spectral velocities were obtained from EIS velocity maps.

4.2.5 Results and Discussion

EUV and soft X-ray jet and BP LCs are displayed in Figure 4.5 (top and middle panels). The jet main phase extends from 12:20 UT to 13:00 UT and peaks at 12:36 UT. Jet main phase is evident in both EUV and XRT LCs with the same start and peak times. This is also the case with the BP LCs. Simultaneous jet and BP start and peak times provide convincing evidence for the reconnection jet model (Yokoyama and Shibata, 1995).

The jet signal is characterized by hotter EUV lines such as Fe XII and Ca XVII/Fe XI, both of which form at 1.3 MK (see Culhane *et al.* (2007a) and Young *et al.* (2007) for Ca XVII/Fe XI blend discussion). Like soft X-ray, these hot ion lines rise, peak and fall back to pre-event levels during the main jet phase, whereas, cooler EUV lines fall off more gradually during the main jet phase and actually rise again to peak approximately 30 minutes after the jet. Post-jet enhancement in intensity occurs in O VI and Fe VIII ions which form at significantly lower temperatures (0.3 MK and 0.6 MK, respectively) than those of the jet.

In both soft X-ray and EUV, the BP LCs rise and fall sharply. There is no post-jet intensity enhancement in cooler lines as seen in the jet LCs. BP EUV LCs are a mixture of hotter (Ca XVII T = 5 MK) and cooler lines (O VI and Mg VII with T = 0.6 MK).

An obvious feature of the EUV LCs is that He II appears to form an event 'envelope' for the jet and BP. He II is formed at 0.05 MK within the transition region. Though the interpretation of He II is complicated by significant blending and difficulties with line formation processes (Young *et al.*, 2007), it is likely to be a transition region response to the magnetic reconnection causing the jet and BP

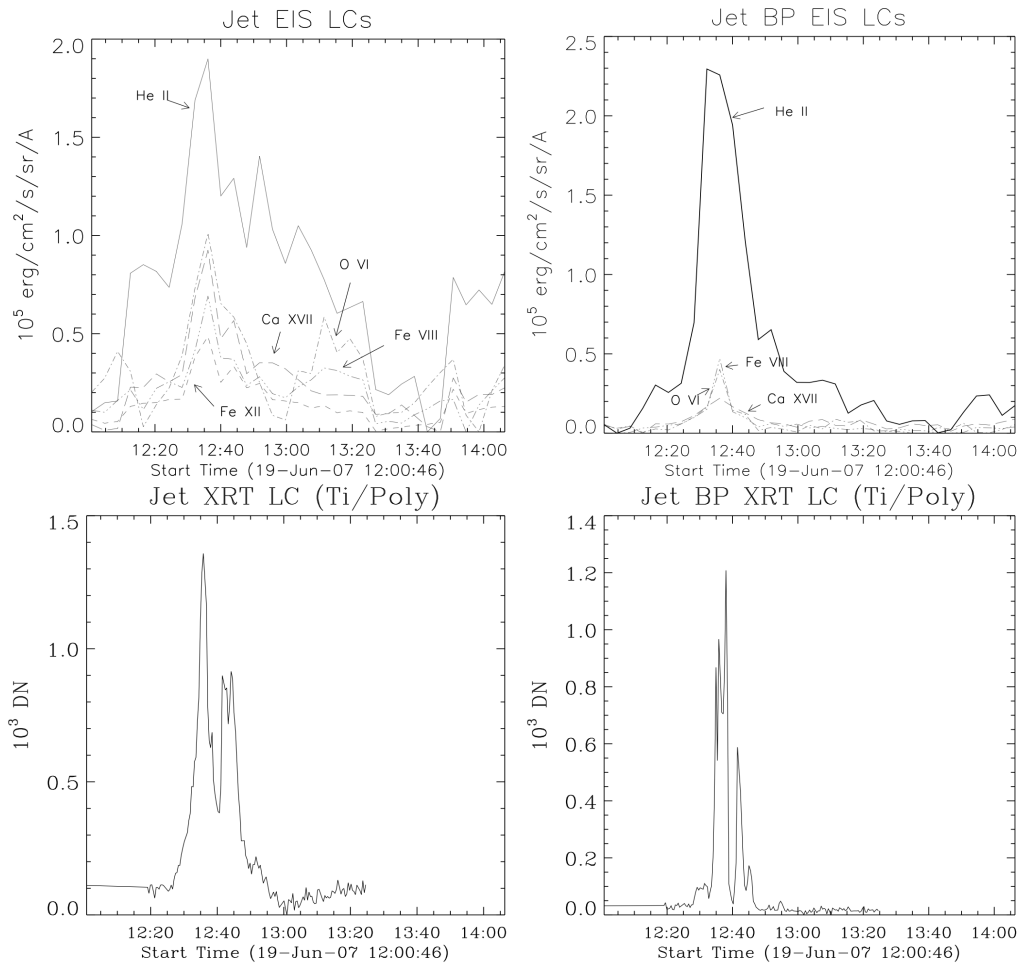

Figure 4.5: Top panel: EIS LCs showing EUV intensity evolution of jet (left) and BP (right). Temperatures: Ca XVII - 5.01 MK, Fe XII - 1.26 MK, Fe VIII - 0.63 MK, O VI - 0.32 MK, He II - 0.05 MK (Young *et al.*, 2007). Bottom panel: XRT LCs showing soft X-ray intensity evolution of jet and BP.

formation.

The jet was found to be blue-shifted by 26 km s^{-1} while the BP was red-shifted. This is consistent with the Kamio *et al.* (2007) study of the velocity structure of BPs in a north polar CH. In the previous study of polar jets, Culhane *et al.* (2007b) argued that the jet plasma, having failed to reach the solar escape velocity, cools and falls back along the near vertical magnetic field lines expected to be in a CH. The measured velocity of the jet found in the on-disk CH is well below the Sun's escape velocity of 618 km s^{-1}, which is consistent with the hypothesis. In a citation of this work, Kamio *et al.* (2009) suggested a possible explanation for the presence of cool downflows in TR lines might be the aftermath of coronal jets, in agreement with Culhane *et al.* (2007b). Again, Kamio *et al.* (2010) cites this work in interpreting the falling back of cool plasma in a macrospicule. They suggest that the delayed enhancement in cool lines, including He II, could be due to macrospicule material.

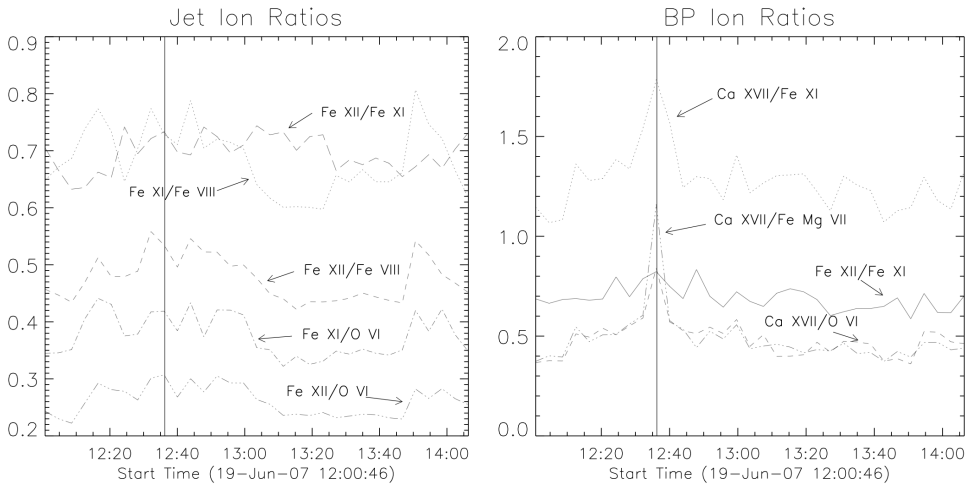

Figure 4.6: Ion ratios of jet and BP calculated from background subtracted flux. Higher temperature ion over lower temperature ion in all cases. Both plots show Fe XII, Fe XI, both of which are formed at 1.26 MK.

Ion ratios for the jet and BP are shown in Figure 4.6. In the on-disk CH, jet plasma moves approximately along the LOS, and is therefore more likely to remain within the contour. Plasma cooling is expected to be continuous and relatively smooth from the time when the jet is at its hottest i.e. at the signal peak. The plot of the jet ion ratios illustrates the expected steady cooling of the jet plasma which lasts until $\approx$ 13:20, depending on the ion. This is just after the peak of the post-jet enhancement. All jet ion ratios reverse direction at 13:45, when cooler lines return to pre-event levels and hotter lines begin to rise. One possible explanation for the rise in the ion ratios after the post-jet enhancement in cooler EUV lines could be heating due to impact of the falling back plasma (private communication with K. Shibata). Evidence of impact heating is more likely to be seen in the LCs of the on-disk jet because the plasma falls back along magnetic field lines within the contour. In a citation of this work, Scullion *et al.* (2009) compared jets observed in a polar CH with and without Ne VIII emission at 0.63 MK. They suggest that those jets which show no such emission have larger rise velocities, implying turbulent and energetic plasma, and are becoming completely ejected to form part of the fast SW. However, jets exhibiting Ne VIII emission with substantially smaller apparent rise velocity and additional line broadening are failing to escape, falling back, and becoming constituents of the corona and heating the outer atmosphere. Cranmer (2010) also cited this work when discussing whether IR is a viable driver of the SW. Plasma from jet-like eruptions plays a role in the mass supply available to accelerate the SW.

BP temperature can be inferred from looking at the Ca XVII/Fe XI ion ratio. The Ca XVII/Fe XI curve shows a distinct rise coincident with the jet signal peak which demonstrates that Ca XVII, formed at 5 MK, dominates the Fe XI blend. With the

jet, Fe XI dominates the blend because the Ca XVII/Fe XI and the Fe XII/Fe XI ion ratios are relatively flat (both ions are formed at 1.3 MK). See Figure 4.6, right panel.

4.3 Case Study 2: Coronal Hole - Active Region Interaction

The main results of this section were published in Baker *et al.* (2007). Preliminary results were presented by the author at the British-Hungarian-French N+N+N Workshop for Young Researchers in Budapest in January 2007 and at NAM in Preston in April 2007. The analysis is the outcome of the author's own work, while collaborations with co-authors are acknowledged as follows: L. van Driel-Gesztelyi acted in the capacity of academic supervisor; G. Attrill contributed with helpful discussions. The paper has ten citations to date.

4.3.1 Abstract

CHs are regions of dominantly monopolar magnetic field on the Sun where the field is considered to be 'open' towards interplanetary space. Magnetic bipoles emerging in proximity to a CH boundary naturally interact with this surrounding 'open' magnetic field. In the case of oppositely aligned polarities between the AR and the CH, IR is expected to take place, driven by the coronal expansion of the emerging bipole as well as occasional eruptive events. Using SOHO EIT (Delaboudinière *et al.*, 1995) and MDI (Scherrer *et al.*, 1995) data, observational evidence of such IR is presented by studying AR 10689 which emerged close to a CH. Closed loops forming between the AR and the CH leading to the retreat of the hole are found. At the same time, on the far side of the AR, there is dimming of the corona which is interpreted as a signature of field line 'opening' there, as a consequence of a topological displacement of the 'open' field lines of the CH.

4.3.2 Introduction

The magnetic field on the Sun's surface is inhomogeneous and complex. It is distributed in numerous structures of varying sizes and strengths. QS is found over most of the solar surface and is characterized by small scale mixed polarities. ARs

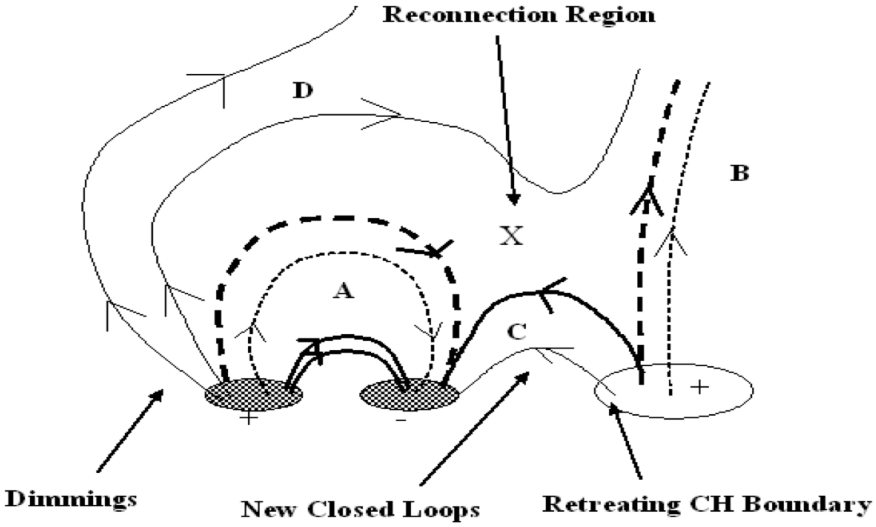

Figure 4.7: Sketch of magnetic field configuration favorable for IR. AR polarities are shown with hash regions on the left. Dashed (solid) lines represent pre (post)-reconnection configuration. AR's expanding loops marked by **A** reconnect with oppositely oriented 'open' CH field lines of **B**. New closed loops are formed at **C** and field lines are 'opened' at **D** as reconnection proceeds.

typically emerge with a bipolar structure containing roughly equal quantities of positive and negative magnetic flux. Emerging bipoles either make up a component of the QS or become ARs if they are larger than 2.5 heliographic deg^2 (Hagenaar *et al.*, 2003). Small ARs have lifetimes of days to weeks and magnetic flux of 1×10^{20} Mx to 5×10^{21} Mx. Large ARs have lifetimes of the order of a few months and magnetic flux at maximum development of $5\times\ 10^{21}$ Mx to $4\ \times\ 10^{22}$ Mx (Zwaan, 1987).

Because of the nature of bipolar ARs, loop structures of closed field lines are created. Coronal loops are filled with plasma of temperatures over 10^6 K. These loops are denser than the background corona and produce bright emission in the extreme ultraviolet and soft X-ray ranges.

Whereas ARs contain mainly closed magnetic field lines, CHs are regions of low emission dominated by 'open' magnetic field lines. Plasma travels out into interplanetary space along the 'open' field lines, therefore, CHs provide the source for high-speed particle streams or the fast SW.

The low emission of CHs is due to lower electron density and temperature, consequently, they appear darker than the QS when observed in EUV emission lines. Typically, CHs are detected in EUV Fe emission lines, soft X-ray emission, radio emission and He I and He II lines (de Toma *et al.* (2005); van Driel-Gesztelyi (2006)). However, CHs can have different extents when observed at different wavelengths (de Toma *et al.*, 2005). This poses a problem for identifying CH boundaries.

The emergence and growth of ARs force topological changes in the magnetic

field of the overlying and surrounding corona. Magnetic reconnection may occur depending on the relative orientation of the AR's field and that of the neighbouring fields. Specifically, it is expected that oppositely oriented components of closed field lines of an AR and 'open' field lines of a nearby CH can provide the magnetic field configuration required for IR (Crooker *et al.*, 2002), which displaces 'open' field lines in a step-wise manner while conserving the amount of field lines 'open' towards the interplanetary space (Fisk, 2005). IR may have important implications for the evolution of CHs as well as for the eruptive activity of ARs.

ARs have been observed expanding into the outer corona at speeds of a few 10 km s^{-1} to 100s km s^{-1} (Uchida *et al.*, 1992). Higher velocities are related to eruptive events such as CMEs. ARs within or on the boundary of CHs are expected to be more eruptive since IR naturally removes overlying field lines that stabilize potentially eruptive AR filaments/flux ropes.

If a CH exists near to an AR, then expansion of the AR can push the closed field lines against the 'open' field lines of the nearby CH. At the interface of the oppositely oriented magnetic field components, a current sheet may form leading to magnetic reconnection. Figure 4.7 illustrates the expected scenario: the expanding magnetic loops of the AR (A) reconnect at (X) with the 'open' field lines of the nearby CH (B). After reconnection, new closed loops are formed which connect the negative polarity of the AR and the positive CH field (C). Here, reconnection of successive field lines closes down the CH field making the boundary retreat as the CH shrinks. As well as creating bright closed loops, reconnection 'opens' field lines on the left of the AR (D). Plasma no longer trapped in the closed AR loops gets evacuated along the 'open' field lines into the heliosphere (Hudson *et al.*, 1996), leading to dimming of the coronal brightness.

Attrill *et al.* (2006) provided evidence for IR happening in the above scenario forced by the expansion of a CME. Evidence is sought of IR during the flux emergence phase of an AR adjacent to a CH.

4.3.3 Active Region NOAA 10689

AR 10689, located $\approx$ 200" east of an extension of the south polar CH, started to emerge at 01:35 UT on 2006 April 5 as a magnetic bipole oriented in an east-west direction. The new flux emergence occurred in the eastern hemisphere just south of the solar equator. At maximum development, magnetic flux was measured to be 2.3×10^{21} Mx. This peak flux puts AR 10689 in the 'small' AR category. The negative (leading) polarity of the AR was in close proximity to the positive polarity

of the CH, thus, AR 10689 is ideal for observing possible signatures of IR.

4.3.4 Data Analysis

This study of AR10869 uses full-disk, calibrated level 1.8 SOHO MDI (Scherrer *et al.*, 1995) magnetograms with 96 min time cadence and a pixel size of 1.98". The data were corrected for geometrical distortions using the standard `zradialize` routine in SolarSoft. MDI full-disk calibration underestimates magnetic flux density (Berger and Lites, 2003), therefore, the data were corrected for both linear and non-linear response using $\Phi_{corrected} = 1.45(\Phi + 0.3\Phi_{B>1200G})$ (Green *et al.*, 2003). Magnetic flux was obtained by fitting a contour defined by eye around the boundary of the AR, limiting the contribution of the unrelated background field. Flux was summed within this region on each magnetogram.

SOHO EIT 195Å $\approx$ 12 min cadence, full-disk images are used to analyze the evolution of AR 10689. All MDI and EIT images were derotated to the same time (12:47 UT on 2006 April 5). Base difference images where the same pre-emergence image (21:59 UT 2006 April 4) is subtracted from all images in the series were used to accentuate the evolving features of the AR. The CH boundary was defined as the intensity level half way between the intensity levels of the south polar CH and a region of QS. The boundary was overlaid on the EIT images. The data series runs from 00:11 UT on 2006 April 5 to 23:47 UT on 2006 April 7.

4.3.5 Results and Discussion

4.3.5.1 Magnetic flux evolution

Figure 4.8 shows the total flux (B $\geq$ 10 G) of AR 10689. The positive (solid line) and negative (dashed line) fluxes are imbalanced with the following polarity (positive) dominating when AR 10689 is in the eastern hemisphere. There are two sources of this imbalance. First, the QS around the AR is dominantly positive and makes up more of the total flux within the contour region during early emergence. Second, the presence of a horizontal magnetic field component gives a stronger contribution to the LOS flux of AR 10689 when it is further from the solar central meridian (Green *et al.*, 2003). The following positive polarity is located further from the central meridian thus its horizontal field component contribution is greater compared to that of the leading polarity. Imbalance of positive over negative flux decreases as the region moves closer to the central meridian.

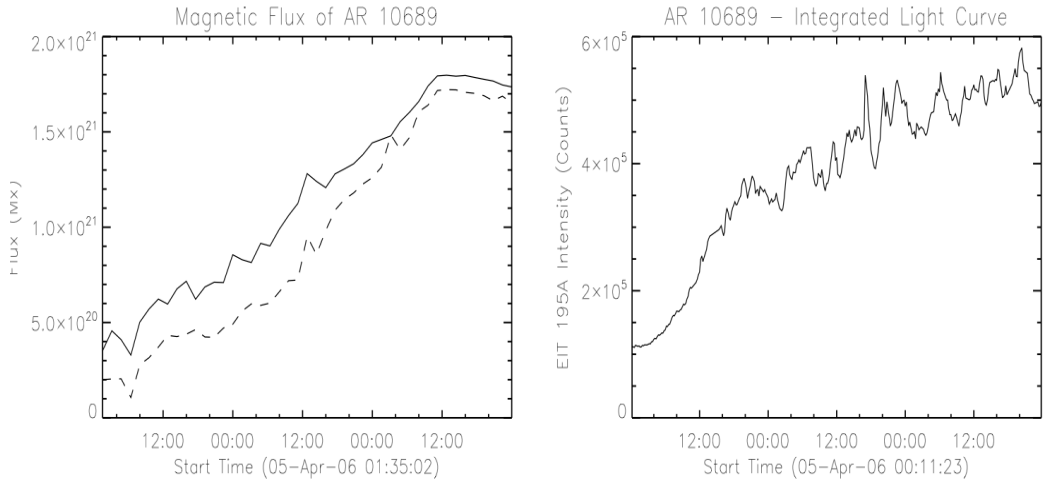

Figure 4.8: Left panel - Magnetic flux evolution of AR 10869. Positive/negative (continuous/dashed) curves are shown. Right panel - LC showing temporal variation in EUV intensity of AR 10689.

The integrated LC of the AR EUV emission at 195 Å is shown in the right panel of Figure 4.8. A comparison of the curves shown in the two panels reveals a reasonable correlation between the increases in magnetic flux and intensity as the AR expands and evolves.

The magnetic evolution over time is shown in Figure 4.9 (1st column). At first, individual bipoles appear with no definitive neutral line. As the flux tube emerges, there is a coalescence of the flux elements after a few hours which can be seen in the 1st frame of MDI images shown. Within 1 1/4 days (2nd frame), the flux elements are organized into distinct polarities with a single magnetic inversion line. As surface area increases so does the magnetic flux of both polarities. Opposite polarities have separated in the last frame. This progression of AR development is consistent with the birth and evolution of emerging regions described in van Driel-Gesztelyi (2002) and references therein.

4.3.5.2 Observed signatures of interchange reconnection

Figure 4.9, 2nd column, contains a series of EIT 195 Å images showing the expansion of the AR and its interaction with the CH. The white contour shows the CH boundary defined as the intensity level half way between the southern polar CH and QS.

Early on, the AR is small surrounded by short, bright loops extending in all directions (see 1st image). By the 2nd image, the AR is expanding and new bright loops (indicated by the white arrows) are forming towards the CH boundary. Increases

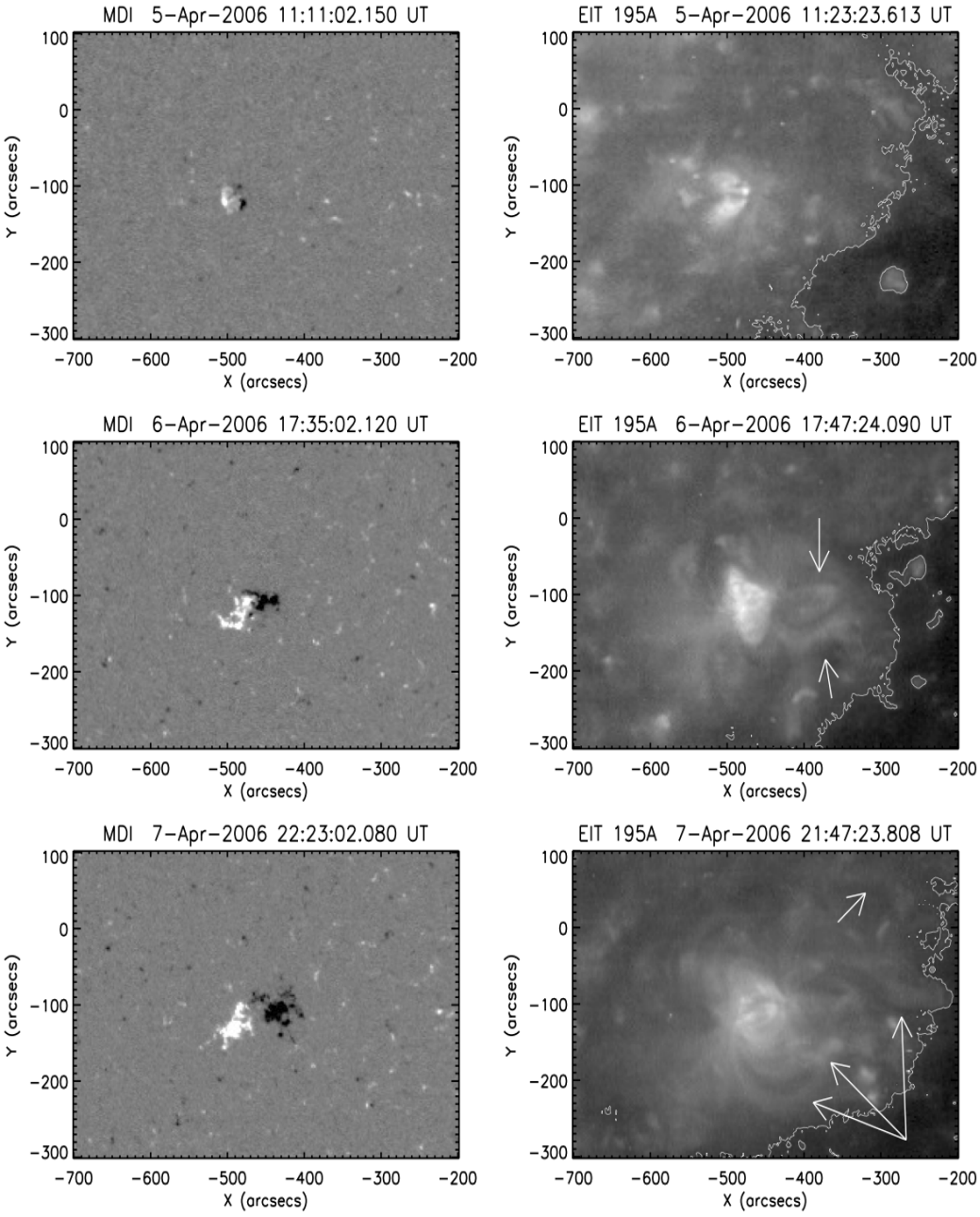

Figure 4.9: Left panel - SOHO MDI images of AR 10689's photospheric magnetic field evolution. White (black) is positive (negative) polarity. Right panel - SOHO EIT 195 Å images of AR 10689 and a nearby CH to the west (right in the images). Overlaid is the CH boundary shown in white. The boundary is defined as the intensity level half way between that of the southern polar CH and QS.

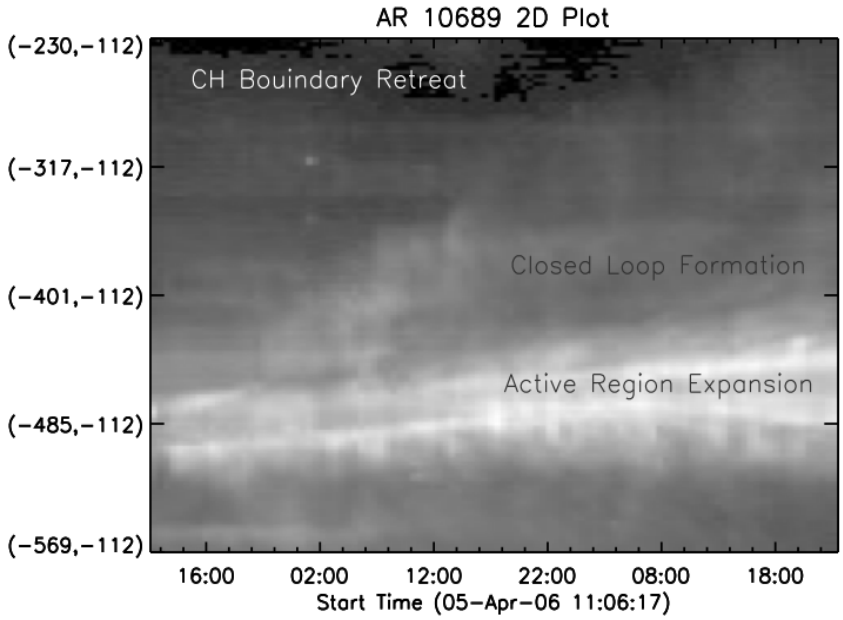

Figure 4.10: EUV intensity stack plot along an east-west cut extending from east of AR 10689 to the CH.

of magnetic flux and area can be seen in the corresponding MDI magnetogram. An extensive system of new loops can be seen towards the west and southwest in the 3rd image. By this time, virtually all of the new closed loops are in the direction of the CH instead of forming isotropically around the AR. Concurrently, the CH boundary is receding as the CH field is closed down by reconnection (see Figure 4.7). The boundary retreats ≈30" directly to the west of the AR core and ≈60" to the southwest.

These observational signatures are evident in the 2-D stack plot of intensity along an east-west slice from the far side of the AR to inside the CH (see Figure 4.10). The AR core expansion, new closed loops formation and CH boundary retreat are indicated in the figure. Yokoyama and Masuda (2010) carried out an analysis of *Yohkoh* SXT, SOHO MDI, and Kitt Peak observations that appears to be based on this work to develop their hypothesis for the formation mechanism of trans-equatorial loop systems (TLS). This work is frequently cited by them. An AR emerged on 1998 May 23 in the vicinity of the north polar CH boundary. A soft X-ray stack plot of the AR-CH region revealed the same features as the EUV stack plot in Figure 4.10. The CH boundary appeared to retreat as the AR expanded. Yokoyama and Masuda (2010) went a step further to show that the CH retreat is in fact real instead of due to projection effects. They compared Kitt Peak daily CH maps which represent the position of the low-latitude boundary of the north polar CH. The Kitt Peak maps showed that the position of the boundary shifting

northward each day. Migration of magnetic flux at the AR-CH interface was also eliminated as a cause of the observed boundary retreat. In addition to the retreating CH boundary, Yokoyama and Masuda (2010) were able to clearly show the formation of new bright loops in the soft X-ray images. Kahler and Hudson (2002) compared CH boundary structures and evolution in two cases - one when the nearby footpoints of ARs were the same polarity of the CHs and the other when the AR footpoints were opposite polarity. In the former case, the boundaries are bright and smooth, however, in the latter, the boundaries were characterized by complexity and multiple loop extensions towards the CHs. This is consistent with what is expected as a result of IR between oppositely oriented polarities.

LCs of regions around AR 10689 present further evidence of IR signatures. Figure 4.11, left panel, consists of two EIT 195 Å images overlaid with contours defining the expected eastern dimming and western new loops regions. The top image shows an early stage of evolution when the AR is relatively small. Both contour regions avoid encroaching AR core light pollution. By the time of the bottom image (2006 April 7 16:59 UT), the AR has expanded and moved into the western contour which means an integrated LC will include light from the bright core. A second western contour is chosen further away from the AR to avoid this problem. The right panel of Figure 4.11 shows integrated LCs of the contour regions. The truncated solid line is a LC of the original western contour close to the AR. The curve ends when the AR core is about to move inside the contour. The other solid line is the LC for the second western contour which avoids core light pollution at the expense of capturing early closed loop formation. Finally, the dashed line is the LC of the far side of the AR region where dimming is expected. The LC of this region is not affected by core light because the eastern boundary of the AR does not change.

The top two LCs evolve approximately parallel as the emerging bipole reconnects with pre-existing magnetic structure in the vicinity of the AR. Divergence begins at $\approx$ 0:00 UT on 6 April. The original western region LC shows a sharp increase concurrent with a dimming in the dashed curve. The LC of the second western contour region does not start to rise for another few hours because the contour excludes intensity from early loop formation. Brightness changes in the western loop formation and the eastern dimming regions continue in opposite directions throughout AR evolution.

Evidence of dimming on the far side of the AR is shown in Figure 4.12. The figure contains two base difference EIT images overlaid with magnetic field contours. Negative field concentration ($\geq$ 20 G) is indicated by black filled contours and positive field concentration is indicated by black open contours. Bright, closed loops lie almost entirely over both AR polarities prior to general dimming (left panel). By

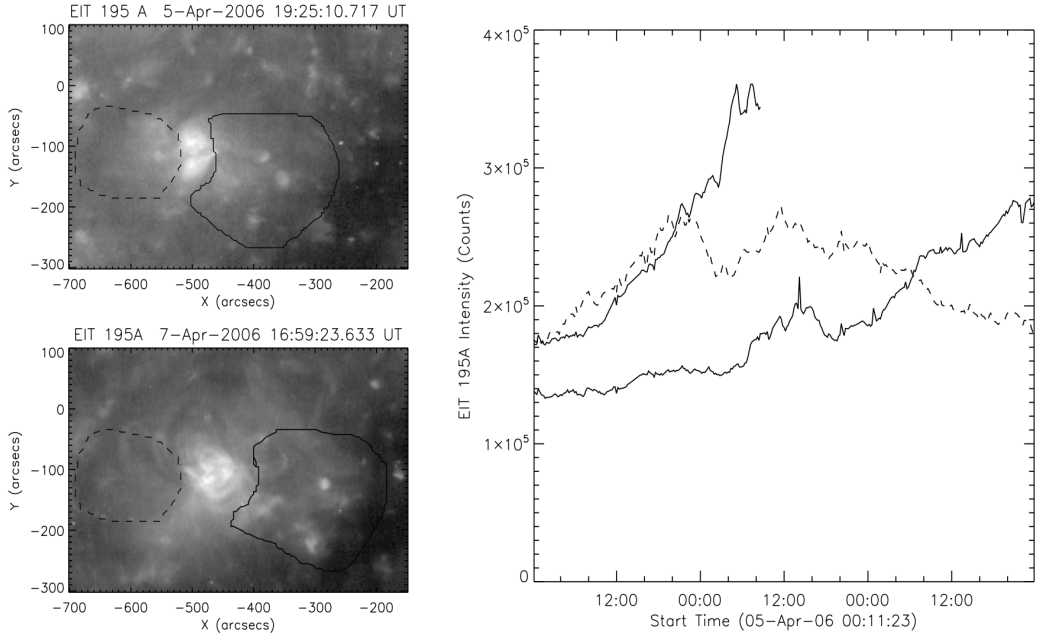

Figure 4.11: Left panel - EIT 195 Å images overlaid with selected contour regions to the east and west of AR 10689. (Top) AR is small and both contour regions avoid AR core light pollution. (Bottom) AR has expanded and moved into the original western contour. A second western contour is selected to avoid core light pollution. Right panel - Integrated LCs of dimming region to the east (dashed line), original western contour (top truncated solid line), and second western contour (bottom solid line).

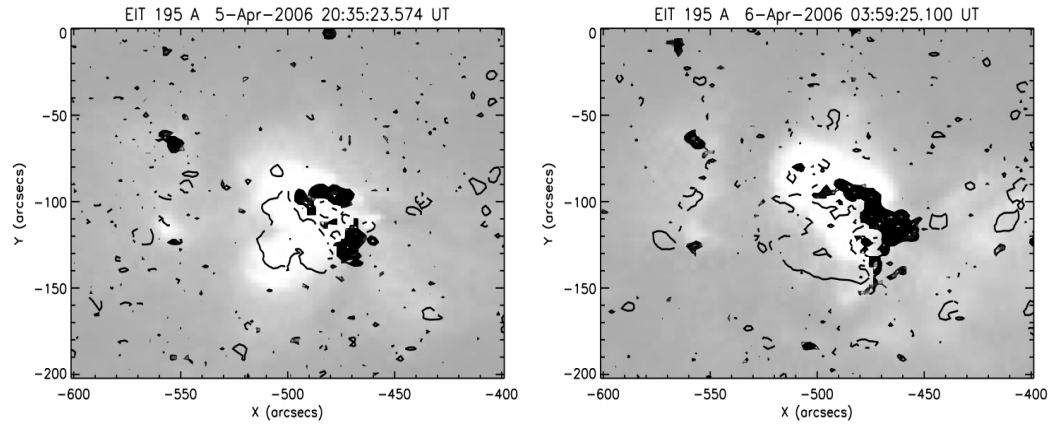

Figure 4.12: SOHO EIT 195 Å base difference images prior to and during deepest dimming (Figure 4.11) overlaid with magnetic field. Negative/positive polarity is indicated by black filled regions/open contours.

04:00 UT on 6 April, at the time of the deepest dimming, closed AR loops no longer fully cover the positive field (see the 'empty' part of the contour) to the east of the AR core (right panel). Pre-dimming EIT images show the protruding foot-points were formerly connected by bright EIT loops. Now the foot-points of the dimmed positive polarity region are end-points of newly forming loops on the west side. As the positive magnetic field in the CH is closed down, new positive field is 'opened' at the positive polarity of the AR. In addition, the dimming on the far side of the AR occurs during a period of accelerated closed loop formation (Figure 4.10), possibly caused by a mini-CME, as evidenced by the sharp rise in EUV intensity (Figure 4.11, truncated curve).

The dimming to the east and the development of the loops to the west appear to be correlated in time. This is interpreted to be coronal signatures of 'open' field lines which are created during IR between the closed field lines of the AR and the 'open' field lines of the CH. Taken together these observations provide strong evidence for the emerging AR - CH interaction predicted.

Edmondson *et al.* (2009, 2010) have conducted a series of 3D simulations to investigate the effects of IR on the dynamics and topology of CH boundaries. A small bipolar magnetic field is driven by photospheric motions and interacts with a large-scale background field. The topology is a basic spine-fan configuration. Theirs is a quasi-steady model where the coronal field is assumed to be static with a smooth structure and 'open' and closed regions remain topologically well separated (Antiochos *et al.*, 2007). The key question is whether the topology would remain smooth with well-separated regions once the field is stressed by photospheric motions and IR is initiated. Simulation results showed that reconnection occurs at the fan surface, primarily at the null and that, indeed, the magnetic topology remains smooth with well-separated 'open' and closed regions throughout the IR process. The topology is continuous therefore reconnection releases energy only after a large current sheet forms, and if the reconnection at the null is highly efficient, then the 'open' field will transfer from one side of the bipole to the other with no heating or mass acceleration. These results are not fully consistent with the interchange model of Fisk *et al.* (1999). Their model proposes a very different topology consisting of 'open' field that is mixed indiscriminately with closed field in the corona where the reconnection between 'open' and closed field is continuous. However, if enough bipoles are present then the evolution of the 'open' flux in the simulations of Edmondson *et al.* (2009, 2010) may be more like the diffusion process of Fisk *et al.* (1999).

Observationally, there are a number of key results of the Edmondson *et al.* (2009, 2010) simulations that are consistent with the AR-CH interaction described here. First and foremost, field lines are transferred from one side of the bipole to the other.

Second, as reconnection occurs, more and more flux from between the bipole and the CH boundary is removed. Third, for a large bipole, a small amount of reconnection can have a large effect on the CH boundary. Last, reconnection does not produce bursty dynamics and the energy is released primarily as mass flows. From the work done, it is not possible to comment on whether the topology remains continuous throughout the IR.

Implications for IR between an AR and CH are wide-ranging.

- Wang and Sheeley (2004) concluded that IR driven by emergence of an AR in the vicinity of 'open' field has two effects - the redistribution of pre-existing 'open' flux via footpoint exchange and a change in total 'open' flux. New 'open' flux is created if the emerging AR is sufficiently strong compared to the background field. This leads to a net increase in the Sun's dipole strength.
- AR-CH interaction may impact the SW as one source region of the slow SW is thought to be at CH boundaries and CHs are the source region of the fast SW. Habbal *et al.* (2008) used the sharp variations of Ne VIII outflows or velocity gradients to analyze the impact of ARs on CH outflows. They found when enhanced unbalanced magnetic flux from ARs extends into neighboring CHs, both outflows and their velocity gradients become significantly enhanced within the CHs and along their boundaries.
- TLS may provide clues to the solar dynamo in the restoration of poloidal fields (van Driel-Gesztelyi, 2006) as ARs are essentially toroidal and CH fields are poloidal. Yokoyama and Masuda (2009, 2010) propose that a TLS originated with large-scale magnetic fields of a CH boundary through the magnetic reconnection between an AR and CH.

4.4 Case Study 3: Interchange Reconnection from the Sun to 1 AU

The main results of this section were published in Baker *et al.* (2009a). Preliminary results were presented by the author at NAM in Hertfordshire in April 2009. The analysis is the outcome of the author's own work, while collaborations with co-authors are acknowledged as follows: L. van Driel-Gesztelyi acted in the capacity of academic supervisor; A. Rouillard provided STEREO HI data (e.g. J-maps) and *in situ* data from STEREO and ACE; P. Démoulin provided the velocity profile in §4.4.5.2. A. Rouillard and P. Démoulin contributed with extremely helpful discussions. The paper has two citations to date.

4.4.1 Abstract

Combining STEREO, ACE, and *Hinode* observations has presented an opportunity to follow a filament eruption and CME on the 17th of October 2007 from an AR inside a CH into the heliosphere. This particular combination of 'open' and closed magnetic topologies provides an ideal scenario for IR to take place. With *Hinode* and STEREO data, the emergence time and type of structure seen in the *in situ* data four days later are identified. On the 21st, ACE observed *in situ* the passage of an ICME with 'open' magnetic topology. The magnetic field configuration of the source, a mature AR located inside an equatorial CH, has important implications for the solar and interplanetary signatures of the eruption. The formation of an 'anemone' structure of the erupting AR and the passage *in situ* of the ICME being disconnected at one leg, as manifested by uni-directional suprathermal electron flux in the ICME, is interpreted to be a direct result of IR between closed loops of the CME originating from the AR and 'open' field lines of the surrounding CH.

4.4.2 Introduction

IR was defined by Crooker *et al.* (2002) to be reconnection between closed and 'open' magnetic field lines. During the process, closed field lines are 'interchanged' and 'open' field lines are transported, or 'jump' distances determined by the length of the reconnecting closed field lines. Gosling *et al.* (1995) and Crooker *et al.* (2002) proposed that the closed field lines in CMEs are 'opened' or disconnected from their solar footpoints by IR. This occurs where 'open' field lines reconnect with one 'leg' of an ICME that is expanding into interplanetary space. In this scenario, a large CME loop is 'opened' leaving a small reconnected loop on the solar surface. Crooker *et al.* (2002) recognized that through IR, the total magnetic flux balance in the heliosphere is maintained as CMEs become magnetically 'open', thus avoiding the 'magnetic field magnitude catastrophe' (Gosling, 1975).

IR may take place in any number of solar, magnetospheric, and heliospheric contexts where 'open' and closed field lines exist in close proximity, e.g. at CH boundaries (Wang and Sheeley, 1993; Fisk *et al.*, 1999; Wang and Sheeley, 2004), between emerging flux and a nearby CH (Baker *et al.*, 2007), an expanding CME structure and a nearby CH (Attrill *et al.*, 2006; Crooker and Webb, 2006; Harra *et al.*, 2007), in the legs of CMEs (Crooker *et al.*, 2002; Owens *et al.*, 2007), and in polar caps (Watanabe and Sofko, 2009).

Consider a scenario where an AR has emerged in an equatorial CH. The magnetic field configuration of the event has important implications for the eruption observed

both on the Sun and in interplanetary space. IR naturally may occur on the side of the AR where the magnetic field is oppositely aligned to the surrounding CH field. Whatever the polarity of the CH, having an embedded bipole will always produce antiparallel magnetic orientation on one side of the bipole. Expansion (e.g. driven by flux emergence and/or eruptions) of the closed field lines/loops will induce reconnection, leading to the formation of a 'sea anemone' structure (Shibata *et al.*, 1994; Asai *et al.*, 2008). The anemone is characterized by loops that connect the AR's positive polarity (in this case) and the opposite negative polarity of the surrounding unipolar CH (see Asai *et al.* (2008) Figure 4 for a cartoon of an anemone AR from the side and top views). As the AR reconnects with the CH field, the location of 'open' field is interchanged between the CH and the AR footpoints. The consequences of IR include X-ray jets and Hα surges (Yokoyama and Shibata, 1994). When a CME erupts from the AR, IR leads to disconnection of the expanding CME at one of its footpoints. The newly 'opened' field line(s) are highly curved, or 'refolded' on themselves (see Figure 1b in Crooker *et al.* (2002) and Figure 3 in Démoulin *et al.* (2007)).

One of the key questions in Sun-Earth Connection science is: How do the properties of interplanetary structures relate to their origins on the Sun? The isolation of the AR in the CH in a very quiet period of solar activity provided an opportunity to make clear associations between solar and interplanetary signatures of IR. There have been only a few cases when interplanetary signatures of IR have been definitively linked to their solar origins, most of which were done in similarly quiet solar periods (Attrill *et al.*, 2006; Crooker and Webb, 2006; Harra *et al.*, 2007; Rouillard *et al.*, 2009b). In this section, the coronal observations of the AR that emerged in a CH and the on-disk observations of an eruption originating from the AR are examined in detail and the propagation of the eruption is followed to 1 AU using 3 spacecraft. It is proposed that the magnetic configuration of the AR in a CH is the most suitable environment for IR to take place and as a result, one 'leg' of the ICME which erupts is disconnected.

The section is organized as follows: In §4.4.3, the remote sensing and *in situ* instruments used in the study are described. Data reduction techniques are briefly mentioned. In §4.4.4, a detailed analysis of solar and *in situ* observations of an eruption that occurred on 2007 October 17 is presented. Days prior to the eruption, it is shown that transients were released intermittently from this same AR. In §4.4.5, the solar and interplanetary evidence for IR is discussed. Finally, conclusions are presented in §4.4.6.

4.4.3 Instrumentation and Data Reduction

STEREO (Kaiser *et al.*, 2008) consists of twin spacecraft, one trails the Earth (referred to as STEREO-B) while the other leads (referred to as STEREO-A). Each STEREO spacecraft is equipped with remote sensing and *in situ* particles and field instruments for the main purpose of understanding CME initiation processes on the solar disk and to follow the propagation of CMEs into the heliosphere. The spacecraft, launched on 2006 October 26, orbit the Sun in the ecliptic plane at a heliocentric distance close to 1 Astromomical Unit (AU). The angle of separation between each spacecraft and the Earth increases by 22.5° per year (Kaiser *et al.*, 2008). Each spacecraft carries a suite of imagers - the Sun-Earth Connection Coronal and Heliospheric Investigation (SECCHI) package (Howard *et al.*, 2008). SECCHI consists of an extreme ultraviolet imager (EUVI), two coronagraphs (COR-1 and COR-2), and the Heliospheric Imager (HI). The EUVI observes the chromosphere and low corona in EUV emission lines at 171, 195, 284, and 304 Å. The HI instrument on each STEREO spacecraft comprises two wide-field, visible-light imagers, HI-1 and HI-2 (Harrison *et al.*, 2008; Eyles *et al.*, 2009; Brown *et al.*, 2009). The HI detectors are CCDs with 2048×2048 pixels and nominal cadence of 40 min for HI-1 and two hours for HI-2. 1024×1024 pixel synoptic science images are routinely downloaded. HI-1 has a 20° square FOV, centered at 14° elongation. The 70°×70° FOV of the outermost HI-2 camera is centered at 53.7° elongation. Note that the elongation of a target is defined as the angle between the observer-Sun vector and the observer-target vector.

In addition to the SECCHI imaging suite described above, each of the STEREO spacecraft also carries a comprehensive suite of *in situ* instrumentation, including the PLASTIC (Galvin *et al.*, 2008) and the IMPACT (Luhmann *et al.*, 2008) packages. Magnetic field measurements from the magnetometer (MAG; (Acuña *et al.*, 2008)) and suprathermal electron observations from the SWEA (Sauvaud *et al.*, 2008), two components of the IMPACT package, together with the SW ion moments derived from measurements made by the PLASTIC package, are used in our analysis of the heliospheric consequences of the eruption. *In situ* measurements of near-Earth SW electrons and ions as well as suprathermal electrons made by the SWEPAM (McComas *et al.*, 1998), SW composition measured by the SWICS/SWIMS (Gloeckler *et al.*, 1998) and measurements of the magnetic field by the magnetic field investigation (MAG; (Smith *et al.*, 1998)) onboard the ACE (Stone *et al.*, 1998) are also used here. The ACE IMF and SW ion parameters are 64-second averages and the SW composition data are hourly averages. The STEREO IMF and SW ion parameters are all 10 minute averages.

Two other spacecraft were used to complement STEREO EUVI 171, 195 and 284

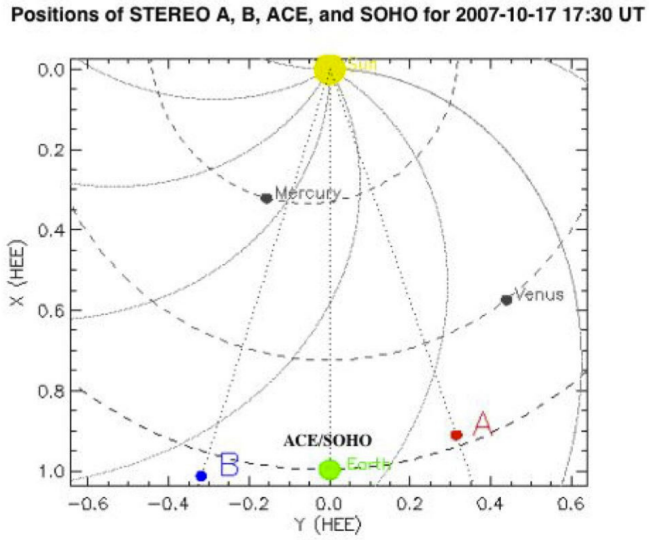

Figure 4.13: Positions of the STEREO-Ahead (red) and Behind (blue) spacecraft relative to the Sun (yellow) and Earth (green). ACE and SOHO are located at L_1. *Hinode* is in a Sun-synchronous orbit around the Earth (not shown). Estimated Parker Spirals are shown. (Adapted from the image produced by the STEREO Orbit Tool available at `http://stereo-ssc.nascom.nasa.gov/where/`.

Å on-disk observations. *Hinode* X-Ray Telescope (XRT) (Golub *et al.*, 2007) is a high-resolution grazing-incidence telescope with a wide temperature coverage. The thin aluminum-on-mesh filter is used to observe the AR and CH evolution in the corona at a cadence of $\sim 1\frac{1}{2}$ minutes at many time intervals around the eruption. The evolution of the photospheric magnetic field is examined and AR and CH polarities are determined using full-disk magnetograms with a 96 min cadence and a pixel size of 1.98" that were obtained with SOHO MDI. The MDI data were corrected for the underestimation of MDI flux as discussed in Green *et al.* (2003). All solar data were calibrated and instrumental effects corrected for using standard SolarSoft routines for the respective instruments.

4.4.4 Observations

Remote and *in situ* data from five spacecraft in different orbits are used in the following analysis. In order to minimize any possible confusion, please refer to Figure 4.13 for the positions of STEREO-A, STEREO-B and ACE on 2007 October 17. At the time of the observations discussed in this section, the separation angle between STEREO-A and B was 36.6° and ACE and SOHO were, as always, at Earth's L_1 point. *Hinode* is in a Sun-synchronous orbit around the Earth. Due to the different viewing angles of each spacecraft, there are offsets in X and Y solar coordinates in STEREO EUVI, SOHO, and *Hinode* solar images.

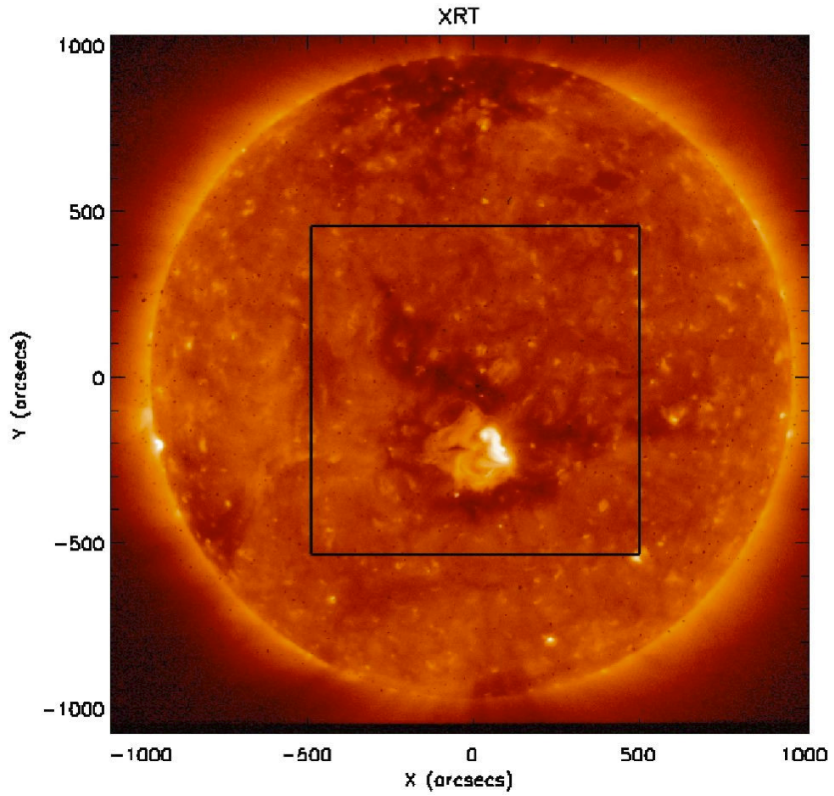

Figure 4.14: *Hinode* XRT thin aluminum-on-mesh filter full-disk image of the Sun on 2007 October 17 at 17:48 UT. The AR and surrounding CH are located at the central meridian just south of the solar equator.

4.4.4.1 Solar On-Disk Observations

Using multi-wavelength data, the evolution of the CME source AR is observed during its passage across the solar disk. It appeared from the eastern limb on 2007 October 11 and was located inside a low-latitude CH approximately 200" south of the solar equator. It crossed the central meridian at ∼17:00 UT on October 17. Images taken with *Hinode* XRT instrument provide context for the AR and the surrounding CH. Figure 4.14 is a full disk X-ray image taken with the thin aluminum-on-mesh filter. At this stage, the extent of the AR is approximately 300"×250". Figure 4.15A shows a zoomed XRT image of the FOV contained in the black box in Figure 4.14. The AR structure appears to have the shape of a 'sea anemone' described in §4.4.2.

From SOHO MDI full-disk magnetograms the AR's signed magnetic flux was measured using the method of Baker *et al.* (2007) to be approximately 3×10^{21} Mx as it crossed the solar central meridian. On October 14, magnetograms show the following AR polarity (positive) has started to break up and disperse while the leading polarity (negative) remains essentially concentrated. By early on the 15th, the negative field has fragmented as well. It is clear that the AR is in the decay phase of its evolution. Figure 4.15B shows a zoomed MDI magnetogram timed at

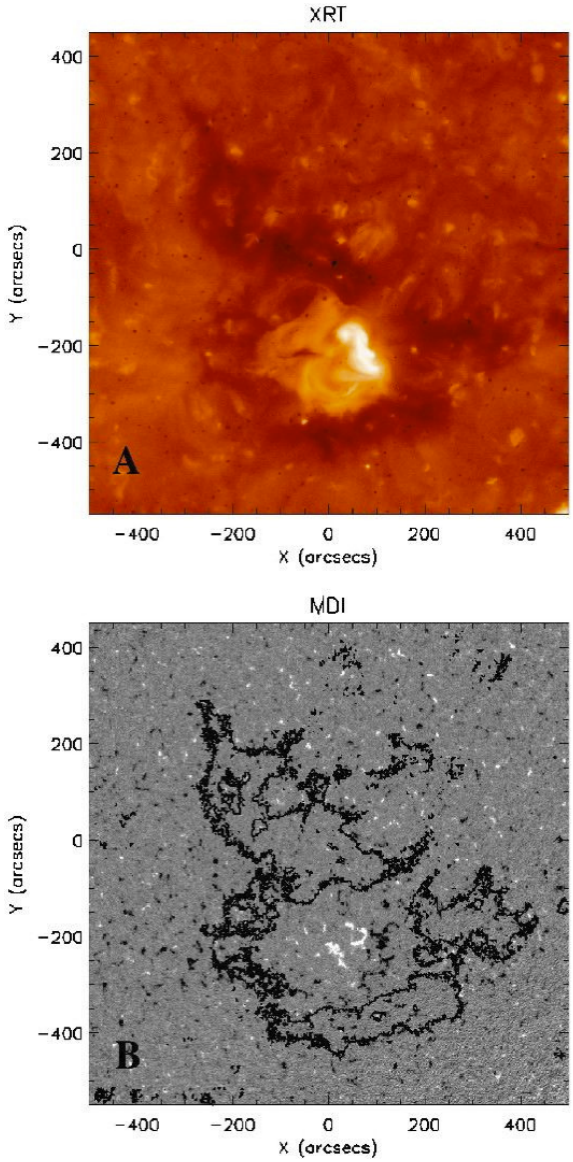

Figure 4.15: A - Zoomed *Hinode* XRT image contained in the black box in Figure 4.14 showing the the AR embedded in the equatorial CH. B - Zoomed MDI magnetogram (at 17:39 UT on October 17) with CH contour overlaid. CH contour level is set to lie halfway between the intensity of an area of the northern polar CH and an area of QS north of the AR (Attrill *et al.*, 2006). The AR's positive polarity (white) is to the solar east and its negative polarity (black) is to the solar west. The CH polarity is negative.

17:39 UT depicting the extent of the magnetic field dispersion on the 17^{th}. Contours outlining the CH as determined by the method discussed in Attrill *et al.* (2006) have been overlaid on the magnetogram. The CH's magnetic polarity is negative and has a typical magnetic field strength of 19 G.

To the northwest, the brightest X-ray loops over the main inversion line of the AR have formed a reverse S-shaped sigmoidal structure indicating left-handed or negative helicity - unusual for an AR in the southern hemisphere. However, it should be noted that this CH/AR complex is north of the heliospheric current sheet (HCS) and the polarity of the CH is the same as the north polar CH (Simunac *et al.*,

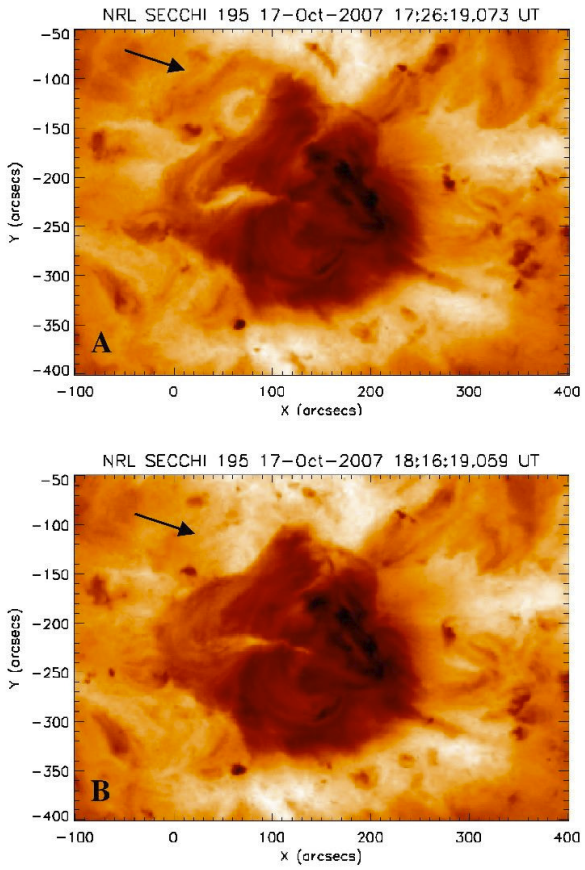

Figure 4.16: STEREO-A EUVI 195 Å reverse color images showing before and after (17:26 UT and 18:16 UT, respectively on October 17) the eruption to the northeast of the AR.

2009). Sigmoidal helicity, CH polarity and the AR/CH complex position relative to the HCS should place it more in the northern hemisphere.

A combination of STEREO EUVI 195 Å and 171 Å data is used to identify the timing and location of an eruption from the AR on the 17^{th}. The early eruption phase began at ∼17:30 UT on the north eastern (NE) side of the AR. Figure 4.16A shows the AR at 195 Å prior to the eruption at 17:26 UT. The soon-to-erupt AR loops are designated by the black arrow. The AR loops start to expand and rise until they eventually disappear by 18:16 UT (Figure 4.16B). A small dimming region (the bright feature in the reverse color image) is visible where the loops used to be prior to the eruption.

Unlike the STEREO-A EUVI 195 Å images of the eruption in Figure 4.16, STEREO-B EUVI 171 Å images show a distinct filament in absorption prior to the eruption. The filament lies along the polarity inversion line (PIL) where opposite polarity flux converges from early on the 17^{th}. Figure 5.4 shows two zoomed STEREO-B 171 Å images containing the filament (indicated by white arrows) located in the NE quadrant of the AR. The eastern portion of the filament moves

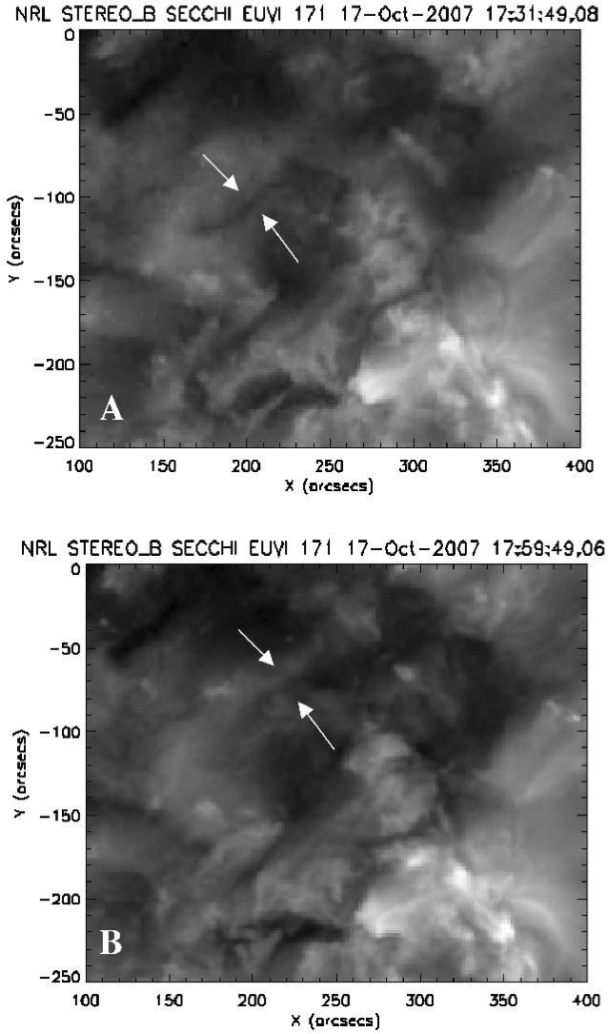

Figure 4.17: STEREO-B EUVI 171 Å images at 17:31 (A) and 17:59 UT (B) on October 17 showing a filament (indicated by the white arrows). The filament has started to erupt by the time of the image in B.

northwards as it rises and is noticeably displaced in the image at 17:59 UT (Figure 4.16A) relative to its position at 17:31 UT (Figure 4.16B). (Compare the position of the eastern most segment of the filament with the Y = -100 tick mark in each image). Movies of both STEREO-A and B EUVI 195 Å observations suggest the overlying loops at the location of the filament disappear by 18:30 UT which is consistent with the fact that the filament is no longer visible in the 171 Å images by 18:29 UT.

The erupting filament lies along the magnetic inversion line surrounding (curving around) the included positive polarity. The erupted section had a SE-NW orientation, with negative (CH) polarity on the E-NE and positive (AR) polarity on the W-SW. When overlying loops expand with the erupting filament, a favourable field line alignment for IR would occur on the west side of the erupting loops, where

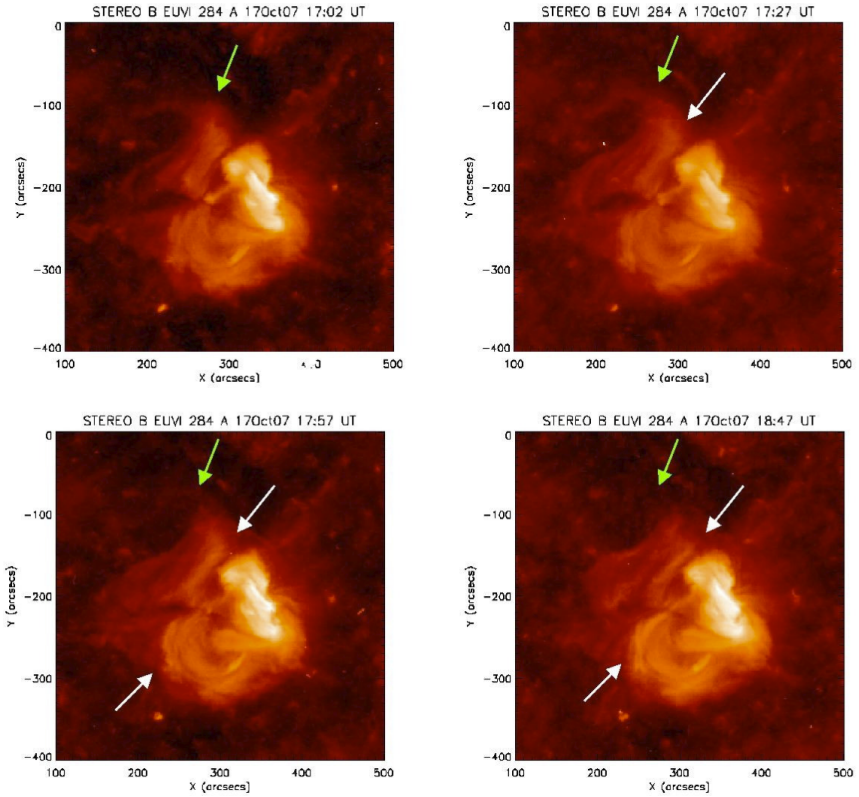

Figure 4.18: STEREO-B EUVI 284 Å images from 17:02 to 18:47 UT on October 17 (left to right, top to bottom). White arrows indicate anemone evolution before, during, and after the eruption. Green arrows mark the eruption observed in EUVI 195 Å at ∼17:30 UT (cf. Figure 4.16). The southern loops of the anemone have brightened as a result of reconnection after the eruption (images timed at 17:57 and 18:47 UT).

positive (anti-sunward) field lines of the expanding CME loops would meet negative 'open' field lines of the CH. Reconnection with CH field lines leads to the formation of new bright loops in the anemone structure connecting the positive polarity to negative fields in the NW and SW. These brightened loops are best visible in STEREO-A 284 Å images (Figure 4.18).

4.4.4.2 STEREO HI Observations

Figure 4.19 presents a view of the ecliptic plane from solar north on 2007 October 17 showing the relative positions of the Sun (S), STEREO-A (A), STEREO-B (B) and the Earth (E). The elongation (see §4.4.3) extents in the ecliptic plane of the FOVs of HI-1 and HI-2 on STEREO-A (termed HI-1A and HI-2A) are marked in red and blue, respectively. Figure 4.20a presents a time-elongation map (or J-map) derived by plotting strips from HI-1A and HI-2A running difference images, extracted along the Position Angle (PA) of 100° which intersects the latitude of the AR when crossing the plane of the sky as viewed from STEREO-A, as a function of elongation (along

Table 4.2: The predicted speed, Vr (km s^{-1}), longitude separation, β (°), elongation, $\alpha_\circ$ (°), and inferred coronal height, $D_\circ$ at which the transient track is first fitted and the estimated launch date/time of transients T1 to T4.

Transient	T1	T2	T3	T4
Vr (km s^{-1})	260±20	320±20	385±32	363±27
β (°)	90±8	90±5	79±10	63±11
$\alpha_\circ$ (°)	6.46	4.68	6.43	5.84
$D_\circ$ (AU)	0.1095	0.0791	0.1086	0.1035
Launch Time:				
yy/mm/dd	07/10/12	07/10/13	07/10/15	07/10/15
hh:mm	10:52 UT	11:58 UT	00:38 UT	13:12 UT

the ordinate) and time (along the absissa). The use of difference images minimizes the contribution of the stable F-corona and is a very useful technique for highlighting faint propagating features. The J-map shown in Figure 4.20 covers the interval from 2007 October 12 - 20 and is based on the technique reported by Davies *et al.* (2009). The J-maps are truncated to 40° elongation due to the presence of the Milky Way in the outer edge of the HI-2A FOV. Many structures erupted during this interval, in particular tracks appear to converge suggesting the passage of a corotating solar source of transients. Rouillard *et al.* (2008) and Sheeley *et al.* (2008a,b) showed that the apparent acceleration/deceleration at the elongations covered by HI J-maps is mostly an effect of projection geometry. The elongation, α, labeled in Figure 4.19, of a point T (e.g. T4) in the SW and observed by the STEREO-A spacecraft, is defined as the Sun - STEREO-A - T angle, being zero at Sun center. The angular separation between the Sun - STEREO-A spacecraft line and the direction of propagation of the point (labeled β in Figure 4.19) equates to the longitude separation in an ecliptic-based heliocentric coordinate system when the transient propagates in the ecliptic plane. The elongation variation, α(t), of a SW transient depends upon its radial speed, Vr, and the angle β (Rouillard *et al.* (2008, 2009b); Figure 4.19). Best-fit values of these parameters can, therefore, be extracted from the elongation variation recorded by HI. Each clearly traceable track was fitted using the technique; the red lines superposed on the same J-map as Figure 4.20a and shown in Figure 4.20b correspond to the best-fit line of the apparent speed variation. The predicted speed, Vr (km s^{-1}), longitude separation β (°), elongation $\alpha_\circ$ (°), and inferred coronal height, $D_\circ$, at which the transient track is first fitted, and the estimated launch date/time of transients T1 to T4 are listed in Table 4.2.

As expected from the convergence of tracks and a corotating source region, the longitude separation between the source region and STEREO-A is decreasing with time (i.e. converging tracks). The location of the source-region in the lower corona of each transient is determined by using a ballistic back-mapping of the transient position assuming constant speed (i.e. ignoring acceleration effects) and a solar

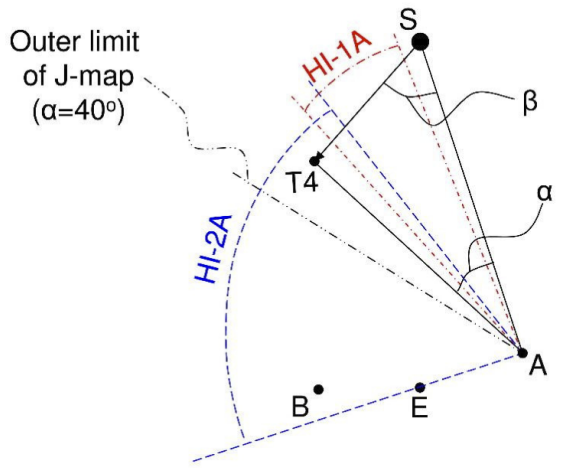

Figure 4.19: View of the ecliptic from solar north with the position of the Sun (S), Earth (E), STEREO-A (A), and STEREO-B (B) spacecraft on 2007 October 17. The limits of the fields of view of HI-1A and HI-2A imagers in the ecliptic plane are shown in red and blue, respectively. The trajectory of transient T4 is shown by a black arrow, the angles α and β which define the position of T4 in the ecliptic plane uniquely are also shown. The outer limit of the J-maps of Figure 4.20 (40°) is also shown.

rotation period as seen from STEREO-A of 28.4 days. The solar rotation period as seen from STEREO-A is longer than the well-known 27.27 day period as viewed from Earth because STEREO-A is propagating faster than the Earth around the Sun. The ballistic back-mapping assumes radial propagation of the transient and has its limitations. The estimate of the source region is accurate only to first approximation.

The launch-sites of T1 to T4 are shown in Figure 4.21 as yellow disks on a subset of a Carrington map (latitude versus longitude map for CR 2062) created from central meridian EUV observations at 195 Å made by STEREO-A. Three of the transients emerge in the vicinity of the AR (T1, T2 and T4). They appear to emerge from the boundary of the AR with the CH although the errors of the estimated longitude of propagation are around 8° (average of the mean error in angle β in Table 4.2) and while it is possible to tell whether a transient propagated along a solar radial rooted on the eastern or western boundary of the AR, it is not possible to tell if the eruption occurred on the boundary or toward the center of the AR.

The HI observations suggest that the AR is continually releasing transients in the SW. There are indications of two of the transients, T2 and T4, in GOES X-ray flux curves at approximately 12:30 UT on October 13 and 12:00 UT on October 15, respectively (`http://www.swpc.noaa.gov/Data/goes.html`). STEREO-B EUVI 284 Å movies (STEREO movie maker at `http://stereo-ssc.nascom.nasa.gov`) show what appear to be transients T2, T3, and T4 erupting within a few hours of

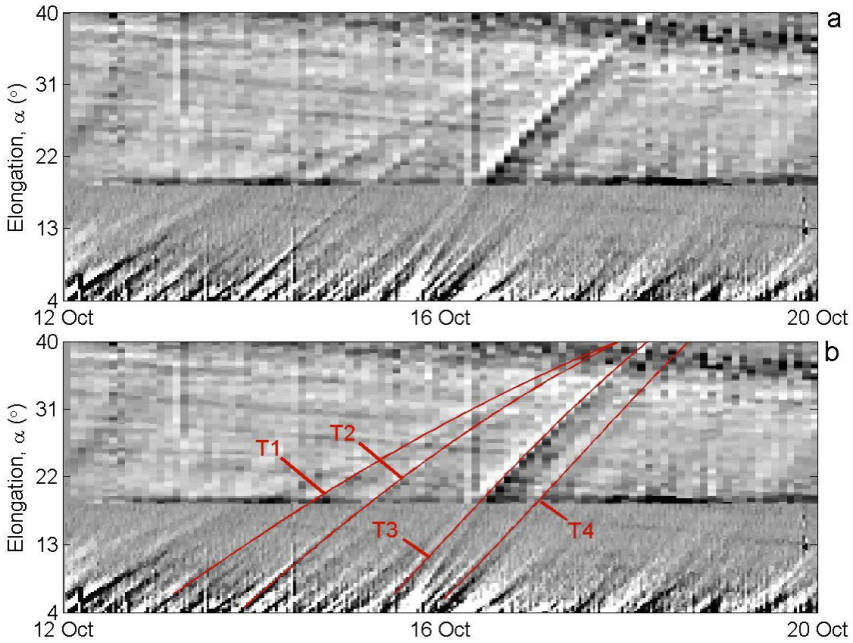

Figure 4.20: Two identical J-maps constructed along PA=100° using HI-1/2A running difference images. In b the results of fitting the tracks (T1 to T4) are shown as red lines superposed on the J-map.

the estimated launch times on the side of the AR indicated in Figure 4.21. This type of intermittent release of transients has been observed by HI during July 2007 and September 2007 and comparison of HI images with *in situ* observations during spacecraft-impacting events showed that these transients had flux-rope topologies (Rouillard *et al.*, 2008, 2009a,b).

The eruption observed in STEREO EUVI data on October 17 at ∼17:30 was close to Sun-center, therefore, as the transient propagates towards STEREO-A, it is not close to the Thomson surface which is the surface of maximum scatter centered halfway between the Sun and observer. Furthermore, the eruption did not lift much plasma from the lower corona. These two facts combined meant the trace was not strong enough to be seen in the J-map in Figure 4.20.

4.4.4.3 *In situ* Observations

The on-disk source of the October 17th eruption was established and it was shown with HI observations that the AR embedded in a CH has produced several transients within a few days prior to the eruption. Now the signatures of the eruption are identified four days later in the SW data using STEREO-A, STEREO-B and ACE spacecraft. All three spacecraft were located in or close to the ecliptic plane which intersected the solar surface 5° north of the AR in the surrounding CH area at the

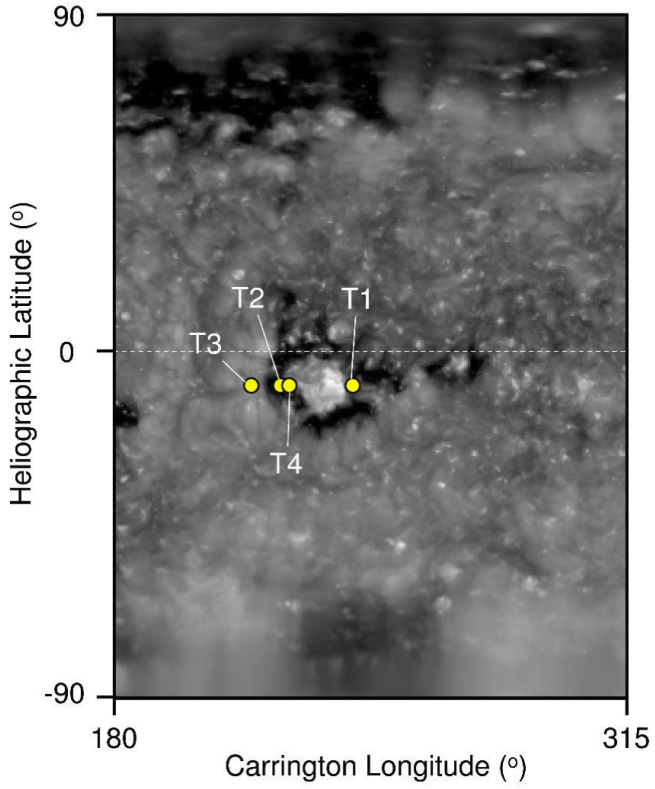

Figure 4.21: The subset of a Carrington map (latitude versus longitude map for CR 2062) created from central meridian EUV observations at 195 Å made by STEREO-A. The small yellow disks mark the estimated launch-site of each transient tracked in HI using the calculated kinematic properties listed in Table 4.2.

time of the event. Though none of the spacecraft was radially aligned with the AR, all spacecraft detected the fast flows from the surrounding CH and in particular, the trailing edge of the corotating fast stream (rarefaction region). The eruption observed by STEREO EUVI and *Hinode* XRT occurred on the NE boundary of the AR close to the latitudes of the three spacecraft.

4.4.4.4 Interplanetary ACE *In situ* Observations

Figure 4.22 shows ACE data for the interval 2007 October 20 - 22. On the 21^{st} at 04:00 UT, 4 days after the eruption to the NE of the AR, a sharp change from 175° (sunward pointing magnetic field or negative polarity footpoints) to 350° (anti-sunward pointing magnetic field or positive polarity footpoints) is observed in the azimuth angle of the magnetic field direction (Figure 4.22c). The azimuth angle remains at 350° for 10 hours and then changes back to 175° (cf. black dashed line in Figure 4.22c for guidance). This change in azimuth angle is not associated with a reversal of the strahl as seen in the pitch angle distribution of suprathermal electrons (272eV) which remains anti-field-aligned at 175° throughout the entire interval (see

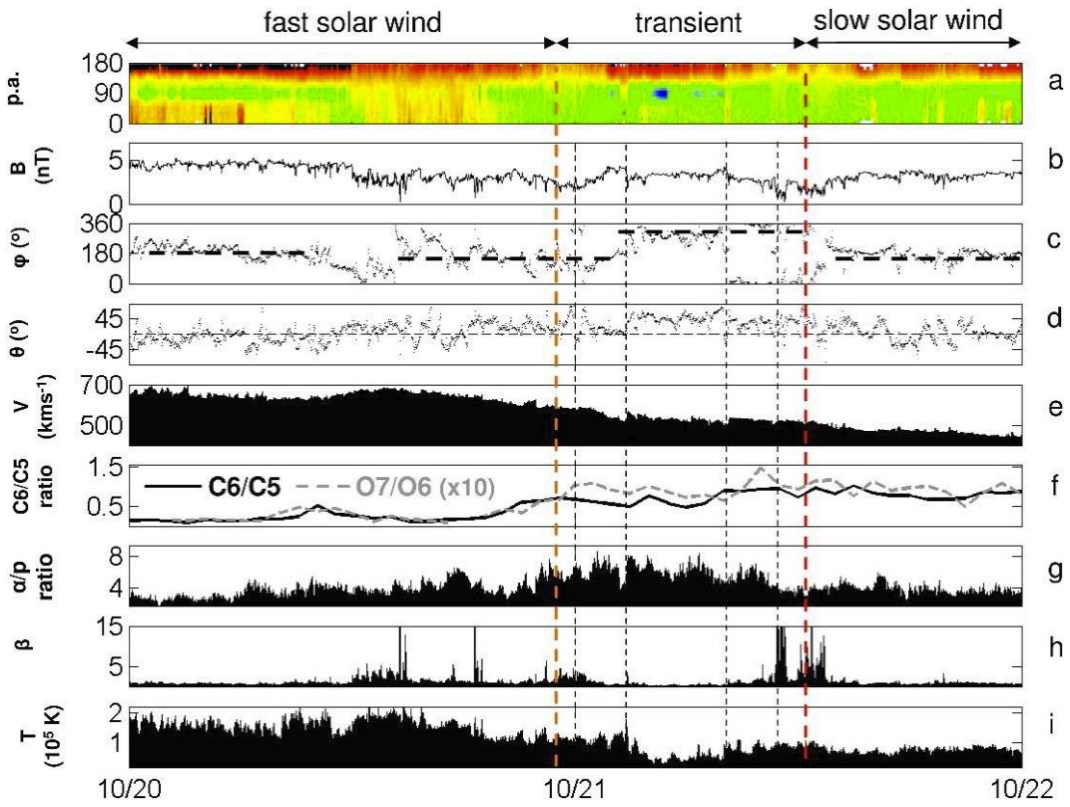

Figure 4.22: *In situ* data measured during the passage of the ICME. Panel a: The 272 eV electron pitch angle [p.a.] distributions recorded by the ACE spacecraft; Panel b: the magnetic field strength [B (nT)]; Panel c: the azimuth of the magnetic field [φ (°)]; Panel d: the elevation of the magnetic field [θ (°)]; Panel e: the SW speed [V (km s^{-1})]; Panel f: the charge state ratios (C6/C5) (black line) and (O7/O6) (grey dashed line) measured by SWICS onboard the ACE spacecraft; Panel g: the alpha to proton ratio [α/p as a percentage (%)]; Panel h: SW plasma beta [β]; Panel i: SW ion temperature [T (K)]. Red dashed lines define the interval of the transient passage defined as the combined changes in magnetic field strength, alpha to proton ratio and plasma beta. Vertical black dashed lines indicate the times of sharp discontinuities in magnetic field direction, strength, and alpha to proton ratio.

Figure 4.22a). The boundaries of this anomalous field direction are indicated by sharp increases in plasma β (Figure 4.22h).

The passage of the transient (see fast SW, transient, and slow SW labels at the top of Figure 4.22) is marked by a change in SW composition with enhanced charge state ratios (Figure 4.22f). The oxygen charge state ratio of the SW as measured by $n(O^{7+})/n(O^{6+})$ changes from <0.05 to >0.14 and the carbon charge state ratio as measured by $n(C^{6+})/n(C^{5+})$ changes from 0.1 to 0.95 (oxygen ratio is the gray dashed line and carbon ratio is the black solid line in Figure 4.22f). The structure is also characterized by enhanced alpha to proton ratio (Figure 4.22g) and lower SW temperature (Figure 4.22i). A preliminary analysis, not shown here, of the correlation between the components of the SW velocity and the magnetic field vectors reveals the presence of large amplitude Alfvén waves inside the transient.

A 500 km s^{-1} constant speed backmapping of the arrival time of the structure

observed *in situ* on October 21 suggests a launch-time on the solar surface on October 17 at 19 UT (see §4.4.4 for discussion of the method). The eruption observed on the NE side of the AR and timed at ∼17:30 on 17^{th} is very near the launch time estimated for the departure of the transient.

4.4.4.5 Interplanetary STEREO-A and B *In situ* Observations

In mid-October, STEREO-A observed a trailing edge of a CIR followed by an increase in SW speed forming a second CIR. The second CIR (on October 22/23) is likely to be associated with the part of the CH located on the eastern side of the AR. The AR causes a dip in SW speed from above 600 km s^{-1} to just above 500 km s^{-1} between the two fast SW streams of the surrounding CH. Unlike the ACE observations, the STEREO-A data is dominated by pure SW as there is little evidence for transient structures with the exception of one small high β structure.

STEREO-B measured the highest speed SW (Figure 4.23e) and the trailing edge of a CIR. There are suprathermal electrons at 0° (Figure 4.23a) escaping from the region of high speed streams on October 19 and 20, as was observed at ACE prior to the transient in Figure 4.22a. Later, on October 21, during the transition from fast to slower SW there are two high plasma β structures marked by dashed vertical lines in Figure 4.23. STEREO-B is observing high-plasma β structures with field line rotations which may be more evidence of transients but there is not enough information available to relate them to the October 17 transient.

4.4.5 Discussion

4.4.5.1 On-Disk Evidence of IR - Presence and Evolution of Anemone Structure

It is proposed that an AR embedded in a low-latitude CH provides the ideal scenario for IR to take place. Oppositely aligned magnetic field of the AR and CH will naturally exist somewhere in the magnetic configuration. STEREO EUVI 171, 195, and 284 Å observations showed that a filament eruption/CME took place on the NE side of the AR where its positive polarity is surrounded by the unipolar negative polarity of the CH. There is little doubt that the magnetic configuration is ideal for IR, but what observational evidence, if any, confirms that reconnection did in fact take place? One possible answer lies in the anemone structure observed in *Hinode* XRT and STEREO EUVI 284 Å images. Crooker and Webb (2006) inter-

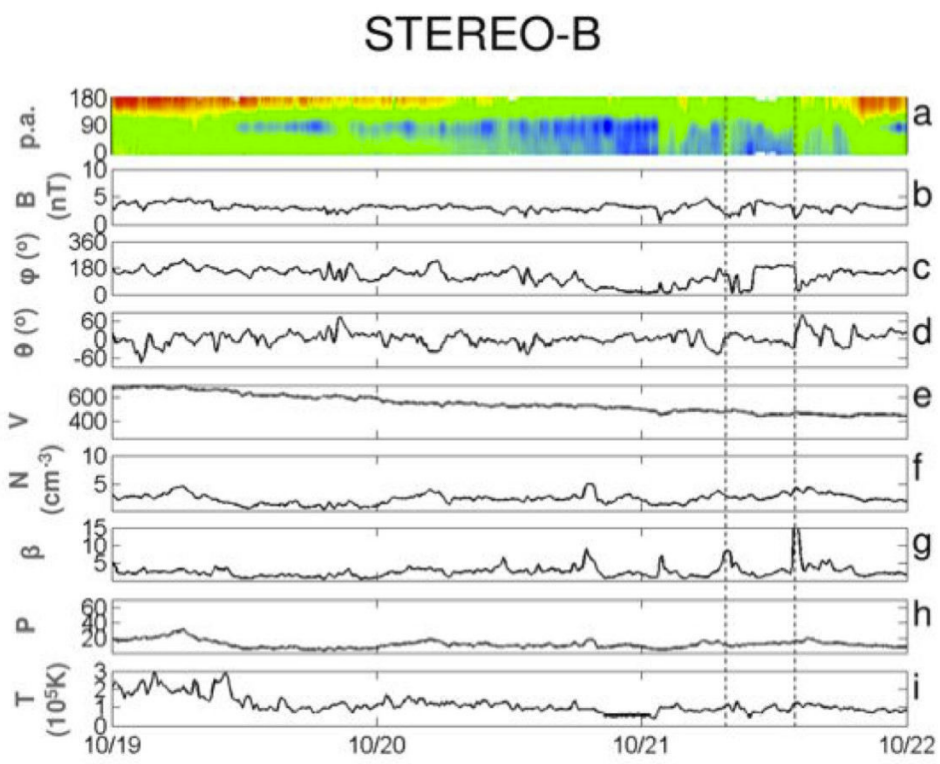

Figure 4.23: STEREO-B *in situ* data. Panel a: The 272 eV electron pitch angle [p.a.] distributions recorded by the STEREO spacecraft; Panel b: the magnetic field strength [B (nT)]; Panel c: the azimuth of the magnetic field [φ (°)]; Panel d: the elevation angle of the magnetic field [θ (°)]; Panel e: the SW speed [V (km s^{-1})]; Panel f: the number density [N (cm^{-3})]; Panel g: SW plasma beta [β]; Panel h: pressure [nPa]; Panel i: SW ion temperature [T (K)]. Dashed lines mark high plasma β structures.

preted bright X-ray regions or anemones, associated with CME source regions, to be the X-ray signatures of IR. Like Crooker and Webb (2006), the author interprets the anemone to be the result of IR induced by several episodes of eruption-driven expansion of the AR. This is consistent with previous studies of anemone ARs that show such structures sometimes generate filament eruptions (Chertok *et al.*, 2002) and CMEs (Asai *et al.*, 2009).

4.4.5.2 ICME Signatures and Characteristics

The link between transient structures such as CMEs and their interplanetary manifestations, ICMEs, is not direct. Transients interact with the ambient SW so that by the time *in situ* instruments measure their plasma properties at 1 AU, the transients have been modified to some extent. The link between CMEs and ICMEs is weakened further by limitations posed by spacecraft position relative to ICME passage. In spite of these concerns, different signatures are used to identify ICMEs *in situ*, some of which are employed here. (See Wimmer-Schweingruber *et al.* (2006) for a

review of ICME signatures).

Analysis of *in situ* data covering the period from October 19 to 22 revealed varying degrees of ICME signatures of the filament eruption/CME from the AR on October 17. Any transients went virtually undetected in STEREO-A data which were dominated by pure SW. STEREO-B data revealed little more. The fact that neither STEREO A nor B observed the transient set an upper boundary to the angular extent of any transient/ICME as the spacecraft were separated by 36.6° at the time, though there is a slight possibility that the non-detection is due to the southward deflection of the ICME.

In the ACE data, the transient passage is marked by a slight increase in magnetic field strength towards the center of the transient and elevation angles (out of ecliptic fields), enhanced alpha to proton ratio (Figure 4.22g), lower plasma β (Figure 4.22h) and lower temperatures (Figure 4.22i), suggesting the passage of an ICME. The rotations of the azimuth and elevation angles are not smooth and the variance of magnetic field does not drop inside the transient which suggests that either the event is not a magnetic cloud (MC) (a well-defined subset of ICMEs) by the strict definition of Burlaga *et al.* (1981) or that ACE intersected the edges of the MC only and the spacecraft failed to sample the central axis of the flux-rope. Wilcox Solar Observatory (WSO) synoptic magnetic maps and source-surface computations (Figure 4.24) show that the warped HCS runs south of the CH/AR complex at about S 30°. Since 'open' field of CHs are known to deflect CMEs (Gopalswamy *et al.*, 2009), it is plausible that the CME was 'channeled' by its surrounding CH field towards the HCS, i.e. southward. This may provide an explanation why ACE, situated in the ecliptic, observed only the flanks of the ICME.

Démoulin *et al.* (2008) proposed a model for the expected *in situ* velocities of expanding ICMEs. The model yields a nearly linear temporal dependence of the velocity which is consistent with observed velocity profiles of 26 MCs not overtaken by fast SW streams. They conclude that for most ICMEs/MCs the observed velocity profile is mainly due to expansion which can be described by the normalized expansion factor ζ computed from the slope of the velocity profile. Démoulin *et al.* (2008) results showed $\zeta = 0.8 \pm 0.2$ for the 26 MCs. The ICME analyzed here has a typical velocity profile (see Figure 4.25) and expansion rate ($\zeta \sim 0.7$) within the range of results Démoulin *et al.* (2008) found for their sample of MCs.

MCs are often enriched in alpha to proton ratio (Hirshberg *et al.*, 1972; Neugebauer *et al.*, 1997; Zurbuchen *et al.*, 2002). Normal SW alpha to proton ratio levels range from 3 to 5% (Neugebauer, 1981; Schwenn and Marsch, 1990). The alpha to proton ratio increases sharply inside the whole ICME structure from 0.01 to 0.06,

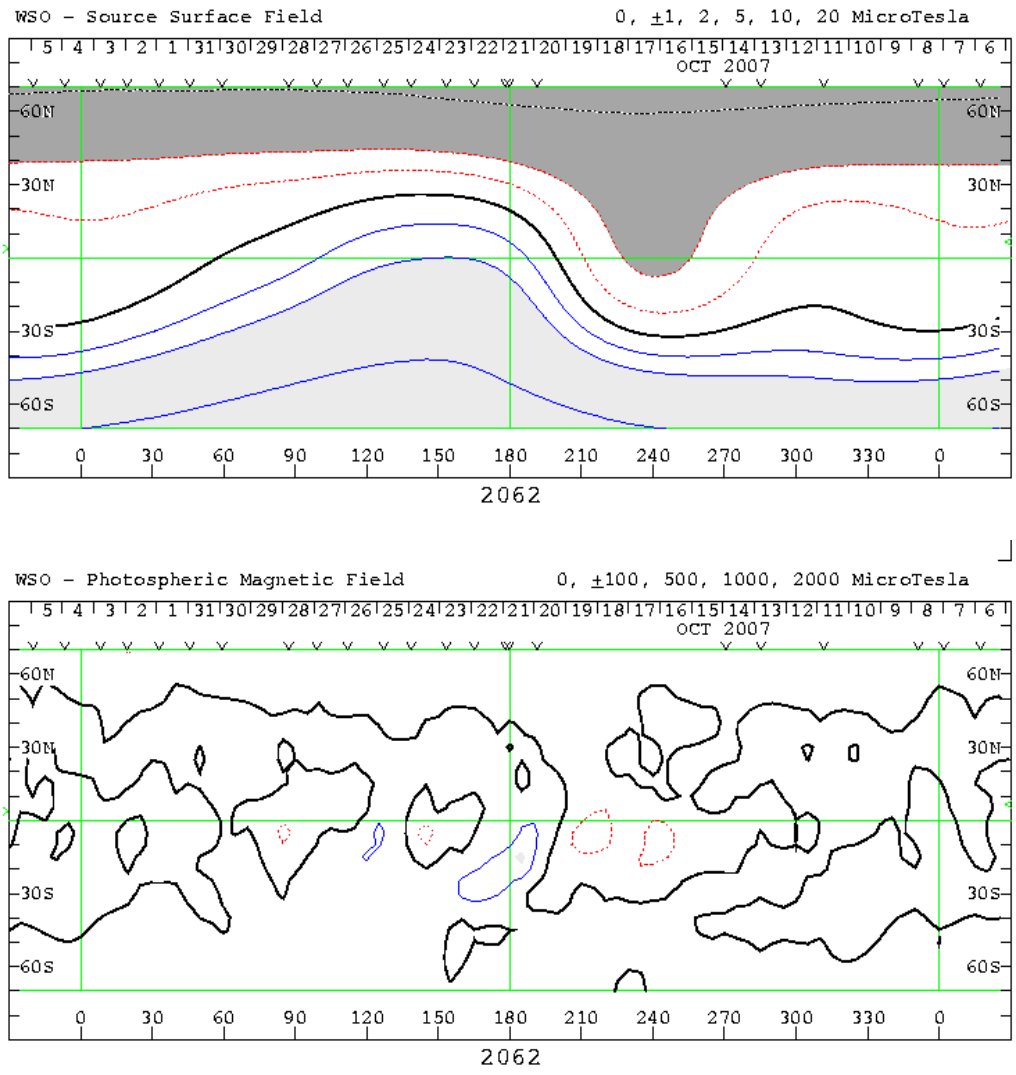

Figure 4.24: Synoptic charts of the source surface field (top) and photospheric field (bottom) for Carrington rotation CR 2062 from Wilcox Observatory. Blue and light shading/red and dark shading designate positive/negative polarity regions. Solid black line represents the neutral line which is the Heliospheric Current Sheet in the top chart and the polarity inversion line in the bottom chart. From: `http://wso.stanford.edu/synsourcel.html` and `http://wso.stanford.edu/synopticl.html`.

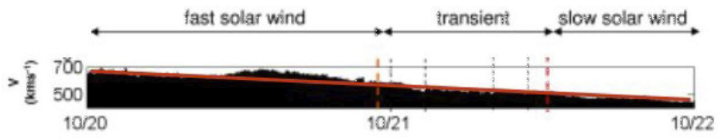

Figure 4.25: Velocity profile of the transient as observed by ACE. The near linear dependence of observed velocity with time and expansion rate $\zeta \approx 0.7$ are consistent with Démoulin *et al.* (2008) results for expanding ICMEs/MCs.

just below the 0.08 limit used to distinguish ICMEs (Hirshberg *et al.*, 1970, 1972; Neugebauer, 1981; Borrini *et al.*, 1982) which could be a result of dynamical effects lower in the corona.

As described in §4.4.4.4, the passage of the ICME is marked by increases in oxygen and carbon charge state ratios. The oxygen charge state ratio has a relatively fast freeze-in process in the low corona, therefore, it is considered to be a good measure of the source of the SW (Zurbuchen *et al.* (2002) and references therein). In addition, Henke *et al.* (1998) found that ICMEs with magnetic cloud structure have an enhanced oxygen charge state ratio compared with non-cloud ICMEs. The n(O7+)/n(O6+) charge-state ratio observed inside the transient is enhanced compared to fast SW but is much less than the n(O7+)/n(O6+)$\geq$1 sometimes observed in ICME magnetic clouds (Zurbuchen *et al.*, 2002). The ICME itself separates pure fast SW from slow SW and is located near the stream interface (SI). The SI on this side of the CIR is often overlooked but is a simpler boundary to study than the SI located on the compression region side of the CIR (Cartwright and Moldwin, 2008; Kilpua *et al.*, 2009). Thus as a counterpart to transients found to be entrained in CIRs, there is a clear case of an ICME in the rarefaction region.

There is good evidence that the transient observed *in situ* 4 days after the eruption to the northeast of the AR on October 17 is a transient/ICME. Indeed, this transient has some characteristics of a MC as suggested by the enhanced alpha to proton and oxygen charge state ratios and the level of the expansion factor ζ, though as previously stated, ACE probably has not sampled the flux rope's central axis.

4.4.5.3 *In situ* Evidence of IR - Disconnection of One Side of the ICME

Suprathermal electrons can be used as an indicator of magnetic connection to the Sun. Counterstreaming (or bidirectional) electrons are one of the benchmark indicators of the passage *in situ* of ICMEs connected at both ends in the photosphere (Gosling *et al.*, 1987). However, not all ICMEs are associated with counterstreaming suprathermal electrons. Shodhan *et al.* (2000) found that most MCs contained

a mixture of closed and 'opened' field lines at 1 AU and Crooker *et al.* (2004a) found an average of 55% closed in their study of 31 MCs at 5 AU. These results are consistent with Riley *et al.* (2004). The ACE suprathermal electron pitch angle spectrogram shows no indication of counterstreaming electrons during the passage of the ICME, suggesting the ICME is 'open' and therefore, disconnected from the Sun on one side.

Crooker *et al.* (2002) and Owens and Crooker (2006) proposed that IR is the mechanism by which ICME field lines are 'opened'. In a case study of a CME on 12 May 1997, Attrill *et al.* (2006) and Crooker and Webb (2006) independently concluded that long-lasting IR occurred throughout the CME release process, disconnecting the negative leg of the CME. Rouillard *et al.* (2009b) recently observed a CME transient located on the anti-sunward flank of the SI associated with the compression side of a CIR. Their analysis also revealed that the transient was only connected at one end to the photosphere inferring IR as the mechanism by which the magnetic field lines of the transient became 'open'.

The event described here is another clear example of the process of IR 'opening' the ICME field. High suprathermal electron fluxes are predominantly at 175° throughout the passage indicating sunward pointing magnetic field or negative polarity footpoints. The CH field surrounding the AR is also negative, suggesting IR took place between the positive field of the AR and the negative field of the CH, 'opening' the positive polarity 'leg' of the ICME to the east and leaving the negative polarity connected to the Sun.

Another possible *in situ* signature of IR is the observation of so-called refolded magnetic field lines (RFL) in the ICME. The azimuth angle of the magnetic field inside the transient (Figure 4.22c) at first stays around 180°, followed by a sharp change in the azimuth angle of the magnetic field direction to ∼340° that lasted for 10 hours before reverting back. This change in the field orientation was not associated with a reversal of the strahl indicating that magnetic field line changed pointing direction but did not change polarity. Crooker *et al.* (2004b) proposed this type of event is a locally refolded magnetic field line (RFL).

Recalling the on-disk observations of the erupting filament described in §4.4.4.1, the sharp changes in azimuth angle observed by ACE can be interpreted: as shown in the cartoon in Figure 4.26, the expanding loops of the ICME are favourably oriented for reconnection with 'open' CH field towards the west, disconnecting the positive magnetic footpoints of the CME/ICME. (Note that as described in §4.4.4.1, the eruption occurred at the NE periphery of the AR, not at its main inversion line). With the magnetic field orientation observed in the eruption, ACE is expected to in-

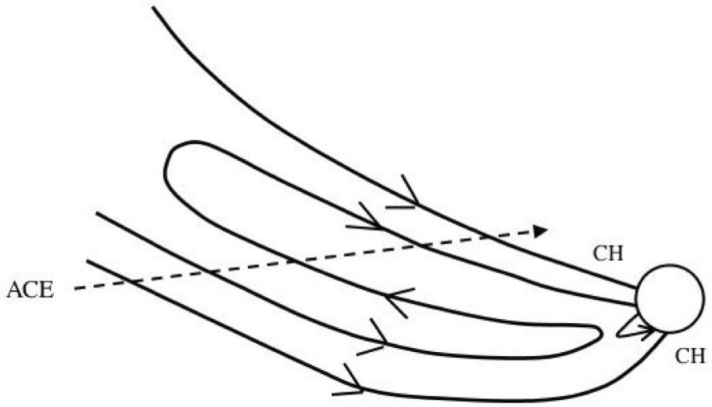

Figure 4.26: Cartoon of the ICME after disconnection of the positive 'leg'. ACE trajectory is indicated by the dashed arrow.

tercept 'open' field lines of the CH then perhaps RFLs, first intercepting the negative fold of the RFL, which appears as the 2-3 hour long ∼180° oriented azimuth angle first part in the transient/ICME. A sharp change is observed when ACE meets the positive leg of the expanding loop-like ICME structure. This phase lasts for about 10 hours. After that, the negative leg of the ICME fieldlines which remain connected to the Sun are observed. In this scenario the transient is more extended than indicated in Figure 4.22, which is not contradicted by SW composition, temperature, nor magnetic field measurements.

4.4.6 Conclusions

Evidence has been provided that an eruption from the Sun on October 17 was linked to a transient observed *in situ* at 1 AU four days later. The transient showed many of the properties of an ICME of 'open' topology. A unique magnetic configuration consisting of an AR embedded inside a CH proved to be highly favorable and effective for IR to take place as the eruption-driven expansion of the AR induced reconnection between oppositely aligned closed positive field of the AR and CH's 'open' negative field. Two clear direct consequences of IR were observed, one on the solar surface - the presence and evolution of an anemone coronal loop structure in the AR while a series of ejecta were traced in HI data to erupt from the AR/CH complex, and *in situ* - the disconnection of one side of the ICME perhaps accompanied by RFL topology observed by ACE.

There are still some open questions requiring further investigation. Though two consequences of IR were identified, are there any other more subtle indications of the process? The substructure clearly evident within the large-scale structure of the

transient may provide clues to other manifestations of IR. The sharp increases in Alfvénicity noted in the ACE data that appear to mark the boundaries of different SW structures may suggest the possibility that distinct bundles of magnetic field lines pass over the ACE spacecraft over successive 2-3 hour periods (Borovsky, 2008). Are the consequences of ongoing IR being observed where the ICME loops expand, becoming 'frayed' as they continually, from the low corona through their propagation to 1 AU, reconnect with the surrounding 'open' (CH) field, creating distinct bundles of field lines with a highly curved (refolded) shape? Are the Alfvén waves signatures of these discreet reconnection processes or were they initiated by the fast-expanding CME along the CH fieldlines? These questions will be addressed in future work.

Chapter 5

CME Precursor

Some of the work presented in this chapter has been previously published in Baker *et al.* (2009c) and Murray *et al.* (2010). For Baker *et al.* (2009c), the analysis is the outcome of the author's own work, while collaborations with co-authors are acknowledged as follows: L. van Driel-Gesztelyi acted in the capacity of academic supervisor; M. Murray carried out 2.5D simulations of the AR-CH complex; L. Green and T. Török contributed with helpful discussions. Preliminary results were presented by the author at the 2nd Hinode Science Meeting in Boulder in September 2008. For Murray *et al.* (2010), the author carried out all data preparation, reduction, and analysis and contributed towards the construction and direction of the paper.

5.1 Abstract

The plasma flows resulting from the interaction between a mature AR and a surrounding equatorial CH observed by *Hinode* EIS and XRT on 2007 October 15 to 18 are investigated. For 3 days, EIS velocity maps showed outflows at the AR's eastern and western edges that were consistently between 5 and 12 km s^{-1}, whereas downflows of up to 30 km s^{-1} were seen in AR loops. However, on October 18, velocity profiles of hotter coronal lines reveal intensification in outflow velocities of up to 18 km s^{-1} at the AR's western footpoint about 6 hours prior to a CME eruption. 3D MHD numerical simulations of the magnetic configuration of the AR-CH complex were carried out and it was found that the expansion of the mature AR's loops drives persistent upflows along the neighboring CH field. Intensification of upflows observed on the AR's western side before a CME eruption is likely to be the result of the expansion of a flux rope containing a filament that provides stronger compression of the neighboring CH field on this side of the AR. Intensification of

upflows in the AR is proposed as a CME precursor.

5.2 Introduction

The Sun is the main driver of space weather phenomena such as CMEs. Their impact on the Earth and the heliosphere in the form of magnetic storms and particle radiation is considered to be significant. As a result, space weather and its predictability have become key research areas in solar-terrestrial physics. High-quality observational data from remote sensing instruments have greatly improved our overall understanding of the pre-eruptive Sun and our ability to identify CME precursors. What follows is a brief summary of some of the well-documented CME precursors, many of which are strongly related to the magnetic configuration and non-potentiality of the CME source region.

- Sigmoids

  Sigmoids are forward or reverse S-shaped loop structures observed in the X-ray solar corona (Sterling and Hudson, 1997), typically in AR during their decay phase. They may be visible in UV and EUV (Sterling and Hudson, 1997) but they are typically hot features. Using *Yohkoh* data, Rust and Kumar (1996) analyzed 103 events (between 1991 October and 1993 January) of transient brightenings associated with Hα filament eruptions and CMEs. Many of the bright features had a distinctly sigmoidal shape. The average width of the sigmoids was found to be 48,000 km and their average length was 200,000 km. There was a global organization to the events in that reverse-S sigmoids dominated the northern hemisphere and forward-S sigmoids were dominant in the southern hemisphere. Further work by Hudson *et al.* (1998), Canfield *et al.* (1999), and Glover *et al.* (2000) confirmed that ARs with a sigmoidal morphology are more likely to erupt. For example, Canfield *et al.* (1999) found 68% of 117 ARs with sigmoidal morphology erupted, regardless of AR size. Moreover, Leamon *et al.* (2002) showed when ARs with sigmoids do erupt, at least moderate geomagnetic storms are likely to be produced. The presence of sigmoids indicates that the magnetic configuration is highly non-potential, sheared, or twisted (e.g. Aulanier *et al.* (2005a)). The strong association of sigmoids with erupting ARs and the ease with which sigmoids are observed especially in X-rays make them a plausible CME precursor.

- X-ray and EUV Brightenings

  Transient brightenings have been long associated with the initiation of CMEs in multi-wavelength observations. Harrison *et al.* (1985) and Harrison (1986)

identified soft X-ray precursors approximately 15 - 30 minutes prior to the linearly extrapolated time of CME onset. The X-ray brightenings occurred in close proximity of the CME source regions. Dere *et al.* (1997) reported small EUV brightenings at the end of an erupting filament in SOHO EIT on-disk observations. Sterling and Moore (2005) found EUV brightenings that begin concurrently with the start of the slow-rise phase of a filament eruption along with soft X-ray brightenings at the same time and location. Quadrupolar brightenings in TRACE 1600 Å observations occurred before an eruption of a highly twisted filament which Williams *et al.* (2005) interpreted to be the result of tether weakening in the overlying field, suggestive of the external tether cutting/breakout model. Gary and Moore (2004) and Harra *et al.* (2005) also observed quadrupolar brightenings in TRACE 1600 Å and SOHO CDS O v emission line intensity maps approximately 30 min prior to a filament eruption and X-class flare. As with the case in Williams *et al.* (2005), the pre-eruption brightenings were interpreted to be indications of breakout reconnection prior to a CME. Chifor *et al.* (2006) observed pre-eruption EUV and X-ray brightenings close to the erupting footpoint of a prominence also during the slow-rise phase, consistent with Sterling and Moore (2005). Chifor *et al.* (2007) observed localized X-ray brightenings between 2 and 50 min before the impulsive phase of flares and filament acceleration in eight events. The filaments began to rise in the vicinity of the transient brightenings which occurred very close to the PIL at the sites of emerging or cancelling flux. Brightenings are created by magnetic reconnection which presumably leads to changes in the magnetic configuration that facilitate subsequent eruptions.

- Emerging Flux

  Observations indicate that emerging flux has a strong correlation with CMEs. Feynman and Martin (1995) investigated a large number of quiescent-filament eruptions and found that 17 of 22 filaments that were associated with new flux emergence erupted and 26 of 31 filaments that were not connected with new flux did not erupt. An important factor in whether a filament erupted was the relative orientation of the new flux with the pre-existing large-scale coronal field. In all cases in which the flux emergence was oriented favorably for reconnection, the filament erupted. Further, Green *et al.* (2003) conducted a systematic study of the magnetic field evolution of four ARs for 7 days as they crossed the solar disk. In their study a majority of the CMEs and flares occurred during or after new flux emergence. These observations are consistent with Chen and Shibata (2000) who proposed an emerging flux trigger model for the onset of CMEs. In their 2D MHD simulations, new flux that emerges in a filament channel cancels the magnetic field below the flux rope where a current sheet forms. The flux rope then rises due to loss of equilibrium of the

flux rope system. A similar sequence of events occurs with emerging flux in proximity of the filament channel. However, Gopalswamy *et al.* (2006) point out that since flux emergence is ubiquitous on the Sun, it is difficult to directly link specific flux emergence events to filament eruptions.

- Type-III Bursts and Radio Noise Storms

  There are possible CME precursors that have been identified in radio wavelength ranges. Jackson *et al.* (1978) investigated the possible association of type-III radio bursts with 40 CMEs observed by Skylab. Type-III radio bursts, which are electron beams propagating along 'open' field at speeds approaching 30% of the speed of light, occurred at 2.5 times the expected number 5 to 10 hrs before the CME observations. They conclude that type-III bursts are a good indicator of energy deposition and storage in the corona prior to a major eruption. Other authors suggest the type-III bursts are indicative of pre-eruption instabilities in the large-scale structure that eventually erupts (Gopalswamy *et al.* (2006) and Pick *et al.* (2006) and references therein). Further, several authors have found that CMEs are preceded by radio noise storms which originate from a persistently non-thermal accelerated particle population in the AR's coronal field (see Gopalswamy *et al.* (2006) and Chen *et al.* (2008) and references therein).

- Prominence Oscillations

  Prominence oscillations were first observed in Hα by Ramsey and Smith (1966). Oscillations can be caused by an internal or external trigger (Vrsnak, 1993). Internal triggers include eruptive MHD instabilities such as the kink instability and external triggers encompass MHD fast-mode blast waves, photospheric convection, and photospheric/chromospheric oscillations. Chen *et al.* (2008) suggest that initiation of CMEs may comprise another class of external trigger. They observed a prominence 'oscillation-and-eruption event' using Hα, white-light EUV imaging and SOHO SUMER spectrometer. The continuous oscillation lasted for four hours preceding the eruption of the prominence as a CME. Chen *et al.* (2008) argue that 90% of CMEs are associated with prominences therefore prominence oscillations are a viable CME precursor.

Here a novel type of CME precursor is reported. Approximately six hours prior to a CME eruption, intensification of plasma outflows from the periphery of an AR embedded in an equatorial CH was observed in velocity maps of *Hinode* EIS.

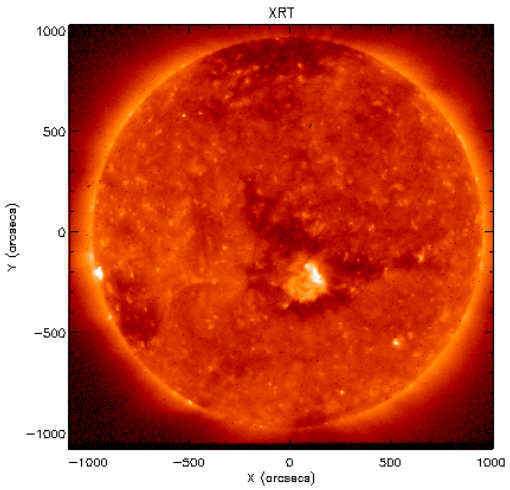

Figure 5.1: *Hinode* XRT al_mesh full disk image showing the AR-CH complex at the solar central meridian on 2007 October 17.

5.3 Data Analysis

Multi-wave length data are used to follow the evolution of an AR embedded in an equatorial CH from 2007 October 15 to 18. Figure 5.1 is a full disk X-ray image taken with the thin aluminum-on-mesh filter showing the AR-CH complex south of disk-center. The main focus of the study is to analyze multi-temperature plasma outflows of the AR and the surrounding CH. *Hinode* EIS (Culhane *et al.*, 2007a) provided the means to methodically examine these plasma flows. Other instruments are used to provide context information, magnetic field evolution, AR loop structure and evolution, and coverage of eruptive events such as a CME attributable to the AR.

(N.B. Both outflows and upflows are used to describe the blue-shifted plasma flows observed in EIS velocity maps. Typically, upflows are used in the context of MHD simulations where there is no attempt to determine whether the field lines that leave the computational box are in fact 'open' field lines along which flowing plasma would be considered to be outflows. By convention, outflows are used when associated with AR observations since these blue-shifted plasma flows are thought to be a possible source of the slow solar wind so that upward plasma flows would be outflows along 'open' field that extends into the heliosphere).

Hinode EIS has high spectral resolution that allows for accurate measurements of Doppler shifts and line broadenings in a wide range of lines formed at temperatures characteristic of the TR and the corona. The observations for this work consist

Table 5.1: EIS study details.

Date (2007)	Time (UT)	Study (No.)	Slit	Exp. Time (s)	FOV	Raster Time (hr)
Oct. 15	20:39	46	1”	15	256” × 256”	1.1
Oct. 16	02:17	46	1”	15	256” × 256”	1.1
Oct. 16	03:28	46	1”	15	256” × 256”	1.1
Oct. 16	04:39	46	1”	15	256” × 256”	1.1
Oct. 16	21:11	205	1”	45	360” × 512”	2.3
Oct. 17	00:26	205	2”	45	360” × 512”	2.3
Oct. 17	02:47	205	2”	45	360” × 512”	2.3
Oct. 18	00:18	198	1”	45	460” × 384”	5.1

of rasters using both the 1” and 2” slits stepped from solar west to east. Rasters contain from 15 to 24 spectral lines, depending on the study. Table 5.1 summarizes the EIS raster details including the FOV, exposure times and total raster time for each study. The quality of the velocity data varies with exposure time and slit size. None of the EIS studies were designed for simultaneous observation of an AR and a CH. Most of the Doppler shift results are obtained from EIS's Fe XII 195 Å core line. Fe XII 195 Å is most suitable for line profile measurements because good count rates are available for bright AR features and the low intensity CH. However, count rates for hotter lines such as Fe XV 284 Å in the CH were not sufficient for short exposure, 1” studies.

Raw spectral data were corrected for dark current, hot pixels, warm pixels, and cosmic rays using eis_prep. An adapted version of eis_auto_fit was used to fit calibrated spectra with a single Gaussian function. Instrumental effects including orbital variation and slit tilt were removed using eis_wave_corr and CCD detector offset was taken into account. Linewidths were calibrated using the eis_width2velocity routine and instrumental width for the SW CCD detector was assumed to be 0.054 Å for the 1” slit and 0.061 Å for the 2” slit (Brown *et al.* (2008); and EIS WIKI: `http://msslxr.mssl.ucl.ac.uk:8080/eiswiki/Wiki.jsp?page=2EISSlit`). All of the routines for data preparation and calibration are included in the standard EIS SolarSoft package in IDL. Chapter 3 has a more detailed discussion on handling EIS data.

STEREO 195 Å, SOHO MDI magnetic field, TRACE 171 Å, and *Hinode* XRT data were prepared and calibrated using standard instrumental routines in SolarSoft. For a detailed discussion of MDI data issues, please see §4.3.4.

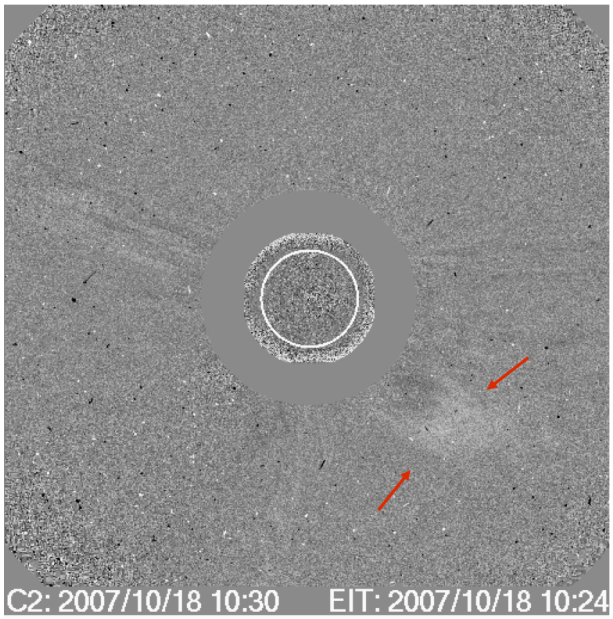

Figure 5.2: Slow CME viewed by LASCO C2 coronagraph on 2007 October 18 at 10:24 UT.

5.4 Coronal Observations

The evolution of a small AR was observed using multi-wavelength data during its passage across the solar disk. It appeared at the east limb on 2007 October 11 and was located inside an on-disk CH approximately 200" south of the solar equator. Central meridian passage occurred at about 17:00 UT on October 17. The AR was associated with a slow coronal mass ejection (CME) of 371 km s^{-1} as viewed by the Large Angle and Spectroscopic Coronagraphs (LASCO) on board SOHO. There were no significant GOES X-ray flares detected with the CME. Figure 5.2 shows the CME eruption located in the southwestern quadrant of the LASCO difference image timed at 10:24 UT on 2007 October 18 (`http://cdaw.gsfc.nasa.gov/CME_list/`).

The on-disk evolution of the CME onset can be followed in STEREO EUVI 195 Å images. At approximately 07:05 UT, the ARs loops are beginning to brighten towards the west as shown in the top panel of Figure 5.3. These images are displayed in reverse color so that bright features such as the AR loops appear dark. By 08:10 UT, the AR's outer loops are expanding and beginning to 'peel' away along the west/southwestern perimeter (red arrows) coincident with the formation of a small dimming region (white arrow) at the AR's center in the middle panel of Figure 5.3. The dimming region is located at approximately X = -50", Y = -175". Loops continue to 'peel' away as the AR erupts until approximately 09:00 UT when the bright post-eruption arcade of loops (blue arrow) begin to form after the CME (bottom panel of Figure 5.3).

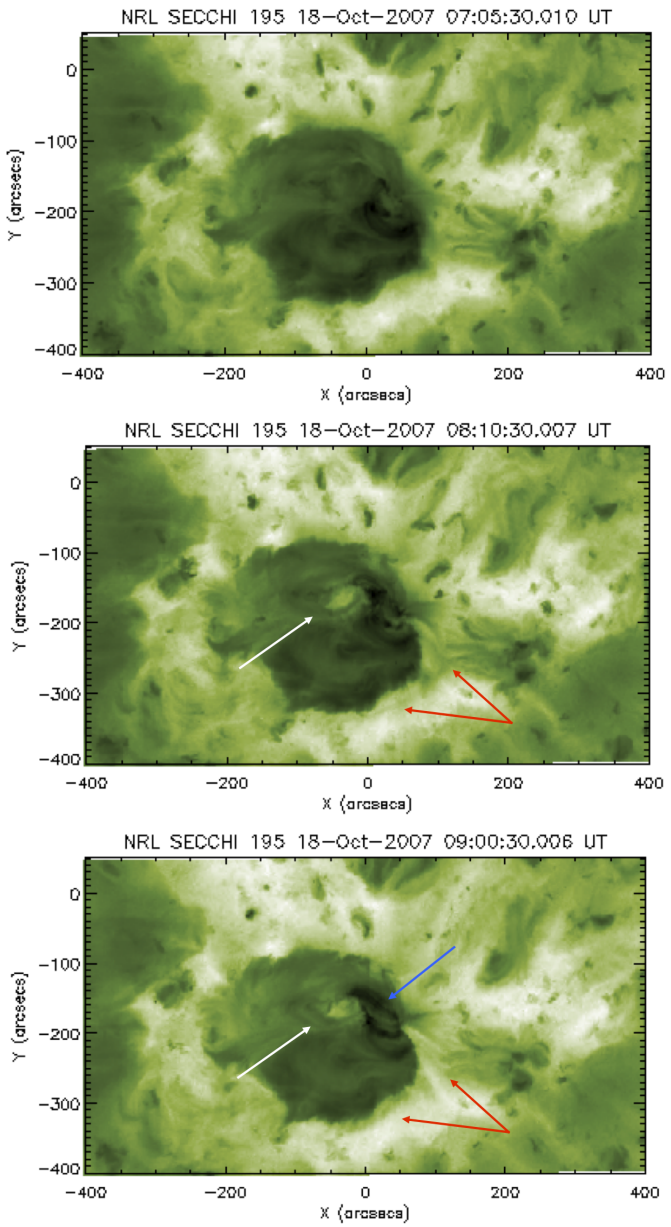

Figure 5.3: Reverse color STEREO A 195 Å images of the AR in an on-disk CH. Top panel shows the AR about 30 mins before the CME eruption. Middle and bottom panels show the AR about 30 mins and 1.5 hrs, respectively, after the CME. The arrows indicate classic CME signatures - white arrows for a dimming region, red arrows for 'peeling away' loops, and blue arrow for the post-eruption loop arcade.

The presence of a filament is evident in TRACE 171 Å data on the October 17th and 18th. Figure 5.4, top panel, shows the smoothly curved reverse S-shaped filament located in the northeastern quadrant of the AR. Hα images from Kanzelhöhe Observatory (Austria) confirm the existence of a filament on the 17th (bottom panel of Figure 5.4). Prior to the CME, from 04:47 to 05:01 on the 18th, plasma is flowing along the filament (though there are gaps on either side of this period in the TRACE data). During the onset of the CME eruption, the filament has developed a kink as shown in the middle panel of Figure 5.4.

Figure 5.5, left panel, is a zoomed XRT image taken with the thin-aluminum/polyamide filter showing the hot loop configuration of the AR. To the northwest, X-ray loops appear highly sheared. This loop structure is evident in XRT movies of various filters from early on the 16th, however, whether the sheared arcade was present earlier can not be determined due to projection effects as the AR's position is close to the eastern limb. On October 18, prior to the eruption/CME, a clear reverse-S sigmoid-shaped loop structure is evident in X-rays as viewed in the right panel of Figure 5.5 and in Figure 5.6. The reverse-S sigmoid is consistent with the counter-clockwise rotation of the AR magnetic structure seen at the time of the eruption. Rotation is observed at multiple coronal temperatures ranging from 1 MK (TRACE 171 Å and STEREO EUVI 195 Å) to 6 MK (XRTs titanium-polyamide filter). A sense of counter-clockwise rotation is apparent as the AR's expanding loops 'peel' away during the eruption as indicated by the yellow arrows in Figure 5.6 and the red arrows in Figure 5.3.

5.5 Magnetic Field Evolution

The AR was measured to have magnetic flux of approximately 3×10^{21} Mx as it crossed the solar central meridian, which suggests it was a relatively small AR (Zwaan, 1987). On October 14th, MDI magnetograms show the following AR polarity (positive) has started to break up and disperse while the leading polarity (negative) remains essentially concentrated. By early on the 15th, the negative field has fragmented as well. It is clear that the AR is in the decay phase of its evolution. Figure 5.7 displays a series of MDI magnetograms on October 17th and 18th leading up to/during/after the CME eruption.

Figure 5.4, top and middle panels, shows TRACE 171 Å images overlaid with SOHO MDI magnetic field $\pm$ 150 G contours. The filament lies along the PIL in the northwestern quadrant of the AR. Opposite polarity flux converges at two different points along the PIL from early on the 17th. These two points of flux cancellation

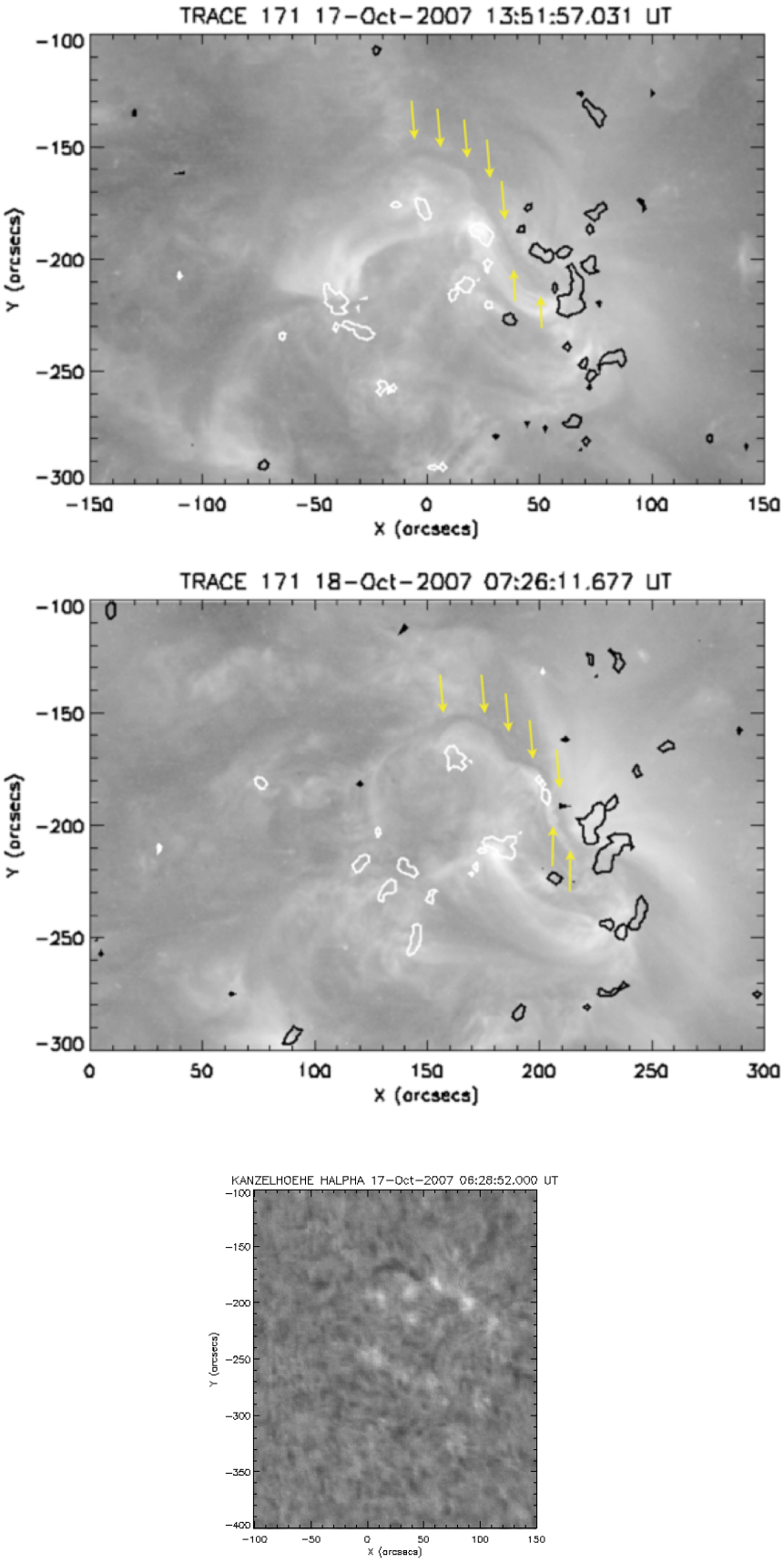

Figure 5.4: Top and middle panels are TRACE 171 Å images of the AR in a CH one day and minutes before the CME. The filament (indicated by yellow arrows) develops a kink minutes before the eruption. MDI magnetic field contours black/white ± 150 G are overlaid on both images. Bottom image is Hα data from Kanzelhöhe Observatory showing the filament at 06:26 UT on October 17.

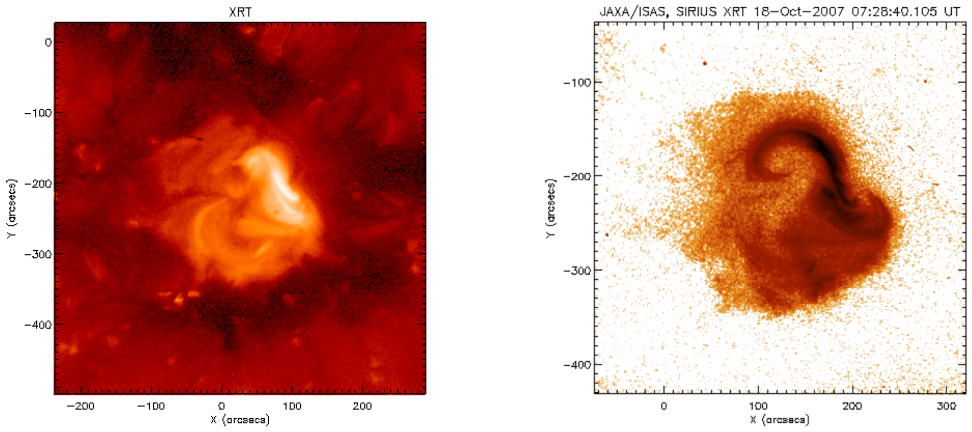

Figure 5.5: Left panel - *Hinode* XRT thin_poly filter zoomed image showing the highly sheared loops in the northwest of the AR. Right panel - Reverse S-shaped sigmoid structure in the AR at the time leading up to/during the eruption.

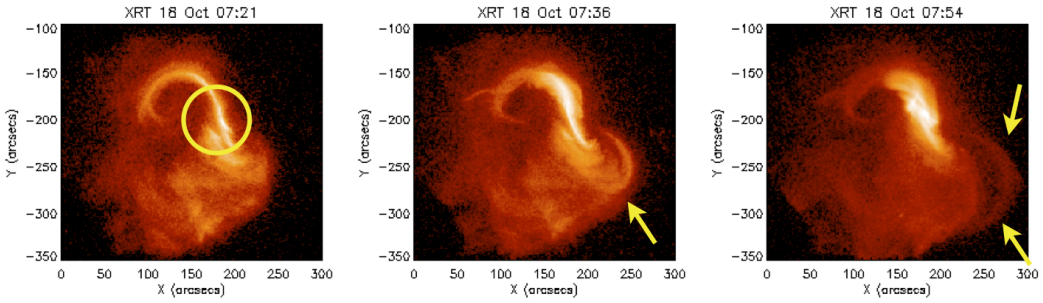

Figure 5.6: *Hinode* XRT images of the sigmoid structure and loops 'peeling' away during the eruption. The bright sigmoid is located over the region of most intense magnetic flux cancellation (cf. §5.5).

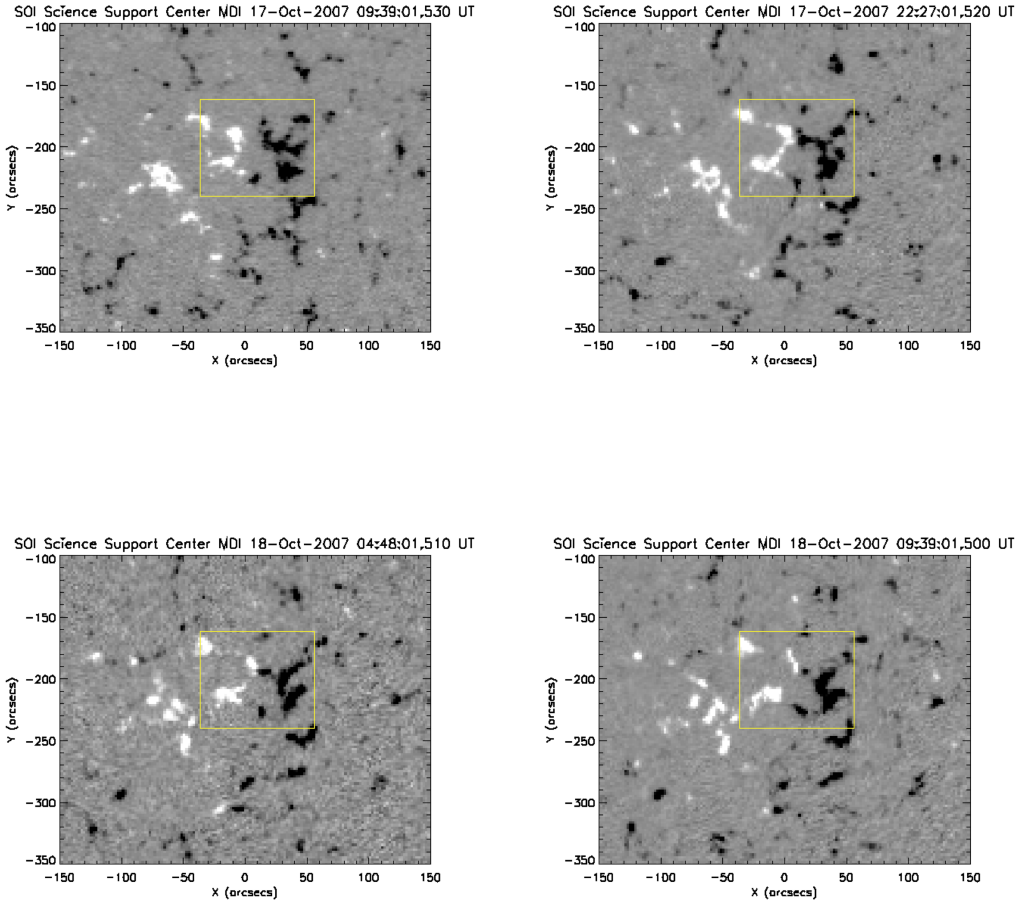

Figure 5.7: Magnetic field evolution indicating the region of principal flux cancellation along the main magnetic inversion line of the AR. Note that a lower level of flux is cancelling all along the boundary of the included positive polarity.

are contained in the yellow boxes in Figure 5.7. Frequency of flux convergence and subsequent cancellation events increases leading up to the CME eruption on the 18th when opposite polarity flux converges beneath the filament preceding the eruption. The brightening of the X-ray sigmoidal loop structure occurs above the site of flux cancellation just prior to the eruption.

The location of the AR in a CH provided a unique opportunity to measure flux cancellation with a high degree of confidence. Typically, flux changes are difficult to measure in an AR located in the quiet Sun or nested amongst other ARs due to the mixing of magnetic fragments. In the AR-CH complex, the positive polarity of the AR is easy to identify in the negative polarity CH so that the change in flux over time can be determined by simply setting a contour around the positive polarity fragments and measuring the positive flux contained within the contour. Figure 5.8 shows the evolution of AR flux determined from SOHO MDI magnetograms from

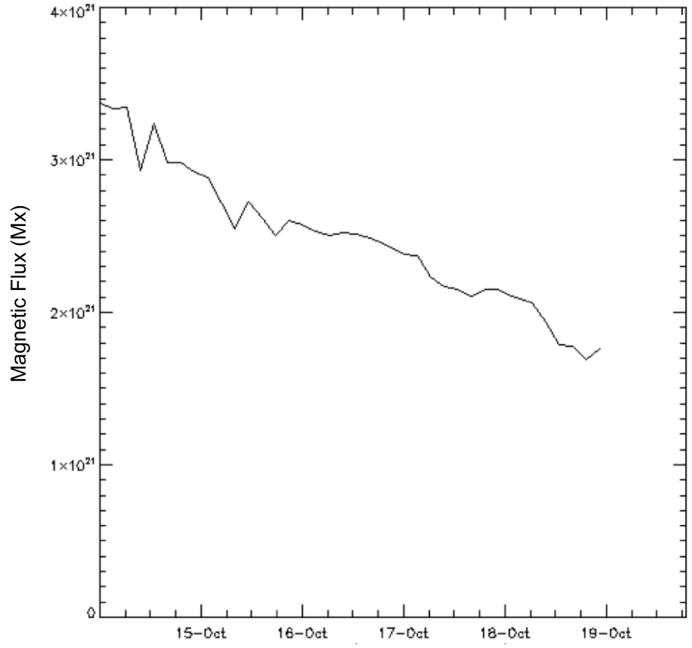

Figure 5.8: Plot of AR positive flux from 00:03 UT on October 14th to 00:03 UT on October 19th. Approximately 10% per day of the total flux is removed from the AR over the four-day period leading up to the eruption.

October 14th to 19th. Approximately 30% of the flux is removed from the AR in the three days leading up to the CME eruption.

5.6 Active Region Outflows

5.6.1 Multi-temperature EIS Intensity and Velocity Maps - 2007 October 17 02:27 UT

Figures 5.9, 5.10, and 5.11 show a range of emission line intensity (left) and velocity (right) maps on October 17 at 02:27 UT. The coolest line is He II 256.32 Å with a temperature of $10^{4.7}$ K. This line is one of the three strong core EIS lines, however, it is a complex blend of much higher temperature Si X, Fe XII, and Fe XIII emission lines (T = $10^{6.1}$ K, $10^{6.2}$ K, and $10^{6.1}$ K, respectively; Young *et al.* (2007)). It is likely that the bright loops are of the higher temperature blends as the same feature is visible in hotter Fe ions intensity maps. The He II velocity map is dominated by red-shifted downflows in the AR. The surrounding CH is a mix of downflows and blue-shifted

outflows though blue-shifts are slightly more characteristic of this region. Mg VII 278.39 Å and Si VII 275.35 Å lines have similar formation temperatures ($10^{5.8}$ K) and, as expected, common features are found in their intensity and velocity maps. Red-shifted, low lying compact loops are located in the core of the AR. A comparison of Si VII and Mg VII (blended with Si VII) velocity maps confirms that the lines have similar strength signals (or counts) in EIS AR spectrum as the red-shifted loops appear roughly the same, however, the Si VII has a stronger signal in the EIS quiet Sun spectrum so the CH portion of velocity map is more distinct. Whereas the cooler chromospheric and TR lines are dominated by red-shifted downflows, hotter coronal lines have definite blue-shifted outflows at the periphery of the AR. The blue-shifted outflow regions appear to expand with temperature as is evident when comparing velocity maps of Fe X 184.54 Å in Figure 5.10 (T = 10^6 K) and Fe XII 195.12 Å and Fe XIII 202.04 Å (T = $10^{6.1}$ K and $10^{6.2}$ K, respectively; Young *et al.* (2007)) in Figure 5.11. The outflow regions fan-out and velocities increase with temperature (Del Zanna, 2008). In this data set the hotter Fe ions also have very bright extended loop structures in common. Fe X and Fe XIII are unblended lines, however, Fe XII is self-blended at 195.18 Å and is at the peak of the EIS sensitivity curve so is the strongest emission line observed by EIS (Young *et al.*, 2007).

5.6.2 Fe XII EIS Observations - 2007 October 15 to 18

In the previous section, multi-temperature intensity and velocity maps of a single EIS observation were described. Here, only the core EIS Fe XII 195 Å emission line outflows are compared over four days of observations. Velocity maps of each of the eight observations are displayed together in Figure 5.12 and linewidths in Figure 5.13. In addition, intensity and velocity maps are shown separately in the right panels of Figures 5.14 to 5.21. These maps are overlaid with SOHO MDI magnetic field contours of ± 100 G (green/black contours).

In the velocity maps of Figure 5.12, there are a series of loops structures connecting positive to negative magnetic field concentrations at the AR's footpoints. These loops are clearly red-shifted, indicating downflows within the loop structures. Downflows are persistent in the AR's loops throughout the observation period. LOS downflow velocities range from a few km s^{-1} up to a maximum of 35 km s^{-1}.

Blue-shifted outflow regions are observed at the periphery of the AR in velocity maps from 15th and early on the 16th. As the AR approaches closer to disk center at 21:11 UT on the 16th, outflows are visible on both sides of the AR, located over the magnetic field concentrations of the ARs footpoints. Outflows are still clearly visible on both sides of the AR on the 17th. The western outflow region has

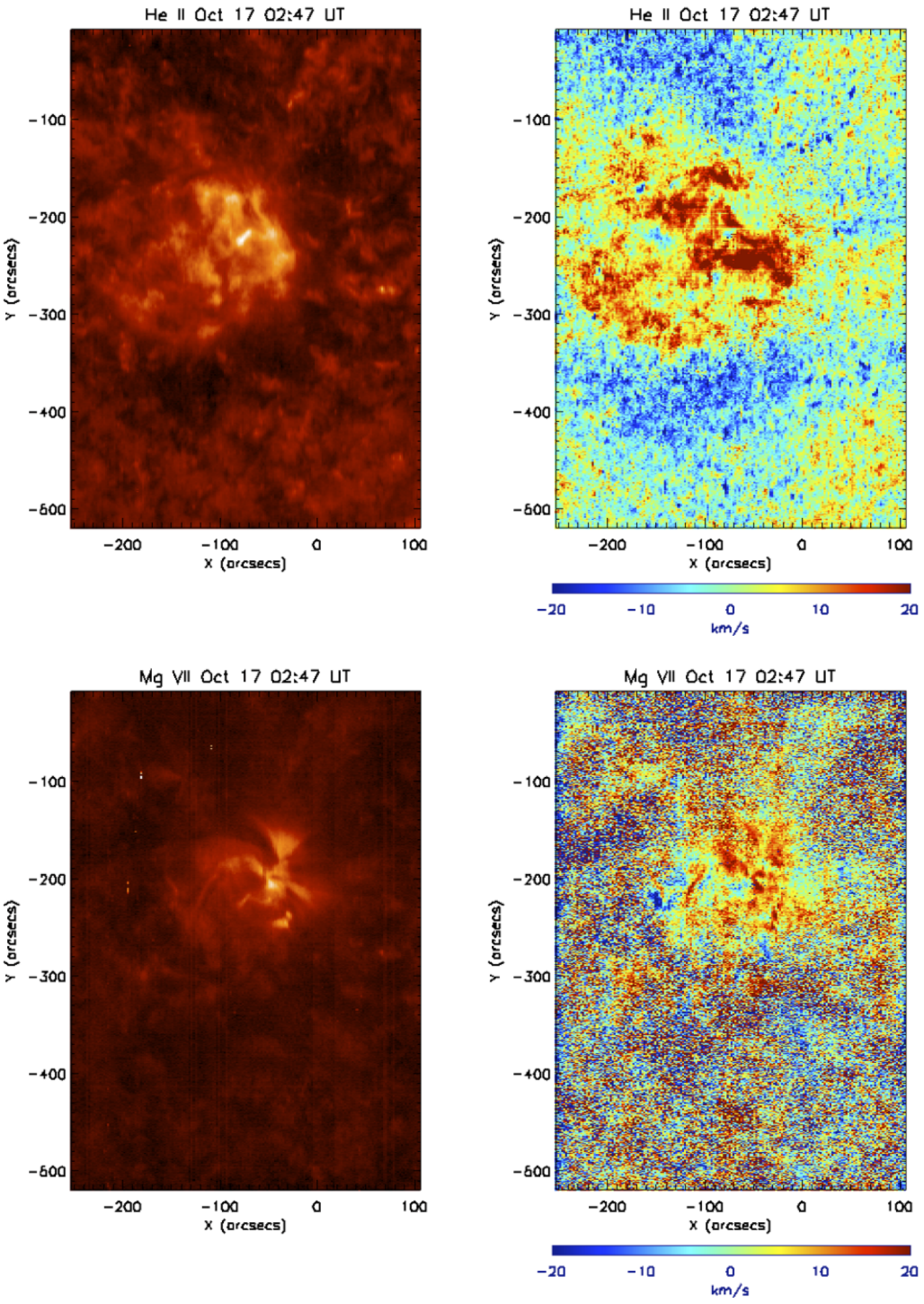

Figure 5.9: He II and Mg VII EIS intensity (left) and velocity (right) maps on 2007 October 17 at 02:47 UT.

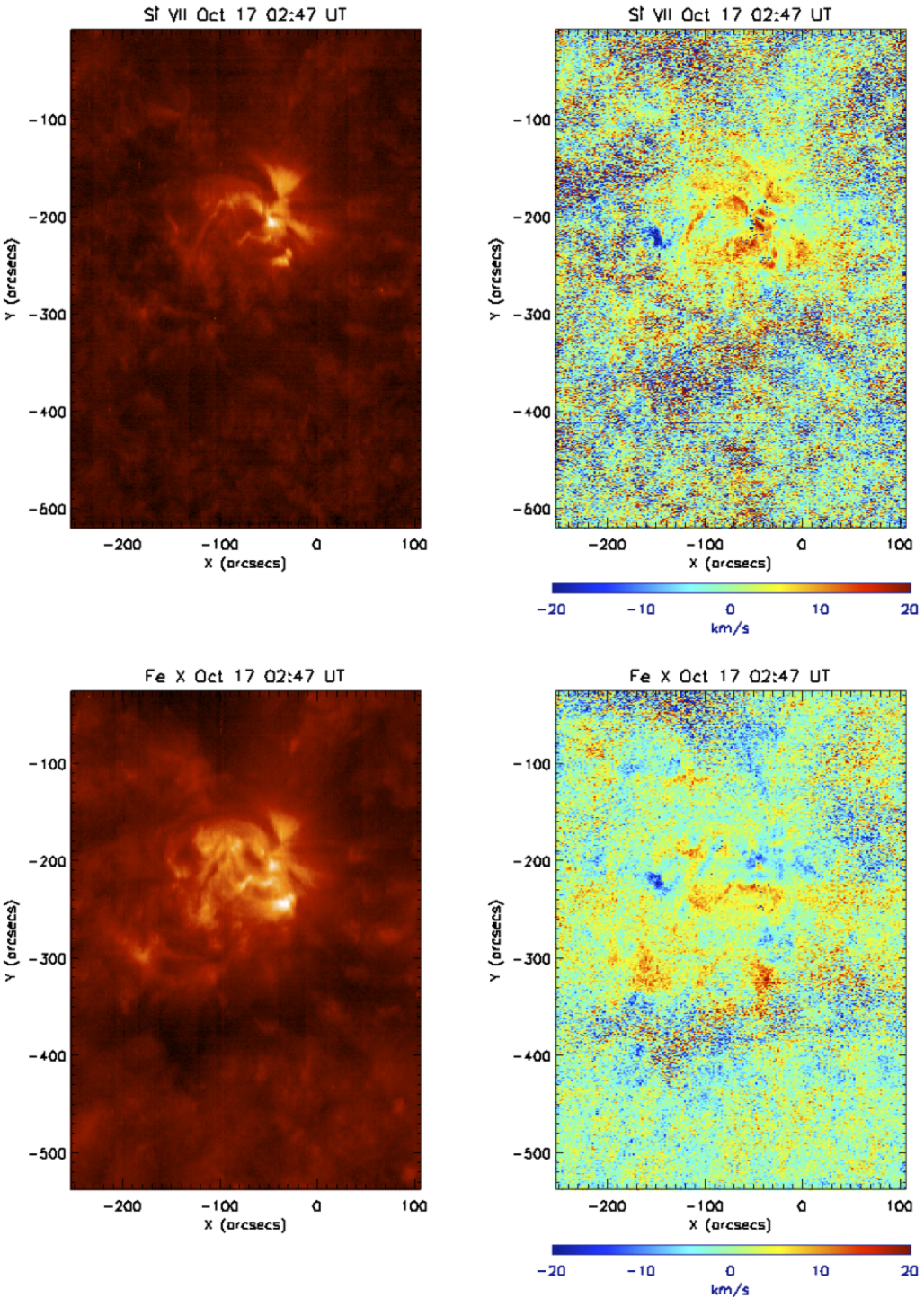

Figure 5.10: Si VII and Fe X EIS intensity (left) and velocity (right) maps on 2007 October 17 at 02:47 UT.

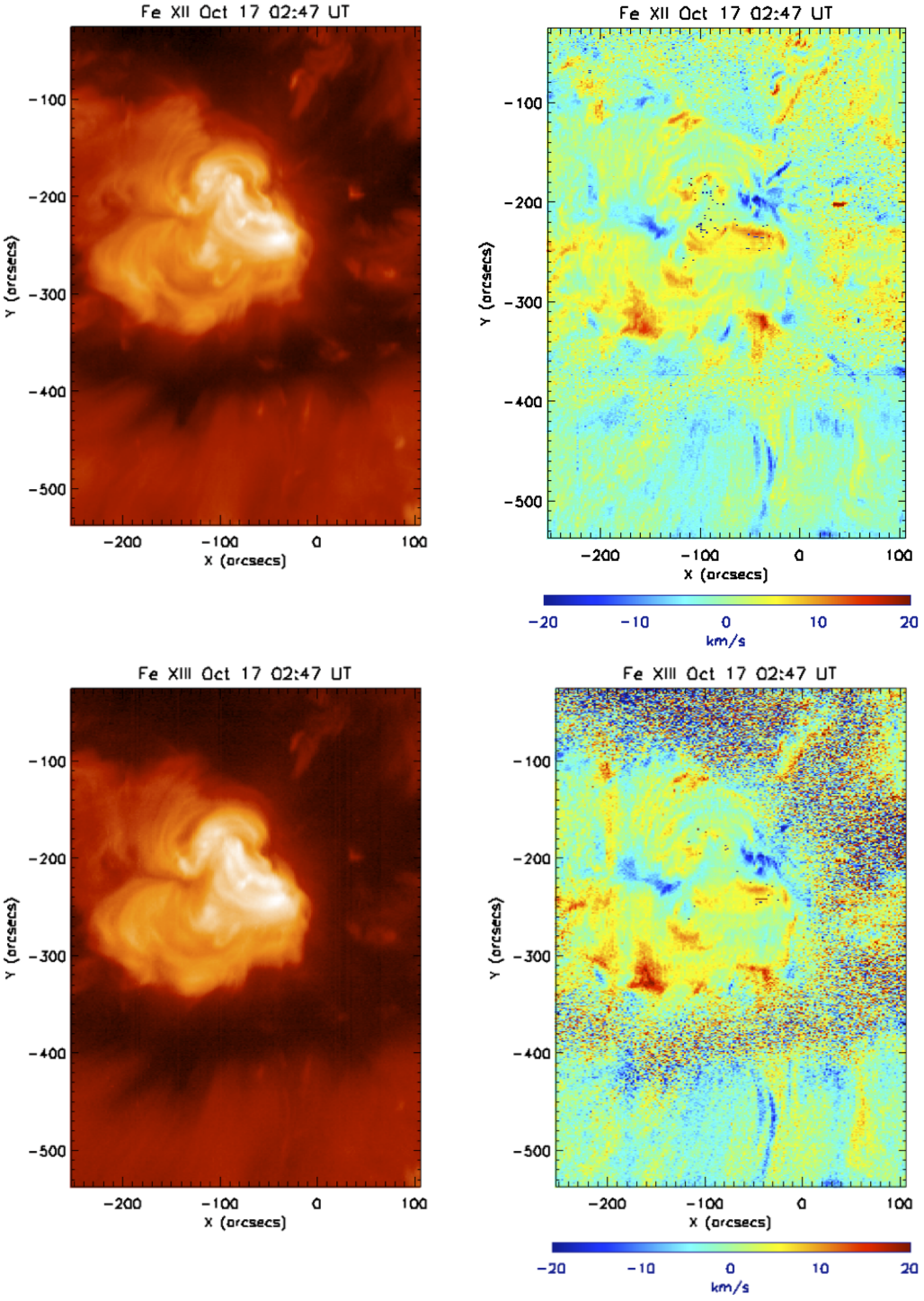

Figure 5.11: Fe XII and Fe XIII EIS intensity (left) and velocity (right) maps on 2007 October 17 at 02:47 UT.

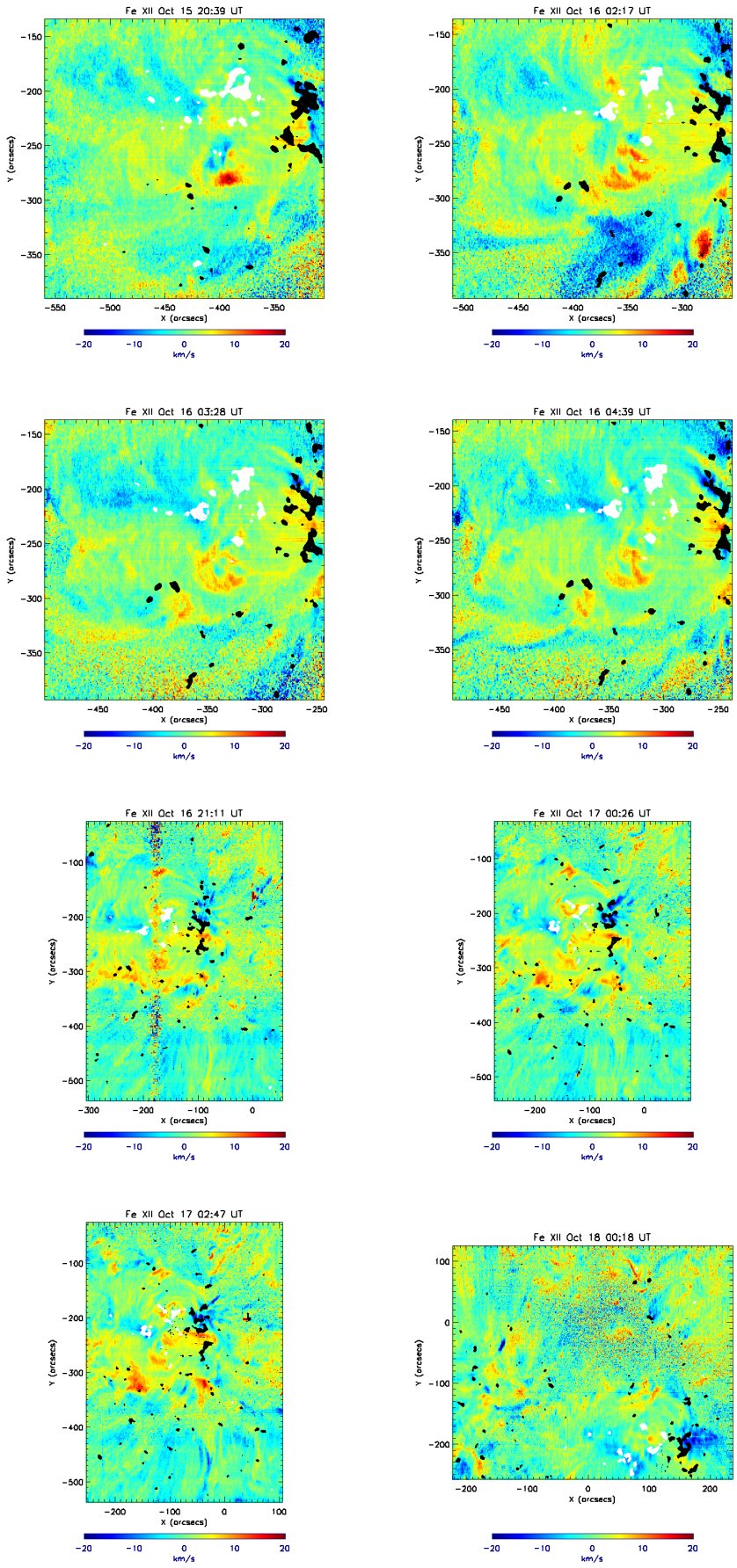

Figure 5.12: EIS Fe XII emission line velocity maps for the observation period. Velocity maps are overlaid with SOHO MDI magnetic field contours of ± 100 G (white/black contours). Outflows occur over monopolar magnetic field concentrations and persist for four days.

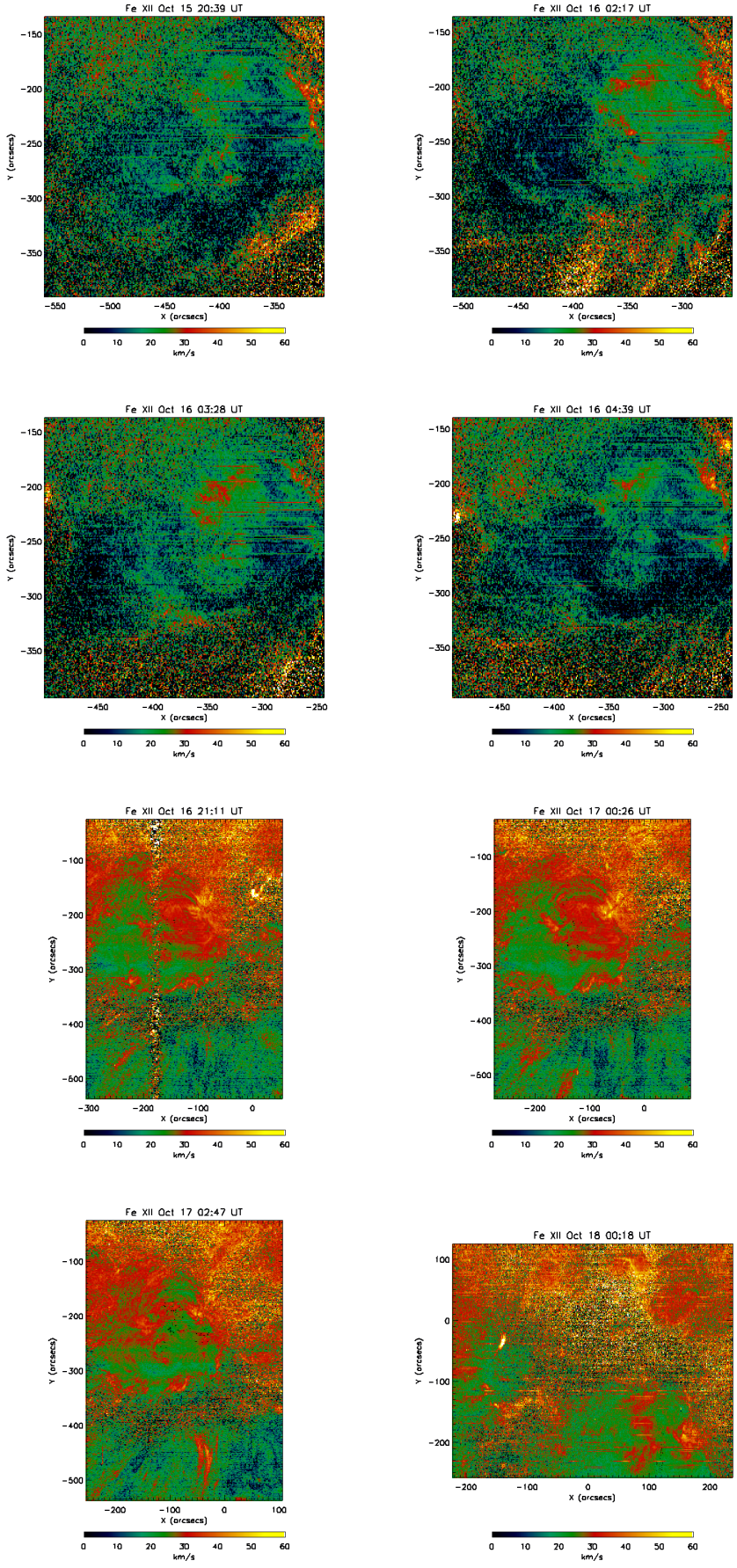

Figure 5.13: EIS Fe XII emission line linewidth maps for the observation period.

formed a rosette-like shape with outflows tracing the dense footpoint structure. On the eastern side, the AR looks similar to a sea anemone. The so-called anemone structure is characterized by loops that connect the AR's positive polarity and the opposite polarity of the surrounding monopolar CH. The eastern outflows appear to originate from a region in the middle of the anemone structure. (See Chapter 4 for the significance of anemone formation in the AR and Chapter 3 for a detailed discussion of AR outflows). Blue-shifted velocities in the core eastern and western outflow regions ranged from approximately 5 to 12 km s^{-1} in velocity maps from the 15th to the 17th.

Though the AR evolved during the observing period, overall, features remained unchanged. The location of the eastern and western outflows changed slightly from day to day, however, the outflows continue to originate from the periphery of the AR, over areas of positive and negative magnetic field concentration. EIS's FOV is no longer centered on the AR on October 18. The FOV covers the top 2/3 of the AR and a significant portion of the surrounding CH to the north. By this time, the outflow regions on both sides of the AR have filled out and expanded as the underlying magnetic field continues to disperse. Red-shifted loop structures are not as pronounced as in earlier velocity maps.

Examination of corresponding velocity and linewidth maps in Figures 5.12 and 5.13 reveal that strongly blue-shifted regions are spatially coincident with regions of strong line broadening. This feature is present throughout the observing period in all rasters. In fact, the strongest line broadening occurs in the areas of the strongest outflow, whether in the AR or along the CH boundary. Strong outflows and broadenings in coincident locations in the AR take place over the footpoints where magnetic field concentrations are largest. The same effect is observed along the CH boundary on the 18th (X = -130 and Y = -20). Strong line broadenings associated with regions of strong outflows were evident in a range of coronal lines in addition to the core Fe XII line.

5.6.3 Intensification of AR Outflows on 2007 October 18

For each EIS raster, the locations of so-called 'core' AR outflows are identified using velocity profiles. Profiles were obtained by making east-west cuts through the outflow regions near the AR's footpoints in each velocity map. These cuts were made parallel to the X-axis at 10" intervals. Velocities were then averaged over the 10" in the Y-direction, ± 5" either side of the cut, for each pixel along the cut.

For the first three days of EIS rasters, velocity profiles showed outflow velocities

consistently between 5 and 12 km s^{-1} on either side of the AR as is clearly evident in the velocity profiles in Figures 5.14 to 5.20. However, on the 18th at 00:18 UT, velocity profiles reveal a distinct intensification in velocities in the western outflow region up to 18 km s^{-1} in profiles along cuts 5 to 8 in Figure 5.21. Similar intensification in outflow velocities on the 18th were observed in all reasonably unblended coronal lines.

5.6.4 Summary of Observations

The following is a summary of the multiple-instrument observations made of the AR-CH complex from October 15 to 18:

- EIS velocity maps of the AR-CH complex revealed blue-shifted outflows at the periphery of the AR that were persistent during four days of EIS observations.
- These outflows range from about 5 to 12 km s^{-1} from October 15 to 17.
- The strongest outflows are spatially coincident with areas of magnetic field concentrations of a single polarity.
- AR outflows were clearly identifiable in hotter coronal lines such as Fe X, Fe XII, and Fe XIII but are much less pronounced or virtually non-existant in cooler lines such as He II, Mg VII and Si VII.
- The strongest line broadening of 40 to 60 km s^{-1} occurs in the regions of strongest outflows.
- At 00:18 UT on 18 October, velocity profiles display a distinct intensification in outflow velocities to 18 km s^{-1} on the western side of the AR where there is a filament lying along the PIL. Similar intensification in outflow velocities occurred in unblended coronal lines where sufficient data count rates were available.
- The southwest side of the AR erupted at approximately 07:30 UT on the 18th. Classic on-disk signatures of CMEs are observed in STEREO EUVI, *Hinode* XRT, and TRACE data including, sigmoidal loop structures, dimming regions, and post-eruption loop arcades.
- A slow CME was observed in LASCO C2 Coronagraph beginning at 09:00 UT.
- Magnetic flux cancellation of approximately 10% per day for over three days precedes the CME eruption.

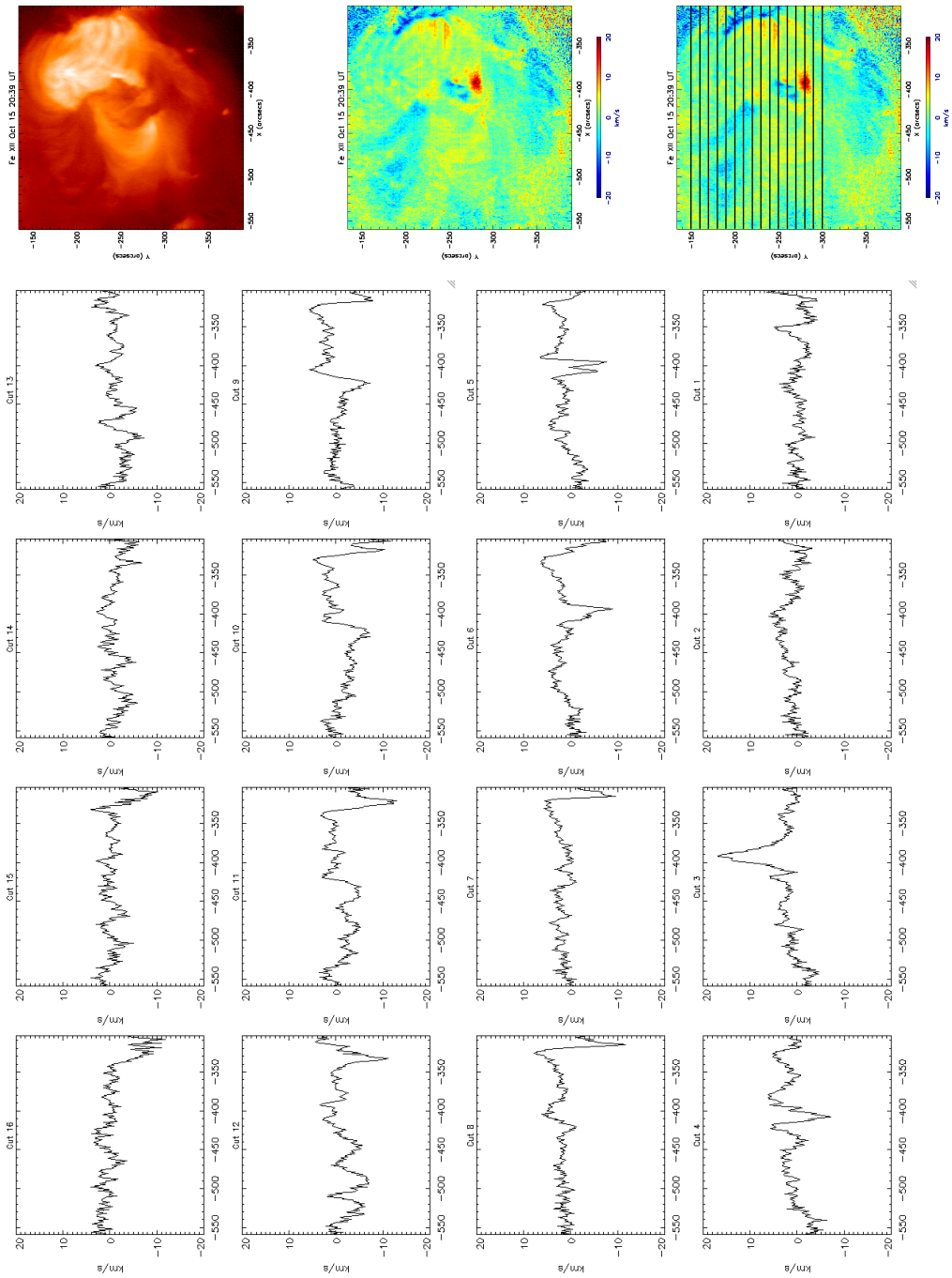

Figure 5.14: 2007 October 15 20:39 UT EIS 195 Å emission line intensity map (top right), velocity map (middle right), velocity map overlaid with latitudinal (Y-axis) locations of velocity cuts (bottom right), and velocity cuts 1 - 16. Velocity Cut 1 is at Y = -300" and Cut 16 is at Y = -150". A velocity cut is averaged over 10" in the Y-direction (±5") along a line in the velocity map.

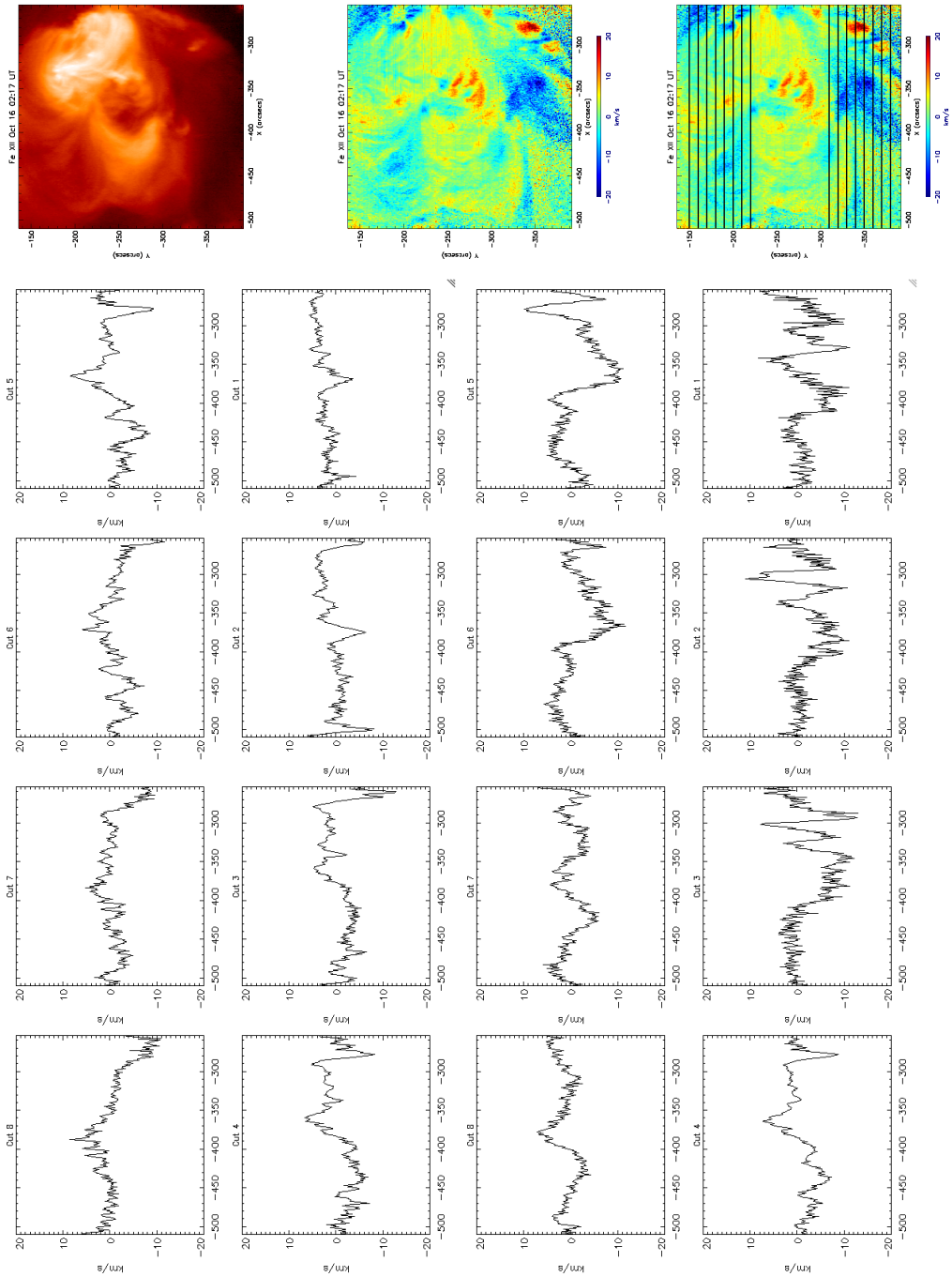

Figure 5.15: 2007 October 16 02:17 UT EIS 195 Å emission line intensity map (top right), velocity map (middle right), velocity map overlaid with latitudinal (Y-axis) locations of velocity cuts (bottom right), and velocity cuts top 1 - 8 and bottom 1 - 8. Velocity Cut 1 (top) is at Y = -220" and Cut 8 (top) is at Y = -150". Velocity Cut 1 (bottom) is at Y = -380" and Cut 8 (bottom) is at Y = -310". A velocity cut is averaged over 10" in the Y-direction (±5") along a line in the velocity map.

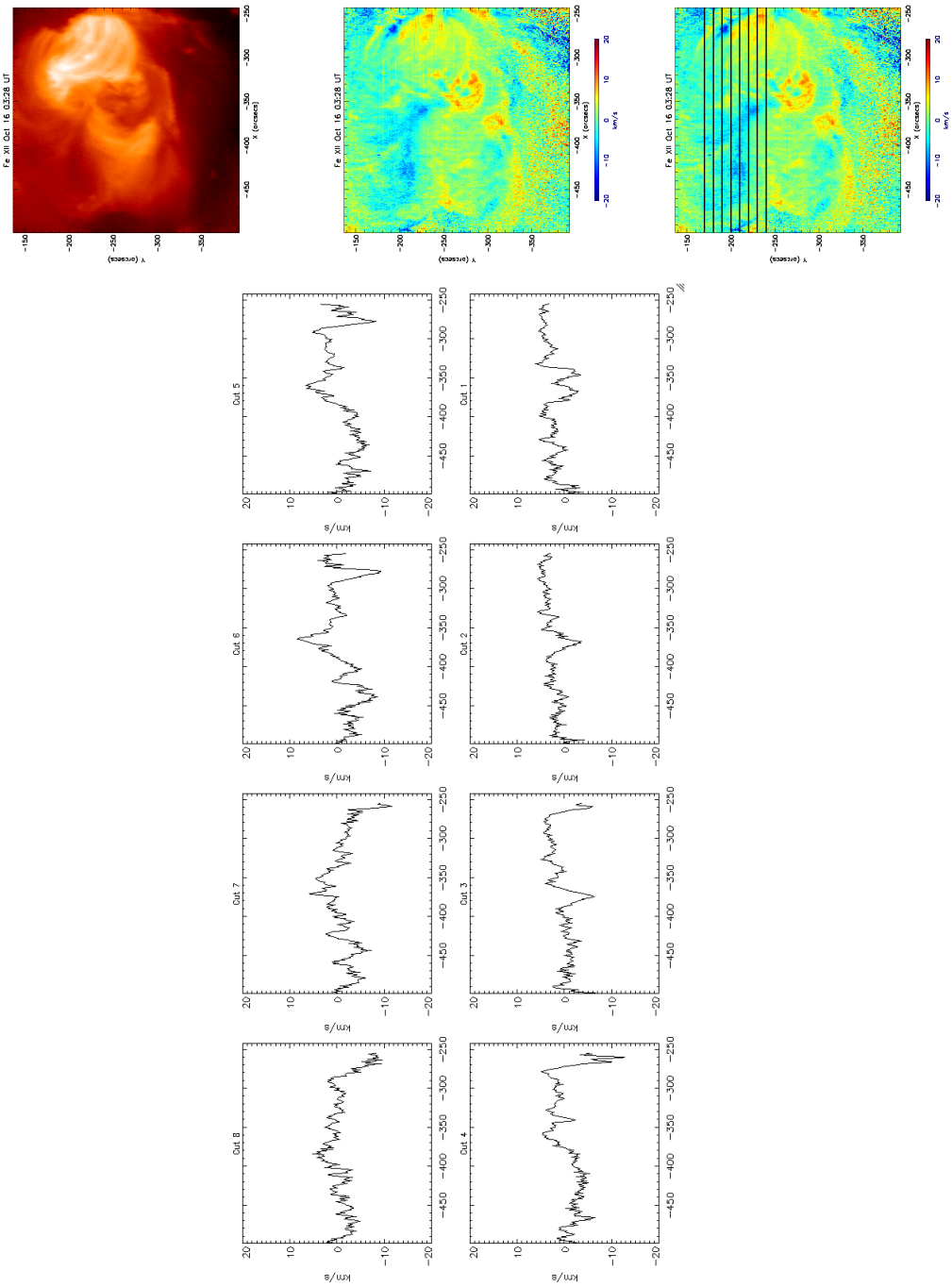

Figure 5.16: 2007 October 16 03:28 UT EIS 195 Å emission line intensity map (top right), velocity map (middle right), velocity map overlaid with latitudinal (Y-axis) locations of velocity cuts (bottom right), and velocity cuts top 1 - 8. Velocity Cut 1 is at Y = -240" and Cut 8 is at Y = -170". A velocity cut is averaged over 10" in the Y-direction (±5") along a line in the velocity map.

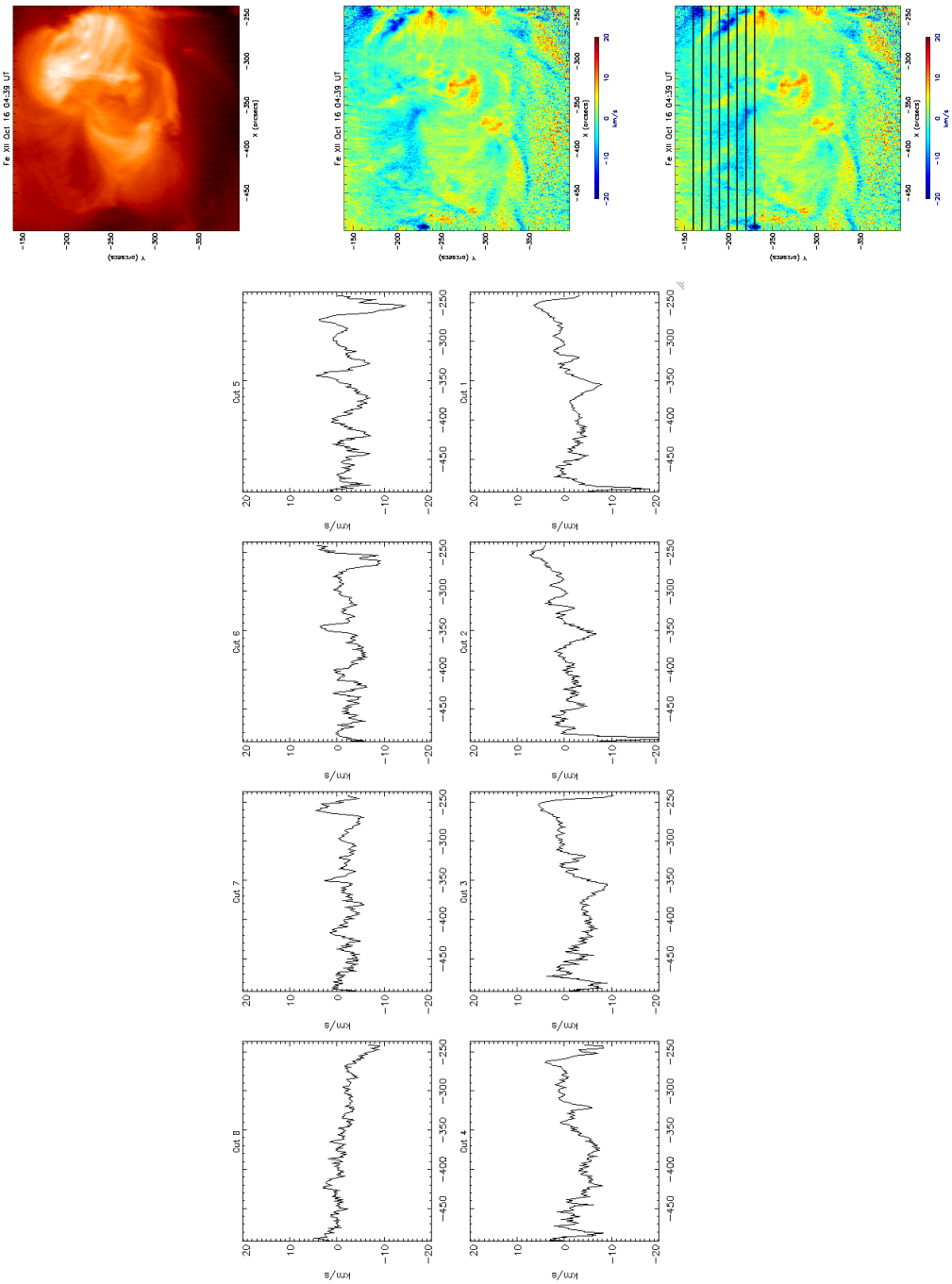

Figure 5.17: 2007 October 16 04:39 UT EIS 195 Å emission line intensity map (top right), velocity map (middle right), velocity map overlaid with latitudinal (Y-axis) locations of velocity cuts (bottom right), and velocity cuts top 1 - 8. Velocity Cut 1 is at Y = -230" and Cut 8 is at Y = -160". A velocity cut is averaged over 10" in the Y-direction (±5") along a line in the velocity map.

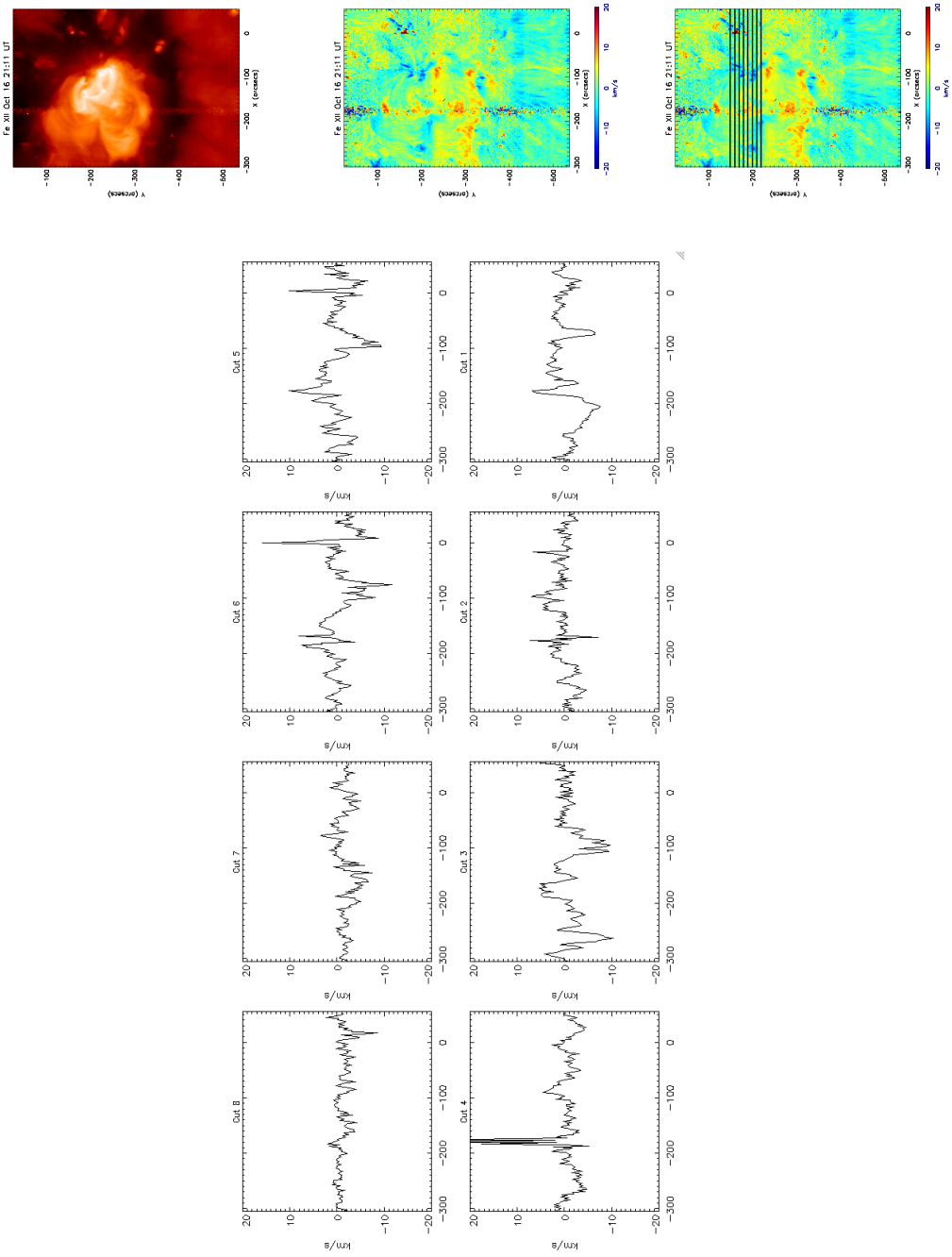

Figure 5.18: 2007 October 16 21:11 UT EIS 195 Å emission line intensity map (top right), velocity map (middle right), velocity map overlaid with latitudinal (Y-axis) locations of velocity cuts (bottom right), and velocity cuts top 1 - 8. Velocity Cut 1 is at Y = -220" and Cut 8 is at Y = -150". A velocity cut is averaged over 10" in the Y-direction (±5") along a line in the velocity map.

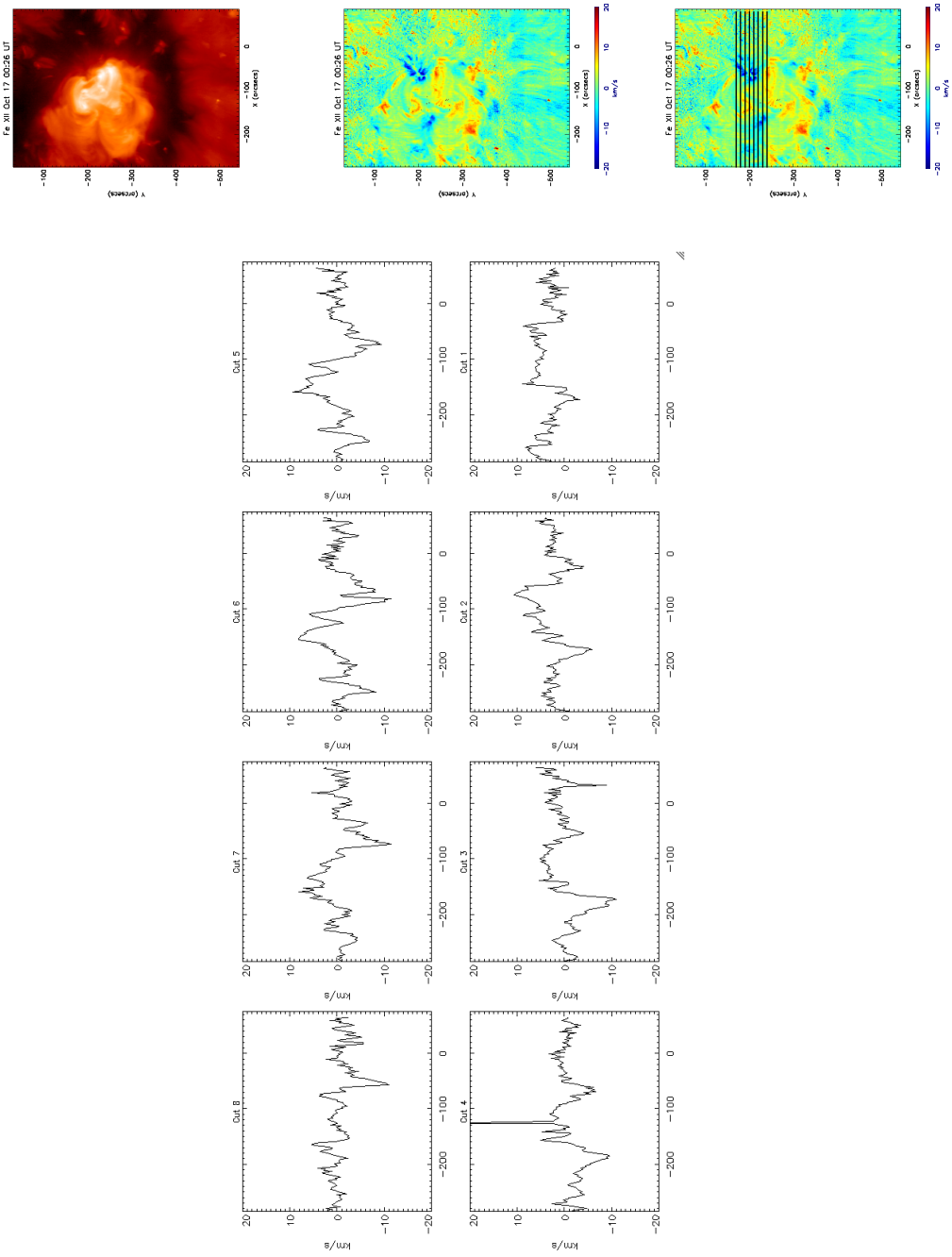

Figure 5.19: 2007 October 17 00:26 UT EIS 195 Å emission line intensity map (top right), velocity map (middle right), velocity map overlaid with latitudinal (Y-axis) locations of velocity cuts (bottom right), and velocity cuts top 1 - 8. Velocity Cut 1 is at Y = -240" and Cut 8 is at Y = -170". A velocity cut is averaged over 10" in the Y-direction (±5") along a line in the velocity map.

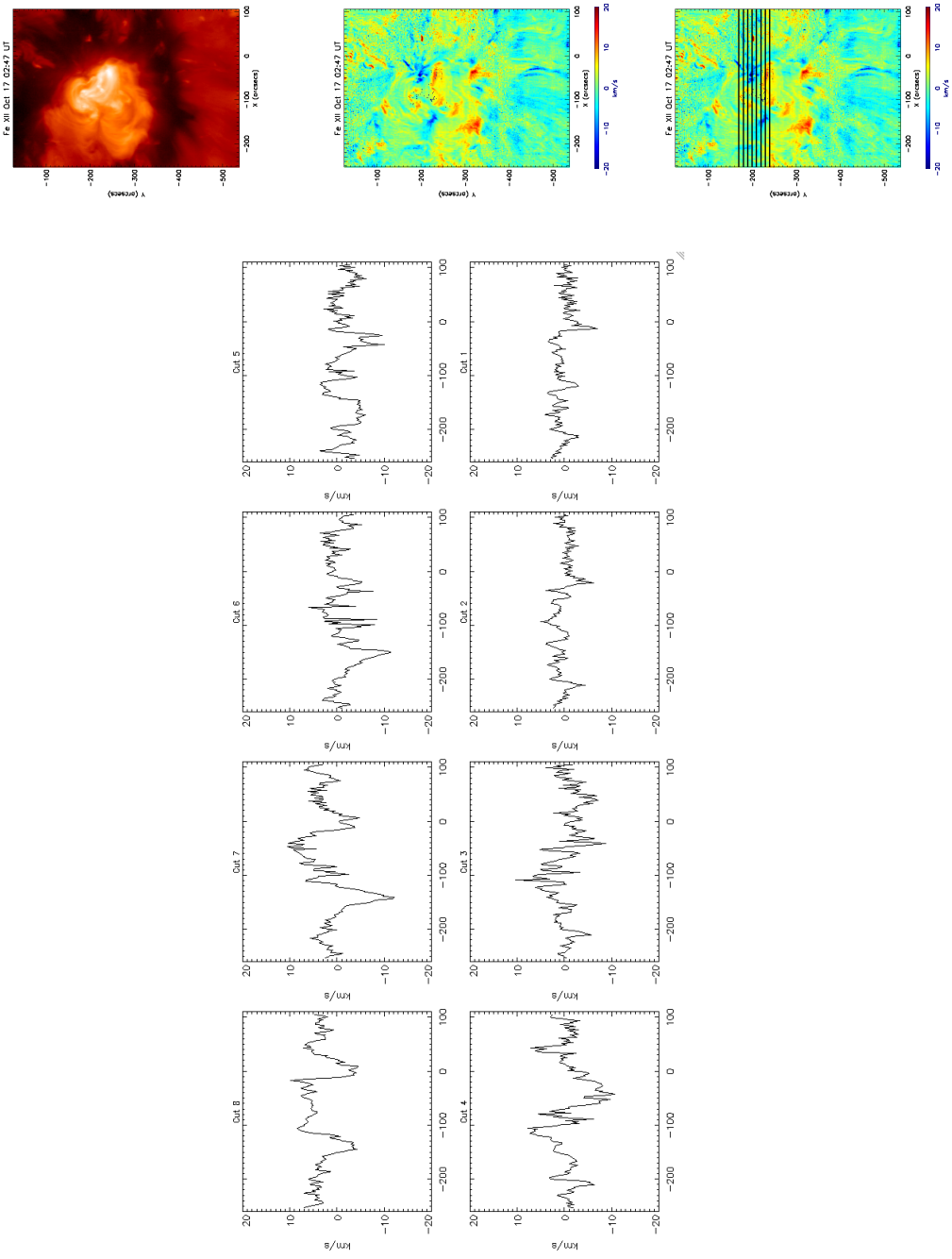

Figure 5.20: 2007 October 17 02:47 UT EIS 195 Å emission line intensity map (top right), velocity map (middle right), velocity map overlaid with latitudinal (Y-axis) locations of velocity cuts (bottom right), and velocity cuts top 1 - 8. Velocity Cut 1 is at Y = -240" and Cut 8 is at Y = -170". A velocity cut is averaged over 10" in the Y-direction (±5") along a line in the velocity map.

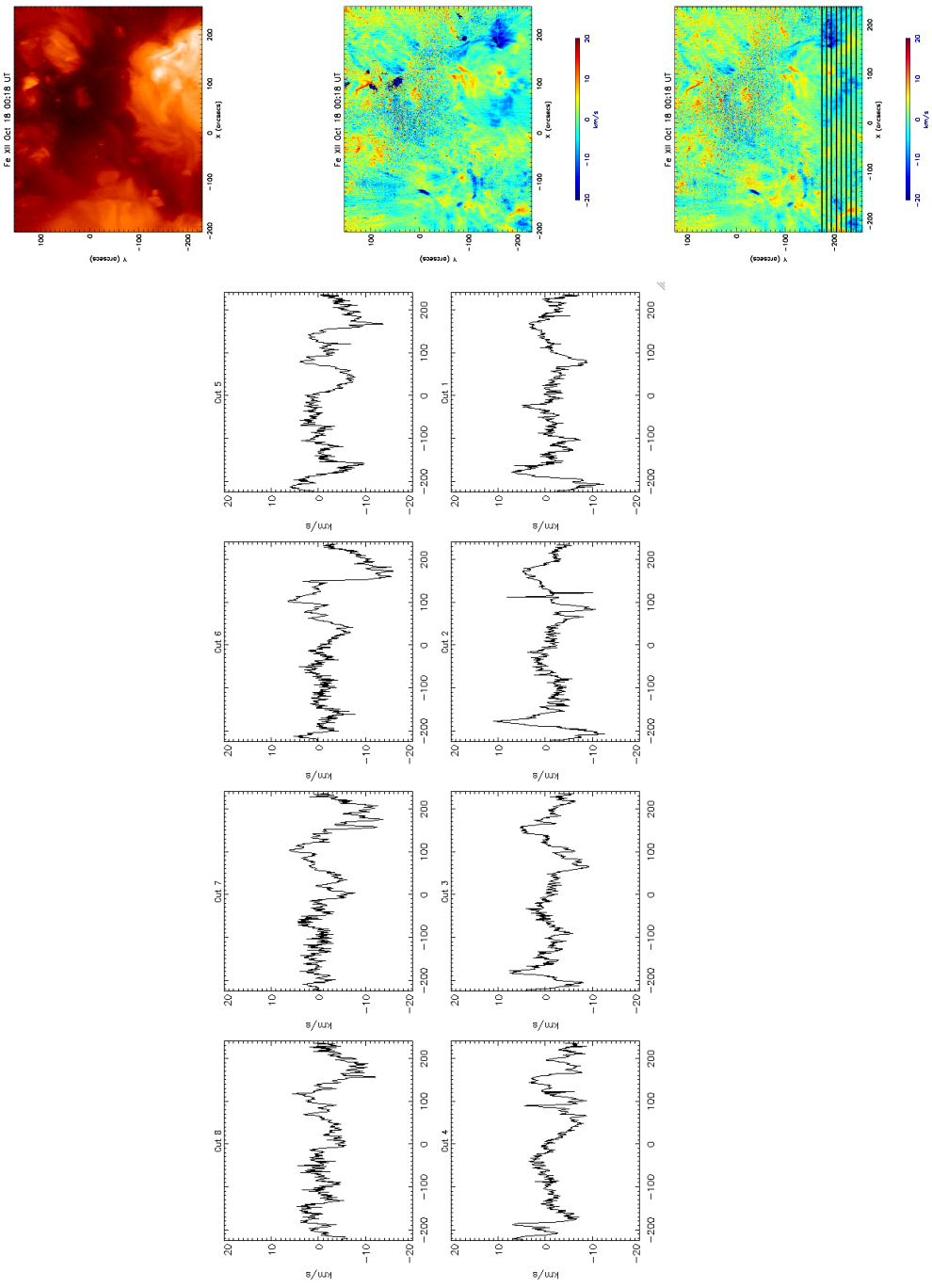

Figure 5.21: 2008 October 17 00:18 UT EIS 195 Å emission line intensity map (top right), velocity map (middle right), velocity map overlaid with latitudinal (Y-axis) locations of velocity cuts (bottom right), and velocity cuts top 1 - 8. Velocity Cut 1 is at Y = -245" and Cut 8 is at Y = -175". A velocity cut is averaged over 10" in the Y-direction (±5") along a line in the velocity map. Profiles along cuts 5 to 8 show a significant enhancement in velocities up to 18 km s^{-1} in the western outflow region compared to previous observations where velocities ranged from 5 to 12 km s^{-1} on either side of the AR.

5.7 Simulations

3D simulations replicating the observed AR-CH complex were carried out by Murray *et al.* (2010) to investigate the possible origin and driver of AR outflows. The AR embedded inside an equatorial CH provided a unique opportunity to investigate the possible drivers of outflows with two different magnetic configurations, one of which is advantageous for reconnection and the other which is not. On the solar eastern side, the AR's positive polarity is oppositely aligned with the CH's negative field and the magnetic configuration is conducive for reconnection. However, on the western side, the the respective polarities are parallel so that reconnection is not expected to take place there.

The model of Murray *et al.* (2010) is as follows. The domain consists of four horizontal layers - the top of the interior, the lower atmosphere (photosphere and chromosphere), the TR, and the corona. Each layer has a defining temperature characteristic from which the density and gas pressure are obtained under the assumption of hydrostatic equilibrium. A buoyant flux tube emerges through the solar surface of the domain which represents the simplified conditions of a uniform field that has a realistic vertical magnetic field strength of -19.5 G. Eventually, an Ω shape develops due to differential buoyancy within the flux tube. The Lagrangian remap scheme Lare3d (Arber *et al.*, 2001) is used to solve time-dependent, resistive, dimensionless MHD equations neglecting heat conduction and radiative effects as laid out in Murray *et al.* (2010).

Simulation results showed the generation of outflows at the periphery of the AR with a maximum vertical velocity of 45 km s^{-1}. The characteristic temperature, density, and structure of the outflows are fully consistent with observations (see Chapter 3). Figure 5.22 provides two different perspectives of the outflow evolution in the simulations. Confined to the magnetic field lines in the low plasma β environment of the corona, outflowing plasma is accelerated in and along the CH field immediately surrounding the AR.

Figure 5.23 contains vertical slices through the domain on the eastern (panels a, c, e) and western (b, d, f) sides of the AR. On the eastern side, there is region of high gas pressure and low magnetic pressure, which is characteristic of a current sheet (Figure 5.23a and c). Reconnection ultimately sets in on this side of the AR. No such indications of a current sheet and reconnection are evident on the western side of the AR. A close examination of the forces generated in the CH field reveals the driving mechanism of the outflows in the absence of reconnection. The outflows occur simply as a consequence of the horizontal expansion of the AR.

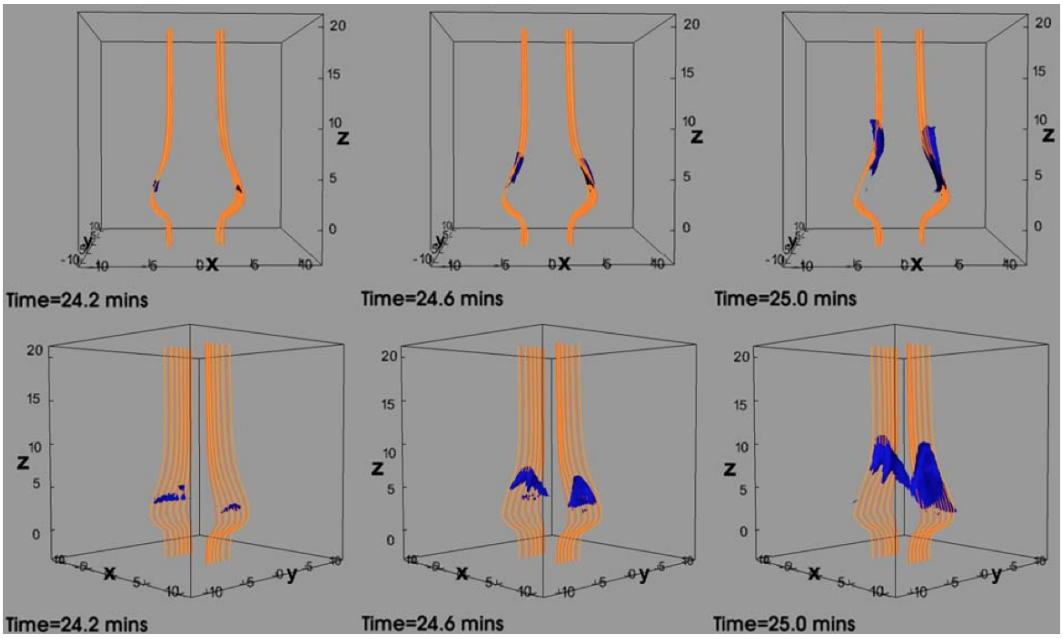

Figure 5.22: Vertical velocity isosurfaces (blue) of 15 km s^{-1} at 24.2, 24.6, and 25.0 mins into the simulation. The plasma outflow evolution is shown from two different perspectives. Selected CH field lines are in yellow/orange. The curved shape of the 'open' field lines is created by the AR embedded within them. From Murray *et al.* (2010).

The horizontal expansion of the AR compresses and deforms the nearby CH field as well as compressing the plasma amassed in the CH field (Murray *et al.*, 2010). The compressive effects result in enhanced gas pressure gradients and gravitational forces in the CH field. This is shown in Figure 5.23a-d where enhanced magnetic pressure and gas pressure occur at approximately ±5.0 Mm. Only gas pressure gradients can drive the outflows along the CH field because it alone acts in a direction parallel to the magnetic field. After the development of the AR, the enhanced gas pressure is not fully balanced by the gravitational force, consequently, the plasma in the CH field is accelerated upwards to become outflows.

The key result of the simulations for this work is that the velocity of the outflowing plasma is dependent upon the size of the components of the enhanced gas pressure gradient and gravitational force that are parallel to the CH field. Faster velocities result from larger imbalances in the forces. In summary, larger expansion forces lead to greater compression along the CH field which in turn results in larger gas pressure gradients and faster outflows.

5.8 Discussion

The simulations carried out by Murray *et al.* (2010) show that where surrounding field lines are nearly parallel, continuous, gentle outflows occur at the periphery of

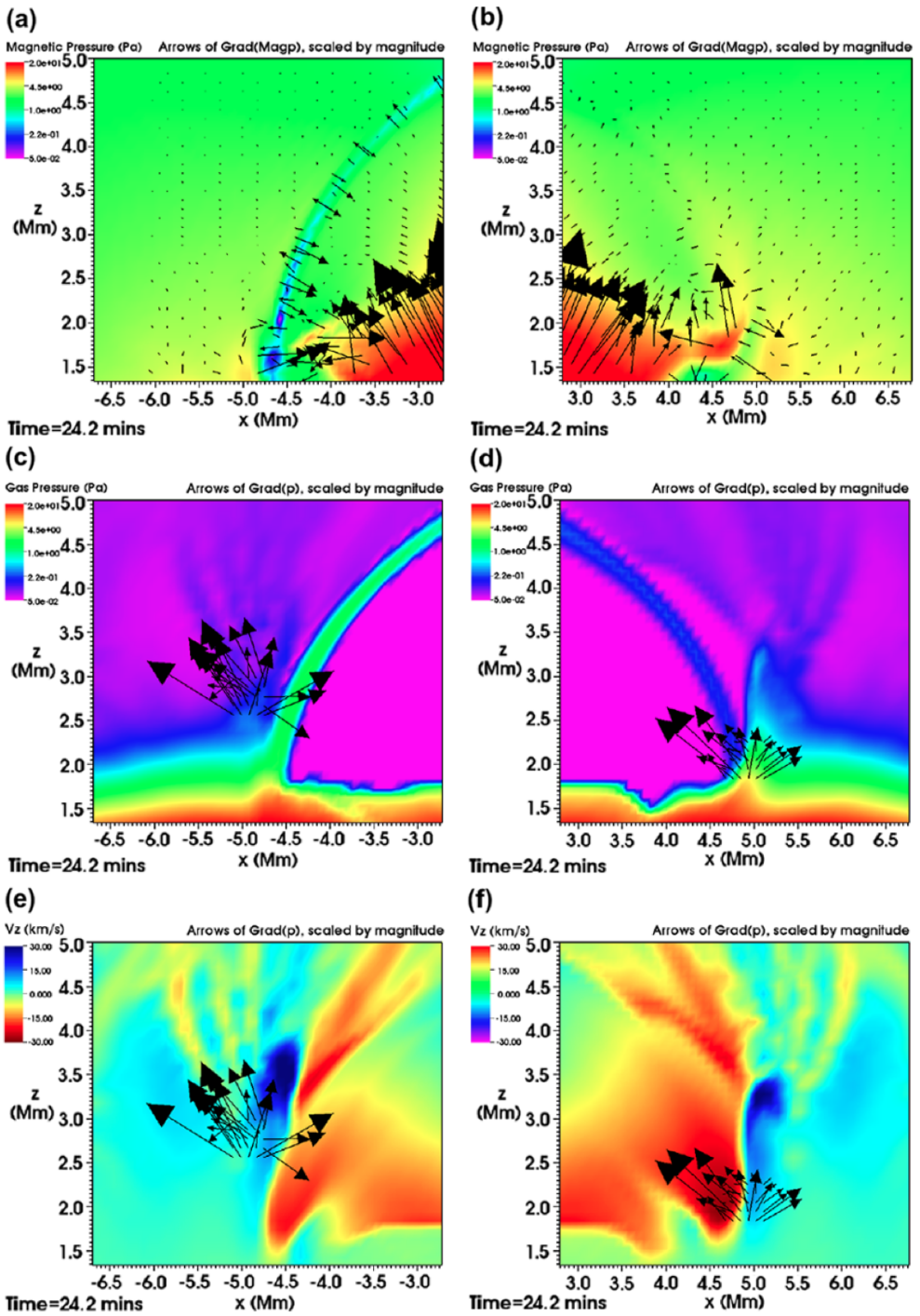

Figure 5.23: Vertical slices through a portion of the computational domain on either side of the AR at 24.2 mins into the simulation. Top panels: Contours of magnetic pressure. Middle panels: Contours of gas pressure. Bottom panels: Contours of vertical velocity in the vicinity of the outflows. Arrows indicate magnitude and direction of the magnetic and gas pressure gradients. From Murray *et al.* (2010).

the AR as a result of the expansion of the loops. This is consistent with *Yohkoh* SXT observations carried out by Uchida *et al.* (1992) who found almost continuous expansion of 'active' ARs. Although the expansion accelerating mechanism provides an adequate explanation for the observed outflows, it is unlikely to be working in isolation of reconnection-related mechanisms. The fact that for four days continuous outflows are observed in EIS rasters on both sides of the AR, irrespective of the relative orientation of the magnetic field lines of the AR and the CH, suggests that other mechanisms are involved in driving outflows. In actuality, AR expansion is one way for current concentrations to increase sufficiently for reconnection to take place so that it may be possible to simultaneously produce outflows by both driving mechanisms. During the studied period, the principal outflows are located where there are drastic connectivity changes of coronal loops, in the center of the 'anemone' of the AR loops, along the CH-quiet Sun boundary, and between closed loops of the AR and 'open' CH field lines, reinforcing the QSL reconnection-driven outflow scenario. However, the extension of the western outflow region well into the 'open' fields of the CH suggests that along the western boundary, compression driven outflows are present. Thus, a combination of driving mechanisms is a plausible explanation for the observed outflows with velocities ranging from 5 to 12 km s^{-1} that persisted for four days on both sides of the AR in the CH. Outflows driven by reconnection along quasi-separatrix layers in ARs is presented in Chapter 3.

Intensification of velocities observed on the western side of the AR requires further investigation. What set of circumstances could lead to the enhancement of velocities observed within the AR-CH complex at a particular time and in a specific location? A key result of the 3D MHD simulations provides a viable mechanism for the enhanced velocities observed on October 18 at 00:18 UT on the western side of the AR. The simulations showed that greater compressive forces lead to faster outflows. A flux rope containing a filament located closer to the western side of the AR is a possible source of additional compressive forces.

The reverse S-shaped pre-eruption filament indicated by yellow arrows in the TRACE 171 Å image in the top panel of Figure 5.4 is located above the PIL that lies very close to the western outflow region of the AR (cf. Figure 5.12). It is also evident in STEREO EUVI 171 Å images in Figure 4.17 of Chapter 4. At approximately 17:30 UT on October 17, the eastern portion of the filament begins to erupt and in the process, the overlying loops disappear in STEREO EUVI 195 Å images by about 18:30 UT. Though STEREO images clearly show that the filament or at least a portion of it begins to erupt, a filament is again visible in TRACE 171 Å data early on the 18th. The reappearance of the filament suggests there was either a failed (confined) or partial eruption. The fact that no CME was apparent in SOHO LASCO C2 observations attributable to the eruption suggests a failed

filament eruption may have occurred. The AR-filament complex goes through what appears to be another failed eruption close to the AR's core at 04:30 UT when the north eastern portion of the sigmoid expands, before finally erupting at 07:35 UT on the 18th towards the SW, leading to the CME seen in LASCO's C2.

Simulations conducted by Gibson and Fan (2006) and Gibson *et al.* (2006) show that the degree to which a flux rope erupts may depend on whether reconnections take place behind or within the flux rope and this in turn depends on whether it lies low enough in the corona to possess a bald-patch separatrix surface where dipping field lines containing the filament graze the photospheric PIL. These field lines are not free to escape upward. Instead, they evolve by reconnecting with surrounding field lines, both within the flux rope and in the surrounding arcade, resulting in a partial eruption (Gibson *et al.*, 2006). If the flux rope is higher in the corona then reconnection takes place at the X-point below the flux rope and it is fully expelled. Another contributing factor as to whether an eruption is confined or an ejective CME depends on the strength of the overlying field. If the field gradient decreases with height or changes sign then the flux rope may stabilize, resulting in a failed eruption (Schrijver and Siscoe, 2009). Török and Kliem (2005) and Török and Kliem (2007) demonstrated that there must be a sufficiently steep decrease of the magnetic field with height above the flux rope for a full eruption/CME.

A partial or full CME eruption changes the field configuration within the AR-CH complex. Expansion of the rising filament in the confined eruption on October 17 is likely to force reconnection on the eastern side of the AR between the antiparallel magnetic field of the positive polarity of the AR and the negative polarity of the surrounding CH. The 'open' field of the CH is transported to the western side thus some of the stabilizing overlying field is likely to be removed. The failed eruption at the core of the AR three hours prior to the full-fledged CME will further remove stabilizing field. This has consequences for the full CME eruption observed hours later.

Both eruptions accelerate what is an ongoing process of the removal of stabilizing overlying field by flux cancellation. Examination of time sequences of MDI magnetograms showed that opposite polarity flux converges in the vicinity of the filament hours before the NE expansion and again, early on the 18^{th}, prior to the failed and main eruptions. Location of the flux cancellation on the 18^{th} is spatially coincident with the center of the transient sigmoid which forms during the CME eruption (Figure 5.5). Measurements of the flux values from MDI magnetograms show that flux falls by $\approx 10^{21}$ Mx, or 10% of total flux per day, throughout the expansion of the AR and series of eruptions, destabilizing tied-down field by flux cancellation and increasing twist in the flux rope. Of course flux is cancelled along

the entire boundary of the AR's positive field, however, along the main PIL where the filament is located, is the interface of the strongest magnetic field.

Martin *et al.* (1985) defined flux cancellation observationally as the disappearance of opposite polarity magnetic field fragments along the PIL separating them. Magnetic fragments can disappear by a number of processes including submergence and annihilation. Flux cancellation occurs everywhere on the Sun especially in regions where filaments are located (Forbes *et al.*, 2006) and in decaying ARs (Martin *et al.*, 1985) where magnetic diffusion drives converging flows towards the PIL as is the case in this work. Using 2.5D numerical simulations, van Ballegooijen and Martens (1989) investigated the effect of flux cancellation in a sheared magnetic field arcade. Flows along a PIL create a sheared magnetic field from an initial potential field. As the shear increases, reconnection occurs between sheared loops crossing the PIL creating a long, helical loop and a short loop which subsequently submerges. Magnetic flux is transferred from the arcade field to the helical field as more flux cancels creating a flux rope in the process (van Ballegooijen and Martens, 1989). The helical field of the flux rope contains dips that are capable of holding filament material.

In 2D flux rope simulations, Forbes *et al.* (1994) and Lin *et al.* (1998) found that the evolution of a flux rope nested within an arcade takes place in two stages. During the first stage, magnetic energy is stored and the evolution of the system occurs on a timescale of hours. The slow evolution can be regarded as quasi-static. The loss of equilibria causes a series of transitions of the flux rope to a lower magnetic energy state at a higher height, leading to the rise of the flux rope. During the transitions a vertical current sheet forms below the flux rope where tether-cutting reconnection takes place as flux cancellation continues. Magnetic pressure forces in the flux rope increase and restraining tension forces in the overlying arcade field decrease as more arcade field is transferred to the helical field of the flux rope until the system reaches a critical point where no nearby equilibrium is accessible (Forbes *et al.*, 2006). At this stage, the system evolves rapidly over an Alfvènic timescale of seconds and the flux rope erupts, releasing part of the magnetic energy stored during the slow-rise phase (Lin *et al.*, 1998).

Results of 3D MHD simulations have shown that flux cancellation may lead to the formation and subsequent eruption of a flux rope in a sheared arcade configuration thus essentially confirming 2D and 2.5D results (Amari *et al.* (2003); Forbes *et al.* (2006); Yeates and Mackay (2009); Yeates *et al.* (2010); Aulanier *et al.* (2010) and references therein). This is the case when flux cancellation is treated as a consequence of photospheric turbulent diffusion such as in a decaying AR (Amari *et al.*, 2010). In 3D flux cancellation models, photospheric reconnection in a bald-patch

separatrix transforms the sheared arcades in the AR into a slowly rising and stable flux rope (Aulanier *et al.*, 2010). The models may differ in how the transition to eruption occurs e.g. torus instability (Aulanier *et al.*, 2010). For a specific case in which the initial state is quite sheared, Amari *et al.* (2010) found that the formation of a twisted flux rope and the subsequent disruption of the configuration can occur when flux has decreased by a relatively small amount over a portion of the AR.

Observational studies and modelling show that filaments that are about to erupt may exhibit two distinct phases (Moore *et al.* (2001), Moore and Sterling (2006), Schrijver *et al.* (2008) and references therein). The initial phase is characterized by a slow-rise during which both the filament and overlying field expand with velocities from 1 to 15 km s^{-1} (Schrijver *et al.*, 2008). A rapid-acceleration phase follows the slow rise where velocities increase to a range of 100 up to over 1000 km s^{-1} (Schrijver *et al.*, 2008). Pre-eruption expansion of the flux rope containing the filament located on the western side of the AR could provide the required increase in compressive forces causing intensification of outflows from less than 12 km s^{-1} to 18 km s^{-1} observed in EIS velocity map at 00:18 UT on the 18^{th}. This suggests that intensification of outflows prior to eruptive activity in the AR-CH complex may be a new class of pre-CME signature which has implications for space weather predications, if verified in future work. Its precursor status is reinforced by being combined with other well known precursors like sigmoids, persistent cancellation along the PIL, and pre-eruption activity. To be a viable tool for CME forecasts, outflow intensification events have to be recognized within a few hours. The current data acquisition and data reduction methods make this presently impossible. However, slitless spectrographs like the rocket-flown MOSES design (Fox *et al.*, 2010), if realized in the future, would make this class of precursor a viable tool for CME forecasting.

Chapter 6

Conclusions and Future Work

Recent results have shown that during solar maximum, slow wind originates from 'open' field in the vicinity of and at the boundaries of ARs (Schrijver and DeRosa (2003) and Liewer *et al.* (2004) and others). A major discovery of *Hinode* XRT and EIS is the presence of persistent plasma outflows at the periphery of all ARs during solar minimum, suggesting that these ubiquitous AR outflows are a viable source of the slow solar wind. Currently there is no consensus of opinion as to the major driving mechanism(s) of these outflows. The work in this thesis has addressed this key issue by combining EIS observations with solar magnetic modeling and MHD simulations to propose that there are two main drivers of the AR outflows depending on the magnetic topology of the outflow source region: (1) AR expansion compressing nearby field which 'squeezes' the plasma along nearby 'open' field creating outflows (Murray *et al.*, 2010) and (2) magnetic reconnection along QSLs (Baker *et al.*, 2009b). QSLs are preferential locations for current layer formation and continuous reconnection in an evolving magnetic field. Reconnection along QSLs involves a slow, continuous restructuring of the magnetic field leading to the release of stored magnetic energy and the acceleration of particles in the solar atmosphere. The most flow-active QSLs were found above the strongest magnetic field concentrations along the interface between field lines closing within the AR and large-scale 'open' magnetic loops connecting elsewhere on the Sun or in interplanetary space. This is the first theory capable of explaining how observed variable outflows from the Sun can persist for days and can be located over areas of a single magnetic sign, something previously considered improbable.

Future work on the relationship between AR outflows and QSLs should take into account how changes in QSLs due to varying magnetic field complexity and strength affect AR outflows within the lifetimes of individual ARs and in aggregate over the solar cycle. Baker *et al.* (2009b) put forward the first theory of how small-

scale, sporadic magnetic or QSL reconnection drives the long-lived, time-varying outflows from regions of strong magnetic field combining observations and modeling of one AR. The author proposes to expand the work in this thesis to a detailed and extensive study of a number of ARs of varying complexity and magnetic field strength. Observations of ARs throughout their evolutionary stages will provide the boundary conditions for and constraints of QSL modeling in order to determine the exact circumstances under which magnetic reconnection along QSLs becomes a driver of plasma outflows. The next step is to understand how the bulk outflows are created from a complex array of flows resulting from QSL reconnection. This would be accomplished by incorporating MHD simulations in the analysis.

A long-term study of the relationship between AR outflows and magnetic field strength and complexity can be combined with the results of Baker *et al.* (2009b) to demonstrate the nature of flow-active QSLs and AR outflows during the rising phase of the solar cycle as activity and magnetic complexity increase which will provide crucial insight into how the acceleration process varies with the solar cycle. How the driver of AR outflows vary over the solar cycle would also help to better understand the source region of the slow SW.

The author would expect to identify wider applications of reconnection along QSLs as a driver of solar outflows, such as a driver of fast wind streams from coronal holes. A major discovery of *Hinode* SOT is the co-existence of very large, kilo gauss magnetic field concentrations in the polar coronal holes (Tsuneta *et al.*, 2008) with much more mixed (closed and 'open') magnetic field. In Baker *et al.* (2009b), the strongest flows were found to have occurred along sections of QSLs located over regions of the highest magnetic field in the AR where 'open' and closed field are in close proximity. It is plausible that the same process is an important component driving the fast solar wind in polar coronal holes, especially along their boundaries where 'open' field lines interface closed coronal loops of the quiet Sun.

The work presented in this thesis has made a significant contribution towards the understanding of magnetic reconnection as a driver of coronal dynamics. Chapter 4 described how multi-wavelength remote sensing and *in situ* observations were used to demonstrate that IR is an important process that occurs on all scales within the heliosphere from polar X-ray jets to ICMEs. Chapters 3 and 5 identified the two main drivers of AR outflows, reconnection along QSLs and AR expansion which has important implications for the origin of the slow solar wind and space weather forecasting.

List of Abbreviations

Abbreviation	Details
ACE	Advanced Composition Explorer
AR	Active Region
AU	Astronomical Unit
BP	Bright Point
CDS	Coronal Diagnostic Spectrometer
CH	Coronal Hole
CIR	Corotating Interaction Region
CME	Coronal Mass Ejection
DEM	Differential Emission Measure
EIS	EUV Imaging Spectrometer
EIT	EUV Imaging Telescope
EUV	Extreme Ultraviolet
EUVI	Extreme Ultraviolet Imager
FIP	First Ionization Potential
FOV	Field of View
FWHM	Full Width Half Maximum
GI	Grazing Incidence
HCS	Heliospheric Current Sheet
HI	Heliospheric Imager
HRTS	High Resolution Telescope and Spectrograph
ICME	Interplanetary Coronal Mass Ejection
IMPACT	In Situ Measurements of Particles and CME Transients
IPS	Interplanetary Space
IR	Interchange Reconnection
ISM	Interstellar Medium
LC	Light Curve
LCP/RCP	Left/Right Circularly Polarized
LFFF	Linear Force Free Field
LOS	Line-of-Sight
LTE	Local Thermodynamic Equilibrium
MC	Magnetic Cloud
MDI	Michelson Doppler Imager
MHD	Magnetohydrodynamics
NLFFF	Non-linear Force Free Field
NSO/KP	National Solar Observatory/Kitt Peak
NTLE	Non-Local Thermodynamic Equilibrium
PIL	Polarity Inversion Line
PLASTIC	Plasma and Suprathermal Ion Composition
PFSS	Potential Field Source Surface
PSF	Point Spread Function
QS	Quiet Sun
QSL(M)	Quasi-Separatrix Layer (Method)
R_{sun}	Solar radius
RFL	Refolded Field Lines
SECCHI	Sun-Earth Connection Coronal and Heliospheric Investigation
SMM	Solar Maximum Mission
S/N	Signal to Noise
SOHO	SOlar Heliospheric Observatory

Abbreviation	**Details**
SOT	Solar Optical Telescope
STEREO	Solar Terrestrial Relations Observatory
SUMER	Solar Ultraviolet Measurements of Emitted Radiation
SW	Solar Wind
SWEA	Solar Wind Plasma Electron Analyzer
SWEPAM	Solar Wind Electron, Proton, and Alpha Monitor
SWICS	Solar Wind Ion Composition Spectrometer
SWS	Solar Wind Sector
SXT	Soft X-ray Telescope
TR	Transition Region
TRACE	Transition Region and Coronal Explorer
USVP	Ultraviolet Spectrometer and Polarimeter
UV	Ultraviolet
WAP	Wide-Angle Partition Sector
WSO	Wilcox Solar Observatory
XBP	X-ray Bright Point
XRT	X-ray Telescope

References

Achour, H., Brekke, P., Kjeldseth-Moe, O., and Maltby, P.: Observed Redshifts in the Solar Transition Region above Active and Quiet Regions, *ApJ*, **453**, 945–+, doi:10.1086/176454, 1995.

Acuña, M. H., Curtis, D., Scheifele, J. L., Russell, C. T., Schroeder, P., Szabo, A., and Luhmann, J. G.: The STEREO/IMPACT Magnetic Field Experiment, *Space Sci. Rev.*, **136**, 203–226, doi:10.1007/s11214-007-9259-2, 2008.

Amari, T., Luciani, J. F., Aly, J. J., Mikic, Z., and Linker, J.: Coronal Mass Ejection: Initiation, Magnetic Helicity, and Flux Ropes. II. Turbulent Diffusion-driven Evolution, *ApJ*, **595**, 1231–1250, doi:10.1086/377444, 2003.

Amari, T., Aly, J., Mikic, Z., and Linker, J.: Coronal Mass Ejection Initiation: On the Nature of the Flux Cancellation Model, *ApJL*, **717**, L26–L30, doi:10.1088/2041-8205/717/1/L26, 2010.

Antiochos, S. K., DeVore, C. R., and Klimchuk, J. A.: A Model for Solar Coronal Mass Ejections, *Astrophys. J.*, **510**, 485–493, doi:10.1086/306563, 1999.

Antiochos, S. K., DeVore, C. R., Karpen, J. T., and Mikić, Z.: Structure and Dynamics of the Sun's Open Magnetic Field, *Astrophys. J.*, **671**, 936–946, doi:10.1086/522489, 2007.

Arber, T. D., Longbottom, A. W., Gerrard, C. L., and Milne, A. M.: A Staggered Grid, Lagrangian-Eulerian Remap Code for 3-D MHD Simulations, *Journal of Computational Physics*, **171**, 151–181, doi:10.1006/jcph.2001.6780, 2001.

Asai, A., Shibata, K., Hara, H., and Nitta, N. V.: Characteristics of Anemone Active Regions Appearing in Coronal Holes Observed with the Yohkoh Soft X-Ray Telescope, *Astrophys. J.*, **673**, 1188–1193, doi:10.1086/523842, 2008.

Asai, A., Shibata, K., Ishii, T. T., Oka, M., Kataoka, R., Fujiki, K., and Gopalswamy, N.: Evolution of the anemone AR NOAA 10798 and the related geo-effective flares and CMEs, *J. Geophys. Res.*, **114**, 0–+, doi:10.1029/2008JA013291, 2009.

Aschwanden, M. J.: Physics of the Solar Corona. An Introduction with Problems and Solutions (2nd edition), 2005.

Aschwanden, M. J. and Acton, L. W.: Temperature Tomography of the Soft X-Ray Corona: Measurements of Electron Densities, Tempuratures, and Differential Emission Measure Distributions above the Limb, *ApJ*, **550**, 475–492, doi:10.1086/319711, 2001.

Attrill, G., Nakwacki, M. S., Harra, L. K., van Driel-Gesztelyi, L., Mandrini, C. H., Dasso, S., and Wang, J.: Using the Evolution of Coronal Dimming Regions to Probe the Global Magnetic Field Topology, *Solar Phys.*, **238**, 117–139, doi:10.1007/s11207-006-0167-5, 2006.

Aulanier, G., Démoulin, P., and Grappin, R.: Equilibrium and observational properties of line-tied twisted flux tubes, *A&A*, **430**, 1067–1087, doi:10.1051/0004-6361:20041519, 2005a.

Aulanier, G., Pariat, E., and Démoulin, P.: Current sheet formation in quasi-separatrix layers and hyperbolic flux tubes, *A&A*, **444**, 961–976, doi:10.1051/0004-6361:20053600, 2005b.

Aulanier, G., Pariat, E., Démoulin, P., and Devore, C. R.: Slip-Running Reconnection in Quasi-Separatrix Layers, *Solar Phys.*, **238**, 347–376, doi:10.1007/s11207-006-0230-2, 2006.

Aulanier, G., Golub, L., DeLuca, E. E., Cirtain, J. W., Kano, R., Lundquist, L. L., Narukage, N., Sakao, T., and Weber, M. A.: Slipping Magnetic Reconnection in Coronal Loops, *Science*, **318**, 1588–, doi:10.1126/science.1146143, 2007.

Aulanier, G., Török, T., Démoulin, P., and DeLuca, E. E.: Formation of Torus-Unstable Flux Ropes and Electric Currents in Erupting Sigmoids, *ApJ*, **708**, 314–333, doi:10.1088/0004-637X/708/1/314, 2010.

Babcock, H. W.: The Topology of the Sun's Magnetic Field and the 22-YEAR Cycle., *ApJ*, **133**, 572–+, doi:10.1086/147060, 1961.

Bahcall, J. N. and Ulrich, R. K.: Solar models, neutrino experiments, and helioseismology, *Reviews of Modern Physics*, **60**, 297–372, doi:10.1103/RevModPhys.60.297, 1988.

Baker, D., van Driel-Gesztelyi, L., and Attrill, G. D. R.: Evidence for interchange reconnection between a coronal hole and an adjacent emerging flux region, *Astronomische Nachrichten*, **328**, 773–+, doi:10.1002/asna.200710787, 2007.

Baker, D., van Driel-Gesztelyi, L., Kamio, S., Culhane, J. L., Harra, L. K., Sun, J., Young, P. R., and Matthews, S. A.: Hinode EIS and XRT Observations of Hot

Jets in Coronal Holes - Does the Plasma Escape?, in First Results From Hinode, edited by S. A. Matthews, J. M. Davis, & L. K. Harra, vol. 397 of *Astronomical Society of the Pacific Conference Series*, pp. 23–+, 2008.

Baker, D., Rouillard, A. P., van Driel-Gesztelyi, L., Demoulin, P., Harra, L. K., Lavraud, B., Davies, J. A., Optiz, A., Luhmann, J. G., Sauvaud, J. A., and Galvin, A. B.: Signatures of Interchange Reconnection: STEREO, ACE and Hinode Observations Combined, *ArXiv e-prints*, 2009a.

Baker, D., van Driel-Gesztelyi, L., Mandrini, C. H., Démoulin, P., and Murray, M. J.: Magnetic Reconnection along Quasi-separatrix Layers as a Driver of Ubiquitous Active Region Outflows, *ApJ*, **705**, 926–935, doi:10.1088/0004-637X/705/1/926, 2009b.

Baker, D., van Driel-Gesztelyi, L., Murray, M. J., Green, L. M., Török, T., and Sun, J.: Intensification of Plasma Upflows in an Active Region—Coronal Hole Complex: A CME Precursor, in Astronomical Society of the Pacific Conference Series, edited by B. Lites, M. Cheung, T. Magara, J. Mariska, & K. Reeves, vol. 415 of *Astronomical Society of the Pacific Conference Series*, pp. 75–+, 2009c.

Balogh, A., Lanzerotti, L. J., and Suess, S. T.: The Heliosphere through the Solar Activity Cycle, Springer-Praxis Books and Springer Science+Business Media, 2008.

Berger, T. E. and Lites, B. W.: Weak-Field Magnetogram Calibration using Advanced Stokes Polarimeter Flux Density Maps - II. SOHO/MDI Full-Disk Mode Calibration, *Solar Physics*, **213**, 213–229, 2003.

Birn, J. and Priest, E. R.: Reconnection of magnetic fields : magnetohydrodynamics and collisionless theory and observations, 2007.

Borovsky, J. E.: Flux tube texture of the solar wind: Strands of the magnetic carpet at 1 AU?, *J. Geophys. Res.*, **113**, 8110–+, doi:10.1029/2007JA012684, 2008.

Borrini, G., Gosling, J. T., Bame, S. J., and Feldman, W. C.: Helium abundance enhancements in the solar wind, *J. Geophys. Res.*, **87**, 7370–7378, doi:10.1029/JA087iA09p07370, 1982.

Brown, C. M., Feldman, U., Seely, J. F., Korendyke, C. M., and Hara, H.: Wavelengths and Intensities of Spectral Lines in the 171-211 and 245-291 Å Ranges from Five Solar Regions Recorded by the Extreme-Ultraviolet Imaging Spectrometer (EIS) on Hinode, *Astrophysical Journal Supplement Series*, **176**, 511–535, doi:10.1086/529378, 2008.

Brown, D. S., Bewsher, D., and Eyles, C. J.: Calibrating the Pointing and Optical Parameters of the STEREO Heliospheric Imagers, *Solar Phys.*, **254**, 185–225, doi:10.1007/s11207-008-9277-6, 2009.

Bryans, P., Young, P. R., and Doschek, G. A.: Multiple Component Outflows in an Active Region Observed with the EUV Imaging Spectrometer on Hinode, *ApJ*, **715**, 1012–1020, doi:10.1088/0004-637X/715/2/1012, 2010.

Brynildsen, N., Brekke, P., Fredvik, T., Haugan, S. V. H., Kjeldseth-Moe, O., Maltby, P., Harrison, R. A., Pike, C. D., Rimmele, T., Thompson, W. T., and Wilhelm, K.: EUV Spectroscopy of the Sunspot Region NOAA 7981 Using SOHO - II. Velocities and Line Profiles, *Solar Phys.*, **179**, 279–312, 1998.

Burkepile, J. T., Hundhausen, A. J., and Seiden, J. A.: A study of GOES X-ray events associated with coronal mass ejections; 1986, in Solar Dynamic Phenomena and Solar Wind Consequences, the Third SOHO Workshop, edited by J. J. Hunt, vol. 373 of *ESA Special Publication*, pp. 57–+, 1994.

Burlaga, L., Sittler, E., Mariani, F., and Schwenn, R.: Magnetic loop behind an interplanetary shock - Voyager, Helios, and IMP 8 observations, *J. Geophys. Res.*, **86**, 6673–6684, doi:10.1029/JA086iA08p06673, 1981.

Canfield, R. C., Hudson, H. S., and McKenzie, D. E.: Sigmoidal morphology and eruptive solar activity, *Geophys. Res. Lett.*, **26**, 627–630, doi:10.1029/1999GL900105, 1999.

Carmichael, H.: A Process for Flares, *NASA Special Publication*, **50**, 451–+, 1964.

Cartwright, M. L. and Moldwin, M. B.: Comparison of small-scale flux rope magnetic properties to large-scale magnetic clouds: Evidence for reconnection across the HCS?, *J. Geophys. Res.*, **113**, 9105–+, doi:10.1029/2008JA013389, 2008.

Chapman, S. and Zirin, H.: Notes on the Solar Corona and the Terrestrial Ionosphere, *Smithsonian Contributions to Astrophysics*, **2**, 1–+, 1957.

Charbonneau, P., Christensen-Dalsgaard, J., Henning, R., Larsen, R. M., Schou, J., Thompson, M. J., and Tomczyk, S.: Helioseismic Constraints on the Structure of the Solar Tachocline, *ApJ*, **527**, 445–460, doi:10.1086/308050, 1999.

Chen, P. F. and Shibata, K.: An Emerging Flux Trigger Mechanism for Coronal Mass Ejections, *Astrophys. J.*, **545**, 524–531, doi:10.1086/317803, 2000.

Chen, P. F., Innes, D. E., and Solanki, S. K.: SOHO/SUMER observations of prominence oscillation before eruption, *A&A*, **484**, 487–493, doi:10.1051/0004-6361:200809544, 2008.

Chertok, I. M., Obridko, E. I., Mogilevsky, V. N., Shilova, N. S., and Hudson, H. S.: Solar Disappearing Filament Inside a Coronal Hole, *Astrophys. J.*, **567**, 1225–1233, doi:10.1086/338584, 2002.

Chifor, C., Mason, H. E., Tripathi, D., Isobe, H., and Asai, A.: The early phases of a solar prominence eruption and associated flare: a multi-wavelength analysis, *A&A*, **458**, 965–973, doi:10.1051/0004-6361:20065687, 2006.

Chifor, C., Tripathi, D., Mason, H. E., and Dennis, B. R.: X-ray precursors to flares and filament eruptions, *A&A*, **472**, 967–979, doi:10.1051/0004-6361:20077771, 2007.

Chifor, C., Young, P. R., Isobe, H., Mason, H. E., Tripathi, D., Hara, H., and Yokoyama, T.: An active region jet observed with Hinode, *A&A*, **481**, L57–L60, doi:10.1051/0004-6361:20079081, 2008.

Cirtain, J. W., Golub, L., Lundquist, L., van Ballegooijen, A., Savcheva, A., Shimojo, M., DeLuca, E., Tsuneta, S., Sakao, T., Reeves, K., Weber, M., Kano, R., Narukage, N., and Shibasaki, K.: Evidence for Alfvén Waves in Solar X-ray Jets, *Science*, **318**, 1580–, doi:10.1126/science.1147050, 2007.

Cranmer, S. R.: Self Consistent Models of the Solar Wind, *ArXiv e-prints*, 2010.

Cranmer, S. R. and van Ballegooijen, A. A.: Can the Solar Wind be Driven by Magnetic Reconnection in the Sun's Magnetic Carpet?, *ArXiv e-prints*, 2010.

Crooker, N. U. and Owens, M. J.: Impact of Coronal Mass Ejections, Interchange Reconnection, and Disconnection on Heliospheric Magnetic Field Strength, in Astronomical Society of the Pacific Conference Series, edited by S. R. Cranmer, J. T. Hoeksema, & J. L. Kohl, vol. 428 of *Astronomical Society of the Pacific Conference Series*, pp. 279–+, 2010.

Crooker, N. U. and Webb, D. F.: Remote sensing of the solar site of interchange reconnection associated with the May 1997 magnetic cloud, *J. Geophys. Res.*, **111**, 8108–+, doi:10.1029/2006JA011649, 2006.

Crooker, N. U., Gosling, J. T., and Kahler, S. W.: Reducing heliospheric magnetic flux from coronal mass ejections without disconnection, *J. Geophys. Res.*, **107**, 1028–+, doi:10.1029/2001JA000236, 2002.

Crooker, N. U., Forsyth, R., Rees, A., Gosling, J. T., and Kahler, S. W.: Counterstreaming electrons in magnetic clouds near 5 AU, *J. Geophys. Res.*, **109**, 6110–+, doi:10.1029/2004JA010426, 2004a.

Crooker, N. U., Kahler, S. W., Larson, D. E., and Lin, R. P.: Large-scale magnetic field inversions at sector boundaries, *J. Geophys. Res.*, **109**, 3108–+, doi:10.1029/2003JA010278, 2004b.

Culhane, J. L., Harra, L. K., James, A. M., Al-Janabi, K., Bradley, L. J., Chaudry, R. A., Rees, K., Tandy, J. A., Thomas, P., Whillock, M. C. R., Winter, B., Doschek, G. A., Korendyke, C. M., Brown, C. M., Myers, S., Mariska, J., Seely, J., Lang, J., Kent, B. J., Shaughnessy, B. M., Young, P. R., Simnett, G. M., Castelli, C. M., Mahmoud, S., Mapson-Menard, H., Probyn, B. J., Thomas, R. J., Davila, J., Dere, K., Windt, D., Shea, J., Hagood, R., Moye, R., Hara, H., Watanabe, T., Matsuzaki, K., Kosugi, T., Hansteen, V., and Wikstol, Ø.: The EUV Imaging Spectrometer for Hinode, *Solar Phys.*, **243**, 19–61, doi:10.1007/s01007-007-0293-1, 2007a.

Culhane, L., Harra, L. K., Baker, D., van Driel-Gesztelyi, L., Sun, J., Doschek, G. A., Brooks, D. H., Lundquist, L. L., Kamio, S., Young, P. R., and Hansteen, V. H.: Hinode EUV Study of Jets in the Sun's South Polar Corona, *PASJ*, **59**, 751–+, 2007b.

Czaykowska, A., de Pontieu, B., Alexander, D., and Rank, G.: Evidence for Chromospheric Evaporation in the Late Gradual Flare Phase from SOHO/CDS Observations, *ApJL*, **521**, L75–L78, doi:10.1086/312176, 1999.

Davies, J. A., Harrison, R. A., Rouillard, A. P., Sheeley, N. R., Perry, C. H., Bewsher, D., Davis, C. J., Eyles, C. J., Crothers, S. R., and Brown, D. S.: A synoptic view of solar transient evolution in the inner heliosphere using the Heliospheric Imagers on STEREO, *Geophys. Res. Lett.*, **36**, 2102–+, doi:10.1029/2008GL036182, 2009.

de Moortel, I.: Longitudinal Waves in Coronal Loops, *Space Science Reviews*, **149**, 65–81, doi:10.1007/s11214-009-9526-5, 2009.

De Moortel, I., Ireland, J., Walsh, R. W., and Hood, A. W.: Longitudinal intensity oscillations in coronal loops observed with TRACE I. Overview of Measured Parameters, *Solar Physics*, **209**, 61–88, doi:10.1023/A:1020956421063, 2002.

De Pontieu, B., Erdélyi, R., and de Wijn, A. G.: Intensity Oscillations in the Upper Transition Region above Active Region Plage, *ApJL*, **595**, L63–L66, doi:10.1086/378843, 2003.

De Pontieu, B., McIntosh, S., Hansteen, V. H., Carlsson, M., Schrijver, C. J., Tarbell, T. D., Title, A. M., Shine, R. A., Suematsu, Y., Tsuneta, S., Katsukawa, Y., Ichimoto, K., Shimizu, T., and Nagata, S.: A Tale of Two Spicules: The Impact of Spicules on the Magnetic Chromosphere, *PASJ*, **59**, 655–+, 2007.

De Pontieu, B., McIntosh, S. W., Hansteen, V. H., and Schrijver, C. J.: Observing the Roots of Solar Coronal Heatin in the Chromosphere, *ApJL*, **701**, L1–L6, doi:10.1088/0004-637X/701/1/L1, 2009.

De Rosa, M. L., Schrijver, C. J., Barnes, G., Leka, K. D., Lites, B. W., Aschwanden, M. J., Amari, T., Canou, A., McTiernan, J. M., Régnier, S., Thalmann, J. K., Valori, G., Wheatland, M. S., Wiegelmann, T., Cheung, M. C. M., Conlon, P. A., Fuhrmann, M., Inhester, B., and Tadesse, T.: A Critical Assessment of Nonlinear Force-Free Field Modeling of the Solar Corona for Active Region 10953, *ApJ*, **696**, 1780–1791, doi:10.1088/0004-637X/696/2/1780, 2009.

de Toma, G., Arge, C. N., and Riley, P.: Observed and Modeled Coronal Holes, in Solar Wind 11/SOHO 16, Connecting Sun and Heliosphere, edited by B. Fleck, T. H. Zurbuchen, & H. Lacoste, vol. 592 of *ESA Special Publication*, pp. 609–+, 2005.

Del Zanna, G.: Flows in active region loops observed by Hinode EIS, *A&A*, **481**, L49–L52, doi:10.1051/0004-6361:20079087, 2008.

del Zanna, G., Schmieder, B., Mason, H., Berlicki, A., and Bradshaw, S.: The Gradual Phase of the X17 Flare on October 28, 2003, *Solar Physics*, **239**, 173–191, doi:10.1007/s11207-006-0184-4, 2006.

Delaboudinière, J., Artzner, G. E., Brunaud, J., Gabriel, A. H., Hochedez, J. F., Millier, F., Song, X. Y., Au, B., Dere, K. P., Howard, R. A., Kreplin, R., Michels, D. J., Moses, J. D., Defise, J. M., Jamar, C., Rochus, P., Chauvineau, J. P., Marioge, J. P., Catura, R. C., Lemen, J. R., Shing, L., Stern, R. A., Gurman, J. B., Neupert, W. M., Maucherat, A., Clette, F., Cugnon, P., and van Dessel, E. L.: EIT: Extreme-Ultraviolet Imaging Telescope for the SOHO Mission, *Solar Phys.*, **162**, 291–312, doi:10.1007/BF00733432, 1995.

Démoulin, P.: Extending the concept of separatrices to QSLs for magnetic reconnection, *Advances in Space Research*, **37**, 1269–1282, doi:10.1016/j.asr.2005.03.085, 2006.

Démoulin, P.: Where will efficient energy release occur in 3-D magnetic configurations?, *Advances in Space Research*, **39**, 1367–1377, doi:10.1016/j.asr.2007.02.046, 2007.

Demoulin, P., van Driel-Gesztelyi, L., Schmieder, B., Hemoux, J. C., Csepura, G., and Hagyard, M. J.: Evidence for magnetic reconnection in solar flares, *A&A*, **271**, 292–+, 1993.

Demoulin, P., Henoux, J. C., Priest, E. R., and Mandrini, C. H.: Quasi-Separatrix layers in solar flares. I. Method., *A&A*, **308**, 643–655, 1996.

Demoulin, P., Bagala, L. G., Mandrini, C. H., Henoux, J. C., and Rovira, M. G.: Quasi-separatrix layers in solar flares. II. Observed magnetic configurations., *A&A*, **325**, 305–317, 1997.

Démoulin, P., Klein, K.-L., Goff, C. P., van Driel-Gesztelyi, L., Culhane, J. L., Mandrini, C. H., Matthews, S. A., and Harra, L. K.: Decametric N Burst: A Consequence of the Interaction of Two Coronal Mass Ejections, *Solar Phys.*, **240**, 301–313, doi:10.1007/s11207-006-0259-2, 2007.

Démoulin, P., Nakwacki, M. S., Dasso, S., and Mandrini, C. H.: Expected in Situ Velocities from a Hierarchical Model for Expanding Interplanetary Coronal Mass Ejections, *Solar Phys.*, **250**, 347–374, doi:10.1007/s11207-008-9221-9, 2008.

Dere, K. P., Brueckner, G. E., Howard, R. A., Koomen, M. J., Korendyke, C. M., Kreplin, R. W., Michels, D. J., Moses, J. D., Moulton, N. E., Socker, D. G., St. Cyr, O. C., Delaboudinière, J. P., Artzner, G. E., Brunaud, J., Gabriel, A. H., Hochedez, J. F., Millier, F., Song, X. Y., Chauvineau, J. P., Marioge, J. P., Defise, J. M., Jamar, C., Rochus, P., Catura, R. C., Lemen, J. R., Gurman, J. B., Neupert, W., Clette, F., Cugnon, P., van Dessel, E. L., Lamy, P. L., Llebaria, A., Schwenn, R., and Simnett, G. M.: EIT and LASCO Observations of the Initiation of a Coronal Mass Ejection, *Solar Physics*, **175**, 601–612, doi:10.1023/A:1004907307376, 1997.

Domingo, V., Fleck, B., and Poland, A. I.: SOHO: The Solar and Heliospheric Observatory, *Space Science Reviews*, **72**, 81–84, doi:10.1007/BF00768758, 1995.

Doschek, G. A., Mariska, J. T., Warren, H. P., Brown, C. M., Culhane, J. L., Hara, H., Watanabe, T., Young, P. R., and Mason, H. E.: Nonthermal Velocities in Solar Active Regions Observed with the Extreme-Ultraviolet Imaging Spectrometer on Hinode, *Astrophys. J. Lett.*, **667**, L109–L112, doi:10.1086/522087, 2007.

Doschek, G. A., Warren, H. P., Mariska, J. T., Muglach, K., Culhane, J. L., Hara, H., and Watanabe, T.: Flows and Nonthermal Velocities in Solar Active Regions Observed with the EUV Imaging Spectrometer on Hinode: A Tracer of Active Region Sources of Heliospheric Magnetic Fields?, *ApJ*, **686**, 1362–1371, doi:10.1086/591724, 2008.

Doschek, G. A., Landi, E., Warren, H. P., and Harra, L. K.: Bright Points and Jets in Polar Coronal Holes Observed by the Extreme-Ultraviolet Imaging Spectrometer on Hinode, *ApJ*, **710**, 1806–1824, doi:10.1088/0004-637X/710/2/1806, 2010.

Driesman, A., Hynes, S., and Cancro, G.: The STEREO Observatory, *Space Science Reviews*, **136**, 17–44, doi:10.1007/s11214-007-9286-z, 2008.

Edmondson, J. K., Lynch, B. J., Antiochos, S. K., De Vore, C. R., and Zurbuchen, T. H.: Reconnection-Driven Dynamics of Coronal-Hole Boundaries, *ApJ*, **707**, 1427–1437, doi:10.1088/0004-637X/707/2/1427, 2009.

Edmondson, J. K., Antiochos, S. K., DeVore, C. R., Lynch, B. J., and Zurbuchen, T. H.: Interchange Reconnection and Coronal Hole Dynamics, *ApJ*, **714**, 517–531, doi:10.1088/0004-637X/714/1/517, 2010.

Einaudi, G., Boncinelli, P., Dahlburg, R. B., and Karpen, J. T.: Formation of the slow solar wind in a coronal streamer, *JGR*, **104**, 521–534, doi:10.1029/98JA02394, 1999.

Eyles, C. J., Harrison, R. A., Davis, C. J., Waltham, N. R., Shaughnessy, B. M., Mapson-Menard, H. C. A., Bewsher, D., Crothers, S. R., Davies, J. A., Simnett, G. M., Howard, R. A., Moses, J. D., Newmark, J. S., Socker, D. G., Halain, J.-P., Defise, J.-M., Mazy, E., and Rochus, P.: The Heliospheric Imagers Onboard the STEREO Mission, *Solar Phys.*, **254**, 387–445, doi:10.1007/s11207-008-9299-0, 2009.

Feldman, U., Warren, H. P., Brown, C. M., and Doschek, G. A.: Can the Composition of the Solar Corona Be Derived from Hinode/Extreme-Ultraviolet Imaging Spectrometer Spectra?, *ApJ*, **695**, 36–45, doi:10.1088/0004-637X/695/1/36, 2009.

Feynman, J. and Hundhausen, A. J.: Coronal mass ejections and major solar flares: The great active center of March 1989, *JGR*, **99**, 8451–8464, doi:10.1029/94JA00202, 1994.

Feynman, J. and Martin, S. F.: The initiation of coronal mass ejections by newly emerging magnetic flux, *JGR*, **100**, 3355–3367, doi:10.1029/94JA02591, 1995.

Fisk, L. A.: The Open Magnetic Flux of the Sun. I. Transport by Reconnections with Coronal Loops, *ApJ*, **626**, 563–573, doi:10.1086/429957, 2005.

Fisk, L. A. and Schwadron, N. A.: The Behavior of the Open Magnetic Field of the Sun, *Astrophys. J.*, **560**, 425–438, doi:10.1086/322503, 2001.

Fisk, L. A., Zurbuchen, T. H., and Schwadron, N. A.: On the Coronal Magnetic Field: Consequences of Large-Scale Motions, *Astrophys. J.*, **521**, 868–877, doi:10.1086/307556, 1999.

Fletcher, L., López Fuentes, M. C., Mandrini, C. H., Schmieder, B., Démoulin, P., Mason, H. E., Young, P. R., and Nitta, N.: A Relationship Between Transition Region Brightenings, Abundances, and Magnetic Topology, *Solar Phys.*, **203**, 255–287, doi:10.1023/A:1013302317042, 2001.

Fontenla, J. M., Avrett, E. H., and Loeser, R.: Energy balance in the solar transition region. I - Hydrostatic thermal models with ambipolar diffusion, *ApJ*, **355**, 700–718, doi:10.1086/168803, 1990.

Forbes, T. G.: A review on the genesis of coronal mass ejections, *J. Geophys. Res.*, **105**, 23 153–23 166, doi:10.1029/2000JA000005, 2000.

Forbes, T. G., Priest, E. R., and Isenberg, P. A.: On the maximum energy release in flux-rope models of eruptive flares, *Solar Physics*, **150**, 245–266, doi:10.1007/BF00712888, 1994.

Forbes, T. G., Linker, J. A., Chen, J., Cid, C., Kóta, J., Lee, M. A., Mann, G., Mikić, Z., Potgieter, M. S., Schmidt, J. M., Siscoe, G. L., Vainio, R., Antiochos, S. K., and Riley, P.: CME Theory and Models, *Space Sci. Rev.*, **123**, 251–302, doi:10.1007/s11214-006-9019-8, 2006.

Forsyth, R. J. and Gosling, J. T.: Corotating and transient structures in the heliosphere, pp. 107–166, 2001.

Fox, J. L., Kankelborg, C. C., and Thomas, R. J.: A Transition Region Explosive Event Observed in He II with the MOSES Sounding Rocket, *ApJ*, **719**, 1132–1143, doi:10.1088/0004-637X/719/2/1132, 2010.

Gabriel, A. H.: A magnetic model of the solar transition region, *Royal Society of London Philosophical Transactions Series A*, **281**, 339–352, 1976.

Gaizauskas, V., Mandrini, C. H., Demoulin, P., Luoni, M. L., and Rovira, M. G.: Interactions between nested sunspots. II. A confined X1 flare in a delta-type sunspot, *A&A*, **332**, 353–366, 1998.

Galvin, A. B., Kistler, L. M., Popecki, M. A., Farrugia, C. J., Simunac, K. D. C., Ellis, L., Möbius, E., Lee, M. A., Boehm, M., Carroll, J., Crawshaw, A., Conti, M., Demaine, P., Ellis, S., Gaidos, J. A., Googins, J., Granoff, M., Gustafson, A., Heirtzler, D., King, B., Knauss, U., Levasseur, J., Longworth, S., Singer, K., Turco, S., Vachon, P., Vosbury, M., Widholm, M., Blush, L. M., Karrer, R., Bochsler, P., Daoudi, H., Etter, A., Fischer, J., Jost, J., Opitz, A., Sigrist, M., Wurz, P., Klecker, B., Ertl, M., Seidenschwang, E., Wimmer-Schweingruber, R. F., Koeten, M., Thompson, B., and Steinfeld, D.: The Plasma and Suprathermal Ion Composition (PLASTIC) Investigation on the STEREO Observatories, *Space Sci. Rev.*, **136**, 437–486, doi:10.1007/s11214-007-9296-x, 2008.

Gary, G. A.: Plasma Beta above a Solar Active Region: Rethinking the Paradigm, *Solar Physics*, **203**, 71–86, 2001.

Gary, G. A. and Moore, R. L.: Eruption of a Multiple-Turn Helical Magnetic Flux Tube in a Large Flare: Evidence for External and Internal Reconnection That Fits the Breakout Model of Solar Magnetic Eruptions, *ApJ*, **611**, 545–556, doi:10.1086/422132, 2004.

Gibson, S. E. and Fan, Y.: The Partial Expulsion of a Magnetic Flux Rope, *ApJL*, **637**, L65–L68, doi:10.1086/500452, 2006.

Gibson, S. E., Fan, Y., Török, T., and Kliem, B.: The Evolving Sigmoid: Evidence for Magnetic Flux Ropes in the Corona Before, During, and After CMES, *Space Sci. Rev.*, **124**, 131–144, doi:10.1007/s11214-006-9101-2, 2006.

Gloeckler, G., Cain, J., Ipavich, F. M., Tums, E. O., Bedini, P., Fisk, L. A., Zurbuchen, T. H., Bochsler, P., Fischer, J., Wimmer-Schweingruber, R. F., Geiss, J., and Kallenbach, R.: Investigation of the composition of solar and interstellar matter using solar wind and pickup ion measurements with SWICS and SWIMS on the ACE spacecraft, *Space Sci. Rev.*, **86**, 497–539, doi:10.1023/A:1005036131689, 1998.

Glover, A., Ranns, N. D. R., Harra, L. K., and Culhane, J. L.: The Onset and Association of CMEs with Sigmoidal Active Regions, *Geophys. Res. Lett.*, **27**, 2161–+, doi:10.1029/2000GL000018, 2000.

Goff, C. P., van Driel-Gesztelyi, L., Démoulin, P., Culhane, J. L., Matthews, S. A., Harra, L. K., Mandrini, C. H., Klein, K. L., and Kurokawa, H.: A Multiple Flare Scenario where the Classic Long-Duration Flare Was Not the Source of a CME, *Solar Physics*, **240**, 283–299, doi:10.1007/s11207-007-0260-4, 2007.

Golub, L. and Pasachoff, J. M.: The Solar Corona, 1997.

Golub, L., Deluca, E., Austin, G., Bookbinder, J., Caldwell, D., Cheimets, P., Cirtain, J., Cosmo, M., Reid, P., Sette, A., Weber, M., Sakao, T., Kano, R., Shibasaki, K., Hara, H., Tsuneta, S., Kumagai, K., Tamura, T., Shimojo, M., McCracken, J., Carpenter, J., Haight, H., Siler, R., Wright, E., Tucker, J., Rutledge, H., Barbera, M., Peres, G., and Varisco, S.: The X-Ray Telescope (XRT) for the Hinode Mission, *Solar Phys.*, **243**, 63–86, doi:10.1007/s11207-007-0182-1, 2007.

Gopalswamy, N., Mikić, Z., Maia, D., Alexander, D., Cremades, H., Kaufmann, P., Tripathi, D., and Wang, Y.: The Pre-CME Sun, *Space Sci. Rev.*, **123**, 303–339, doi:10.1007/s11214-006-9020-2, 2006.

Gopalswamy, N., Mäkelä, P., Xie, H., Akiyama, S., and Yashiro, S.: CME interactions with coronal holes and their interplanetary consequences, *J. Geophys. Res.*, **114**, 0–+, doi:10.1029/2008JA013686, 2009.

Gosling, J. T.: Large-scale inhomogeneities in the solar wind of solar origin, *Rev. Geophys. Space Phys.*, **13**, 1053–1058, 1975.

Gosling, J. T., Baker, D. N., Bame, S. J., Feldman, W. C., Zwickl, R. D., and Smith, E. J.: Bidirectional solar wind electron heat flux events, *J. Geophys. Res.*, **92**, 8519–8535, doi:10.1029/JA092iA08p08519, 1987.

Gosling, J. T., Birn, J., and Hesse, M.: Three-dimensional magnetic reconnection and the magnetic topology of coronal mass ejection events, *Geophys. Res. Lett.*, **22**, 869–872, doi:10.1029/95GL00270, 1995.

Green, L. M., López fuentes, M. C., Mandrini, C. H., Démoulin, P., Van Driel-Gesztelyi, L., and Culhane, J. L.: The Magnetic Helicity Budget of a cme-Prolific Active Region, *Solar Physics*, **208**, 43–68, 2002a.

Green, L. M., Matthews, S. A., van Driel-Gesztelyi, L., Harra, L. K., and Culhane, J. L.: Multi-wavelength observations of an X-class flare without a coronal mass ejection., *Solar Physics*, **205**, 325–339, 2002b.

Green, L. M., Démoulin, P., Mandrini, C. H., and Van Driel-Gesztelyi, L.: How are Emerging Flux, Flares and CMEs Related to Magnetic Polarity Imbalance in MDI Data?, *Solar Phys.*, **215**, 307–325, 2003.

Gurman, J. B. and Athay, R. G.: Fluid motions in the solar chromosphere-corona transition region. IV - Mass motions over sunspot umbrae, *ApJ*, **273**, 374–380, doi:10.1086/161376, 1983.

Habbal, S. R., Esser, R., and Arndt, M. B.: How reliable are coronal hole temperatures deduced from observations?, *ApJ*, **413**, 435–444, doi:10.1086/173011, 1993.

Habbal, S. R., Scholl, I. F., and McIntosh, S. W.: Impact of Active Regions on Coronal Hole Outflows, *Astrophys. J. Lett.*, **683**, L75–L78, doi:10.1086/591315, 2008.

Hagenaar, H. J., Schrijver, C. J., and Title, A. M.: The Properties of Small Magnetic Regions on the Solar Surface and the Implications for the Solar Dynamo(s), *ApJ*, **584**, 1107–1119, doi:10.1086/345792, 2003.

Hale, G. E. and Nicholson, S. B.: The Law of Sun-Spot Polarity, *ApJ*, **62**, 270–+, doi:10.1086/142933, 1925.

Hara, H., Watanabe, T., Harra, L. K., Culhane, J. L., Young, P. R., Mariska, J. T., and Doschek, G. A.: Coronal Plasma Motions near Footpoints of Active Region Loops Revealed from Spectroscopic Observations with Hinode EIS, *Astrophys. J. Lett.*, **678**, L67–L71, doi:10.1086/588252, 2008.

Harra, L. K. and Mason, K. O.: Space Science, Imperial College Press, 2004.

Harra, L. K., Démoulin, P., Mandrini, C. H., Matthews, S. A., van Driel-Gesztelyi, L., Culhane, J. L., and Fletcher, L.: Flows in the solar atmosphere due to the eruptions on the 15th July, 2002, *A&A*, **438**, 1099–1106, doi:10.1051/0004-6361:20052965, 2005.

Harra, L. K., Crooker, N. U., Mandrini, C. H., van Driel-Gesztelyi, L., Dasso, S., Wang, J., Elliott, H., Attrill, G., Jackson, B. V., and Bisi, M. M.: How Does Large Flaring Activity from the Same Active Region Produce Oppositely Directed Magnetic Clouds?, *Solar Phys.*, **244**, 95–114, doi:10.1007/s11207-007-9002-x, 2007.

Harra, L. K., Sakao, T., Mandrini, C. H., Hara, H., Imada, S., Young, P. R., van Driel-Gesztelyi, L., and Baker, D.: Outflows at the Edges of Active Regions: Contribution to Solar Wind Formation?, *Astrophys. J. Lett.*, **676**, L147–L150, doi:10.1086/587485, 2008.

Harrison, R. A.: Solar coronal mass ejections and flares, *A&A*, **162**, 283–291, 1986.

Harrison, R. A.: The nature of solar flares associated with coronal mass ejection., *A&A*, **304**, 585–+, 1995.

Harrison, R. A., Waggett, P. W., Bentley, R. D., Phillips, K. J. H., Bruner, M., Dryer, M., and Simnett, G. M.: The X-ray signature of solar coronal mass, *Solar Physics*, **97**, 387–400, doi:10.1007/BF00165998, 1985.

Harrison, R. A., Bryans, P., and Bingham, R.: EUV Sprays: Jet-like eruptive activity on the solar limb, *A&A*, **379**, 324–335, doi:10.1051/0004-6361:20011171, 2001.

Harrison, R. A., Davis, C. J., Eyles, C. J., Bewsher, D., Crothers, S. R., Davies, J. A., Howard, R. A., Moses, D. J., Socker, D. G., Newmark, J. S., Halain, J.-P., Defise, J.-M., Mazy, E., Rochus, P., Webb, D. F., and Simnett, G. M.: First Imaging of Coronal Mass Ejections in the Heliosphere Viewed from Outside the Sun Earth Line, *Solar Phys.*, **247**, 171–193, doi:10.1007/s11207-007-9083-6, 2008.

Harvey, K. L. and Zwaan, C.: Properties and emergence of bipolar active regions, *Solar Physics*, **148**, 85–118, doi:10.1007/BF00675537, 1993.

Henke, T., Woch, J., Mall, U., Livi, S., Wilken, B., Schwenn, R., Gloeckler, G., von Steiger, R., Forsyth, R. J., and Balogh, A.: Differences in the O^{7+}/O^{6+} ratio of magnetic cloud and non-cloud Coronal Mass Ejections, *Geophys. Res. Lett.*, **25**, 3465–3468, doi:10.1029/98GL02632, 1998.

Hirayama, T.: Theoretical Model of Flares and Prominences. I: Evaporating Flare Model, *Solar Physics*, **34**, 323–338, doi:10.1007/BF00153671, 1974.

Hirshberg, J., Alksne, A., Colburn, D. S., Bame, S. J., and Hundhausen, A. J.: Observations of a solar flare induced interplanetary shock and helium-enriched driver gas., *J. Geophys. Res.*, **75**, 1–15, doi:10.1029/JA075i001p00001, 1970.

Hirshberg, J., Bame, S. J., and Robbins, D. E.: Solar flares and solar wind helium enrichments: July 1965 July 1967, *Solar Phys.*, **23**, 467–486, doi:10.1007/BF00148109, 1972.

Hood, A. W. and Priest, E. R.: Critical conditions for magnetic instabilities in force-free coronal loops, *Geophysical and Astrophysical Fluid Dynamics*, **17**, 297–318, doi:10.1080/03091928108243687, 1981.

Howard, R. A., Moses, J. D., Vourlidas, A., Newmark, J. S., Socker, D. G., Plunkett, S. P., Korendyke, C. M., Cook, J. W., Hurley, A., Davila, J. M., Thompson, W. T., St Cyr, O. C., Mentzell, E., Mehalick, K., Lemen, J. R., Wuelser, J. P., Duncan, D. W., Tarbell, T. D., Wolfson, C. J., Moore, A., Harrison, R. A., Waltham, N. R., Lang, J., Davis, C. J., Eyles, C. J., Mapson-Menard, H., Simnett, G. M., Halain, J. P., Defise, J. M., Mazy, E., Rochus, P., Mercier, R., Ravet, M. F., Delmotte, F., Auchere, F., Delaboudiniere, J. P., Bothmer, V., Deutsch, W., Wang, D., Rich, N., Cooper, S., Stephens, V., Maahs, G., Baugh, R., McMullin, D., and Carter, T.: Sun Earth Connection Coronal and Heliospheric Investigation (SECCHI), *Space Sci. Rev.*, **136**, 67–115, doi:10.1007/s11214-008-9341-4, 2008.

Howard, R. F.: Axial tilt angles of sunspot groups, *Solar Physics*, **136**, 251–262, doi:10.1007/BF00146534, 1991.

Hudson, H. S., Acton, L. W., and Freeland, S. L.: A Long-Duration Solar Flare with Mass Ejection and Global Consequences, *ApJ*, **470**, 629–+, doi:10.1086/177894, 1996.

Hudson, H. S., Lemen, J. R., St. Cyr, O. C., Sterling, A. C., and Webb, D. F.: X-ray coronal changes during halo CMEs, *Geophys. Res. Lett.*, **25**, 2481–2484, doi:10.1029/98GL01303, 1998.

Jackson, B. V., Sheridan, K. V., Dulk, G. A., and McLean, D. J.: A possible association of solar type III bursts and white light transients, *Proceedings of the Astronomical Society of Australia*, **3**, 241–+, 1978.

Kahler, S. W. and Hudson, H. S.: Boundary Structures and Changes in Long-lived Coronal Holes, *ApJ*, **574**, 467–476, doi:10.1086/340937, 2002.

Kahler, S. W., Sheeley, Jr., N. R., and Liggett, M.: Coronal mass ejections and associated X-ray flare durations, *ApJ*, **344**, 1026–1033, doi:10.1086/167869, 1989.

Kaiser, M. L., Kucera, T. A., Davila, J. M., St. Cyr, O. C., Guhathakurta, M., and Christian, E.: The STEREO Mission: An Introduction, *Space Sci. Rev.*, **136**, 5–16, doi:10.1007/s11214-007-9277-0, 2008.

Kamio, S., Hara, H., Watanabe, T., Matsuzaki, K., Shibata, K., Culhane, L., and Warren, H. P.: Velocity Structure of Jets in a Coronal Hole, *PASJ*, **59**, 757–+, 2007.

Kamio, S., Hara, H., Watanabe, T., and Curdt, W.: Distribution of jets and magnetic fields in a coronal hole, *A&A*, **502**, 345–353, doi:10.1051/0004-6361/200811125, 2009.

Kamio, S., Curdt, W., Teriaca, L., Inhester, B., and Solanki, S. K.: Observations of a rotating macrospicule associated with an X-ray jet, *A&A*, **510**, L1+, doi:10.1051/0004-6361/200913269, 2010.

Kilpua, E. K. J., Luhmann, J. G., Gosling, J., Li, Y., Elliott, H., Russell, C. T., Jian, L., Galvin, A. B., Larson, D., Schroeder, P., Simunac, K., and Petrie, G.: Small Solar Wind Transients and Their Connection to the Large-Scale Coronal Structure, *Solar Phys.*, **256**, 327–344, doi:10.1007/s11207-009-9366-1, 2009.

Kivelson, M. G. and Russell, C. T.: Introduction to Space Physics, 1995.

Klimchuk, J. A.: On Solving the Coronal Heating Problem, *Solar Physics*, **234**, 41–77, doi:10.1007/s11207-006-0055-z, 2006.

Ko, Y., Raymond, J. C., Gibson, S. E., Alexander, D., Strachan, L., Holzer, T., Gilbert, H., Cyr, O. C. S., Thompson, B. J., Pike, C. D., Mason, H. E., Burkepile, J., Thompson, W., and Fletcher, L.: Multialtitude Observations of a Coronal Jet during the Third Whole Sun Month Campaign, *ApJ*, **623**, 519–539, doi:10.1086/428479, 2005.

Ko, Y.-K., Raymond, J. C., Zurbuchen, T. H., Riley, P., Raines, J. M., and Strachan, L.: Abundance Variation at the Vicinity of an Active Region and the Coronal Origin of the Slow Solar Wind, *Astrophys. J.*, **646**, 1275–1287, doi:10.1086/505021, 2006.

Kopp, R. A. and Pneuman, G. W.: Magnetic reconnection in the corona and the loop prominence phenomenon, *Solar Physics*, **50**, 85–98, doi:10.1007/BF00206193, 1976.

Kosugi, T., Matsuzaki, K., Sakao, T., Shimizu, T., Sone, Y., Tachikawa, S., Hashimoto, T., Minesugi, K., Ohnishi, A., Yamada, T., Tsuneta, S., Hara, H., Ichimoto, K., Suematsu, Y., Shimojo, M., Watanabe, T., Shimada, S., Davis, J. M., Hill, L. D., Owens, J. K., Title, A. M., Culhane, J. L., Harra, L. K.,

Doschek, G. A., and Golub, L.: The Hinode (Solar-B) Mission: An Overview, *Solar Phys.*, **243**, 3–17, doi:10.1007/s11207-007-9014-6, 2007.

Laming, J. M.: A Unified Picture of the First Ionization Potential and Inverse First Ionization Potential Effects, *ApJ*, **614**, 1063–1072, doi:10.1086/423780, 2004.

Lawrence, E. E. and Gekelman, W.: Identification of a Quasiseparatrix Layer in a Reconnecting Laboratory Magnetoplasma, *Physical Review Letters*, **103**, 105 002–+, doi:10.1103/PhysRevLett.103.105002, 2009.

Leamon, R. J., Canfield, R. C., and Pevtsov, A. A.: Properties of magnetic clouds and geomagnetic storms associated with eruption of coronal sigmoids, *Journal of Geophysical Research (Space Physics)*, **107**, 1234–+, doi:10.1029/2001JA000313, 2002.

Leibacher, J. W. and Stein, R. F.: A New Description of the Solar Five-Minute Oscillation, *aplett*, **7**, 191–192, 1971.

Liewer, P. C., Neugebauer, M., and Zurbuchen, T.: Characteristics of active-region sources of solar wind near solar maximum, *Solar Phys.*, **223**, 209–229, doi:10.1007/s11207-004-1105-z, 2004.

Lin, J. and Forbes, T. G.: Effects of reconnection on the coronal mass ejection process, *JGR*, **105**, 2375–2392, doi:10.1029/1999JA900477, 2000.

Lin, J., Forbes, T. G., Isenberg, P. A., and Demoulin, P.: The Effect of Curvature on Flux-Rope Models of Coronal Mass Ejections, *ApJ*, **504**, 1006–+, doi:10.1086/306108, 1998.

Liu, Y.: Coronal magnetic fields inferred from IR wavelength and comparison with EUV observations, *Annales Geophysicae*, **27**, 2771–2777, 2009.

Liu, Y., Luhmann, J. G., Lin, R. P., Bale, S. D., Vourlidas, A., and Petrie, G. J. D.: Coronal Mass Ejections and Global Coronal Magnetic Field Reconfiguration, *ApJL*, **698**, L51–L55, doi:10.1088/0004-637X/698/1/L51, 2009.

Luhmann, J. G., Curtis, D. W., Schroeder, P., McCauley, J., Lin, R. P., Larson, D. E., Bale, S. D., Sauvaud, J.-A., Aoustin, C., Mewaldt, R. A., Cummings, A. C., Stone, E. C., Davis, A. J., Cook, W. R., Kecman, B., Wiedenbeck, M. E., von Rosenvinge, T., Acuna, M. H., Reichenthal, L. S., Shuman, S., Wortman, K. A., Reames, D. V., Mueller-Mellin, R., Kunow, H., Mason, G. M., Walpole, P., Korth, A., Sanderson, T. R., Russell, C. T., and Gosling, J. T.: STEREO IMPACT Investigation Goals, Measurements, and Data Products Overview, *Space Sci. Rev.*, **136**, 117–184, doi:10.1007/s11214-007-9170-x, 2008.

Mandrini, C. H., Demoulin, P., Henoux, J. C., and Machado, M. E.: Evidence for the interaction of large scale magnetic structures in solar flares, *A&A*, **250**, 541–547, 1991.

Mandrini, C. H., Démoulin, P., van Driel-Gesztelyi, L., Schmieder, B., Cauzzi, G., and Hofmann, A.: 3D Magnetic Reconnection at an X-Ray Bright Point, *Solar Phys.*, **168**, 115–133, doi:10.1007/BF00145829, 1996.

Mandrini, C. H., Demoulin, P., Bagala, L. G., van Driel-Gesztelyi, L., Henoux, J. C., Schmieder, B., and Rovira, M. G.: Evidence of Magnetic Reconnection from Hα, Soft X-Ray and Photospheric Magnetic Field Observations, *Solar Phys.*, **174**, 229–240, 1997.

Mandrini, C. H., Démoulin, P., and Klimchuk, J. A.: Magnetic Field and Plasma Scaling Laws: Their Implications for Coronal Heating Models, *ApJ*, **530**, 999–1015, doi:10.1086/308398, 2000.

Marsch, E., Wiegelmann, T., and Xia, L. D.: Coronal plasma flows and magnetic fields in solar active regions. Combined observations from SOHO and NSO/Kitt Peak, *A&A*, **428**, 629–645, doi:10.1051/0004-6361:20041060, 2004.

Marsch, E., Tian, H., Sun, J., Curdt, W., and Wiegelmann, T.: Plasma Flows Guided by Strong Magnetic Fields in the Solar Corona, *Astrophys. J.*, **685**, 1262–1269, doi:10.1086/591038, 2008.

Martin, S. F., Livi, S. H. B., and Wang, J.: The cancellation of magnetic flux. II - In a decaying active region, *Australian Journal of Physics*, **38**, 929–959, 1985.

Mason, H. E. and Fossi, B. C. M.: Spectroscopic diagnostics in the VUV for solar and stellar plasmas, *Astronomy and Astrophysics Review*, **6**, 123–179, doi:10.1007/BF01208253, 1994.

Masson, S., Pariat, E., Aulanier, G., and Schrijver, C. J.: The Nature of Flare Ribbons in Coronal Null-Point Topology, *ApJ*, **700**, 559–578, doi:10.1088/0004-637X/700/1/559, 2009.

Masuda, S., Kosugi, T., Hara, H., Sakao, T., Shibata, K., and Tsuneta, S.: Hard X-Ray Sources and the Primary Energy-Release Site in Solar Flares, *PASJ*, **47**, 677–689, 1995.

McComas, D. J., Bame, S. J., Barker, P., Feldman, W. C., Phillips, J. L., Riley, P., and Griffee, J. W.: Solar Wind Electron Proton Alpha Monitor (SWEPAM) for the Advanced Composition Explorer, *Space Sci. Rev.*, **86**, 563–612, doi:10.1023/A:1005040232597, 1998.

McComas, D. J., Ebert, R. W., Elliott, H. A., Goldstein, B. E., Gosling, J. T., Schwadron, N. A., and Skoug, R. M.: Weaker solar wind from the polar coronal holes and the whole Sun, *Geophys. Res. Lett.*, **35**, 18 103–+, doi:10.1029/2008GL034896, 2008.

McEwan, M. P. and de Moortel, I.: Longitudinal intensity oscillations observed with TRACE: evidence of fine-scale structure, *A&A*, **448**, 763–770, doi:10.1051/0004-6361:20054041, 2006.

McIntosh, S. W. and De Pontieu, B.: High-Speed Transition Region and Coronal Upflows in the Quiet Sun, *ApJ*, **707**, 524–538, doi:10.1088/0004-637X/707/1/524, 2009.

Melrose, D. B.: A Solar Flare Model Based on Magnetic Reconnection between Current-carrying Loops, *ApJ*, **486**, 521–+, doi:10.1086/304521, 1997.

Miesch, M. S.: Large-Scale Dynamics of the Convection Zone and Tachocline, *Living Reviews in Solar Physics*, **2**, 1–+, 2005.

Milano, L. J., Dmitruk, P., Mandrini, C. H., Gómez, D. O., and Démoulin, P.: Quasi-Separatrix Layers in a Reduced Magnetohydrodynamic Model of a Coronal Loop, *ApJ*, **521**, 889–897, doi:10.1086/307563, 1999.

Miyagoshi, T. and Yokoyama, T.: Magnetohydrodynamic Numerical Simulations of Solar X-Ray Jets Based on the Magnetic Reconnection Model That Includes Chromospheric Evaporation, *Astrophys. J. Lett.*, **593**, L133–L136, doi:10.1086/378215, 2003.

Moore, R. L. and Sterling, A. C.: Initiation of Coronal Mass Ejections, *Washington DC American Geophysical Union Geophysical Monograph Series*, **165**, 43–+, 2006.

Moore, R. L., Sterling, A. C., Hudson, H. S., and Lemen, J. R.: Onset of the Magnetic Explosion in Solar Flares and Coronal Mass Ejections, *ApJ*, **552**, 833–848, doi:10.1086/320559, 2001.

Moreno-Insertis, F., Galsgaard, K., and Ugarte-Urra, I.: Jets in Coronal Holes: Hinode Observations and Three-dimensional Computer Modeling, *Astrophys. J. Lett.*, **673**, L211–L214, doi:10.1086/527560, 2008.

Murray, M. J., Baker, D., van Driel-Gesztelyi, L., and Sun, J.: Outflows at the Edges of an Active Region in a Coronal Hole: A Signature of Active Region Expansion?, *Solar Physics*, **261**, 253–269, doi:10.1007/s11207-009-9484-9, 2010.

Nakariakov, V. M., Verwichte, E., Berghmans, D., and Robbrecht, E.: Slow magnetoacoustic waves in coronal loops, *A&A*, **362**, 1151–1157, 2000.

Nash, A. G., Sheeley, Jr., N. R., and Wang, Y.: Mechanisms for the rigid rotation of coronal holes, *Solar Physics*, **117**, 359–389, doi:10.1007/BF00147253, 1988.

Neugebauer, M.: Observations of solar-wind helium, *Fundamentals of Cosmic Physics*, **7**, 131–199, 1981.

Neugebauer, M., Goldstein, R., and Goldstein, B. E.: Features observed in the trailing regions of interplanetary clouds from coronal mass ejections, *J. Geophys. Res.*, **102**, 19 743–19 752, doi:10.1029/97JA01651, 1997.

Nisticò, G., Bothmer, V., Patsourakos, S., and Zimbardo, G.: Characteristics of EUV Coronal Jets Observed with STEREO/SECCHI, *Solar Physics*, **259**, 87–108, doi:10.1007/s11207-009-9424-8, 2009.

Nisticò, G., Bothmer, V., Patsourakos, S., and Zimbardo, G.: Observational features of equatorial coronal hole jets, *Annales Geophysicae*, **28**, 687–696, 2010.

Ofman, L., Romoli, M., Poletto, G., Noci, G., and Kohl, J. L.: Ultraviolet Coronagraph Spectrometer Observations of Density Fluctuations in the Solar Wind, *ApJL*, **491**, L111+, doi:10.1086/311067, 1997.

Ogawara, Y., Takano, T., Kato, T., Kosugi, T., Tsuneta, S., Watanabe, T., Kondo, I., and Uchida, Y.: The Solar-A Mission - an Overview, *Solar Physics*, **136**, 1–16, doi:10.1007/BF00151692, 1991.

Owens, M. J. and Crooker, N. U.: Coronal mass ejections and magnetic flux buildup in the heliosphere, *J. Geophys. Res.*, **111**, 10 104–+, doi:10.1029/2006JA011641, 2006.

Owens, M. J., Schwadron, N. A., Crooker, N. U., Hughes, W. J., and Spence, H. E.: Role of coronal mass ejections in the heliospheric Hale cycle, *Geophys. Res. Lett.*, **34**, 6104–+, doi:10.1029/2006GL028795, 2007.

Pariat, E., Antiochos, S. K., and DeVore, C. R.: A Model for Solar Polar Jets, *ApJ*, **691**, 61–74, doi:10.1088/0004-637X/691/1/61, 2009.

Parker, E. N.: Sweet's Mechanism for Merging Magnetic Fields in Conducting Fluids, *JGR*, **62**, 509–520, doi:10.1029/JZ062i004p00509, 1957.

Parker, E. N.: Dynamics of the Interplanetary Gas and Magnetic Fields., *ApJ*, **128**, 664–+, doi:10.1086/146579, 1958.

Parker, E. N.: The Solar-Flare Phenomenon and the Theory of Reconnection and Annihiliation of Magnetic Fields., *Astrophysical Journal Supplement Series*, **8**, 177–+, doi:10.1086/190087, 1963.

Parker, E. N.: Heating solar coronal holes, *ApJ*, **372**, 719–727, doi:10.1086/170015, 1991.

Parnell, C. E.: Magnetic reconnection and some solar applications, in Astronomy, physics and chemistry of Hplus3, vol. 358 of *Royal Society of London Philosophical Transactions Series A*, pp. 669–688, doi:10.1098/rsta.2000.0552, 2000.

Parnell, C. E. and Haynes, A. L.: Three-Dimensional Magnetic Reconnection, *ArXiv e-prints*, 2009.

Parnell, C. E., Haynes, A. L., and Galsgaard, K.: Structure of magnetic separators and separator reconnection, *Journal of Geophysical Research (Space Physics)*, **115**, 2102–+, doi:10.1029/2009JA014557, 2010.

Patsourakos, S. and Klimchuk, J. A.: Nonthermal Spectral Line Broadening and the Nanoflare Model, *ApJ*, **647**, 1452–1465, doi:10.1086/505517, 2006.

Patsourakos, S., Pariat, E., Vourlidas, A., Antiochos, S. K., and Wuelser, J. P.: STEREO SECCHI Stereoscopic Observations Constraining the Initiation of Polar Coronal Jets, *ApJL*, **680**, L73–L76, doi:10.1086/589769, 2008.

Peter, H.: Asymmetries of solar coronal extreme ultraviolet emission lines, *ArXiv e-prints*, 2010.

Petschek, H. E.: Magnetic Field Annihilation, *NASA Special Publication*, **50**, 425–+, 1964.

Phillips, K. J. H., Feldman, U., and Landi, E.: Ultraviolet and X-ray Spectroscopy of the Solar Atmosphere, Cambridge University Press, 2008.

Pick, M., Forbes, T. G., Mann, G., Cane, H. V., Chen, J., Ciaravella, A., Cremades, H., Howard, R. A., Hudson, H. S., Klassen, A., Klein, K. L., Lee, M. A., Linker, J. A., Maia, D., Mikic, Z., Raymond, J. C., Reiner, M. J., Simnett, G. M., Srivastava, N., Tripathi, D., Vainio, R., Vourlidas, A., Zhang, J., Zurbuchen, T. H., Sheeley, N. R., and Marqué, C.: Multi-Wavelength Observations of CMEs and Associated Phenomena. Report of Working Group F, *Space Sci. Rev.*, **123**, 341–382, doi:10.1007/s11214-006-9021-1, 2006.

Pizzo, V. J.: The nature of the distant solar wind, *Advances in Space Research*, **6**, 353–367, doi:10.1016/0273-1177(86)90051-7, 1986.

Priest, E. R.: Three-dimensional reconnection on the Sun, *Earth, Planets, and Space*, **53**, 483–490, 2001.

Priest, E. R. and Démoulin, P.: Three-dimensional magnetic reconnection without null points. 1. Basic theory of magnetic flipping, *J. Geophys. Res.*, **100**, 23 443–23 464, doi:10.1029/95JA02740, 1995.

Priest, E. R. and Titov, V. S.: Magnetic Reconnection at Three-Dimensional Null Points, *Royal Society of London Proceedings Series A*, **354**, 2951–2992, 1996.

Qiu, J., Wang, H., Chae, J., and Goode, P. R.: Counter-streaming Mass Flow and Transient Brightening in Active Region Loops, *Solar Physics*, **190**, 153–165, doi:10.1023/A:1005209504270, 1999.

Ramsey, H. E. and Smith, S. F.: Flare-initiated filamei it oscillations, *AJ*, **71**, 197–+, doi:10.1086/109903, 1966.

Raouafi, N., Georgoulis, M. K., Rust, D. M., and Bernasconi, P. N.: Micro-sigmoids as Progenitors of Coronal Jets: Is Eruptive Activity Self-similarly Multi-scaled?, *ApJ*, **718**, 981–987, doi:10.1088/0004-637X/718/2/981, 2010.

Régnier, S.: Nonlinear force-free field extrapolation: numerical methods and applications, *Memorie della Societa Astronomica Italiana*, **78**, 126–+, 2007.

Régnier, S.: What Can we Learn from Nonlinear Force-Free Extrapolations?, in First Results From Hinode, edited by S. A. Matthews, J. M. Davis, & L. K. Harra, vol. 397 of *Astronomical Society of the Pacific Conference Series*, pp. 75–+, 2008.

Riley, P., Gosling, J. T., and Crooker, N. U.: Ulysses Observations of the Magnetic Connectivity between Coronal Mass Ejections and the Sun, *Astrophys. J.*, **608**, 1100–1105, doi:10.1086/420811, 2004.

Rouillard, A. P., Davies, J. A., Forsyth, R. J., Rees, A., Davis, C. J., Harrison, R. A., Lockwood, M., Bewsher, D., Crothers, S. R., Eyles, C. J., Hapgood, M., and Perry, C. H.: First imaging of corotating interaction regions using the STEREO spacecraft, *Geophys. Res. Lett.*, **35**, 10 110–+, doi:10.1029/2008GL033767, 2008.

Rouillard, A. P., Davies, J. A., Lavraud, B., Forsyth, R. J., Savani, N. P., and et al.: Intermittent release of small-scale transients in the slow solar wind: I, Remote sensing observations, *J. Geophys. Res.*, **submitted**, doi:NA, 2009a.

Rouillard, A. P., Savani, N. P., Davies, J. A., Lavraud, B., Forsyth, R. J., Morley, S. K., Opitz, A., Sheeley, N. R., Burlaga, L. F., Sauvaud, J.-A., Simunac, K. D. C., Luhmann, J. G., Galvin, A. B., Crothers, S. R., Davis, C. J., Harrison, R. A., Lockwood, M., Eyles, C. J., Bewsher, D., and Brown, D. S.: A Multispacecraft Analysis of a Small-Scale Transient Entrained by Solar Wind Streams, *Solar Phys.*, **256**, 307–326, doi:10.1007/s11207-009-9329-6, 2009b.

Rust, D. M. and Kumar, A.: Evidence for Helically Kinked Magnetic Flux Ropes in Solar Eruptions, *ApJL*, **464**, L199+, doi:10.1086/310118, 1996.

Sakao, T., Kano, R., Narukage, N., Kotoku, J., Bando, T., DeLuca, E. E., Lundquist, L. L., Tsuneta, S., Harra, L. K., Katsukawa, Y., Kubo, M., Hara,

H., Matsuzaki, K., Shimojo, M., Bookbinder, J. A., Golub, L., Korreck, K. E., Su, Y., Shibasaki, K., Shimizu, T., and Nakatani, I.: Continuous Plasma Outflows from the Edge of a Solar Active Region as a Possible Source of Solar Wind, *Science*, **318**, 1585–, doi:10.1126/science.1147292, 2007.

Sauvaud, J.-A., Larson, D., Aoustin, C., Curtis, D., Médale, J.-L., Fedorov, A., Rouzaud, J., Luhmann, J., Moreau, T., Schröder, P., Louarn, P., Dandouras, I., and Penou, E.: The IMPACT Solar Wind Electron Analyzer (SWEA), *Space Sci. Rev.*, **136**, 227–239, doi:10.1007/s11214-007-9174-6, 2008.

Savcheva, A., Cirtain, J., Deluca, E. E., Lundquist, L. L., Golub, L., Weber, M., Shimojo, M., Shibasaki, K., Sakao, T., Narukage, N., Tsuneta, S., and Kano, R.: A Study of Polar Jet Parameters Based on Hinode XRT Observations, *PASJ*, **59**, 771–+, 2007.

Scherrer, P. H., Bogart, R. S., Bush, R. I., Hoeksema, J. T., Kosovichev, A. G., Schou, J., Rosenberg, W., Springer, L., Tarbell, T. D., Title, A., Wolfson, C. J., Zayer, I., and MDI Engineering Team: The Solar Oscillations Investigation - Michelson Doppler Imager, *Solar Phys.*, **162**, 129–188, doi:10.1007/BF00733429, 1995.

Schindler, K., Hesse, M., and Birn, J.: General magnetic reconnection, parallel electric fields, and helicity, *JGR*, **93**, 5547–5557, doi:10.1029/JA093iA06p05547, 1988.

Schindler, K., Hornig, G., and Murdin, P.: Magnetic Reconnection, doi:10.1888/0333750888/2224, 2000.

Schmieder, B. and Aulanier, G.: What can we learn from lfff magnetic extrapolations, *Advances in Space Research*, **32**, 1875–1881, doi:10.1016/S0273-1177(03)90621-1, 2003.

Schrijver, C. and Siscoe, G.: Heliophysics Plasma Physics of the Local Cosmos., 2009.

Schrijver, C. J. and DeRosa, M. L.: Photospheric and heliospheric magnetic fields, *Solar Phys.*, **212**, 165–200, doi:10.1023/A:1022908504100, 2003.

Schrijver, C. J., Title, A. M., Harvey, K. L., Sheeley, N. R., Wang, Y., van den Oord, G. H. J., Shine, R. A., Tarbell, T. D., and Hurlburt, N. E.: Large-scale coronal heating by the small-scale magnetic field of the Sun, *Nature*, **394**, 152–154, doi:10.1038/28108, 1998.

Schrijver, C. J., Elmore, C., Kliem, B., Török, T., and Title, A. M.: Observations and Modeling of the Early Acceleration Phase of Erupting Filaments Involved in Coronal Mass Ejections, *ApJ*, **674**, 586–595, doi:10.1086/524294, 2008.

Schrijver, C. J., DeRosa, M. L., and Title, A. M.: Magnetic Field Topology and the Thermal Structure of the Corona over Solar Active Regions, in American Astronomical Society Meeting Abstracts, vol. 216 of *American Astronomical Society Meeting Abstracts*, p. 312.01, 2010.

Schwenn, R. and Marsch, E.: Physics of the Inner Heliosphere I. Large-Scale Phenomena., 1990.

Scullion, E., Popescu, M. D., Banerjee, D., Doyle, J. G., and Erdélyi, R.: Jets in Polar Coronal Holes, *ApJ*, **704**, 1385–1395, doi:10.1088/0004-637X/704/2/1385, 2009.

Sheeley, Jr., N. R.: A Volcanic Origin for High-FIP Material in the Solar Atmosphere, *ApJ*, **440**, 884–+, doi:10.1086/175326, 1995.

Sheeley, Jr., N. R.: Elemental Abundance Variations in the Solar Atmosphere, *ApJ*, **469**, 423–+, doi:10.1086/177792, 1996.

Sheeley, Jr., N. R., Howard, R. A., Koomen, M. J., and Michels, D. J.: Associations between coronal mass ejections and soft X-ray events, *ApJ*, **272**, 349–354, doi:10.1086/161298, 1983.

Sheeley, Jr., N. R., Herbst, A. D., Palatchi, C. A., Wang, Y.-M., Howard, R. A., Moses, J. D., Vourlidas, A., Newmark, J. S., Socker, D. G., Plunkett, S. P., Korendyke, C. M., Burlaga, L. F., Davila, J. M., Thompson, W. T., St Cyr, O. C., Harrison, R. A., Davis, C. J., Eyles, C. J., Halain, J. P., Wang, D., Rich, N. B., Battams, K., Esfandiari, E., and Stenborg, G.: Heliospheric Images of the Solar Wind at Earth, *Astrophys. J.*, **675**, 853–862, doi:10.1086/526422, 2008a.

Sheeley, Jr., N. R., Herbst, A. D., Palatchi, C. A., Wang, Y.-M., Howard, R. A., Moses, J. D., Vourlidas, A., Newmark, J. S., Socker, D. G., Plunkett, S. P., Korendyke, C. M., Burlaga, L. F., Davila, J. M., Thompson, W. T., St Cyr, O. C., Harrison, R. A., Davis, C. J., Eyles, C. J., Halain, J. P., Wang, D., Rich, N. B., Battams, K., Esfandiari, E., and Stenborg, G.: SECCHI Observations of the Sun's Garden-Hose Density Spiral, *Astrophys. J. Lett.*, **674**, L109–L112, doi:10.1086/529020, 2008b.

Shibata, K., Ishido, Y., Acton, L. W., Strong, K. T., Hirayama, T., Uchida, Y., McAllister, A. H., Matsumoto, R., Tsuneta, S., Shimizu, T., Hara, H., Sakurai, T., Ichimoto, K., Nishino, Y., and Ogawara, Y.: Observations of X-ray jets with the YOHKOH Soft X-ray Telescope, *PASJ*, **44**, L173–L179, 1992.

Shibata, K., Nitta, N., Strong, K. T., Matsumoto, R., Yokoyama, T., Hirayama, T., Hudson, H., and Ogawara, Y.: A gigantic coronal jet ejected from a compact active

region in a coronal hole, *Astrophys. J. Lett.*, **431**, L51–L53, doi:10.1086/187470, 1994.

Shibata, K., Yokoyama, T., and Shimojo, M.: Coronal X-ray jets observed with Yohkoh/SXT, *Advances in Space Research*, **17**, 197–, doi:10.1016/0273-1177(95)00567-X, 1996.

Shimojo, M. and Shibata, K.: Physical Parameters of Solar X-Ray Jets, *ApJ*, **542**, 1100–1108, doi:10.1086/317024, 2000.

Shimojo, M., Hashimoto, S., Shibata, K., Hirayama, T., Hudson, H. S., and Acton, L. W.: Statistical Study of Solar X-Ray Jets Observed with the YOHKOH Soft X-Ray Telescope, *PASJ*, **48**, 123–136, 1996.

Shimojo, M., Shibata, K., and Harvey, K. L.: Magnetic Field Properties of Solar X-Ray Jets, *Solar Physics*, **178**, 379–392, 1998.

Shimojo, M., Shibata, K., Yokoyama, T., and Hori, K.: One-dimensional and Pseudo-Two-dimensional Hydrodynamic Simulations of Solar X-Ray Jets, *ApJ*, **550**, 1051–1063, doi:10.1086/319788, 2001.

Shodhan, S., Crooker, N. U., Kahler, S. W., Fitzenreiter, R. J., Larson, D. E., Lepping, R. P., Siscoe, G. L., and Gosling, J. T.: Counterstreaming electrons in magnetic clouds, *J. Geophys. Res.*, **105**, 27 261–27 268, doi:10.1029/2000JA000060, 2000.

Simunac, K., Kistler, L., Galvin, A., Lee, M., Popecki, M., Farrugia, C., Moebius, E., Blush, L., Bochsler, P., Wurz, B., and Klecker, B.: In-Situ Observations of Solar Wind Stream Interface Evolution, *Solar Phys.*, **in press**, 2009.

Smith, C. W., L'Heureux, J., Ness, N. F., Acuña, M. H., Burlaga, L. F., and Scheifele, J.: The ACE Magnetic Fields Experiment, *Space Sci. Rev.*, **86**, 613–632, doi:10.1023/A:1005092216668, 1998.

Spadaro, D., Lanzafame, A. C., Consoli, L., Marsch, E., Brooks, D. H., and Lang, J.: Structure and dynamics of an active region loop system observed on the solar disc with SUMER on SOHO, *A&A*, **359**, 716–728, 2000.

Sterling, A. C. and Hudson, H. S.: YOHKOH SXT Observations of X-Ray "Dimming" Associated with a Halo Coronal Mass Ejection, *ApJL*, **491**, L55+, doi:10.1086/311043, 1997.

Sterling, A. C. and Moore, R. L.: Slow-Rise and Fast-Rise Phases of an Erupting Solar Filament, and Flare Emission Onset, *ApJ*, **630**, 1148–1159, doi:10.1086/432044, 2005.

Stone, E. C., Frandsen, A. M., Mewaldt, R. A., Christian, E. R., Margolies, D., Ormes, J. F., and Snow, F.: The Advanced Composition Explorer, *Space Sci. Rev.*, **86**, 1–22, doi:10.1023/A:1005082526237, 1998.

Strong, K. T., Harvey, K., Hirayama, T., Nitta, N., Shimizu, T., and Tsuneta, S.: Observations of the variability of coronal bright points by the Soft X-ray Telescope on YOHKOH, *PASJ*, **44**, L161–L166, 1992.

Sturrock, P. A.: Model of the High-Energy Phase of Solar Flares, *Nature*, **211**, 695–697, doi:10.1038/211695a0, 1966.

Suess, S. T. and Nerney, S.: Flow in streamer boundaries, and streamer stability, *Advances in Space Research*, **33**, 668–675, doi:10.1016/S0273-1177(03)00237-0, 2004.

Sweet, P. A.: The Neutral Point Theory of Solar Flares, in Electromagnetic Phenomena in Cosmical Physics, edited by B. Lehnert, vol. 6 of *IAU Symposium*, pp. 123–+, 1958.

Teriaca, L., Banerjee, D., and Doyle, J. G.: SUMER observations of Doppler shift in the quiet Sun and in an active region, *A&A*, **349**, 636–648, 1999.

Thompson, M. J., Christensen-Dalsgaard, J., Miesch, M. S., and Toomre, J.: The Internal Rotation of the Sun, *Ann. Rev. Astron. Astrophys.*, **41**, 599–643, doi:10.1146/annurev.astro.41.011802.094848, 2003.

Title, A. M. and Schrijver, C. J.: The Sun's Magnetic Carpet, in Cool Stars, Stellar Systems, and the Sun, edited by R. A. Donahue & J. A. Bookbinder, vol. 154 of *Astronomical Society of the Pacific Conference Series*, pp. 345–+, 1998.

Titov, V. S., Hornig, G., and Démoulin, P.: Theory of magnetic connectivity in the solar corona, *Journal of Geophysical Research (Space Physics)*, **107**, 1164–+, doi:10.1029/2001JA000278, 2002.

Titov, V. S., Mikic, Z., Linker, J. A., and Lionello, R.: 1997 May 12 Coronal Mass Ejection Event. I. A Simplified Model of the Preeruptive Magnetic Structure, *Astrophys. J.*, **675**, 1614–1628, doi:10.1086/527280, 2008.

Török, T. and Kliem, B.: Confined and Ejective Eruptions of Kink-unstable Flux Ropes, *Astrophys. J. Lett.*, **630**, L97–L100, doi:10.1086/462412, 2005.

Török, T. and Kliem, B.: Numerical simulations of fast and slow coronal mass ejections, *Astronomische Nachrichten*, **328**, 743–+, doi:10.1002/asna.200710795, 2007.

Tsuneta, S., Acton, L., Bruner, M., Lemen, J., Brown, W., Caravalho, R., Catura, R., Freeland, S., Jurcevich, B., and Owens, J.: The soft X-ray telescope for the SOLAR-A mission, *Solar Physics*, **136**, 37–67, doi:10.1007/BF00151694, 1991.

Tsuneta, S., Ichimoto, K., Katsukawa, Y., Lites, B. W., Matsuzaki, K., Nagata, S., Orozco Suárez, D., Shimizu, T., Shimojo, M., Shine, R. A., Suematsu, Y., Suzuki, T. K., Tarbell, T. D., and Title, A. M.: The Magnetic Landscape of the Sun's Polar Region, *ApJ*, **688**, 1374–1381, doi:10.1086/592226, 2008.

Uchida, Y., McAllister, A., Strong, K. T., Ogawara, Y., Shimizu, T., Matsumoto, R., and Hudson, H. S.: Continual expansion of the active-region corona observed by the YOHKOH Soft X-ray Telescope, *PASJ*, **44**, L155–L160, 1992.

Ulrich, R. K.: The Five-Minute Oscillations on the Solar Surface, *ApJ*, **162**, 993–+, doi:10.1086/150731, 1970.

van Ballegooijen, A. A. and Martens, P. C. H.: Formation and eruption of solar prominences, *ApJ*, **343**, 971–984, doi:10.1086/167766, 1989.

van Driel-Gesztelyi, L.: Emergence and loss of magnetic flux on the solar surface, in SOLMAG 2002. Proceedings of the Magnetic Coupling of the Solar Atmosphere Euroconference, edited by H. Sawaya-Lacoste, vol. 505 of *ESA Special Publication*, pp. 113–120, 2002.

van Driel-Gesztelyi, L.: Magnetic Fields and Large-Scale SXR and EUV Coronal Structures, in Solar Activity and its Magnetic Origin, edited by V. Bothmer & A. A. Hady, vol. 233 of *IAU Symposium*, pp. 205–214, doi:10.1017/S1743921306001888, 2006.

van Driel-Gesztelyi, L. and Culhane, J. L.: Magnetic Flux Emergence, Activity, Eruptions and Magnetic Clouds: Following Magnetic Field from the Sun to the Heliosphere, *Space Sci. Rev.*, **144**, 351–381, doi:10.1007/s11214-008-9461-x, 2009.

Vrsnak, B.: Classification of Prominence Oscillations, *Hvar Observatory Bulletin*, **17**, 23–+, 1993.

Wang, Y. and Sheeley, Jr., N. R.: Coronal White-Light Jets near Sunspot Maximum, *ApJ*, **575**, 542–552, doi:10.1086/341145, 2002.

Wang, Y. and Zhang, J.: A Comparative Study between Eruptive X-Class Flares Associated with Coronal Mass Ejections and Confined X-Class Flares, *ApJ*, **665**, 1428–1438, doi:10.1086/519765, 2007.

Wang, Y.-M. and Sheeley, Jr., N. R.: Understanding the rotation of coronal holes, *Astrophys. J.*, **414**, 916–927, doi:10.1086/173135, 1993.

Wang, Y.-M. and Sheeley, Jr., N. R.: Footpoint Switching and the Evolution of Coronal Holes, *Astrophys. J.*, **612**, 1196–1205, doi:10.1086/422711, 2004.

Warren, H. P. and Brooks, D. H.: The Temperature and Density Structure of the Solar Corona. I. Observations of the Quiet Sun with the EUV Imaging Spectrometer on Hinode, *ApJ*, **700**, 762–773, doi:10.1088/0004-637X/700/1/762, 2009.

Watanabe, M. and Sofko, G. J.: Role of interchange reconnection in convection at small interplanetary magnetic field clock angles and in transpolar arc motion, *J. Geophys. Res.*, **114**, 1209–+, doi:10.1029/2008JA013426, 2009.

Wedemeyer-Böhm, S. and Wöger, F.: Small-scale structure and dynamics of the lower solar atmosphere, in IAU Symposium, edited by R. Erdélyi & C. A. Mendoza-Briceño, vol. 247 of *IAU Symposium*, pp. 66–73, doi:10.1017/S1743921308014671, 2008.

Williams, D. R., Török, T., Démoulin, P., van Driel-Gesztelyi, L., and Kliem, B.: Eruption of a Kink-unstable Filament in NOAA Active Region 10696, *Astrophys. J. Lett.*, **628**, L163–L166, doi:10.1086/432910, 2005.

Wimmer-Schweingruber, R. F., Crooker, N. U., Balogh, A., Bothmer, V., Forsyth, R. J., Gazis, P., Gosling, J. T., Horbury, T., Kilchenmann, A., Richardson, I. G., Richardson, J. D., Riley, P., Rodriguez, L., Steiger, R. V., Wurz, P., and Zurbuchen, T. H.: Understanding Interplanetary Coronal Mass Ejection Signatures. Report of Working Group B, *Space Sci. Rev.*, **123**, 177–216, doi:10.1007/s11214-006-9017-x, 2006.

Winebarger, A. R., DeLuca, E. E., and Golub, L.: Apparent Flows above an Active Region Observed with the Transition Region and Coronal Explorer, *Astrophys. J. Lett.*, **553**, L81–L84, doi:10.1086/320496, 2001.

Winebarger, A. R., Warren, H., van Ballegooijen, A., DeLuca, E. E., and Golub, L.: Steady Flows Detected in Extreme-Ultraviolet Loops, *ApJL*, **567**, L89–L92, doi:10.1086/339796, 2002.

Withbroe, G. L.: Activity and Outer Atmosphere of the Sun, in Saas-Fee Advanced Course 11: Activity and Outer Atmosphere of the Sun and Stars, edited by A. O. Benz, Y. Chimielewski, M. C. E. Huber, & H. Nussbaumer , pp. 1–+, 1981.

Wuelser, J., Lemen, J. R., Tarbell, T. D., Wolfson, C. J., Cannon, J. C., Carpenter, B. A., Duncan, D. W., Gradwohl, G. S., Meyer, S. B., Moore, A. S., Navarro, R. L., Pearson, J. D., Rossi, G. R., Springer, L. A., Howard, R. A., Moses, J. D., Newmark, J. S., Delaboudiniere, J., Artzner, G. E., Auchere, F., Bougnet, M., Bouyries, P., Bridou, F., Clotaire, J., Colas, G., Delmotte, F., Jerome, A.,

Lamare, M., Mercier, R., Mullot, M., Ravet, M., Song, X., Bothmer, V., and Deutsch, W.: *EUVI: the STEREO-SECCHI extreme ultraviolet imager*, **5171**, 111–122, doi:10.1117/12.506877, 2004.

Yashiro, S., Gopalswamy, N., Akiyama, S., Michalek, G., and Howard, R. A.: Visibility of coronal mass ejections as a function of flare location and intensity, *Journal of Geophysical Research (Space Physics)*, **110**, 12–+, doi:10.1029/2005JA011151, 2005.

Yeates, A. R. and Mackay, D. H.: Initiation of Coronal Mass Ejections in a Global Evolution Model, *ApJ*, **699**, 1024–1037, doi:10.1088/0004-637X/699/2/1024, 2009.

Yeates, A. R., Attrill, G. D. R., Nandy, D., Mackay, D. H., Martens, P. C. H., and van Ballegooijen, A. A.: Comparison of a Global Magnetic Evolution Model with Observations of Coronal Mass Ejections, *ApJ*, **709**, 1238–1248, doi:10.1088/0004-637X/709/2/1238, 2010.

Yokoyama, M. and Masuda, S.: Formation Mechanism of Soft X-Ray Transient Trans-Equatorial Loop System, *Solar Physics*, **254**, 285–296, doi:10.1007/s11207-008-9292-7, 2009.

Yokoyama, M. and Masuda, S.: Trans-Equatorial Loop System Arising from Coronal Hole Boundaries through Interactions between Active Regions and Coronal Holes, *Solar Physics*, pp. 33–+, doi:10.1007/s11207-010-9525-4, 2010.

Yokoyama, T. and Shibata, K.: What is the condition for fast magnetic reconnection?, *Astrophys. J. Lett.*, **436**, L197–L200, doi:10.1086/187666, 1994.

Yokoyama, T. and Shibata, K.: Magnetic Reconnection as the Origin of X-Ray Jets and Hα Surges on the Sun, *Nature*, **375**, 42–+, doi:10.1038/375042a0, 1995.

Yokoyama, T. and Shibata, K.: Numerical Simulation of Solar Coronal X-Ray Jets Based on the Magnetic Reconnection Model, *PASJ*, **48**, 353–376, 1996.

Young, P. R.: The element abundance FIP effect in the quiet Sun, *A&A*, **439**, 361–366, doi:10.1051/0004-6361:20052963, 2005.

Young, P. R., Del Zanna, G., Mason, H. E., Dere, K. P., Li, E., Lini, M., Doschek, G. A., Brown, C. M., Culhane, L., Harra, L. K., Watanabe, T., and Hara, H.: EUV Emission Lines and Diagnostics Observed with Hinode/EIS, *PASJ*, **59**, 857–+, 2007.

Young, P. R., Watanabe, T., Hara, H., and Mariska, J. T.: High precision density measurements in the solar corona: I. Analysis methods and results for Fe XII and Fe XIII, *ArXiv e-prints*, **805**, 2008.

Young, P. R., Watanabe, T., Hara, H., and Mariska, J. T.: High-precision density measurements in the solar corona. I. Analysis methods and results for Fe XII and Fe XIII, *A&A*, **495**, 587–606, doi:10.1051/0004-6361:200810143, 2009.

Zurbuchen, T. H. and Richardson, I. G.: In-Situ Solar Wind and Magnetic Field Signatures of Interplanetary Coronal Mass Ejections, *Space Sci. Rev.*, **123**, 31–43, doi:10.1007/s11214-006-9010-4, 2006.

Zurbuchen, T. H., Fisk, L. A., Gloeckler, G., and von Steiger, R.: The solar wind composition throughout the solar cycle: A continuum of dynamic states, *Geophys. Res. Lett.*, **29**, 090 000–1, doi:10.1029/2001GL013946, 2002.

Zwaan, C.: Elements and patterns in the solar magnetic field, *ARA&A*, **25**, 83–111, doi:10.1146/annurev.aa.25.090187.000503, 1987.